Topology Optimization of Flow Problems Modeled by the Incompressible Navier-Stokes Equations

by

Sebastian Kreissl

Dipl.-Ing., Technische Universität München, 2007

A thesis submitted to the

Faculty of the Graduate School of the

University of Colorado in partial fulfillment

of the requirements for the degree of

Doctor of Philosophy

Department of Aerospace Engineering

2011

This thesis entitled:
Topology Optimization of Flow Problems Modeled by the Incompressible Navier-Stokes Equations
written by Sebastian Kreissl
has been approved for the Department of Aerospace Engineering

_____
Dr. Kurt Maute

_____
Dr. Carlos Felippa

_____
Dr. Daven Henze

_____
Dr. Mahmoud Hussein

_____
Dr. Georg Pingen

Date _____

The final copy of this thesis has been examined by the signatories, and we find that both the content and the form meet acceptable presentation standards of scholarly work in the above mentioned discipline.

Kreissl, Sebastian (Ph.D., Aerospace Engineering)

Topology Optimization of Flow Problems Modeled by the Incompressible Navier-Stokes Equations

Thesis directed by Prof. Dr. Kurt Maute

This work is concerned with topology optimization of incompressible flow problems. While size and shape optimization methods are limited to modifying existing boundaries, topology optimization allows for merging boundaries as well as creating new ones. Since topology optimization methods do not require a good initial guess, they are powerful tools for finding new and non-intuitive designs. The latter is particularly beneficial for flow problems which are typically nonlinear as well as transient. Depending on the complexity of the flow problem, predicting a solution may be challenging. Determining an improved or optimized design for complex flow problems is an even greater challenge as it not only requires a solution to the flow problem for a given design, but also a prediction on how a design change will affect the flow. Fluid topology optimization commonly uses a material interpolation approach for describing the geometry during the optimization process: solid material is modeled via an artificial porosity that penalizes the flow velocities. While this approach works well for simple steady-state problems aiming to minimize the dissipated energy, the current study shows that using the porosity approach may cause issues for more complex problems such as coupled fluid-structure-interaction (FSI) systems, unsteady flow problems or problems aiming to match a target performance. To overcome these issues a geometric boundary description based on level sets is developed. This geometric boundary description is applied to both, a steady-state hydrodynamic lattice Boltzmann formulation and a stabilized finite element formulation of the steady-state Navier-Stokes equations. The enforcement of the no-slip condition along the fluid-solid interface is handled via an immersed boundary technique in case of the lattice Boltzmann method, while the Navier-Stokes formulation uses an extended finite element method (XFEM). Through the research conducted in this work, the spectrum of flow problems that can be solved by topology optimization techniques has been broadened significantly.

Acknowledgements

The work presented in this document was conducted during my time as a Ph.D. student in the Aerospace Department at the University of Colorado at Boulder, from January 2008 until October 2011. I would like to acknowledge the support from the National Science Foundation under grant number DMI-0348759 and DMI-0729529. The opinions and conclusions presented in this thesis are those of the author and do not necessarily reflect the views of the sponsoring organization.

Special thanks to my advisor, Professor Kurt Maute for his continuous support and the countless fruitful discussions. I truly enjoyed working in the demanding yet informal environment of his research group. To the members of my defense committee - Professor Carlos Felippa, Professor Daven Henze, Professor Mahmoud Hussein and Professor Georg Pingen - I would like to express my gratitude for providing helpful comments. Many thanks to my fellow Ph.D. students both within and outside of Professor Maute's research group for turning the time in Boulder into great experience. Finally, I thank my family for their support through the course of my education.

Contents

Chapter

Figures

Figure

Publications

This thesis includes the following publications:

[P1] S. Kreissl, G. Pingen, and K. Maute. An Explicit Level Set Approach for Generalized Shape Optimization of Fluids with the Lattice Boltzmann Method. International Journal for Numerical Methods in Fluids, 2009, DOI: 10.1002/fld.2193.

[P2] S. Kreissl, G. Pingen, A. Evgrafov, and K. Maute. Topology Optimization of Flexible Micro-Fluidic Devices. Structural and Multidisciplinary Optimization, 2010, DOI: 10.1007/s00158-010-0526-6.

[P3] S. Kreissl, G. Pingen, and K. Maute. Topology Optimization for Unsteady Flow. International Journal for Numerical Methods in Engineering, 2011, DOI: 10.1002/nme.3151.

[P4] S. Kreissl, and K. Maute. Fluid Topology Optimization Based on the Extended Finite Element Method. Submitted to Structural and Multidisciplinary Optimization.

Chapter 1

Introduction

1.1 Motivation

The origins of fluid mechanics can be traced back over 2000 years to the ancient Greeks, when Aristotle developed the concept of the continuum and discovered the effect of aerodynamic resistance. However, it was not until the middle of the 19th century that two mathematicians/physicians - Claude Navier, Fig. 1.1 and Sir George Stokes, Fig. 1.2 - independently of each other, laid the foundations of modern fluid dynamics [46]. Since then the Navier-Stokes (NS) equations have been applied to solve a wide range of flow problems. With the advent of computational fluid dynamics (CFD) in the late 1960s more complex flow geometries could be simulated and analyzed numerically. The ever advancing computational capabilities/technologies and the improvements of numerical methods for solving the NS equations now allows us to solve flow around entire cars, planes, etc. with hundreds of millions of degrees of freedom. While further research is necessary to solve even larger and more complex flows, CFD has reached a level of maturity where standard mid-to-large scale engineering problems can be simulated in a reasonable amount of time. The capability of analyzing an existing design often evokes the desire to use these simulation tools to also improve the design. This is where the current thesis fits in: its goal is to apply topology optimization techniques to flow problems in order to improve the performance of an existing design or to find a new design that performs in the desired way.

The NS equations are described by a set of time-dependent nonlinear partial differential equations. Their complexity makes both the computation of a flow solution (flow problem) and even more so the prediction of an improving design change (optimization problem) a challenging task. Therefore, solving

Figure 1.1: Claude L. M. H. Navier (1785-1836) [1].

Figure 1.2: Sir George G. Stokes (1819-1903) [1].

flow optimization problems with mere 'engineering intuition' can be difficult or even infeasible. Instead of relying on intuition, black-box optimization modules can be employed: the design engineer formulates the flow problem including boundary conditions and initial design, defines a design space and utilizes the optimizer to find a better design. While this approach will simplify and speed up the design process, it generally will still require an experienced design engineer to setup the optimization problem, monitor the optimization process, and subsequently interpret the final design.

This thesis focuses on topology optimization as it is - compared to size and shape optimization - the most general optimization technique: existing fluid-solid boundaries can be merged and new ones can be created. Therefore, the results of topology optimization are far less sensitive to the initial design than results obtained with size and shape optimization techniques. This feature makes topology optimization well suited for complex flow problems, where a 'good' initial design might be difficult to find. Furthermore, due to its flexibility topology optimization might facilitate finding new non-intuitive designs making it a powerful tool for the design process.

Employing optimization techniques to flow problems will aid in the design of cars, planes, etc., further advancing performance as well as efficiency. However, since topology optimization methods require tens to hundreds of (flow) analyses, this technology is currently still limited to simple and relatively small problems. This thesis focuses on the development of numerical methodologies to widen the range of flow problems

that can be solved by topology optimization techniques.

1.2 Thesis Structure

This document summarizes the work that has been conducted during the author's Ph.D. study. The bulk of this work has already been published or submitted for publication. Therefore, to minimize redundancies, only the relevant fundamental aspects and basic concepts are presented. For thoroughness, the publications [P1]–[P4] that stemmed from this Ph.D. study are included in the appendix of this document. The thesis structure is outlined in the following , cp. Fig. 1.3.

Chapter 2 introduces the incompressible NS equations in non-dimensional variables. This is followed by a section on the lattice Boltzmann method (LBM) which approximates the NS equations for low Mach number flows. The LBM is employed for describing the flow field in publications [P1] and [P2]. Section 2.2 outlines the finite element formulation of the incompressible NS equations which is used for discretizing the flow field in publications [P3] and [P4].

Chapter 3 focuses on design optimization. It starts with an overview of optimization techniques in Section 3.1. This is followed by a section that briefly outlines different optimization strategies/algorithms. Section 3.3 describes the sensitivity analysis and explains the difference between direct and adjoint methods. Section 3.4 gives an overview of a set of optimality conditions commonly utilized in topology optimization. In Section 3.5 the basics of structural topology optimization are outlined. The latter is employed in publication [P2]. Finally, Section 3.6 presents the concept of fluid topology optimization which is utilized in publications [P1]–[P4].

The document is summarized in Chapter 4. A set of ideas for potential future work can be found in Section 4.2.

1.3 Summary of Publications

This section briefly outlines the publications [P1]-[P4] that are included in the appendix of this document.

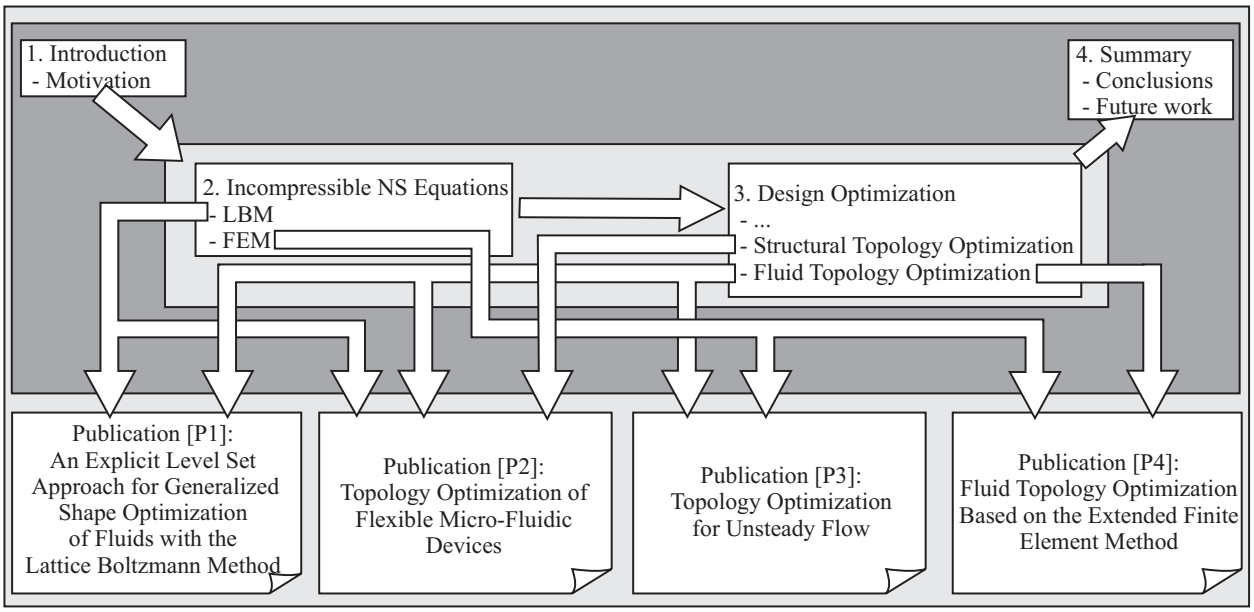

Figure 1.3: Thesis structure.

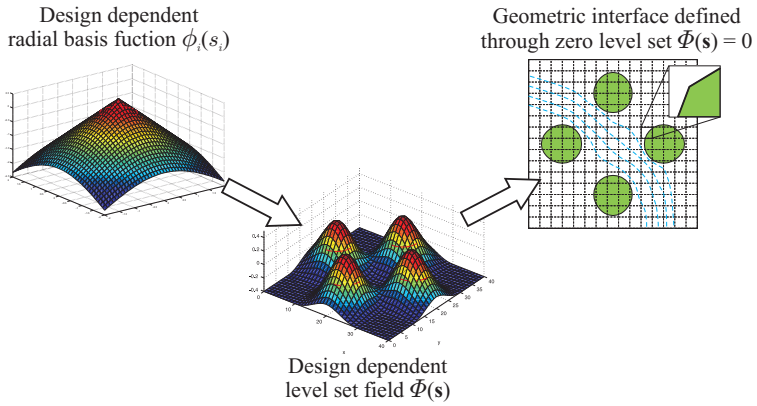

Figure 1.4: [P1]: Level sets for geometric boundary description.

1.3.1 Summary of [P1]: An Explicit Level Set Approach for Generalized Shape Optimization of Fluids with the Lattice Boltzmann Method

This study is concerned with a generalized shape optimization approach for finding the geometry of fluidic devices and obstacles immersed in incompressible flows. The approach is based on a level set representation of the fluid-solid interface and a hydrodynamic LBM to predict steady-state flow fields. An explicit level set method is introduced that does not involve the solution of the Hamilton-Jacobi equation and allows using standard nonlinear programming methods. In contrast to previous works on fluid topology optimization, the boundary conditions along the fluid-structure interface are enforced by second-order accurate interpolation schemes, cp. Fig. 1.4, avoiding shortcomings of flow penalization methods and Brinkman formulations frequently used in topology optimization. To ensure smooth boundaries and mesh independent results, a simple, computationally inexpensive filtering method is applied to regularize the level set field.

One drawback of the developed method is the fact that no new boundaries can be created which limits the topological complexity of the final design. This disadvantage can be mitigated by choosing a proper initial design that has a sufficient number of separated solid regions (‘islands’). Inclusions or holes completely surrounded by solid, on the other hand, have no influence of the flow solution and are therefore irrelevant for pure fluid topology optimization.

The employed approach has proved to produce results that are consistent with studies that used a material interpolation approach.

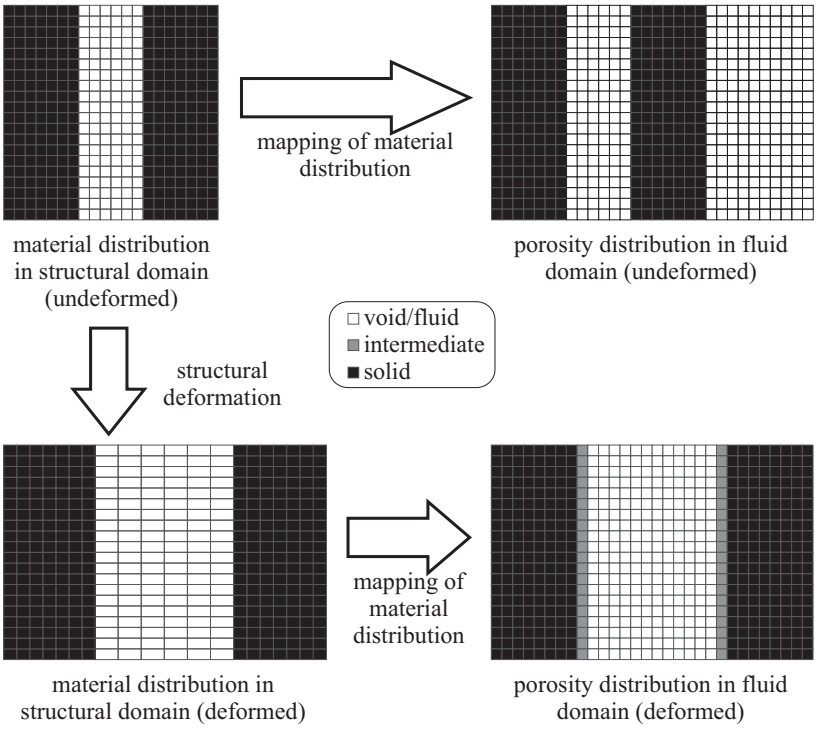

Figure 1.5: [P2]: One-way coupled fluid-structure systems.

1.3.2 Summary of [P2]: Topology Optimization of Flexible Micro-Fluidic Devices

A multi-objective topology optimization formulation for the design of dynamically tunable fluidic devices is introduced. The flow is manipulated via external and internal mechanical actuation, leading to elastic deformations of flow channels. The design objectives characterize the performance in the undeformed and deformed configuration. The layout of fluid channels is optimized using a material interpolation approach, cp. Fig. 1.5. In addition, the thickness distribution, the distribution of active material for internal actuation, and the support conditions are optimized. The coupled fluid-structure response is described by a nonlinear finite element model and a hydrodynamic LBM. Focusing on applications with low flow velocities and low pressure, structural deformations due to fluid-forces are neglected. A mapping scheme is defined that couples the material distributions in the structural and fluid domain.

The study proved the applicability of topology optimization to fluid-structure systems. The developed mapping method allows for a simple coupling between the two domains. While this approach leads to reasonable results for the employed simplified fluid-structure model - the structural displacements affect the fluid flow but the fluid does not affect the structure - it will cause issues when applied to a fully coupled system. Modeling the effect of fluid pressure on the structural deformation of porous elements is a challenging task. The proposed mapping procedure is based on the intersection of structural and fluid elements. Therefore, its implementation is rather simple and computationally inexpensive for 2D. In 3D problems however, this approach would be significantly more complex and expensive.

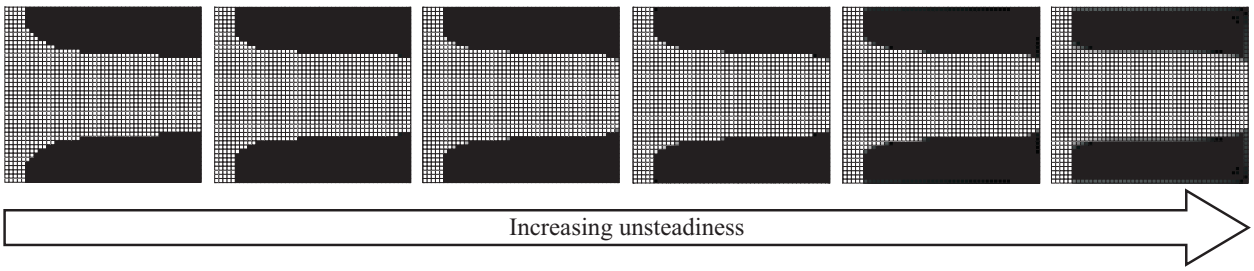

Figure 1.6: [P3]: Optimized diffuser designs for various levels of unsteadiness.

1.3.3 Summary of [P3]: Topology Optimization for Unsteady Flow

This publication is concerned with optimizing the layout of devices for unsteady incompressible flow at low Reynolds and Mach numbers. The flow is predicted by a stabilized finite element formulation of the incompressible Navier-Stokes equations. A Brinkman penalization is used to enforce zero-velocities in solid material allowing for overall topological changes in the geometry of the fluid-solid interface. A design-dependent stabilization scheme is introduced to mitigate numerical instabilities in porous material. Unlike previous studies on fluid topology optimization the study focuses on unsteady flows, since many engineering applications involve time-dependent phenomena. The transient effects can be due to time-varying boundary conditions - as considered in this study - or due to the fact that the flow field is inherently unstable: e.g. the flow past a cylinder becomes unstable for Reynolds numbers $Re > 40$ [52].

The emergence of non-physical artifacts in the optimized material distribution is observed and linked to an insufficient resolution of the flow field and an improper representation of the pressure field within solid material by the Brinkman penalization. Numerical examples demonstrate that the designs optimized for unsteady flow differ significantly from their steady-state counterparts, cp. Fig. 1.6. The performance of steady-state designs deteriorates as the flow varies more rapidly in time. Several key issues regarding the application of the Brinkman penalization to topology optimization are identified and addressed. While only 2D problems with Reynolds numbers up to $Re = 1000$ are studied, the proposed formulations and numerical methods can be easily extended onto 3D problems and are applicable to flows with larger Reynolds numbers. However, the stringent requirements on mesh refinement and the associated numerical costs for forward and sensitivity analysis are expected to limit the range of optimization problems that can be solved with the proposed method.

1.3.4 Summary of [P4]: Fluid Topology Optimization Based on the Extended Finite Element Method

This study focuses on finding the optimal layout of fluidic devices subjected to incompressible flow at low Reynolds and Mach numbers. The proposed approach uses a level set method to describe the fluid-

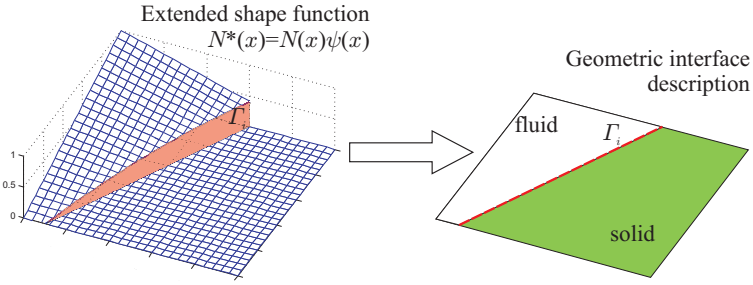

Figure 1.7: [P4]: Geometric boundary description via the extended finite element method.

solid interface geometry. The flow field is modeled by the incompressible Navier-Stokes equations and discretized by the extended finite element method (XFEM), cp. Fig. 1.7. The no-slip condition along the fluid-solid interface is enforced via a stabilized Lagrange multiplier method. Unlike the commonly used porosity approach, the XFEM approach does not rely on a material interpolation, which allows for more flexibility in formulating the design problems. Further, it mitigates shortcomings of the porosity approach, such as: spurious pressure diffusion through solid material, large sensitivity of the accuracy of the boundary enforcement with respect to the model parameters, which may affect the optimization results, and poor boundary resolution. Numerical studies verify that the proposed method is able to recover optimization results obtained with the porosity approach. Furthermore, it is demonstrated that the XFEM approach provides great flexibility in solving optimization problems with a broad range of objectives and constraints. The proposed methodology yields physical results for problems that cannot be solved with the porosity approach.

However, since the sensitivities only differ from zero within a band around the interface, it is only possible to systematically merge existing boundaries, but no new domains of solid can emerge. This limitation can be mitigated by seeding the initial design with a sufficient number of separated solid areas. Compared to the Brinkman penalization, the proposed approach is significantly more complex in regards of implementation, potentially preventing the use of commercial software tools.

Chapter 2

Incompressible Navier-Stokes Equations

This chapter outlines the governing equations of motion employed for describing the fluid state. The incompressible, temperature dependent, unsteady NS equations are given by:

$$\text{Momentum equation:}\quad \hat{\rho}\left(\frac{\partial \hat{v}_i}{\partial \hat{t}}+\frac{\partial \hat{v}_i}{\partial \hat{x}_j}\hat{v}_j\right)=\frac{\partial \hat{\sigma}_{ij}}{\partial \hat{x}_j}+\hat{f}_i^B, \tag{2.1}$$

$$\text{Incompressibility condition:}\quad \frac{\partial \hat{v}_i}{\partial \hat{x}_i}=0, \tag{2.2}$$

$$\text{Energy conservation:}\quad \frac{\partial \hat{T}}{\partial \hat{t}}+\hat{v}_i\frac{\partial \hat{T}}{\partial \hat{x}_i}=\frac{\hat{\nu}}{\hat{c}_p}\left(2\left(\frac{\partial \hat{v}_i}{\partial \hat{x}_i}\right)^2+\left(\frac{\partial \hat{v}_i}{\partial \hat{x}_j}\right)^2\right)\hat{\alpha}_T\frac{\partial^2 \hat{T}}{\partial \hat{x}_i^2}, \tag{2.3}$$

where $\hat{\rho},\hat{v}_i,\hat{p},\hat{t},\hat{T}$ describe the dimensional density, velocity, pressure, time and temperature respectively. The scalars $\hat{\nu}$, $\hat{c}_p$ and $\hat{\alpha}_T$ are the dimensional kinematic viscosity, specific heat, and coefficient of thermal conductivity. The subscripts i,j define the spatial directions. The external body forces are given by $\hat{f}_i^B$. The stress tensor $\hat{\sigma}_{ij}$ is defined as:

$$\hat{\sigma}_{ij}=-\hat{p}\delta_{ij}+2\hat{\mu}\frac{1}{2}\left(\frac{\partial \hat{v}_i}{\partial \hat{x}_j}+\frac{\partial \hat{v}_j}{\partial \hat{x}_i}\right). \tag{2.4}$$

The current study focuses on isothermal cases, i.e. Eq. (2.3) is neglected in the following. For deriving the non-dimensional form of the NS equations, the following definitions are used:

$$\begin{aligned}
\hat{\rho}&=\hat{\rho}_r\rho, & \hat{v}_i&=\hat{v}_r v_i,\\
\hat{x}_i&=\hat{L}_r x_i, & \hat{p}&=\hat{\rho}_r\hat{v}_r^2 p,\\
\hat{t}_i&=\tfrac{\hat{L}_r}{\hat{v}_r}t, & \hat{\sigma}_{ij}&=\hat{\rho}_r\hat{v}_r^2\sigma_{ij},
\end{aligned} \tag{2.5}$$

where '$\hat{\square}$' and '$\square$' describe dimensional and non-dimensional quantities. The subscript 'r' indicates dimensional reference quantities. Substituting the definitions from Eqs. (2.4) and (2.5) in Eqs. (2.1) and (2.2)

yields the common form of the incompressible isothermal NS equations:

$$\text{Momentum equation: } \rho\left(\frac{\partial v_i}{\partial t}+\frac{\partial v_i}{\partial x_j}v_j\right)=-\frac{\partial p}{\partial x_j}\delta_{ij}+2\mu\frac{1}{2}\left(\frac{\partial^2 v_i}{\partial x_j\partial x_j}+\frac{\partial^2 v_j}{\partial x_i\partial x_j}\right)+f_i^B, \tag{2.6}$$

$$\text{Incompressibility condition: } \frac{\partial v_i}{\partial x_i}=0, \tag{2.7}$$

where the scalar μ defines the non-dimensional dynamic viscosity:

$$\mu=\frac{\hat{\mu}}{\hat{L}_r\hat{v}\hat{\rho}}=\frac{1}{Re}, \tag{2.8}$$

with *Re* being the Reynolds number.

For solving partial differential equations (PDEs), like the NS equations, different discretization techniques have been developed. The three most common are: (a) *Finite Difference Method*: while this approach is well established and straightforward it is no longer an area of active research [43]. (b) *Finite Volume Method*: first introduced by MacCormack and Paullay [57], this method has gained popularity for solving flow problems. (c) *Finite Element Method (FEM)*: this method was first developed for solving structural problems [86]. Hughes and Tezduyar later extended it to fluid flows [44].

In this thesis both a finite difference and a finite element discretization are considered. In case of the finite difference discretization a hydrodynamic LBM is chosen since previous theoretical and numerical studies have shown promising results [29, 68, 69].

2.1 Lattice Boltzmann Method for Incompressible Flows

The LBM, which can be derived from the Boltzmann equation [3], approximates the NS equations for low Mach number flows [17, 81, 88]. While it was originally intended for modeling gases, it can be used to describe various particle-like quantities such as molecules, electrons, and photons making it a flexible approach, see e.g. [16]. Further advantages are its simplicity and as a result its straightforward implementation. The derivations in this section closely follow the work by Pingen and co-workers. For more details the reader is referred to [68, 69].

The LBM models hydrodynamic flows based on kinetic theory. Yu et al. [89] derived the LBM from

(a) Velocity vector $\mathbf{e}_\alpha$ (b) Distribution function $\mathbf{f}_\alpha$

Figure 2.1: Velocity distribution for the D2Q9 lattice [68].

the Boltzmann equation with the Bhatnagar-Gross-Krook collision operator [10, 69]:

$$\frac{\partial f}{\partial t} + \xi \cdot \nabla f = -\frac{1}{\lambda}\left(f - f^{eq}\right), \tag{2.9}$$

where f, f^{eq}, ξ, λ define the distribution function, the equilibrium distribution function, the velocity and the relaxation time. The right hand side of Eq. (2.9) defines the collision operator [69].

Discretizing Eq. (2.9) in space, time and velocity, cp. Fig. 2.1, yields:

$$f_\alpha\left(\mathbf{x}_i + \mathbf{e}_\alpha \delta t, t + \delta t\right) = f_\alpha\left(\mathbf{x}_i, t\right) - \frac{1}{\tau_R}\left(f_\alpha\left(\mathbf{x}_i, t\right) - f_\alpha^{eq}\left(\mathbf{x}_i, t\right)\right), \tag{2.10}$$

where $\mathbf{e}_\alpha$ is the velocity vector, f_α is the distribution function in α-direction at the location $\mathbf{x}_i$; δt is the time step and τ_R is the dimensionless relaxation time. Separating Eq. (2.10) into a local collision and a global propagation step yields [69]:

$$\text{Collision: } \widetilde{f_\alpha}(\mathbf{x}_i, t) = f_\alpha(\mathbf{x}_i, t) - \frac{1}{\tau_R}\left(f_\alpha(\mathbf{x}_i, t) - f_\alpha^{eq}(\mathbf{x}_i, t)\right), \tag{2.11}$$

$$\text{Propagation: } f_\alpha(\mathbf{x}_i + \delta t \mathbf{e}_\alpha, t + \delta t) = \widetilde{f_\alpha}(\mathbf{x}_i, t). \tag{2.12}$$

For flows with low Mach numbers, the equilibrium distribution function f_α^{eq} in Eq. (2.11) can be derived by a Taylor series expansion of the Maxwell–Boltzmann equilibrium distribution [41, 69]:

$$f_\alpha^{eq} = w_\alpha \rho \left(1 + 3(\mathbf{e}_\alpha \cdot \mathbf{v}) + \frac{9}{2}(\mathbf{e}_\alpha \cdot \mathbf{v})^2 - \frac{3}{2}\mathbf{v}^2\right), \tag{2.13}$$

where ρ represents the macroscopic density, the vector $\mathbf{v}$ is the macroscopic velocity, and w_α are lattice weights that depend on the lattice geometry. The macroscopic parameters, density and velocity, are evaluated by taking statistical moments of the distribution function f_α, and are given by [69]:

$$\rho(\mathbf{x},t) = \sum_{\alpha=0}^{8} f_\alpha(\mathbf{x},t), \tag{2.14}$$

$$\rho\mathbf{v}(\mathbf{x},t) = \sum_{\alpha=0}^{8} \mathbf{e}_\alpha f_\alpha(\mathbf{x},t). \tag{2.15}$$

2.2 Finite Element Method for Incompressible Flows

Analogous to structural problems, FEM for fluid flows employs a Galerkin discretization: the strong form of the equations (2.6)-(2.7) are weighted with elemental test functions and integrated over the domain which is divided into elements. The resulting weak form can be written as follows:

$$R = \underbrace{\int_\Omega w_i \left(\rho\left(\frac{\partial v_i}{\partial t} + \frac{\partial v_i}{\partial x_j}v_j\right) - \frac{\partial \sigma_{ij}}{\partial x_j} - f_i^B\right) d\Omega}_{\text{momentum term}} + \underbrace{\int_\Omega q \frac{\partial v_i}{\partial x_i} d\Omega}_{\text{incompressibility term}} = 0, \tag{2.16}$$

where R defines the residual, w_i and q are a velocity and pressure test functions. Generally, the derivative of the stress tensor $\partial\sigma_{ij}/\partial x_j$ is integrated by parts:

$$\begin{aligned} R = &\underbrace{\int_\Omega w_i \rho \frac{\partial v_i}{\partial t} d\Omega}_{\text{inertia term}} + \underbrace{\int_\Omega w_i \rho \frac{\partial v_i}{\partial x_j} v_j d\Omega}_{\text{convective term}} - \underbrace{\int_\Omega \frac{1}{2}\left(\frac{\partial w_i}{\partial x_j} + \frac{\partial w_j}{\partial x_i}\right) p\delta_{ij} d\Omega}_{\text{pressure term}} \\ &+ \underbrace{\int_\Omega \frac{1}{2}\left(\frac{\partial w_i}{\partial x_j} + \frac{\partial w_j}{\partial x_i}\right) 2\mu \frac{1}{2}\left(\frac{\partial v_i}{\partial x_j} + \frac{\partial v_j}{\partial x_i}\right) d\Omega}_{\text{shear term}} + \underbrace{\int_\Omega q \frac{\partial v_i}{\partial x_i} d\Omega}_{\text{incompressibility term}} \\ &- \underbrace{\int_\Gamma w_i n_j \left(-p\delta_{ij} + 2\mu \frac{1}{2}\left(\frac{\partial v_i}{\partial x_j} + \frac{\partial v_j}{\partial x_i}\right)\right) d\Gamma}_{\text{boundary term}} = 0. \end{aligned} \tag{2.17}$$

In this form the boundary term contains the traction t_i explicitly:

$$t_i = n_j \left(-p\delta_{ij} + 2\mu \frac{1}{2}\left(\frac{\partial v_i}{\partial x_j} + \frac{\partial v_j}{\partial x_i}\right)\right), \tag{2.18}$$

which allows for a convenient implementation of various boundary conditions: e.g. the common 'traction-free' condition in which case the boundary term is simply set to zero.

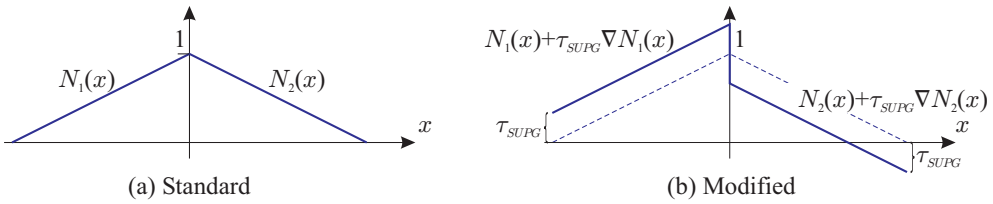

Figure 2.2: Shape functions.

The convective term in Eq. (2.17) causes major difficulties when standard Galerkin based finite elements are used for fluid problems: in practice the flow solution often shows spurious node-to-node oscillations [23]. To eliminate these oscillations different stabilization techniques have been developed, such as the Galerkin-Least-Squares method, e.g. [67], the Bubble method, e.g. [31] as well the Streamline-Upwind/Pedrov-Galerkin (SUPG) method [85]. Due to the straightforwardness of the SUPG formulation, the current study focuses on the latter. Figure 2.2 illustrates the motivation behind the SUPG stabilization: the standard shape functions, Fig. 2.2(a), have equal weights for upstream and downstream direction. This can lead to instabilities as the upstream information affects the solution at location P more than the downstream information, cp. Fig. 2.3. As a consequence, the upstream information needs to be weighted more heavily. To accomplish this, the shape functions $N_i(x)$ are modified as depicted in Fig. 2.2(b): the weight of the upstream direction is increased by $\tau_{SUPG}\nabla N_1(x)$, where τ_{SUPG} is a scalar stabilization parameter. Given the negative slope of $N_2(x)$, the term $\tau_{SUPG}\nabla N_2(x)$ reduces the weight of the downstream direction. The challenge lies in finding a proper τ_{SUPG} value that adds an appropriate amount of diffusion preventing instabilities without perturbing the solution too much.

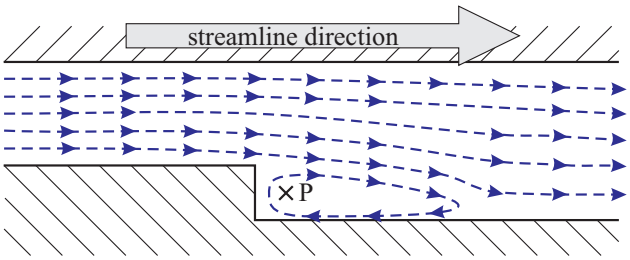

Figure 2.3: Importance of upstream information.

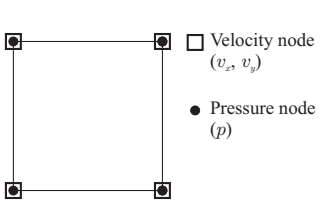

(a) Bilinear four node 2D element (v4p4-element)

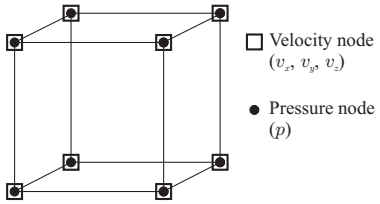

(b) Trilinear eight node 3D element (v8p8-element)

Figure 2.4: Equal order velocity and pressure elements.

Besides the convective term, incompressible flow problems have another potential source for instabilities: if an inappropriate combination of interpolation functions is used for the velocity and the pressure, oscillations may occur in the pressure field [85]. For the sake of a simple implementation, equal order interpolation functions are chosen for pressure and velocities in this work, cp. Fig 2.4. However, since these equal order elements violate the Ladyzhenskaya [53], Babuška [6] and Brezzi [13] (LBB) stability condition, the pressure field needs to be stabilized as well. In the current work the Pressure-Stabilizing/Petrov-Galerkin (PSPG) scheme is employed to prevent pressure oscillations. For more details on the stabilization used in this work the reader is referred to [P3] and the references therein.

Figure 2.5 shows the flow around a cylinder at Reynolds number $Re = 100$ and the characteristic Kármán-vortex street. The flow domain is discretized by 576,000 SUPG/PSPG-stabilized v8p8-elements, cp. Fig. 2.4b.

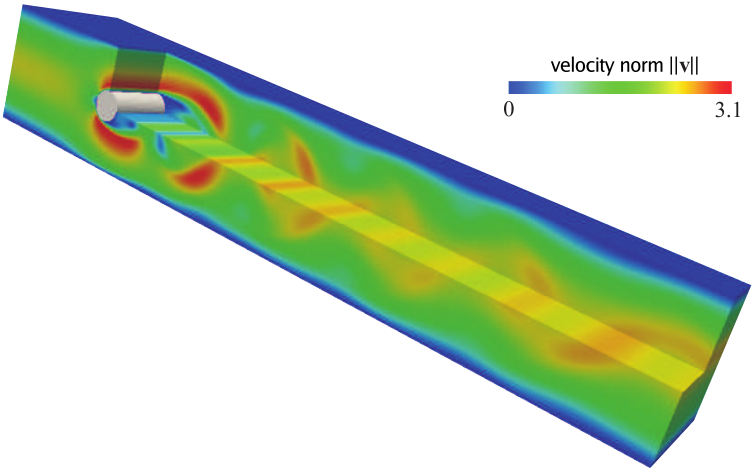

Figure 2.5: Flow around 3D cylinder at $Re = 100$.

Chapter 3

Design Optimization

Design optimization is the discipline that, starting from an initial design and a given design space, aims at finding a geometry that improves an objective while satisfying a set of constraints. Mathematically, this problem can be written as:

$$
\begin{aligned}
&\min_{\mathbf{s}} \; z\left(\mathbf{s},\mathbf{f}(\mathbf{s})\right), \\
&\text{s.t.} \begin{cases}
h_i\left(\mathbf{s},\mathbf{f}(\mathbf{s})\right) = 0 & \text{satisfy the equality constraints} \quad \forall i = 1,\ldots,N_h, \\
g_j\left(\mathbf{s},\mathbf{f}(\mathbf{s})\right) \leq 0 & \text{satisfy the inequality constraints} \quad \forall j = 1,\ldots,N_g, \\
\mathbf{R}\left(\mathbf{s},\mathbf{f}(\mathbf{s})\right) = \mathbf{0} & \mathbf{f}(\mathbf{s}) \text{ solves the governing equations}, \\
s_k^{\min} \leq s_k \leq s_k^{\max} & \text{satisfy the design constraints} \quad \forall k = 1,\ldots,N_s,
\end{cases}
\end{aligned}
\tag{3.1}
$$

where z, h_i, g_j define the objective as well as equality and inequality constraints. The vectors $\mathbf{s}$ and $\mathbf{f}$ contain the design and state variables; $s_k^{\min}$ and $s_k^{\max}$ are the upper and lower bounds for the k-th design variable. $\mathbf{R}$ is the residual vector of the underlying governing equations of motion. This formulation, (3.1) - where only the design variables $\mathbf{s}$ are independent - is referred to as Nested Analysis and Design (NAND) approach. In this case, the state vector $\mathbf{f}$ is computed, for a given design vector $\mathbf{s}$, from solving $\mathbf{R}\left(\mathbf{s},\mathbf{f}(\mathbf{s})\right) = \mathbf{0}$.

If both the design and state variables, $\mathbf{s}$ and $\mathbf{f}$, are independent and solved for simultaneously, the

optimization problem (3.1) can be re-written as:

$$\min_{\mathbf{s}} \; z(\mathbf{s},\mathbf{f}),$$
$$\text{s.t.} \begin{cases} h_i(\mathbf{s},\mathbf{f}) = 0 & \text{satisfy the equality constraints} \quad \forall i = 1,\ldots,N_h, \\ g_j(\mathbf{s},\mathbf{f}) \leq 0 & \text{satisfy the inequality constraints} \quad \forall j = 1,\ldots,N_g, \\ \mathbf{R}(\mathbf{s},\mathbf{f}) = \mathbf{0} & \text{satisfy the governing equations,} \\ s_k^{\min} \leq s_k \leq s_k^{\max} & \text{satisfy the design constraints} \quad \forall k = 1,\ldots,N_s. \end{cases} \tag{3.2}$$

Due to the simultaneous solution for design and state variables the optimization problem (3.2) is referred to as Nested Analysis and Design (NAND) approach or one-shot method. The current study only employs the NAND approach as it separates the physics and the optimization problem. This allows utilizing standard flow solvers as well as standard nonlinear programming schemes. Further, the size of the problem the nonlinear programming scheme is operating on is smaller when a NAND approach is used.

3.1 Geometry Variation in Design Optimization

Optimization methods can be categorized in numerous ways. In this section the focus lies on classifying different types of geometry variations for optimization. Distinctions are made between size, shape and topology optimization. The characteristics of each type as well as their applicability are briefly discussed in the following:

Size optimization: this is the simplest form of design optimization. The design parameters define the size of certain features, e.g. the radius of a cylinder, cp. Fig. 3.1. The advantage of a straightforward parameterization comes with the restriction that the optimal geometry strongly resembles the initial one. Due to the restrictive design space both initial and final design are cylinders in Fig. 3.1. The final optimization result is therefore highly dependent on the initial guess. Generally, this approach is used to fine-tune an existing design.

Shape optimization: compared to size optimization, this approach is more general. The design parameters define the shape of the geometry, cp. Fig. 3.2. The geometry can be described via splines or through parameterizing an existing CAD model, allowing for changes in the shape of the geometry's boundary. The

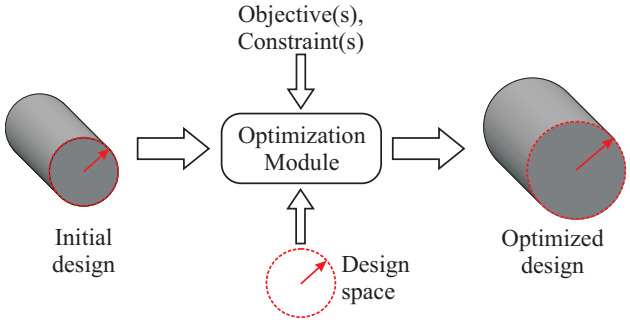

Figure 3.1: Size optimization.

more general the boundary description, the more complex the parameterization becomes: in case of a CAD parameterization it might be necessary to define constraints ensuring that features do not intersect. The optimized results are still strongly dependent on the initial guess as well as the parameterization.

Topology optimization: is the most general optimization technique. The geometry is commonly described via a material distribution function that interpolates the material on an elemental level between 'void' (white), 'intermediate' (gray), and 'solid' (black), Fig. 3.3. The design variables define the material distribution and allow for merging of existing and creation of new boundaries, cp. Figs. 3.3 and 3.4. More details on the material distribution are presented in Section 3.5 and 3.6. The ability to find an optimized geometry without a 'good' initial guess makes topology optimization a powerful tool for finding a conceptual design. The latter is particularly advantageous for complex, nonlinear and thus hard to predict problems such as flow problems. To further improve the geometry obtained from topology optimization, shape/size optimization techniques can be applied in a second stage.

3.2 Optimization Algorithms

Optimization algorithms can be grouped into two categories: gradient-free and gradient-based ones. As the name implies, the former do not rely on gradient information and therefore have no requirement for continuity/differentiability, cp. Fig. 3.5. This makes them well-suited for discrete problems, i.e. problems where the design variable can only have discrete values such as the number of bolts in a structure. Common gradient-free optimization algorithms are branch-and-bound methods [54], simulated annealing [77] and

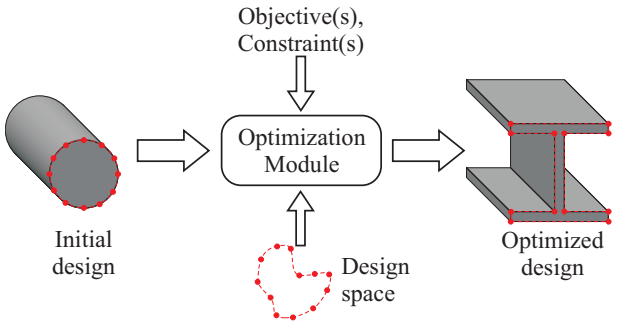

Figure 3.2: Shape optimization.

genetic algorithms [7]. While these methods are usually simple to implement, they are restrictive with respect to the dimension of the design space that can be handled: a large number of design variables quickly leads to unacceptably high computational costs. For example, genetic algorithms are unsuited for problems with both many design variables and computationally expensive forward analysis, such as fluid topology optimization problems. Generally a large number of design variables is necessary to sufficiently resolve the design domain of topology optimization problems, which usually requires a large population size for genetic algorithms. Since every individual within this population requires the solution of a forward problem, it becomes evident that this quickly leads to exorbitant costs, cp. [79].

For topology optimization problems, gradient-based algorithms pose a more efficient alternative since they employ derivative information to guide the search process. However in case of non-differentiable problems, gradient-based optimizers cannot be used as the derivative is ambiguous or even meaningless at discontinuities, Fig. 3.5b. To utilize the derivative information, gradient-based algorithms require the computation of sensitivities, i.e. the derivative of the performance with respect to the design variables, which often entails a cumbersome implementation. When applying gradient-based algorithms to optimization problems with a large number of design variables, the implementation of (semi-) analytical sensitivities is imperative. An approximation via finite difference techniques would lead to immense computational costs. Generally, gradient-based optimization algorithms require less than a few hundred forward analyses even for optimization problems with up to millions of design variables, while gradient-free approaches often require orders of magnitude more forward analyses [79]. Since each forward analysis entails the solution of

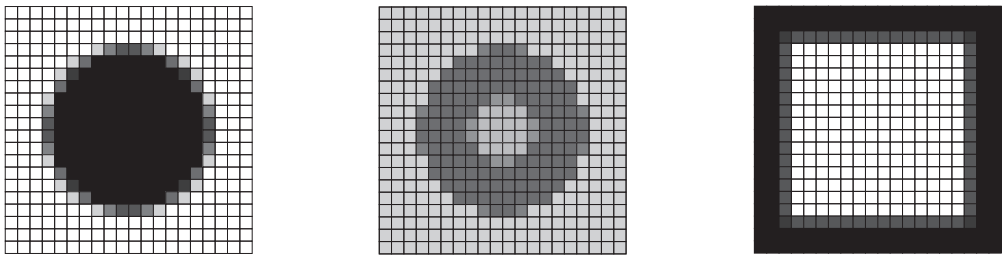

(a) Material distribution of initial design

(b) Material distribution of intermediate design

(c) Material distribution of final design

Figure 3.3: Material distribution for topology optimization, cp. Fig. 3.4.

a (costly) flow problem, only gradient-based optimization problems are considered in this study.

Common optimization algorithms for solving continuous nonlinear constrained problems as at hand in nonlinear programming include interior point methods and sequential quadratic programming (SQP). For more details on these algorithms, the reader is referred to Nocedal and Wright [64]. In the current study the method of moving asymptotes (MMA) as well as a derivation thereof, the globally convergent method of moving asymptotes (GCMMA) are employed. Both of which were developed by Svanberg [83, 84].

3.3 Sensitivity Analysis for Topology Optimization Problems

The following section outlines the computation of the sensitivities for a typical nonlinear program 3.1. For the sake of generality, the sensitivities are derived for a criterion c which can describe either the objective or a constraint:

$$\frac{dc}{ds_k} = \frac{\partial c}{\partial s_k} + \left(\frac{\partial c}{\partial \mathbf{f}}\right)^T \frac{\partial \mathbf{f}}{\partial s_k}. \tag{3.3}$$

Assuming that the residual $\mathbf{R}$ equals zero, cp. Eq. (3.1), the derivative $\partial \mathbf{f}/\partial s_k$ is computed from:

$$\frac{d\mathbf{R}}{ds_k} = \frac{\partial \mathbf{R}}{\partial s_k} + \frac{\partial \mathbf{R}}{\partial \mathbf{f}} \frac{\partial \mathbf{f}}{\partial s_k} = 0. \tag{3.4}$$

Solving this equation for $\partial \mathbf{f}/\partial s_k$ yields:

$$\frac{\partial \mathbf{f}}{\partial s_k} = -\left(\frac{\partial \mathbf{R}}{\partial \mathbf{f}}\right)^{-1} \frac{\partial \mathbf{R}}{\partial s_k}. \tag{3.5}$$

Substituting Eq. (3.5) into Eq. (3.3) results in:

$$\frac{dc}{ds_k} = \frac{\partial c}{\partial s_k} - \left(\frac{\partial c}{\partial \mathbf{f}}\right)^T \left(\frac{\partial \mathbf{R}}{\partial \mathbf{f}}\right)^{-1} \frac{\partial \mathbf{R}}{\partial s_k}. \tag{3.6}$$

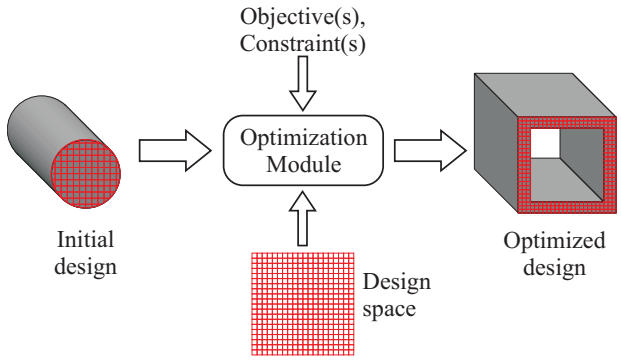

Figure 3.4: Topology optimization.

At this point there are two options for calculating the sensitivity dc/ds:

$$\text{Direct method:} \quad \frac{dc}{ds_k} = \frac{\partial c}{\partial s_k} - \left(\frac{\partial c}{\partial \mathbf{f}}\right)^T \boldsymbol{\gamma} \qquad \text{with} \quad \frac{\partial \mathbf{R}}{\partial \mathbf{f}}\boldsymbol{\gamma} = \frac{\partial \mathbf{R}}{\partial s_k}, \tag{3.7}$$

$$\text{Adjoint method:} \quad \frac{dc}{ds_k} = \frac{\partial c}{\partial s_k} - \boldsymbol{\lambda}^T \frac{\partial \mathbf{R}}{\partial s_k} \qquad \text{with} \quad \left(\frac{\partial \mathbf{R}}{\partial \mathbf{f}}\right)^T \boldsymbol{\lambda} = \frac{\partial c}{\partial \mathbf{f}}. \tag{3.8}$$

Examining the linear systems necessary for computing $\boldsymbol{\gamma}$ and $\boldsymbol{\lambda}$ in Eqs. (3.7) and (3.8) shows that the direct method requires N_s linear solves, where N_s is the number of design variables s_k. Contrary, the adjoint method requires as many linear solves as there are criteria $(1+N_h+N_g)$. From this simple observation it can be concluded:

$$\text{if } (1+N_h+N_g) > N_s: \text{ direct method is more efficient,} \tag{3.9}$$

$$\text{if } (1+N_h+N_g) < N_s: \text{ adjoint method is more efficient.} \tag{3.10}$$

For topology optimization problems where the number of design variables is generally orders of magnitude larger than the number of criteria, the adjoint method should be chosen in order to reduce the computational cost.

In case of transient topology optimization problems, the computation of the sensitivities quickly becomes expensive, both in terms of memory requirements and computational time. For a derivation of transient sensitivities and a more detailed discussion of this issue the reader is referred to [P3].

For optimizing structures that undergo a transient response, the approach of equivalent static loads has been developed to reduce the computational cost [20, 21, 47]. It is based on the idea of transforming

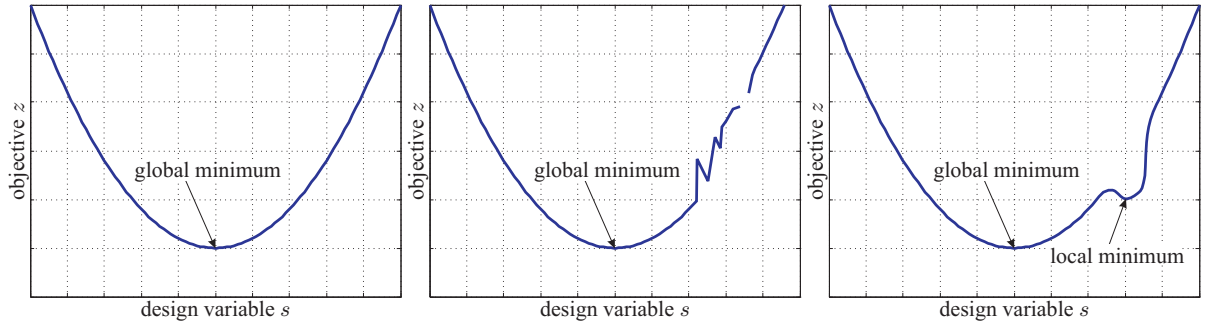

(a) Differentiable, convex (b) Non-differentiable, non-convex (c) Differentiable, non-convex

Figure 3.5: Categorization of functions.

dynamic forces into static loads that yield the same displacement field as the dynamic system. Similar approaches have been developed for optimization of nonlinear (dynamic) systems [48, 63, 78]. Assuming a nonlinear dynamic system, written in pseudo-linear form [48]:

$$\mathbf{M}(\mathbf{s})\,\ddot{\mathbf{u}}^{nd}(t_n) + \mathbf{K}\left(\mathbf{u}^{nd}(t_n), \mathbf{s}\right)\mathbf{u}^{nd}(t_n) = \mathbf{f}^{nd}(t_n), \tag{3.11}$$

where $\mathbf{M}(\mathbf{s})$ is the mass matrix, $\mathbf{K}\left(\mathbf{u}^{nd}(t_n), \mathbf{s}\right)$ the pseudo tangential stiffness matrix, $\mathbf{f}^{nd}(t_n)$ the load vector, and $\mathbf{u}^{nd}(t_n)$ the displacement field that corresponds to this nonlinear, dynamic system. The vector $\mathbf{s}$ defines the design variables. Given the displacement vector $\mathbf{u}^{nd}(t_n)$, the equivalent loads can be computed from:

$$\mathbf{R}\left(\mathbf{s}, \mathbf{u}^{nd}(t_n)\right) = \mathbf{K}^{l}(\mathbf{s})\,\mathbf{u}^{nd}(t_n) - \mathbf{f}_n^{eq}\left(\mathbf{s}, \mathbf{u}^{nd}(t_n)\right) = \mathbf{0}, \tag{3.12}$$

where $\mathbf{R}$ defines the residual, $\mathbf{K}^{l}$ is the linear stiffness matrix and $\mathbf{f}_n^{eq}$ are the equivalent loads that lead to the displacement field $\mathbf{u}^{nd}$. These equivalent forces can either be computed at every time step t_n or at dominant ones, e.g. the time of maximum amplitude. Subsequently, the equivalent loads are utilized as multiple loading conditions [21].

Given the equivalent loads, the optimization process is split into two modules, one for the analysis and one for the design [21]. The former computes the nonlinear response based on the system (3.11), the latter employs the linearized system (3.12) for determining the search direction, i.e. for computing the sensitivities in case of a gradient-based optimization algorithm, thus avoiding a transient/nonlinear sensitivity analysis. The computation of the sensitivities in the linearized optimization module can be derived as fol-

lows: employing Eq. (3.12), the derivative of a criterion c with respect to a design variable s_k is be defined analogous to Eq. (3.6):

$$\frac{dc(t_n)}{ds_k} = \frac{\partial c(t_n)}{\partial s_k} - \left(\frac{\partial c}{\partial \mathbf{u}}\right)^T \mathbf{K}_l^{-1} \frac{\partial \mathbf{R}(t_n)}{\partial s_k}, \tag{3.13}$$

where $\mathbf{R}(t_n)$ is the residual corresponding to Eq. (3.12). From that, the adjoint sensitivity at time t_n can be computed, cp. Eq. (3.8):

$$\frac{dc(t_n)}{ds_k} = \frac{\partial c(t_n)}{\partial s_k} - \boldsymbol{\lambda}^T \frac{\partial \mathbf{R}(t_n)}{\partial s_k}, \tag{3.14}$$

While this approach appears to work reasonably well for structural systems, it is not further explored in the current work as there is no adequate linear static equivalent of the NS equations. Neglecting the time dependency, $\partial v_i/\partial t$, and the nonlinear convective term $(\partial v_i/\partial x_j)\, v_j$ in the momentum equation (2.6) leads to the linear Stokes equations. The latter however, only describe creeping flows, i.e. $Re \ll 1$. Therefore it is assumed that the Stokes equations are unsuitable as a linear system to determine equivalent static loads that yield the same states, $\mathbf{v}$, $\mathbf{p}$, as the nonlinear NS equations. Just neglecting the time dependent inertia term $\partial v_i/\partial t$ would circumvent the need for a transient sensitivity analysis. However, as shown in [P3], the optimization results are often sensitive to unsteady effects.

3.4 Optimality Conditions

Section 3.3 briefly outlines the derivation of sensitivities which determine the search direction for gradient-based optimization algorithms. The following addresses at which point the algorithm should be considered converged to an - at least local - optimum. For defining these optimality conditions the optimization problem (3.1) is revisited. The solution to the latter can be expressed via the corresponding Lagrangian function that is defined as:

$$L(\mathbf{s}, \mathbf{f}(\mathbf{s})) = z(\mathbf{s}, \mathbf{f}(\mathbf{s})) + \sum_{i=1}^{N_h} \mu_i h_i(\mathbf{s}, \mathbf{f}(\mathbf{s})) + \sum_{j=1}^{N_g} \lambda_j g_j(\mathbf{s}, \mathbf{f}(\mathbf{s})), \tag{3.15}$$

where μ_i and λ_j are the Lagrange multipliers for the equality constraints h_i and the inequality constraints $g_j \leq 0$. The Lagrange multipliers are also referred to as dual variables to distinguish them from the design or primal variables. The Lagrangian, which is a saddle point problem, cp. Fig. 3.6, can be interpreted as a

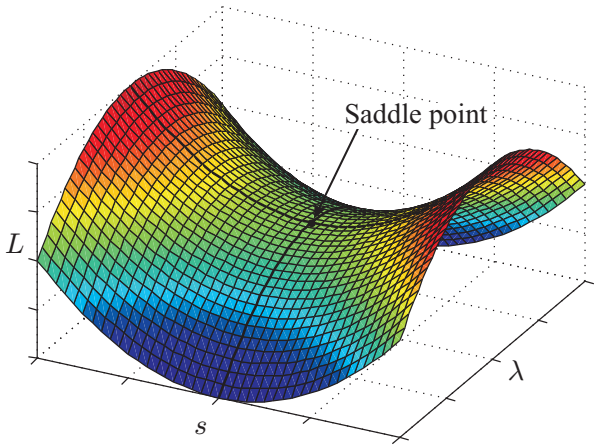

Figure 3.6: Saddle point of simplified Lagrangian $L = z + \lambda g$.

re-formulation of the constrained optimization problem (3.1) into an unconstrained min-max problem. For $\lambda_j \geq 0$, the saddle point is a stationary point of L. Assuming a simplified case of Eq. (3.15) with only inequality constraints this can be expressed as, cp. [12]:

$$L(\mathbf{s}^*, \boldsymbol{\lambda}) \leq L(\mathbf{s}^*, \boldsymbol{\lambda}^*) \leq L(\mathbf{s}, \boldsymbol{\lambda}^*), \tag{3.16}$$

where $\mathbf{s}^*$ and $\boldsymbol{\lambda}^*$ characterize the design variables and Lagrange multipliers at the saddle point. Equation (3.16) states that $\mathbf{s}$ minimizes while $\boldsymbol{\lambda}$ maximizes L [12]. In order to determine whether a certain $\mathbf{s}^*$ is a (local) solution to the constrained optimization problem (3.1), the Karush-Kuhn-Tucker (KKT) conditions can be employed: they define the saddle point of the Lagrangian, cp. Fig. 3.6, and are a necessary but not sufficient condition for a (local) optimum. The KKT conditions can be written as follows [51, 64]:

$$\frac{\partial L(\mathbf{s}^*, \mathbf{f}(\mathbf{s}^*))}{\partial s_k} = 0, \tag{3.17}$$

$$h_i(\mathbf{s}^*, \mathbf{f}(\mathbf{s}^*)) = 0 \quad \forall i = 1, \ldots, N_h, \tag{3.18}$$

$$g_j(\mathbf{s}^*, \mathbf{f}(\mathbf{s}^*)) \leq 0 \quad \forall j = 1, \ldots, N_g, \tag{3.19}$$

$$\lambda_j^* \geq 0 \quad \forall j = 1, \ldots, N_g, \tag{3.20}$$

$$\lambda_j^* g_j(\mathbf{s}^*, \mathbf{f}(\mathbf{s}^*)) = 0 \quad \forall j = 1, \ldots, N_g. \tag{3.21}$$

If the Hessian of L, $\nabla^2_{s_k} L$, is positive definite in the vicinity of the solution of Eqs. (3.17)-(3.21), the KKT conditions are a sufficient condition for a local optimum. In case of a convex optimization problem (3.1), cp. Fig. 3.5a, - that is $\nabla^2_{s_k} L$ is positive definite in the entire solution space - a local solution is automatically the global solution [64].

To determine the convergence based on the KKT conditions they are turned into a linear system, e.g. [30]. The norm of the residual corresponding to this linear system $\left\|\mathbf{R}^{KKT}\right\|$ is utilized as a measure of how well the KKT conditions are satisfied, for example $\left\|\mathbf{R}^{KKT}\right\| < \varepsilon^{KKT} \ll 1$.

Apart from the KKT conditions often times practical conditions are used to determine convergence such as limits for the change of design variables, $\Delta(\mathbf{s}) < \varepsilon_s \ll 1$ or limits for the change of the criteria $\Delta(c) < \varepsilon_c \ll 1$.

3.5 Structural Topology Optimization

Structural topology optimization dates back to the beginning of the 20th century when Michell applied optimization techniques to truss structures [60]. It was not until the 1970s that researchers again gained interested in Michell's work [75]. With the advent of computers structural (topology) optimization became more popular, cp. [18, 19, 42, 76]. Another leap in applicability and thus popularity of structural topology optimization came with the material interpolation approach, first introduced in 1988 by Bendsøe and Kikuchi [9]. Since then, it has become a well established design tool. For more details on structural topology optimization the reader is referred to [25, 38, 39, 40, 80, 82].

The following briefly outlines the most common approach to describe the material distribution in structural topology optimization problems: the Solid Isotropic Material with Penalization (SIMP) approach [8, 90]. It is based on the idea of penalizing intermediate porosities, i.e. design variable value between s^{void} and s^{solid}. Given that the material interpolation approach is only a vehicle to describe the material distribution, the final optimization result should ideally only consist of 'black' (100% solid) and 'white' (100% void) elements. Intermediate elements are an artifact of this interpolation approach.

The SIMP approach is tailored to problems that involve stiffness and mass as design criteria, e.g. max-

imizing the stiffness subject to a mass constraint that limits the amount of solid material:

$$\begin{aligned} &\min_{\mathbf{s}} \; z(\mathbf{s},\mathbf{u}(\mathbf{s})) = \int_{\Omega} \boldsymbol{\varepsilon}^T \boldsymbol{\sigma} d\Omega, \\ &\text{s.t.} \quad g(\mathbf{s}) = \frac{1}{N_s} \sum_{k=1}^{N_s} s_k \leq \phi, \\ &\qquad s_k^{\min} \leq s_k \leq s_k^{\max} \quad \forall k = 1,\ldots,N_s, \end{aligned} \tag{3.22}$$

where the objective z is a measure for the compliance which is the inverse of the stiffness. The tensors $\boldsymbol{\varepsilon}$ and $\boldsymbol{\sigma}$ define the strain and stress. The scalar $0 \leq \phi \leq 1$ limits maximum allowable amount of solid material. The penalization of the intermediate porosities is achieved through two different interpolations for density and stiffness:

$$\text{Linear density interpolation:} \quad \rho_k(s_k) = \rho_s s_k, \tag{3.23}$$

$$\text{Nonlinear stiffness interpolation:} \quad E_k(s_k) = E_{\min} + E_s s_k^{\beta} \quad \text{with } 0 < E_{\min} \ll 1, \tag{3.24}$$

where ρ_k, E_k are the density and stiffness of the k-th element; ρ_s and E_s are the density and stiffness of a 100% solid element. E_{min} is a minimum element stiffness to prevent singularities in the stiffness matrix caused by void elements. For the sake of brevity $E_{\min}$ is set to zero in the following. An exponent $\beta > 1$ penalizes the stiffness interpolation as can seen in Fig. 3.7: for intermediate s-values, e.g. $s = 0.5$, the relative stiffness $E(s=0.5)/E_s = 0.25$ while the relative mass $\rho(s=0.5)/\rho = 0.5$. As the amount of solid material is limited by a mass constraint, it is disadvantageous to 'waste' material for intermediate elements that do not deliver a proportional amount of stiffness. It should be noted that the penalization only works for problems as in Eq. (3.22) that involve stiffness and mass related criteria. Furthermore, an exact 0-1 material distribution is only obtained for $\beta \to \infty$.

3.6 Fluid Topology Optimization

Due to limited computational resources, earlier works of fluid optimization were limited to simple shape optimization problems, cp. [74]. Nowadays, with faster and more powerful computers, more complex fluid shape optimization problems can be considered. For more details on the advancements in fluid shape optimization the reader is referred to [4, 36, 37, 55, 61, 62].

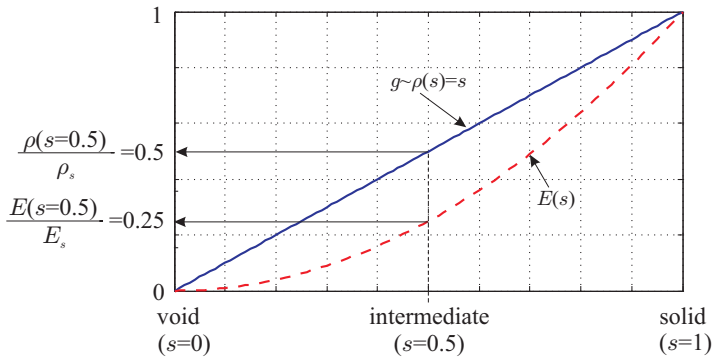

Figure 3.7: SIMP approach for $\beta = 2$.

With advancing computational power a second branch of fluid optimization evolved: fluid topology optimization. Inspired by the success of structural topology optimization, most approaches employ a finite element discretization of the flow domain. As an alternative to finite elements, Pingen and coworkers applied a finite difference based hydrodynamic LBM to solve fluid topology optimization problems [69, 70, 71, 72, 73]. Only recently, Evgrafov et al. have used a finite volume method for fluid topology optimization [28].

In 2003 Klarbring et al. applied topology optimization to flow networks, where the flow was governed by the Hagen-Poiseuille equation [50]. In that same year, Borrvall and Peterson [11] proposed their pioneering study for topology optimization of Stokes problems. It is based on a material interpolation approach - similar to the SIMP approach - which is still widely used and therefore will be discussed later in this section. Evgrafov studied the limits of material porosity in Stokes flow [26]. Gersborg-Hansen et al. applied topology optimization to Stokes flow to meet target flow rates [32]. Duan et al. [24] as well as Challis and Guest [15] employed a level set approach to optimize Stokes flow problems. Large scale - 2D and 3D - fluid topology optimization problems governed by Stokes flow have been solved by Aage et al. [2]. Guest and Prévost optimized unit cells for maximum permeability [35] as well as maximum permeability and stiffness [34]. In both cases a Stokes flow model has been employed.

The above mentioned studies on fluid topology optimization are all limited to Stokes flow. Evgrafov [27], Okkels et al. [65] as well as Olesen et al. [66] extended fluid topology optimization to flow problems described by the steady-state NS equations. Gersborg-Hansen et al. [33] applied fluid topology

optimization to the steady-state NS equations using a new approach: instead of interpolating the material/porosity, they varied the height of the flow channels, where zero-height means solid material. Liu et al. analysed problems with flow rate constraints described by the steady-state NS equations [56]. Zhou and Li [91] as well as Deng et al. [22] applied level set methods in combination with fluid topology optimization of steady-state NS flows. Andreasen et al. employed fluid topology optimization for the design of micro mixers [5]. Pingen and co-workers applied the LBM to solve steady-state flow problems [69, 70, 71, 72, 73].

Recently, the porosity approach has also been applied to the unsteady NS flow problems [22, P3]. Kirk et al. used an unsteady LBM to solve transient fluid topology optimization problems [49]. Further, topology optimization has been employed to coupled fluid-structure systems [45, 58, 59, 87, P2].

Due to the large success of Borvall and Petersson's approach for fluid topology optimization the basic ideas of their work are outlined in the following, cp. [11]. Their study focused on Stokes flow discretized by finite elements. The Stokes equations can be obtained from the NS equations by neglecting the inertia and convection term, i.e. the left hand side in Eq. (2.6) is set to zero. Borrvall and Petersson augmented the Stokes equations with a design dependent term that penalizes the velocity - often referred to as a Brinkman term [14]:

$$\text{Momentum equation:} \quad \underbrace{\alpha(s)\, v_i}_{\text{Brinkman term}} = \frac{\partial \sigma_{ij}}{\partial x_j} + f_i^B, \tag{3.25}$$

$$\text{Incompressibility condition:} \quad \frac{\partial v_i}{\partial x_i} = 0. \tag{3.26}$$

$$\tag{3.27}$$

Equations (3.25) and (3.26) describe the flow of a viscous fluid through a porous medium [68]. The porosity is defined by the design dependent impermeability $\alpha(s)$ which is defined on an elemental level.

Borrvall and Peterson propose a convex interpolation function for the impermeability $\alpha(s)$ [11]:

$$\alpha(s) = \overline{\alpha} + (\underline{\alpha} - \overline{\alpha})\, s \frac{1 + p_\alpha}{s + p_\alpha} \quad \text{with } 0 \leq s \leq 1, \tag{3.28}$$

where $\underline{\alpha}$ and $\overline{\alpha}$ define the minimum and maximum α-values. The parameter p_α is a penalty factor that affects the amount of gray elements, cp. Fig. 3.8. Note, that for this interpolation $s = 0$ defines 'solid' and $s = 1$ 'fluid' material. To illustrate how the interpolation in Eq. (3.28) relates to the common SIMP approach

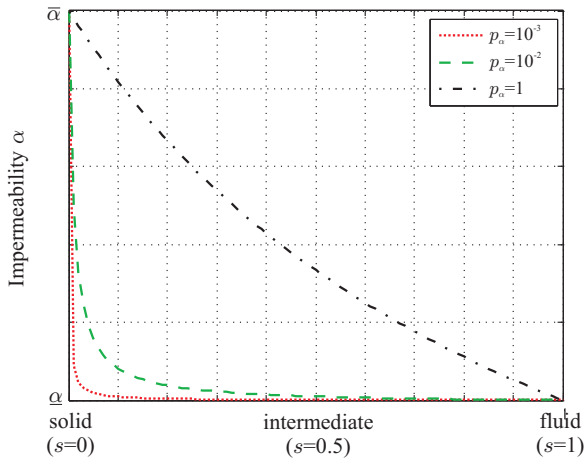

Figure 3.8: Impermeability interpolation.

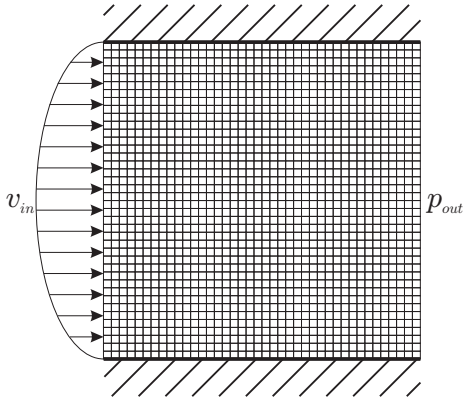

Figure 3.9: Flow problem to illustrate impermeability interpolation.

in structures, c.p Fig. 3.7, the flow problem in Fig. 3.9 is considered: the boundary conditions are a parabolic inlet velocity profile, a pressure outlet condition and stick conditions at the top and bottom.

A typical example for optimizing this flow problem is to minimize the dissipation subject to a constraint that limits the amount of fluid material. Mathematically such a problem can be expressed as:

$$\begin{aligned} &\min_{\mathbf{s}} \; z(\mathbf{s},\mathbf{f}(\mathbf{s})) = (p_{in}^{tot}(\mathbf{s},\mathbf{f}(\mathbf{s})) - p_{out}^{tot}(\mathbf{s},\mathbf{f}(\mathbf{s}))), \\ &\text{s.t.} \quad g(\mathbf{s}) = \frac{1}{N_s}\sum_{k=1}^{N_s} s_k \leq \phi, \\ &\qquad s_k^{\min} \leq s_k \leq s_k^{\max} \quad \forall k = 1,\ldots,N_s, \end{aligned} \tag{3.29}$$

where p_{in}^{tot} and p_{out}^{tot} are the total inlet and outlet pressure. The difference $z = p_{in}^{tot} - p_{out}^{tot}$ is a measure for the dissipation in the system. The scalar $0 \leq \phi \leq 1$ limits maximum allowable amount of fluid material. For the remainder of this section, the design space $\mathbf{s}$ of dimension N_s is reduced to a single design variable s, i.e. $N_s = 1$ that controls the impermeability of all elements. Figure 3.10a shows that the relation between the dissipation and the design variable becomes more nonlinear as the penalization p_α decreases.

Recalling that in structures, the compliance is a measure for the inverse of the stiffness E, cp. Section 3.5, we define an analogous relationship for the fluid problem in Eq. (3.29) – the efficiency η as the inverse of the dissipation z:

$$\eta = \frac{1}{z} = \frac{1}{p_{in}^{tot} - p_{out}^{tot}}. \tag{3.30}$$

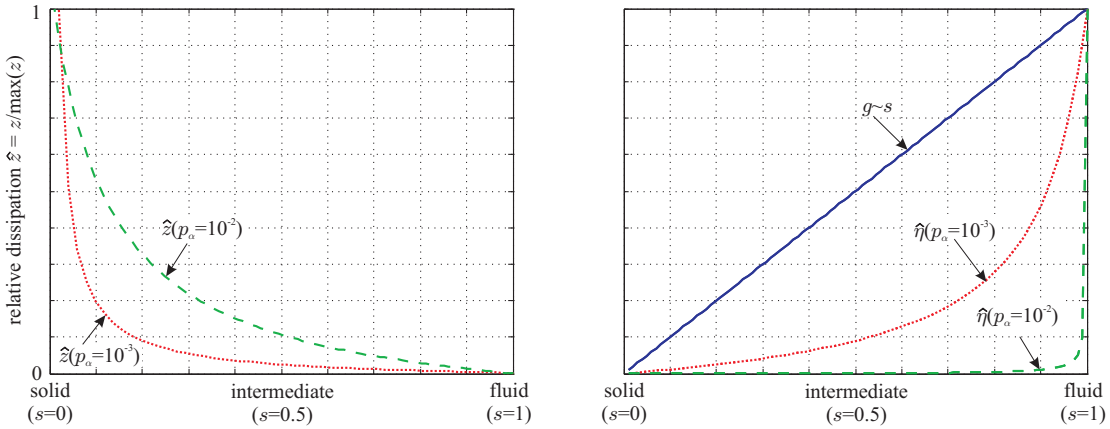

(a) Dependency of dissipation on design variable

(b) Penalization of intermediate material

Figure 3.10: Material interpolation for fluid topology optimization.

After normalizing we obtain the relative efficiency $\hat{\eta}$:

$$\hat{\eta} = \frac{\eta}{\max(\eta)}. \tag{3.31}$$

Figure 3.10b graphs the relative efficiency $\hat{\eta}$ over the design variable s for two different penalty values p_α. Comparing Fig. 3.7 with Fig. 3.10b reveals that in both cases intermediate material is penalized: since the amount of solid (fluid) material is limited, it is disadvantageous to 'waste' material for intermediate elements that do not deliver a proportional amount of stiffness (efficiency) .

While the overall relation between the design variable s and the inverse of the objective $1/z$ is same for both solid and fluid, Figs. 3.7 and 3.10b, the effect of the material interpolation is different. In the structural case, the more nonlinear the material interpolation $E(s)$, Eq. (3.24), the higher the penalty for intermediate material, cp. Fig. 3.7. For the porosity interpolation of fluids the opposite holds: the penalization of intermediate material decreases as $\alpha(s)$, Eq. (3.28), becomes more nonlinear, cp. Figs. 3.8 and 3.10b. In other words, the nonlinearity between the porosity α and the efficiency can be compensated by a nonlinear (convex) material interpolation $\alpha(s)$, Eq. (3.28).

Figure 3.11 shows an example of material interpolation based fluid topology optimization: the boundary conditions are one inlet with a parabolic velocity and four traction-free outlets. The remaining surfaces are described by a stick-condition, cp. Fig. 3.11a. The problem has 1,523,704 degrees of freedom and 364,500 design variables. The objective is to minimize the pressure drop from the inlet to the outlets subject

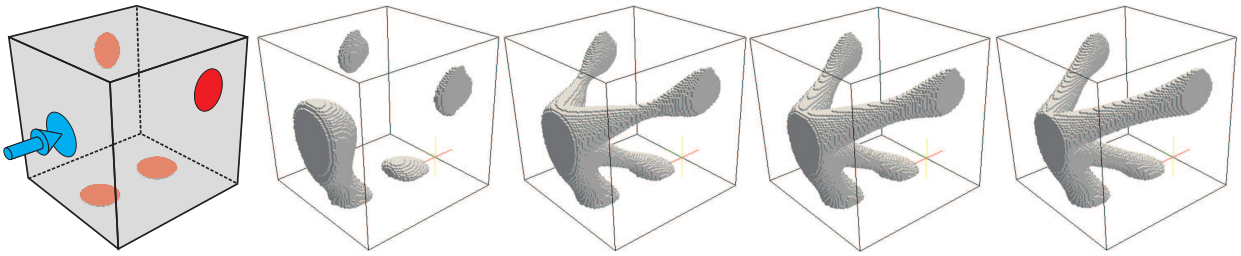

(a) Boundary conditions: intlet (blue), outlets (red) (b) Iteration 5 (c) Iteration 10 (d) Iteration 20 (e) Iteration 50

Figure 3.11: 3D fluid topology optimization.

to a mass constraint that limits the amount of fluid to 15% of the design domain. The evolution of the design is depicted in Figs. 3.11b-3.11e.

As an alternative to describing the layout via a material interpolation, the author has studied geometric interface descriptions for both the LBM, [P1], and the NS equations, [P4].

Chapter 4

Summary

4.1 Concluding Remarks

This thesis aims at improving the capabilities of fluid topology optimization techniques, such that a wider spectrum of flow problems can be optimized. The focus lies on incompressible flows at low to intermediate Reynolds numbers. Different approaches are considered for describing the fluid flow: a finite difference based LBM, cp. [P1] and [P2], as well as a finite element discretization of the NS equations, cp. [P3] and [P4]. It is demonstrated that fluid topology optimization can be applied to transient flow problems, cp. [P3] and that the optimization results for unsteady flows may differ significantly from those of steady-state flows. Furthermore, coupled fluid-structure problems are optimized in [P2]. While the common porosity interpolation approach is straightforward to implement it has a number of disadvantages and shortcomings, such as the need for a material interpolation model, spurious pressure diffusion through solid material, as well as requiring refined meshes. These shortcomings become obvious for both the coupled fluid solid problems, [P2], and unsteady flows, [P3]. To avoid these issues, an alternative to the material interpolation approach is developed. Based on a level set method a geometric description of the interface is introduced. For the LBM it is shown in [P1] that this level set based geometric boundary description produces results in good agreement with the material interpolation approach while circumventing the disadvantages of the porosity interpolation and yielding a higher spatial accuracy than the latter. In [P4] a geometric boundary description based on level sets and an XFEM approach is introduced. This study shows that the geometric boundary description allows for solving fluid topology optimization problems that cannot easily be solved via the standard material interpolation approach.

The overall conclusion from this study is that while the commonly used porous material interpolation approach works well for flow simple problems, it shows shortcomings for more complex problems, such as coupled fluid-solid systems and unsteady flows. Many of issues can be avoided by a geometric boundary representation. Since the latter does not rely on a fictitious porous material it provides a greater flexibility for solving (fluid) optimization problems with a broad range of objectives and constraints. However, the geometric boundary representation is significantly more complex in terms of implementation, potentially preventing the use of commercial software tools, cp. [P4]. When applying a geometric boundary representation to fluid optimization, it generally requires a smoothing operation to avoid spatial oscillations of the boundary, cp. [P1]. Finally, the proposed geometric boundary representation can only merge existing boundaries but no new boundaries can emerge, cp. [P1] and [P4]. The latter is of less importance for fluid topology optimization problems and can be circumvented by seeding the initial design with a sufficient number of solid regions.

Through the work conducted in this study the knowledge about and the applicability of fluid topology optimization techniques have been broadened significantly. However, more research is necessary to fully establish fluid topology optimization as an efficient design tool in industry.

4.2 Future Work

With fluid topology optimization being a rather young discipline, there are still numerous open questions and problems which give rise to many ideas for future work. The list below gives suggestions for potential future research:

- *Further development of parallelized codes that allow for solving large scale fluid optimization problems efficiently:* due to the high computational cost of (fluid) topology optimization parallelized implementations are imperative for solving 'non-academic'/realistic engineering problems, such as large scale, 3D, unsteady flows at high Reynolds numbers.

- *Further research on enforcing the boundary conditions along XFEM interfaces:* the employed stabilized Lagrange multiplier method in [P4] has proven to work sufficiently well for the considered

simple, low Reynolds number flows; it would be interesting to investigate how this approach behaves at higher Reynolds numbers and how well the no-slip condition can be enforced, especially for intersections that lead to very small fluid or solid areas.

- *Extension of the XFEM-based geometric boundary representation to 3D problems:* the current implementation is limited to 2D problems. In 3D the number of possible cases for intersections of a hex-element increases significantly compared to a quad-element in 2D. For the 3D implementation it must be ensured that all relevant intersection cases are considered.

- *Incorporation of coupled/multiphysics problems, such as fluid-structure-interaction, reacting flows, multiphase flows:* so far, most of the research on fluid topology optimization has been limited to rather simple flows. A reason for this might be the commonly used porosity approach: defining consistent interpolation models that capture the coupling between two domains is a challenging task, especially for systems that are coupled via the interface, cp. [P2]. In case of a material interpolation approach no geometric boundary exists, instead the boundary is smeared out over several elements via a fictitious porous material. Applying a geometric boundary representation, such as XFEM, should mitigate this issue.

Bibliography

[1] http://histoire.ec-lyon.fr/index.php?id=768, accessed October 27, 2011.

[2] N. Aage, T. Poulsen, A. Gersborg-Hansen, and O. Sigmund. Topology Optimization of Large Scale Stokes Flow Problems. Structural and Multidisciplinary Optimization, 35:175–180, 2008.

[3] T. Abe. Derivation of the Lattice Boltzmann Method by Means of the Discrete Ordinate Method for the Boltzmann Equation. Journal of Computational Physics, 131(1):241–246, February 1997.

[4] J. J. Alonso and M. R. Colonno. Multidisciplinary Optimization with Applications to Sonic-Boom Minimization. Annual Review of Fluid Mechanics, 44(1), 2012.

[5] C. S. Andreasen, A. R. Gersborg, and O. Sigmund. Topology Optimization of Microfluidic Mixers. International Journal for Numerical Methods in Fluids, 61(5):498–513, 2009.

[6] I. Babuška. Error-Bounds for Finite Element Method. Numerische Mathematik, 16:322–333, 1971.

[7] R. Balamurugan, C. V. Ramakrishnan, and N. Singh. Performance Evaluation of a Two Stage Adaptive Genetic Algorithm TSAGA in Structural Topology Optimization. Applied Soft Computing, 8(4):1607 – 1624, 2008.

[8] M. P. Bendsøe. Optimal Shape Design as a Material Distribution Problem. Structural and Multidisciplinary Optimization, 1(4):193–202, 1989.

[9] M. P. Bendsøe and N. Kikuchi. Generating Optimal Topologies in Structural Design Using a Homogenization Method. Computer Methods in Applied Mechanics and Engineering, 71(2):197–224, 1988.

[10] P. L. Bhatnagar, E. P. Gross, and M. Krook. A Model for Collision Processes in Gases. I. Small Amplitude Processes in Charged and Neutral One-Component Systems. Physical Review, 94:511–525, May 1954.

[11] T. Borrvall and J. Petersson. Topology Optimization of Fluids in Stokes Flow. International Journal for Numerical Methods in Fluids, 41(1):77–107, 2003.

[12] S. P. Boyd and L. Vandenberghe. Convex Optimization. Cambridge University Press, 2004.

[13] F. Brezzi. On the Existance, Uniqueness and Approximation of Saddle Point Problems Arising from Lagrangian Multipliers. Revue Française d'Automatique Informatique Recherche Operationnelle, 8(2):129–151, 1974.

[14] H. C. Brinkman. A Calculation of the Viscous Force Exerted by a Flowing Fluid on a Dense Swarm of Particles. Applied Scientific Research, Sect. A, 1:27, 1947.

[15] V. Challis and J. K. Guest. Level Set Topology Optimization of Fluids in Stokes Flow. International Journal for Numerical Methods in Engineering, 79(10):1284–1308, 2009.

[16] G. Chen. Nanoscale Energy Transport and Conversion. Oxford University Press, 2005.

[17] S. Chen and G. D. Doolen. Lattice Boltzmann Method for Fluid Flows. Annual Review Of Fluid Mechanics, 30:329–364, 1998.

[18] K. T. Cheng and N. Olhoff. An Investigation Concerning Optimal-Design of Solid Elastic Plates. International Journal of Solids and Structures, 17(3):305–323, 1981.

[19] K. T. Cheng and N. Olhoff. Regularized Formulation for Optimal-Design of Axisymmetric Plates. International Journal of Solids and Structures, 18(2):153–169, 1982.

[20] W. S. Choi and G. J. Park. Transformation of Dynamic Loads into Equivalent Static Loads Based on Modal Analysis. International Journal for Numerical Methods in Engineering, 46(1):29–43, 1999.

[21] W. S. Choi and G. J. Park. Structural Optimization Using Equivalent Static Loads at All Time Intervals. Computer Methods in Applied Mechanics and Engineering, 191(19-20):2105 – 2122, 2002.

[22] Y. Deng, Z. Liu, P. Zhang, Y. Liu, and Y. Wu. Topology Optimization of Unsteady Incompressible Navier-Stokes Flows. Journal of Computational Physics, In Press, Corrected Proof, 2011.

[23] J. Donea and A. Huerta. Finite Element Methods for Flow Problems. John Wiley & Sons, Ltd., 2003.

[24] X. B. Duan, Y. C. Ma, and R. Zhang. Shape-Topology Optimization of Stokes Flow via Variational Level Set Method. Applied Mathematics and Computation, 202(1):200 – 209, 2008.

[25] H. A. Eschenauer and N. Olhoff. Topology Optimization of Continuum Structures: A Review. Applied Mechanics Reviews, 54(4):331–390, 2001.

[26] A. Evgrafov. The Limits of Porous Materials in the Topology Optimization of Stokes Flows. Applied Mathematics & Optimization, 52:263–277, 2005.

[27] A. Evgrafov. Topology Optimization of Slightly Compressible Fluids. ZAMM - Zeitschrift für Angewandte Mathematik und Mechanik, 86(1):46–62, January 2006.

[28] A. Evgrafov, M. M. Gregersen, and M. P. Sørensen. Finite Volumes Discretization of Topology Optimization Problems. In USNCCM - 11, July 25-28, Minneapolis and St. Paul, MN, USA, 2011.

[29] A. Evgrafov, G. Pingen, and K. Maute. Topology Optimization of Fluid Domains: Kinetic Theory Approach. ZAMM - Zeitschrift für Angewandte Mathematik und Mechanik, 88(2):129–141, 2008.

[30] R. Fletcher and T. Johnson. On a the stability of null-space methods for KKT systems. SIAM Journal on Matrix Analysis and Applications, 18(4):938–958, October 1997.

[31] F. Franco Brezzi, M.-O. Bristeau, L. P. Franca, M. Mallet, and G. Rogé. A Relationship Between Stabilized Finite Element Methods and the Galerkin Method with Bubble Functions. Computer Methods in Applied Mechanics and Engineering, 96(1):117 – 129, 1992.

[32] A. Gersborg-Hansen, M. Berggren, and B. Dammann. Topology Optimization of Mass Distribution Problems in Stokes Flow. In IUTAM Symposium on Topological Design Optimization of Structures, Machines and Materials, volume 137 of Solid Mechanics and Its Applications, pages 365–374. Springer Netherlands, 2006.

[33] A. Gersborg-Hansen, O. Sigmund, and R. B. Haber. Topology Optimization of Channel Flow Problems. Structural and Multidisciplinary Optimization, 30(3):181–192, 2005.

[34] J. K. Guest and J. H. Prévost. Optimizing Multifunctional Materials: Design of Microstructures for Maximized Stiffness and Fluid Permeability. International Journal of Solids and Structures, 43(22–23):7028–7047, 2006.

[35] J. K. Guest and J. H. Prévost. Design of Maximum Permeability Material Structures. Computer Methods in Applied Mechanics and Engineering, 196(4-6):1006 – 1017, 2007.

[36] M. D. Gunzburger. Advances in Design and Control. SIAM, 2003.

[37] M. D. Gunzburger, H. Kim, and S. Manservisi. On a Shape Control Problem for the Stationary Navier-Stokes Equations. ESAIM-Mathematical Modelling and Numerical Analysis – Modelisation Mathematique et Analyse Numerique, 34(6):1233–1258, November-December 2000.

[38] B. Hassani and E. Hinton. A Review of Homogenization and Topology Opimization II - Analytical and Numerical Solution of Homogenization Equations. Computers & Structures, 69(6):719 – 738, 1998.

[39] B. Hassani and E. Hinton. A Review of Homogenization and Topology Optimization I - Homogenization Theory for Media with Periodic Structure. Computers & Structures, 69(6):707 – 717, 1998.

[40] B. Hassani and E. Hinton. Review of Homogenization and Topology Opimization III - Topology Optimization Using Optimality Criteria. Computers & Structures, 69(6):739 – 756, 1998.

[41] X. Y. He and L. S. Luo. Theory of the Lattice Boltzmann Method: From the Boltzmann Equation to the Lattice Boltzmann Equation. Physical Review E, 56(6):6811–6817, December 1997.

[42] W. S. Hemp. Optimum Structures. Clarendon Press, 1973.

[43] M. Howard. Finite Element Modeling and Optimization of High-Speed Aerothermoelastic Systems. PhD thesis, University of Colorado at Boulder, 2010.

[44] T. J. R. Hughes and T. E. Tezduyar. Finite Element Methods for First-Order Hyperbolic Systems with Particular Emphasis on the Compressible Euler Equations. Computer Methods in Applied Mechanics and Engineering, 45:218–284, September 1984.

[45] K. A. James, G. J. Kennedy, and J. R. R. A. Martins. Aerostructural Topology Optimization of an Aircraft Wingbox. In Proceedings of the CASI AERO 2011 Conference, Montreal, QC, April 2011.

[46] R. W. Johnson. The Handbook of Fluid Dynamics. Springer, 1998.

[47] B. S. Kang, W. S. Choi, and G. J. Park. Structural Optimization under Equivalent Static Loads Transformed from Dynamic Loads Based on Displacement. Computers & Structures, 79(2):145 – 154, 2001.

[48] Y.-I. Kim and G. J. Park. Nonlinear Dynamic Response Structural Optimization Using Equivalent Static Loads. Computer Methods In Applied Mechanics And Engineering, 199(9-12):660–676, 2010.

[49] A. Kirk, S. Kreissl, G. Pingen, and K. Maute. Lattice Boltzmann Topology Optimization for Transient Flow. In MAESC 2011, May 3, Memphis, TN, USA, 2011.

[50] A. Klarbring, J. Petersson, B. Torstenfelt, and M. Karlsson. Topology Optimization of Flow Networks. Computer Methods in Applied Mechanics and Engineering, 192(35-36):3909 – 3932, 2003.

[51] H. W. Kuhn and A. W. Tucker. Nonlinear Programming. In Proceedings of the Second Berkeley Symposium on Mathematical Statistics and Probability, 1950, pages 481–492, Berkeley and Los Angeles, 1951. University of California Press.

[52] P. K. Kundu and I. M. Cohen. Fluid Mechanics. Elsevier Academic Press, 2004.

[53] O. A. Ladyzhenskaya. The Mathematical Theory of Viscous Incompressible Flow. Gordon and Breach, 1969.

[54] A. H. Land and A. G. Doig. An Automatic Method of Solving Discrete Programming Problems. Econometrica, 28(3):497–520, 1960.

[55] T. Lehnhäuser and M. Schäfer. A Numerical Approach for Shape Optimization of Fluid Flow Domains. Computer Methods in Applied Mechanics and Engineering, 194(50-52):5221 – 5241, 2005.

[56] Z. Liu, Q. Gao, P. Zhang, M. Xuan, and Y. Wu. Topology Optimization of Fluid Channels with Flow Rate Equality Constraints. Structural and Multidisciplinary Optimization, 44:31–37, 2011.

[57] R. W. MacCormack and A. J. Paullay. Computational Efficiency Achieved by Time Splitting of Finite Difference Operators. AIAA Paper, pages 72–154, 1972.

[58] K. Maute and M. Allen. Conceptual Design of Aeroelastic Structures by Topology Optimization. Structural and Multidisciplinary Optimization, 27:27–42, 2004.

[59] K. Maute and G. W. Reich. Integrated Multidisciplinary Topology Optimization Approach to Adaptive Wing Design. AIAA Journal of Aircraft, 43(1):253–263, 2006.

[60] A. G. M. Michell. The limits of economy of material in frame-structures. Philosophical Magazine Series 6, 8(47):589–597, 1904.

[61] B. Mohammadi and O. Pironneau. Shape Optimization in Fluid Mechanics. Annual Review of Fluid Mechanics, 36:255–279, 2004.

[62] B. Mohammadi and O. Pironneau. Applied Shape Optimization for Fluids. Oxford University Press, 2009.

[63] P. Motamarri, A. Ramani, and A. Kaushik. Structural Topology Synthesis with Dynamics and Nonlinearities Using Equivalent Linear Systems. Structural and Multidisciplinary Optimization, pages 1–14, 2011.

[64] J. Nocedal and S. J. Wright. Numerical Optimization. Springer, 1999.

[65] F. Okkels, L. H. Olesen, and H. Bruus. Applications of Topology Optimization in the Design of Miro- and Nanofluidic Systems. In NSTI-Nanotech 2005, volume 1, pages 575–578, 2005.

[66] L. H. Olesen, F. Okkels, and B. Bruus. A High-Level Programming-Language Implementation of Topology Optimization Applied to Steady-State Navier-Stokes Flow. International Journal for Numerical Methods in Engineering, 65:975–1001, 2006.

[67] Franca L. P. and T. J. R. Hughes. Convergence analyses of Galerkin least-squares methods for symmetric advective-diffusive forms of the Stokes and incompressible Navier-Stokes equations. Computer Methods in Applied Mechanics and Engineering, 105(2):285 – 298, 1993.

[68] G. Pingen. Optimal Design for Fluidic Systems: Topology and Shape Optimization with the Lattice Boltzmann Method. PhD thesis, University Of Colorado at Boulder, 2008.

[69] G. Pingen, A. Evgrafov, and K. Maute. Topology Optimization of Flow Domains Using the Lattice Boltzmann Method. Structural and Multidisciplinary Optimization, 36(6):507–524, 2007.

[70] G. Pingen, A. Evgrafov, and K. Maute. Adjoint Parameter Sensitivity Analysis for the Hydrodynamic Lattice Boltzmann Method with Applications to Design Optimization. Computers & Fluids, 38:910–923, 2008.

[71] G. Pingen and K. Maute. Optimal Design for Non-Newtonian Flows Using a Topology Optimization aApproach. Computers & Mathematics with Applications, 59(7):2340–2350, April 2010.

[72] G. Pingen, M. Waidmann, A. Evgrafov, and K. Maute. Application of a Parametric Level-Set Approach to Topology Optimization Fluid with the Navier-Stokes and Lattice Boltzmann Equations. In WCSMO07, May 21-25, Seoul, Korea, 2007. ISSMO.

[73] G. Pingen, M. Waidmann, A. Evgrafov, and K. Maute. A Parametric Level-Set Approach for Topology Optimization of Flow Domains . Structural and Multidisciplinary Optimization, 41(1):117–131, 2009.

[74] O. Pironneau. On Optimum Design in Fluid Mechanics. Journal of Fluid Mechanics, 64(01):97–110, 1974.

[75] W. Prager. A note on discretized michell structures. Computer Methods in Applied Mechanics and Engineering, 3(3):349 – 355, 1974.

[76] W. Prager and G. I. N. Rozvany. Optimization of Structural Geometry. In Dynamical Systems, pages 265–293. Academic Press, 1977.

[77] P. Y. Shim and S. Manoochehri. Generating Optimal Configurations in Structural Design Using Simulated Annealing. International Journal for Numerical Methods in Engineering, 40(6):1053–1069, 1997.

[78] M. K. Shin, K. J. Park, and G. J. Park. Optimization of Structures with Nonlinear Behavior Using Equivalent Loads. Computer Methods in Applied Mechanics and Engineering, 196(4-6):1154 – 1167, 2007.

[79] O. Sigmund. On The Usefulness of Non-Gradient Approaches in Topology Optimization. Structural and Multidisciplinary Optimization, 43(5):589–596, May 2011.

[80] O. Sigmund and J. Petersson. Numerical Instabilities in Topology Optimization: A Survey on Procedures Dealing with Checkerboards, Mesh-Dependencies and Local Minima. Structural and Multidisciplinary Optimization, 16(1):168–75, August 1998.

[81] S. Succi. The Lattice Boltzmann Equation: for Fluid Dynamics and Beyond. Oxford University Press, 2001.

[82] K. Suzuki and N. Kikuchi. A Homogenization Method for Shape and Topology Optimization. Computer Methods in Applied Mechanics And Engineering, 93(3):291–318, December 1991.

[83] K. Svanberg. The Method of Moving Asymptotes - A New Method for Structural Optimization. International Journal for Numerical Methods in Engineering, 24(2):359–373, February 198.

[84] K. Svanberg. A Globally Convergent Version of MMA Without Linesearch. In Proceedings of the First World Congress of Structural and Multidisciplinary Optimization, 28 May - 2 June 1995, pages 9–16, Goslar, Germany, 1995.

[85] T. E. Tezduyar, S. Mittal, S. E. Ray, and R. Shih. Incompressible Flow Computations with Stabilized Bilinear and Linear Equal-Order-Interpolation Velocity-Pressure Elements. Computer Methods in Applied Mechanics and Engineering, 95:221–242, 1992.

[86] M. J. Turner, R. W. Clough, H. C. Martin, and L. J. Topp. Stiffness and Deflection Analysis of Complex Structures. Journal of Aeronautical Sciences, 23, 1956.

[87] G. H. Yoon. Topology Optimization for Stationary Fluid-Structure Interaction Problems Using a New Monolithic Formulation. In 8th World Congress on Structural and Multidisciplinary Optimization, June 2009.

[88] D. Yu, R. Mei, L. S. Luo, and W. Shyy. Viscous Flow Computations with the Method of Lattice Boltzmann Equation. Progress in Aerospace Sciences, 39(5):329–367, July 2003.

[89] D. Z. Yu, R. W. Mei, and W. Shyy. Improved Treatment of the Open Boundary in the Method of Lattice Boltzmann Equation. Progress Ii Computational Fluid Dynamics, 5(1-2):3–12, 2005.

[90] M. Zhou and G. I. N. Rozvany. The COC algorithm, Part II: Topological, Geometrical and Generalized Shape Optimization. Computer Methods in Applied Mechanics and Engineering, 89(1-3):309 – 336, 1991.

[91] S. Zhou and Q. Li. A Variational Level Set Method for the Topology Optimization of Steady-State Navier-Stokes Flow. Journal of Computational Physics, 227(24):10178 – 10195, 2008.

Appendix A

Publication [P1]: An Explicit Level Set Approach for Generalized Shape Optimization of Fluids with the Lattice Boltzmann Method

INTERNATIONAL JOURNAL FOR NUMERICAL METHODS IN FLUIDS
Int. J. Numer. Meth. Fluids 2011; **65**:496–519
Published online 7 October 2009 in Wiley Online Library (wileyonlinelibrary.com). DOI: 10.1002/fld.2193

An explicit level set approach for generalized shape optimization of fluids with the lattice Boltzmann method

Sebastian Kreissl[1], Georg Pingen[2] and Kurt Maute[1,*,†]

[1]*Department of Aerospace Engineering Sciences, Center for Aerospace Structures, University of Colorado, Boulder, CO 80309-0429, U.S.A.*
[2]*Mechanical and Aerospace Engineering, University of Colorado, Colorado Springs, CO 80933-7150, U.S.A.*

SUMMARY

This study is concerned with a generalized shape optimization approach for finding the geometry of fluidic devices and obstacles immersed in flows. Our approach is based on a level set representation of the fluid–solid interface and a hydrodynamic lattice Boltzmann method to predict the flow field. We present an explicit level set method that does not involve the solution of the Hamilton–Jacobi equation and allows using standard nonlinear programming methods. In contrast to previous works, the boundary conditions along the fluid–structure interface are enforced by second-order accurate interpolation schemes, overcoming shortcomings of flow penalization methods and Brinkman formulations frequently used in topology optimization. To ensure smooth boundaries and mesh-independent results, we introduce a simple, computationally inexpensive filtering method to regularize the level set field. Furthermore, we define box constraints for the design variables that guarantee a continuous evolution of the boundaries. The features of the proposed method are studied by two numeric examples of two-dimensional steady-state flow problems.

Received 28 March 2009; Revised 19 August 2009; Accepted 20 August 2009

KEY WORDS: immersed boundary technique; interpolation boundary condition; regularity control; adjoint sensitivity analysis; nonlinear programming

1. INTRODUCTION

This study is concerned with a computational method for optimizing the geometry of fluidic devices and obstacles immersed in low Mach and Reynolds number flows. We allow for variations in the shape of boundaries as well as changes in the topological layout. In solid mechanics, numerical methods for optimizing the shape and topology are well established [1–5]. Much less work has been done on optimizing the layout of flow problems. Borrvall and Petersson [6] employed topology optimization for Stokes-flows. Gersborg-Hansen *et al.* [7] extended this approach to Navier–Stokes flows. Guest and Prévost [8] carried out fluid topology optimization using a Darcy–Stokes flow model. Othmer *et al.* optimized the layout of 3D airduct manifolds for automotive applications employing an incompressible Navier–Stokes model [9, 10]. Pingen *et al.* [11] introduced a lattice Boltzmann method (LBM) approach to solve fluid topology optimization problems.

For topology optimization of fluids, the geometry of a body is typically described via a material distribution function (see Figure 1 on the left). The material state is defined by the optimization

*Correspondence to: Kurt Maute, Department of Aerospace Engineering Sciences, Center for Aerospace Structures, University of Colorado, Boulder, CO 80309-0429, U.S.A.
†E-mail: maute@colorado.edu

Contract/grant sponsor: National Science Foundation; contract/grant number: DMI-0348759

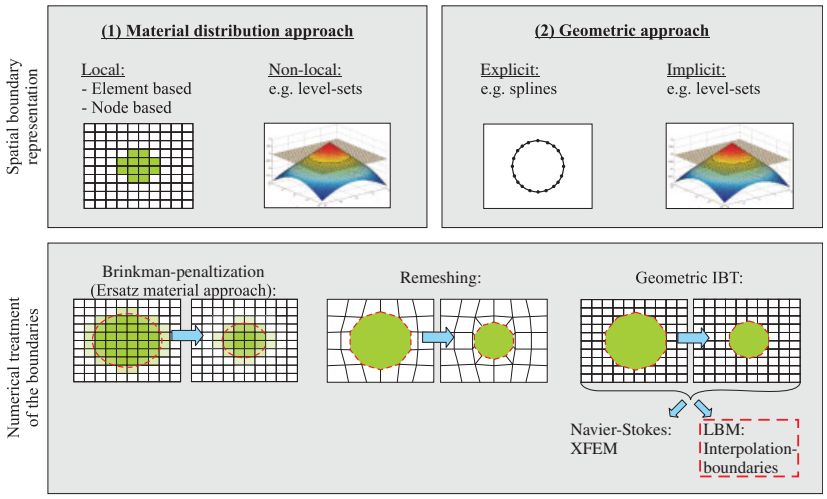

Figure 1. Boundary representation for fluid optimization.

variables s_i: for example, $s_i = 1$ for solid material, and $s_i = 0$ for fluid. This approach leads to an integer optimization problem. The solution of which quickly causes unacceptable computational cost as the number of optimization variables increases. To mitigate this issue the material distribution function is relaxed [3], allowing a continuous transition between fluid and solid material. This is referred to as the density or porosity approach as it interprets intermediate material states between solid ($p = 1$) and fluid ($p = 0$) as porous material, with p being the porosity. For optimization problems that involve, for example, the minimization of the total pressure drop across the design domain, constraining the volume occupied by fluid leads to optimized material distributions with no or only a small amount of porous material ($0 < p < 1$). To represent the desired, spatially discontinuous material distribution, an element-wise constant discretization of the material distribution is typically chosen.

In the flow model, the intermediate states ($0 < p < 1$) are commonly treated through a Brinkman formulation [12], which scales down flow velocities through porous materials, yielding zero-velocities in solid material. Although the Brinkman approach allows for a rather simple representation of fluid–solid boundaries in fluid topology optimization, it leads to several issues that can be grouped into the following two categories:

(I) *Physical modeling*: Describing the spatially discontinuous material distribution by an element-wise constant discretization leads to a stair-step-like representation of the fluid–solid interface, which may result in unrealistic flow field predictions, such as premature flow separation and vortex shedding at higher Reynolds numbers. Furthermore, extending the porosity concept and the Brinkman formulation to the multi-physics problems, such as fluid–structure interaction, is problematic if multiple constitutive parameters need to be interpolated [13–15]. For LBM flow models, in particular, the porosity approach leads to inaccuracies in the analysis of unsteady flows due to an incorrect damping of pressure waves [16]. For the steady-state problems considered in this study, the damping characteristic of the porous material may affect the convergence of time-marching schemes toward the steady-state solution.

(II) *Geometric modeling*: Representing the geometry by an element-wise constant discretization of the material distribution requires highly refined grids to resolve curved surfaces [3], in particular, for flows at higher Reynolds numbers. The perimeter of the fluid–structure interface, often used to regularize the optimization problem, can only be determined approximately [3]. Local geometric measures, such as the orientation and curvature of the interface, can only be computed indirectly using some form of post-processing [17, 18]. The latter is, in particular, an issue for inviscid flows, which require information about the local orientation of the surface to enforce slip boundary conditions. Since the porosity value is typically constant in every element, the Brinkman approach

DOI: 10.1002/fld

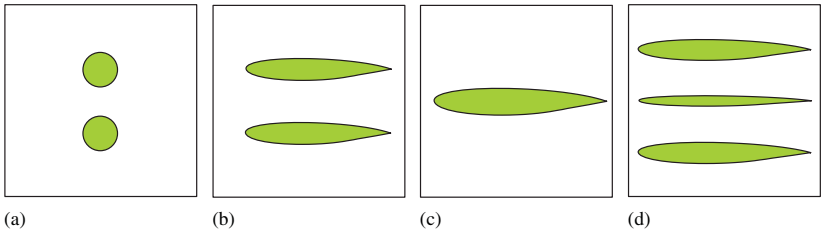

Figure 2. Comparison between the different types of optimization for an airfoil: (a) initial design; (b) shape optimization; (c) generalized shape optimization; and (d) topology optimization.

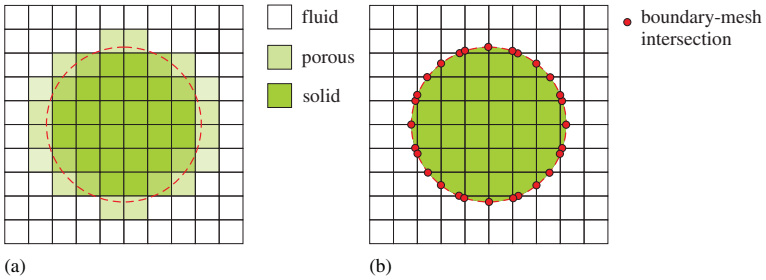

Figure 3. Immersed boundary techniques: (a) material distribution and (b) boundary interpolation.

generally requires as many design variables as there are elements, leading to a '1:1' coupling between the computational domain and the geometry describing design variables [6, 19].

In order to overcome, in particular, the geometric modeling issues of the material approach, level set methods have recently gained popularity for topology optimization (see right side of Figure 1). In comparison with explicit boundary representations via line and surface interpolations, level set methods describe the geometry implicitly by the zero-level of an auxiliary function, the level set function, and allow for changes in the topology by merging boundaries of different geometrical features. However, in contrast to topology methods based on the porosity approach, level set methods do typically not allow for the emergence of new features. To account for this difference, we refer to level set based approaches as generalized shape optimization methods in this paper. Figure 2 illustrates the difference between shape, generalized shape and topology optimization for an airfoil example.

Two classes of level set methods can be distinguished: (i) methods that satisfy the Hamilton–Jacobi equation (HJE), which implicitly describes the evolution of the level set function and (ii) explicit methods that do not consider the HJE. Given the interface geometry via level sets, the boundary conditions can be enforced by: (a) conventional schemes that require adapting the mesh to match the interface geometry, for example, via dynamic meshes or re-meshing, (b) so-called Ersatz material methods [20, 21] that closely follow the material approach described above, and (c) geometric immersed boundary techniques (IBTs). In contrast to the Brinkman approach, geometric IBTs enforce the flow boundary conditions locally at the fluid–structure interface (see Figure 3). Depending on the flow model and discretization method, different geometric IBTs are used [22]. For example, using a finite element formulation of a Navier–Stokes model the boundary conditions can be enforced via an extended finite element method (XFEM) using Lagrange-multipliers [23]. Using an LBM-solver, stick and slip conditions can be imposed through interpolation bounce-back schemes [24].

The majority of the work on level set-based optimization methods focuses on structural optimization problems. Sethian and Wiegmann [25] introduced a Hamilton–Jacobi (HJ) approach in combination with a geometric IBT. Wang *et al.* [26] and Allaire *et al.* [20] presented HJ level set

DOI: 10.1002/fld

methods using an Ersatz material approach. Xia *et al.* [27] proposed a semi-Lagrange scheme in order to improve the efficiency of the HJ level set method. Wei and Wang [28] used radial basis functions (RBFs) to parameterize the classical HJ level set function. Luo and Tong [29] applied this parametric HJ level set method to the optimization of compliant mechanisms undergoing large displacements. De Ruiter [13, 30] developed an explicit level set method that is not based on the solution of the HJE. If not stated otherwise, all of the above methods employ an Ersatz material approach and only few approaches have been presented based on geometric IBTs. Wang and Wang [21] used the HJ level set method in combination with an S-FEM approach. Van Miegroet and Duysinx [31] combined a level set method with XFEM to minimize stress concentrations.

Only limited work has been done so far on level set methods for optimizing flow problems. Cunha [32] used level sets to find the shape of obstacles that re-produces a given velocity field for a stationary, viscous, incompressible fluid. Duan *et al.* [33] applied a modified HJ level set method to solve fluid optimization problems for Stokes-flow and Navier–Stokes-flow. Mohammadi and Pironneau [34] employed the HJ level set method for the shape optimization of supersonic applications using an Euler flow model. Pingen *et al.* [35] have recently presented an explicit level set method for the optimization of flow problems using a hydrodynamic LBM fluid solver. While these level set implementations improve the smoothness of the boundaries and decouple the parameterization of the material distribution from the discretization of the flow field, all of the above approaches are based on an Ersatz material concept as well as a Brinkman formulation and therefore suffer from the disadvantages of this formulation described previously.

The goal of this study is to develop an alternative approach that overcomes the disadvantages of the Brinkman formulation. We therefore propose a geometrically accurate boundary representation. We describe the geometry of the fluid–structure interface via an explicit level set method that does not require solving the HJE but allows the use of standard nonlinear programming schemes. Steady–steady flow fields are predicted by a hydrodynamic LBM and the boundary conditions are enforced locally via a second order accurate interpolation bounce-back scheme [36]. LBM is well suited for our optimization approach as it is inherently based on IBT and allows switching from fluid to solid state and vice versa in a simple manner.

The current study introduces a geometric boundary representation for fluid optimization problems. Numerical studies have shown that the geometric boundary representation requires a smoothing operation, i.e. a filter, when applied to generalized shape optimization. In topology optimization, filters are generally employed to eliminate the dependency of the optimum design on the spatial discretization [1]. In the current study the filter also ensures smooth boundaries, which are essential for the convergence of the flow solution. Furthermore, we introduce constraints for the design variables that ensure a continuous evolution of the boundary. The design sensitivities for the employed geometric boundary representation are computed by an adjoint method. The proposed generalized shape optimization method is illustrated and the influence of key algorithmic parameters is studied with two two-dimensional problems.

The remainder of this paper is structured as follows: In Section 2 we will give a short introduction into LBM. This will be followed by a section on the level set method. There we outline the classical and parametric HJ level set method, as well as explicit level set methods, including the proposed approach. In Section 4 we describe the overall computational optimization procedure, along with the sensitivity analysis for both level sets and LBM. Finally, we will demonstrate the key features of the proposed approach with two numerical examples. The main results of this study are summarized in Section 6.

2. LATTICE BOLTZMANN METHOD

In the recent years, the LBM has gained increasing popularity as an alternative to the incompressible Navier–Stokes equations [16, 37]. Besides the previous work by the authors, that employed LBM for solving fluid topology optimization problems [11, 19, 35, 38, 39], Geier *et al.* [40] used a heuristics-based lattice Boltzmann topology optimization approach to solve the basic Stokes flow problems introduced by Borrvall and Petersson [6].

DOI: 10.1002/fld

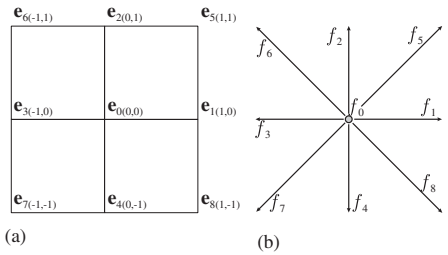

Figure 4. Velocity distribution for the D2Q9 lattice [19]: (a) velocity vector $\mathbf{e}_\alpha$ and (b) distribution function f_α.

The lattice Boltzmann equation models hydrodynamic flows based on kinetic theory and can be derived from the Boltzmann equation, leading to a two-step computational process:

$$\text{(1) Collision:} \quad \widetilde{f}_\alpha(\mathbf{x}_i, t) = f_\alpha(\mathbf{x}_i, t) - \frac{1}{\tau}[f_\alpha(\mathbf{x}_i, t) - f_\alpha^{\text{eq}}(\mathbf{x}_i, t)] \tag{1}$$

$$\text{(2) Propagation:} \quad f_\alpha(\mathbf{x}_i + \delta t \mathbf{e}_\alpha, t + \delta t) = \widetilde{f}_\alpha(\mathbf{x}_i, t) \tag{2}$$

where $\mathbf{e}_\alpha$ is the velocity vector, f_α is the distribution function associated with the corresponding velocity $\mathbf{e}_\alpha$, $\mathbf{x}_i$ represents the location in physical space, $\mathbf{e}_\alpha \delta t$ is the lattice spacing, δt is the time step, and $\tau = \lambda/\delta t$ is the dimensionless relaxation time. For the current study, the D2Q9 lattice model as illustrated in Figure 4 is used. For low Mach number flow conditions, the equilibrium distribution function f^{eq} in Equation (1) can be derived by a Taylor series expansion of the Maxwell–Boltzmann equilibrium distribution as:

$$f_\alpha^{\text{eq}} = w_\alpha \rho [1 + 3(\mathbf{e}_\alpha \cdot \mathbf{u}) + \tfrac{9}{2}(\mathbf{e}_\alpha \cdot \mathbf{u})^2 - \tfrac{3}{2}\mathbf{u}^2] \tag{3}$$

where ρ represents the macroscopic density, the vector $\mathbf{u}$ is the macroscopic velocity, and w_α are lattice weights that depend on the lattice geometry. The macroscopic parameters, density and velocity, are evaluated by taking statistical moments of the distribution function f_α, and are given by:

$$\rho(\mathbf{x}, t) = \sum_{\alpha=0}^{8} f_\alpha(\mathbf{x}, t) \tag{4}$$

$$\rho \mathbf{u}(\mathbf{x}, t) = \sum_{\alpha=0}^{8} \mathbf{e}_\alpha f_\alpha(\mathbf{x}, t) \tag{5}$$

The boundary conditions at the fluid–solid interfaces are imposed via a no-slip interpolation bounce-back formulation. This approach allows for a continuous change in the position of the fluid–solid interface by modeling the exact point of intersection between lattice link and boundary location with second-order accuracy in the velocity and first-order accuracy in the pressure [41]. In this study we use the interpolation boundary condition introduced by Bouzidi *et al.* [42]. The spatial location of the boundary along each lattice link is defined by

$$\Delta_{(h,\alpha)} = \frac{|x_h - x_w|}{|x_h - x_b|} \quad \text{with } 0 < \Delta_{(h,\alpha)} \leqslant 1 \tag{6}$$

where x_h is the location of the closest fluid node, x_w is the location of the wall, x_b is the location of the closest boundary node (see Figure 5). The subscripts h and α on $\Delta_{(h,\alpha)}$ define the index of the node and the direction in which the boundary lies, according to Figure 4. To distinguish between neighboring nodes, we introduce a second index h^+ (that defines the node neighboring h).

DOI: 10.1002/fld

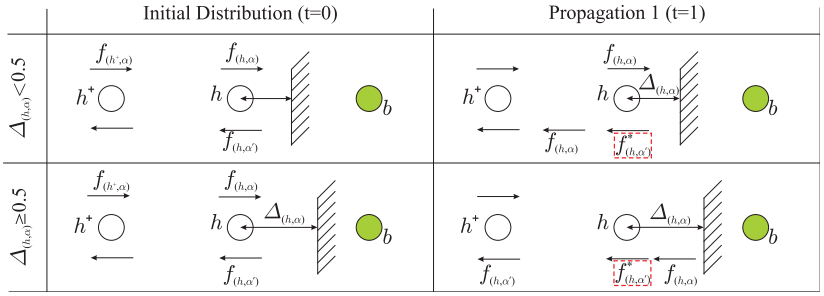

Figure 5. Illustration of interpolation boundary conditions [19].

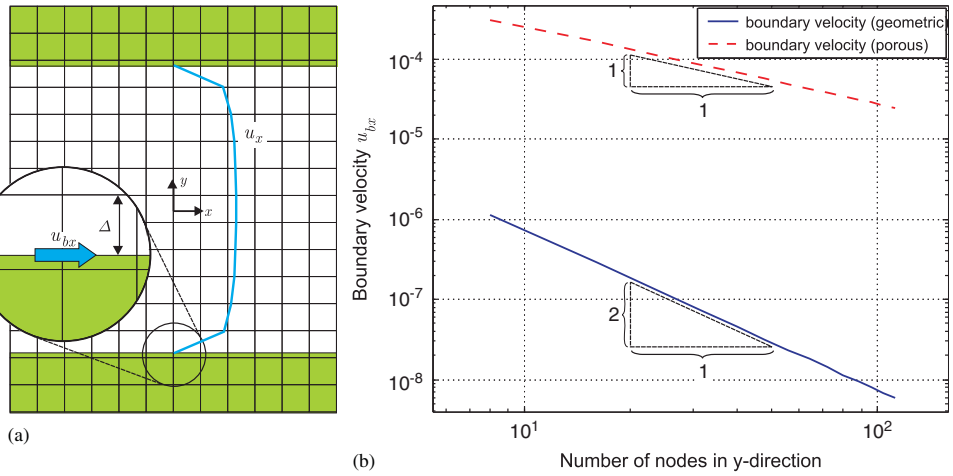

Figure 6. Convergence of boundary velocity: (a) channel with 'no-slip' boundaries and (b) convergence diagram.

The underlying concept behind the interpolation boundary conditions is illustrated in Figure 5, showing that when $\Delta_{(h,\alpha)} \neq 0.5$, the reflected distribution function, $f_{(h,\alpha')}$, must be interpolated. Bouzidi *et al.* [42] recommend the following linear interpolations:

$$f^*_{(h,\alpha')} = 2\Delta_{(h,\alpha)} f_{(h,\alpha)} + (1 - 2\Delta_{(h,\alpha)}) f_{(h^+,\alpha)} \quad \forall \Delta_{(h,\alpha)} < 0.5 \tag{7}$$

$$f^*_{(h,\alpha')} = \frac{1}{2\Delta_{(h,\alpha)}} f_{(h,\alpha)} + \frac{2\Delta_{(h,\alpha)} - 1}{2\Delta_{(h,\alpha)}} f_{(h,\alpha')} \quad \forall \Delta_{(h,\alpha)} \geqslant 0.5 \tag{8}$$

where the subscript α' indicates the opposite direction of α, the superscript $*$ indicates the unknown distribution function. The subscripts h and h^+ denote the first and second fluid node from the boundary, as illustrated in Figure 5.

Figure 6 illustrates the convergence of the boundary velocity of a flow through a straight channel with 'no-slip' boundaries as the mesh is refined. The plots show the velocities for porous and geometric boundary representation. During the mesh refinement, the relative values for Δ and porosity p are kept constant. In both cases, the velocities at the wall are computed based on a second-order extrapolation from the nodal values [36]. As can be seen from the logarithmic graphs, the porous approach converges linearly, whereas the geometric approach shows quadratic convergence. Furthermore, the geometric boundary representation leads to a significantly smaller error in the velocities; for example, for 8 nodes: $u_{bx} \approx 10^{-6}$ compared with $u_{bx} \approx 3 \cdot 10^{-4}$ for the porosity-based approach.

DOI: 10.1002/fld

In this study, we consider only steady-state flows, which are described by the solution of the following fixed-point problem:

$$\mathbf{R}(\mathbf{f}, \boldsymbol{\Delta}) = \mathbf{M}(\mathbf{f}, \boldsymbol{\Delta}) - \mathbf{f} = \mathbf{0} \tag{9}$$

where $\mathbf{R}$ denotes the residual vector. In Equation (9) the operator $\mathbf{M}$ performs a combination of propagation (Equation (2)) for fluid nodes, denoted by $\boldsymbol{\Pi}$, and interpolation (Equations (7) and (8)) for boundary nodes, denoted by $\boldsymbol{\Lambda}$, followed by one collision (Equation (1)) denoted by $\boldsymbol{\Omega}$. Thus, the operator $\mathbf{M} = [\boldsymbol{\Pi} + \boldsymbol{\Lambda}](\boldsymbol{\Omega})$ advances the flow to the next time step. The fixed point problem (9) is solved by advancing the transient solution in time until the difference between two consecutive flow states is negligible (i.e. steady state is reached). For monitoring the convergence to steady state we use the following criterion:

$$\frac{\mathbf{R}}{\mathbf{R}_{\text{ref}}} \leqslant 10^{-6} \tag{10}$$

where $\mathbf{R}$ is the current residual vector and $\mathbf{R}_{\text{ref}}$ is the residual vector for the initial time step.

3. LEVEL SET METHOD

In this section we briefly discuss two formulations of the level set method, the HJE-based approach and the explicit approach. To point out the differences/similarities between these two approaches later, we start by discussing the main features of the classical Hamilton–Jacobi level set method. Then, we describe the general characteristics of the explicit level set method used in the current study.

3.1. Hamilton–Jacobi level set method

The level set method, first developed by Osher and Sethian [43], uses an $(N+1)$-dimensional function Φ to describe the interface within an N-dimensional space (see Figure 7):

$$\Phi : \Re^{N+1} \rightarrow \Re^{N} \tag{11}$$

The interface is implicitly defined through the zero level set:

$$\Gamma = \{\mathbf{x} : \Phi(\mathbf{x}, t) = 0\} \tag{12}$$

The value of the scalar function Φ defines whether the domain belongs to material A (Ω^A, e.g. fluid), to material B (Ω^B, e.g. solid) or to the fluid–structure interface Γ:

$$\Phi(\mathbf{x}, t) < 0 \quad \forall \mathbf{x} \in \Omega^A \tag{13}$$

$$\Phi(\mathbf{x}, t) = 0 \quad \forall \mathbf{x} \in \Gamma = \delta\Omega \tag{14}$$

$$\Phi(\mathbf{x}, t) > 0 \quad \forall \mathbf{x} \in \Omega^B \tag{15}$$

As the value of the level set function at the boundary is constant (cf. Equation (14)), the evolution of Φ can be described as follows:

$$\frac{\mathrm{d}\Phi}{\mathrm{d}t} = \Phi_t + \nabla\Phi \cdot \frac{\mathrm{d}\mathbf{x}}{\mathrm{d}t} = 0 \tag{16}$$

where $\mathrm{d}\mathbf{x}/\mathrm{d}t$ is the velocity of the boundary. In order to eliminate the undesired tangential components of the boundary velocity, Equation (16) is rearranged in the following way:

$$\Phi_t + |\nabla\Phi| \underbrace{\frac{\nabla\Phi}{|\nabla\Phi|} \frac{\mathrm{d}\mathbf{x}}{\mathrm{d}t}}_{\mathbf{v_n}} = \Phi_t + |\nabla\Phi| \cdot \mathbf{v_n} = 0 \tag{17}$$

DOI: 10.1002/fld

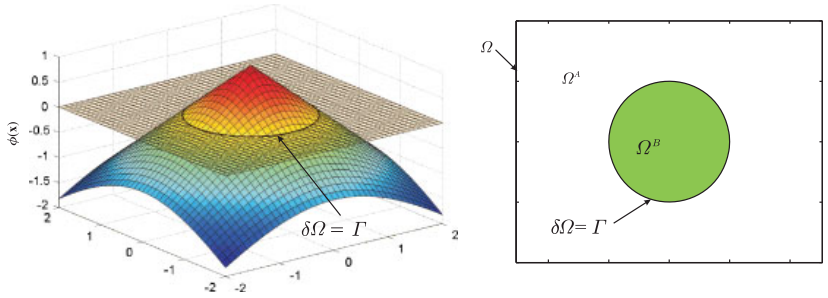

Figure 7. Three-dimensional level set function $\Phi(\mathbf{x})$, cut-off at $\Phi(\mathbf{x})=0$ leads to 2-dimensional boundaries Γ.

where $\mathbf{v_n}$ is the normal velocity of the boundary. Substituting the normal velocity $\mathbf{v_n}$ with a more general speed function $\mathbf{F_n}$ (in normal direction), leads to the Hamilton–Jacobi level set equation given by Osher and Sethian:

$$\Phi_t + |\nabla\Phi| \cdot \mathbf{F_n} = 0 \tag{18}$$

This classical Hamilton–Jacobi level set method has become a popular approach in topology optimization to describe the geometry of bodies as it allows a simple treatment of complex geometrical changes [27]. During the optimization process the evolution of the level set function Φ is governed by the HJE (18) and the speed function $\mathbf{F_n}$ is dependent on the Lagrangian function of the underlying optimization problem. The steady-state solution of Equation (18) is equivalent to the solution to the optimization problem [44]. As there is an infinite number of functions Φ that have the same zero level set, Φ is usually re-initialized as a signed distance function every couple of time steps [45]. This re-initialization is time consuming and tends to generate errors in the boundary position, which might lead to accuracy-problems [46]. Furthermore, since for practical reasons Equation (18) is typically solved with explicit schemes, the Courant–Friedrichs–Lewy condition requires that the boundary only moves a maximum distance of d^2 (d: gridsize) within each time step Δt [27]. In the context of optimization, the time t can be interpreted as a pseudo-time that increases by Δt at every optimization step.

In the classical HJ level set approach the Φ-function is generally discretized through a uniformly structured finite element mesh and approximated on an element level by

$$\Phi(x,t) = \sum_i \phi_i(t) N_i(x) \tag{19}$$

where $\phi_i(t)$ are the nodal level set values and $N_i(x)$ are the standard local shape functions [26]. The level set mesh is typically the same as the one used to approximate the solution of the underlying partial differential equation. The classical HJ level set method has one major drawback: the optimization problem requires solving Equation (18) and thus cannot utilize standard nonlinear programming methods.

Wang and Wang [47] introduced an alternative parametric level set method that avoids solving the HJE explicitly. In contrast to the classical approach, the parametric HJ level set method uses globally supported RBFs to discretize Φ (cf. Equation (19)):

$$\Phi(\mathbf{x},t) = \sum_i \alpha_i(t) \phi_i(\mathbf{x}) \tag{20}$$

where $\phi_i(\mathbf{x})$ is the ith RBF and $\alpha_i(t)$ is the corresponding weight for that RBF. Wang and Wang [47] suggest multi-quadric splines as RBF:

$$\phi_i(\mathbf{x}) = \sqrt{\|\mathbf{x}-\mathbf{x}_i\|^2 + c_i^2} \tag{21}$$

where $\mathbf{x}_i$ describes the position of the center of the ith RBF and c_i is a free shape parameter that is commonly kept constant for all i [48]. By substituting the Φ-function defined in Equation (20) into Equation (18), the problem can be transformed into a parameter optimization problem in $\alpha_i(t)$ that explicitly satisfies the HJE [28].

DOI: 10.1002/fld

3.2. Explicit level set method

De Ruiter [13, 30] developed an alternative level set approach and applied it to structural optimization problems. Similar to the approach developed by Wang and Wang [47] this method also employs RBFs to discretize the Φ-function:

$$\Phi(\mathbf{x}, s_i) = \sum_i \phi_i(\mathbf{x}, s_i) \quad \text{with } \phi_i(\mathbf{x}, s_i) = s_i \cdot \exp\left(\frac{(\mathbf{x}-\mathbf{x}_i)^2}{w^2}\right) \tag{22}$$

where $\phi_i(\mathbf{x}, s_i)$ are the Gaussian normal distribution RBFs. The parameter w determines the width and s_i the height of the RBF. However, in contrast to the previous techniques this method does not satisfy the HJE but chooses a more straightforward approach: the heights of the RBFs (s_i) are treated as independent optimization variables and during the optimization process the evolution of the level set function $\Phi(\mathbf{x}, s_i)$ is explicitly controlled by the optimization algorithm. The linear relation between the design variables s_i and the Φ-function simplifies the computation of the sensitivities of the interface position with respect to the optimization variables. Standard gradient-based optimization algorithms can be used to solve this optimization problem.

3.3. Comparison between level set methods

Table I shows a brief overview of the aforementioned level set formulations and their corresponding features. When employing the classical HJ level set method for optimization purposes, it requires solving Equation (18) using some form of stabilization methods, such as upwinding [50]. Explicitly solving the HJE prevents the use of standard optimization algorithms. The parametric HJ level set method circumvents solving the HJE directly, by transforming the HJE into a parameter optimization problem (using globally supported RBFs). Finally, in the explicit level set method, the interface motion is controlled by directly modifying the heights of the RBFs.

According to Mohammadi [34, 49] and Jameson *et al.* [51], regularity control (i.e. smoothing) is essential for the success of the fluid optimization process when using level set methods. The convective term in fluid problems transports perturbations only in the downstream direction, and therefore localizes the effect of the perturbation. Structural systems are more well-behaved in this regard, since according to Saint Venant's principle the perturbation gets evenly distributed in the surrounding domain [52].

As previously demonstrated by the authors [35, 39], the explicit level set method works well for fluid optimization problems when a Brinkman formulation is used to enforce the boundary conditions. In this case, the level set function does not need to be smoothed explicitly. Numerical studies [39] suggest that the blurred boundaries of the Brinkman formulation (see Figure 3(a)) add regularity to the problem. Contrarily, as we will show later in this paper, using a geometric IBT leads to regularity issues and requires explicit smoothing.

3.4. Explicit level set method for fluid optimization

The level set method in this paper follows the ideas of De Ruiter [13, 30] described in Section 3.2 and combines it with the concept of smoothness control, thus transforming the originally ill-posed optimization problem into a well-posed one.

Table I. Overview over level set methods for general shape and topology optimization.

	Classical HJ level set method	Parametric HJ level set method	Explicit level set method
Spatial discretization	Local shape functions	RBFs	RBFs
Dependence on design variables	Implicit	Explicit	Explicit
Interface advancing governed by	HJE	Optim. algorithm	Optim. algorithm
References	[20, 25, 27, 33, 49]	[28, 29, 35]	[13, 30, 35, 39]

DOI: 10.1002/fld

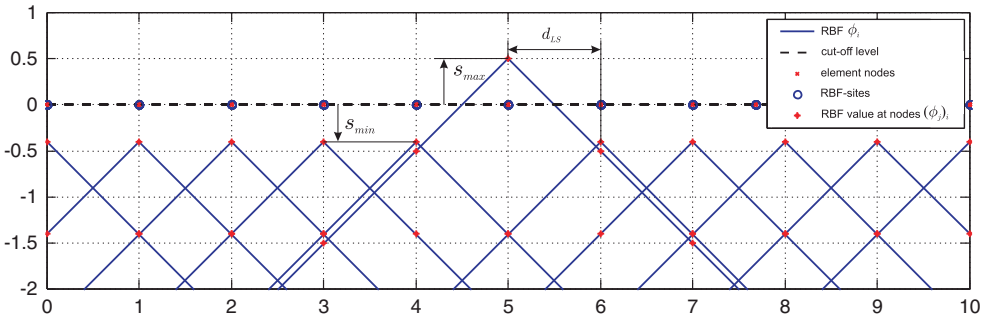

Figure 8. Evaluation of every RBF at every node.

As basis functions we use multi-quadric RBFs, similar to the ones defined by Equation (21):

$$\phi_i(\mathbf{x}, s_i) = s_i - \sqrt{\|\mathbf{x}-\mathbf{x}_i\|^2 + c^2} \tag{23}$$

This function describes a cone with a slightly flattened tip (due to the free shape parameter c) whose position in the vertical direction is determined by the design variable s_i. Figure 8 shows a 2D plot of RBFs as described in Equation (23).

If the box constraints for the design variables ($s_{\min}, s_{\max}$) are chosen properly, it can be guaranteed that the Φ-function grows gradually around the zero-level. This is important because overshadowing RBFs can potentially lead to holes that cannot be filled in subsequent iterations of the optimization process (see Section 5.1), since the sensitivities of the overshadowed RBFs become negligible. To prevent this constellation, the lower and upper limits for the design variables s_i are chosen as follows:

$$s_{\min} > -(d_{LS} - s_{\max}) \tag{24}$$

$$0 < s_{\max} < d_{LS} \tag{25}$$

The variable d_{LS} in Equations (24) and (25) defines the distance between the origins of two neighboring RBFs (i.e. the gridsize of the level set mesh).

Owing to the global support of the RBFs there are n ϕ_j-values at every node, with n being the number of RBFs:

$$(\phi_j)_i \quad \text{for } j = 1, \ldots, n \tag{26}$$

In order to obtain the level set value $\tilde{\Phi}_i$ (at node i) from the n RBF values $(\phi_j)_i$, $j = 1, \ldots, n$, we approximate the maximum by a Kreisselmeier–Steinhauser (KS) function [53]:

$$\tilde{\Phi}_i = \frac{1}{k} \ln \left(\sum_{j=1}^{n} (\mathrm{e}^{(k \cdot (\phi_j)_i)}) \right) \quad \forall j : |\mathbf{x}_j - \mathbf{x}_i| \leqslant R_\phi \tag{27}$$

where k is the KS-factor. Unlike an exact maximum function, this KS-approximation effectively prevents discontinuities when superposing the nodal $\tilde{\Phi}_i$ values. Additionally we only consider ϕ_j-values within a radius R_ϕ of the ith node, which leads to a compact support of the RBFs. This limitation of the support of the RBFs is essential for reducing the computational cost of the sensitivity analysis (see Section 4.2). Figure 9 shows a comparison between the exact maximum and the KS-approximated maximum $\tilde{\Phi}$-function. The bar below the plot shows the resulting design when the $\tilde{\Phi}$-function is cut off at $\tilde{\Phi} = 0$ (cf. Equations (13)–(15)).

To ensure smooth boundaries, which are essential when working with a geometric boundary representation, we introduce a smoothing operator that regularizes the fluid shape optimization problem. The geometric smoothing operator follows the idea of Sigmund and Petersson [54] as

DOI: 10.1002/fld

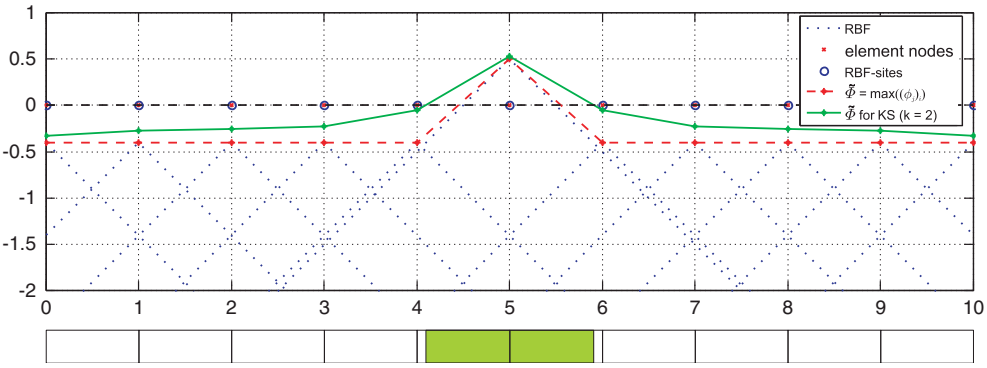

Figure 9. Comparison between the exact and the KS-approximated maximum nodal $\tilde{\Phi}$-values. The bar shows the corresponding geometry for the KS-approximated maximum.

well as Daoud *et al.* [55], who used it to filter the gradients of the design criteria with respect to the design variables in structural optimization. However, in this study the filter is applied to the nodal $\tilde{\Phi}$ values. As this filtering operation is also considered in the sensitivity analysis the derivatives with respect to the design variables are numerically consistent:

$$\Phi_i = \frac{\sum_l (R - r_{il})\tilde{\Phi}_l}{\sum_l (R - r_{il})} \quad \forall l : r_{il} \leqslant R = R_r \sqrt{2} d_{LS} \tag{28}$$

where r_{il} is the distance between the ith and the lth node, R_r is the relative smoothing radius and d_{LS} is the gridsize of the level set mesh. Equation (28) effectively limits the spatial oscillations of the level set function, which results in a reduction of the total length of the perimeter.

Figure 10 shows a comparison between a Φ-function based on Gaussian-normal-distribution-functions (22) without smoothing and a Φ-function based on cone-shaped RBFs (23) with smoothing. The resulting designs, illustrated by bars below the plots in Figure 10, show that the Gaussian-RBFs also require regularity control to prevent checkerboard-like designs.

Given the smoothened Φ-function, we capture the geometry based on the nodal Φ_i-values as illustrated in Figure 11. For example, the value $\Delta_{(b,3)}$ is calculated according to the following formula:

$$\Delta_{(b,3)} = \begin{cases} \dfrac{\Phi_b}{\Phi_b - \Phi_a} \cdot d & \forall \Phi_a \cdot \Phi_b \leqslant 0 \\ 0 & \forall \Phi_a \cdot \Phi_b > 0 \end{cases} \tag{29}$$

where d is the gridsize of the fluid-domain. All horizontal/vertical values, $\Delta_{(h,1-4)}$, are calculated in the same manner. The values on the diagonal, $\Delta_{(h,5-8)}$, are computed based on bilinear interpolation.

4. GENERALIZED SHAPE OPTIMIZATION FOR FLUIDS

In this study we consider nonlinear constrained optimization problems of the following form:

$$\min_{\mathbf{s}} \quad \mathscr{F}(\mathbf{s}, \mathbf{f}(\mathbf{s})) \qquad \text{s.t.} \quad \begin{cases} \mathbf{s} & \text{satisfy the design constraints} \\ \mathbf{f} & \text{solves the governing equations for given } \mathbf{s} \\ \mathbf{h}(\mathbf{s}, \mathbf{f}) = \mathbf{0} & \text{satisfy the equality constraints} \\ \mathbf{g}(\mathbf{s}, \mathbf{f}) \leqslant \mathbf{0} & \text{satisfy the inequality constraints} \end{cases} \tag{30}$$

where $\mathscr{F}$ is a particular performance (objective) functional, $\mathbf{s}$ is the vector of design variables, $\mathbf{f}$ is the corresponding state vector (cf. Equation (9)) and $\mathbf{h}, \mathbf{g}$ are equality, inequality constraints,

DOI: 10.1002/fld

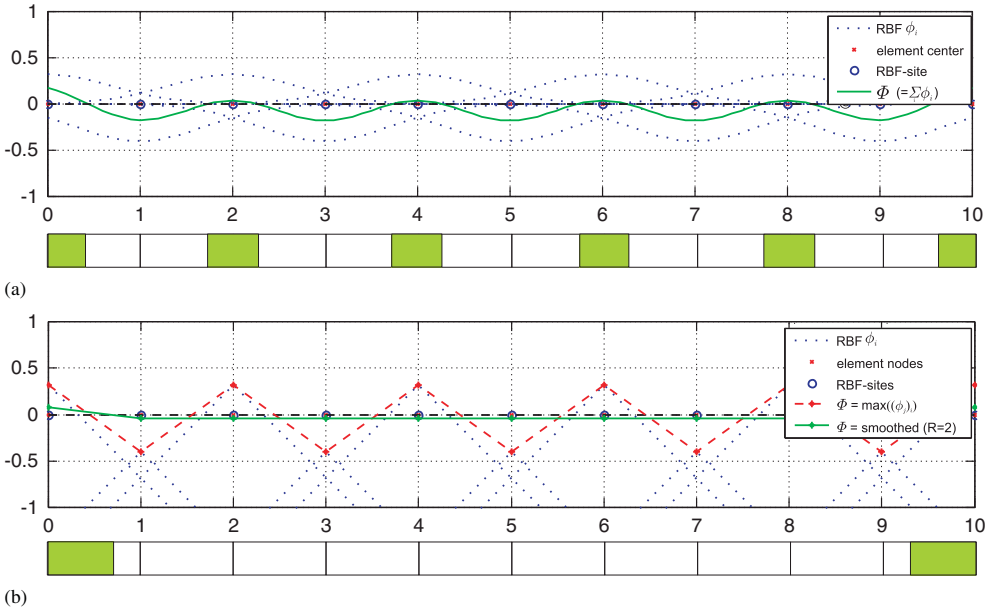

Figure 10. Comparison between Gaussian-RBFs without geometric smoothing and multi-quadric RBFs with geometric smoothing: (a) ϕ-function based on Gaussian-normal-distribution-RBFs and resulting design without geometric smoothing and (b) ϕ-function based on cone-shaped RBFs and resulting design with geometric smoothing.

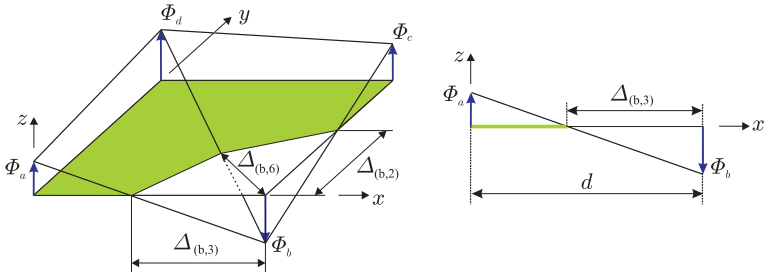

Figure 11. Determining the geometry, based on the nodal Φ_i-values.

respectively. Typical objectives and constraints include pressure drop, drag, flow rate, energy loss, and volume. We solve Equation (30) by a nested loop approach using a gradient-based optimization method. The computation of the gradients is outlined subsequently.

4.1. Sensitivity analysis

The following discussion focuses on the sensitivity analysis for the design objective $\mathscr{F}$, but can be analogously applied to design constraints. Owing to the large number of design variables, we compute the sensitivity of the design objective $\mathscr{F}$ with respect to the design variables by an adjoint method:

$$\frac{\mathrm{d}\mathscr{F}}{\mathrm{d}\mathbf{s}} = \underbrace{\frac{\partial\mathscr{F}}{\partial\boldsymbol{\Delta}}}_{(A)}\underbrace{\frac{\partial\boldsymbol{\Delta}}{\partial\mathbf{s}}}_{(B)} - \left[\underbrace{\left(\frac{\partial\mathbf{R}}{\partial\mathbf{f}}\right)^{-\mathrm{T}}}_{(C)}\underbrace{\frac{\partial\mathscr{F}}{\partial\mathbf{f}}}_{(D)}\right]^{\mathrm{T}}\underbrace{\frac{\partial\mathbf{R}}{\partial\boldsymbol{\Delta}}}_{(E)}\underbrace{\frac{\partial\boldsymbol{\Delta}}{\partial\mathbf{s}}}_{(B)} \tag{31}$$

DOI: 10.1002/fld

Table II. Sensitivity terms for LBM (n: number of domain nodes).

Term	Derivative of	With respect to	Matrix-size
(A)	Objective $\mathscr{F}$	Geometry $\Delta_{(h,\alpha)}$	Geometry dependent
(B)	Geometry $\Delta_{(h,\alpha)}$	Design variables s_k	Geometry dependent
(C)	Residual of flow solution R_p	Fluid state variables $f_{(h,\alpha)}$	$9n \times 9n$
(D)	Objective $\mathscr{F}$	Fluid state variables $f_{(h,\alpha)}$	$9n \times 1$
(E)	Residual of flow solution R_p	Geometry $\Delta_{(h,\alpha)}$	Geometry dependent

Table III. Sensitivity terms for the level sets (n: number of domain nodes, m: number of design variables).

Term	Derivative of	With respect to	Matrix-size
(B_1)	Geometry $\Delta_{(h,\alpha)}$	Smoothed nodal Φ_i-values	Geometry dependent
(B_2)	Smoothed nodal Φ_i-values	Nodal $\tilde{\Phi}_l$-values	$n \times n$
(B_3)	Nodal $\tilde{\Phi}_l$-values	RBFs ϕ_j	$n \times m$
(B_4)	RBFs ϕ_j	Design variables s_k	$m \times m$

The terms (A), (B), (C) and (E) in the sensitivity equation (31) are dependent on the current geometric boundary representation. The remaining term (D) is identical to the one from the material distribution-based topology optimization and has been discussed in detail in the authors' recent work [38]. Therefore, only the terms unique to geometric shape optimization ((A), (B), (C) and (E)) will be discussed here. Furthermore, it should be noted that while (A) is zero for the objectives used in the present work (flow rate and pressure drop), objectives involving force calculations via the LBM momentum exchange method [56] would lead to non-zero sensitivities, for example. Table II briefly summarizes the terms in Equation (31).

4.2. Sensitivity analysis for level sets (B)

The level set method describes the geometry (i.e. the $\Delta_{(h,\alpha)}$-values) based on the design variables s_k. According to Equations (23) and (27)–(29), the sensitivities of the geometry with respect to the design variables can be split up into the following four terms:

$$\underbrace{\frac{\partial \boldsymbol{\Delta}}{\partial \mathbf{s}}}_{(B)} = \underbrace{\frac{\partial \boldsymbol{\Delta}}{\partial \boldsymbol{\Phi}}}_{(B_1)} \cdot \underbrace{\frac{\partial \boldsymbol{\Phi}}{\partial \tilde{\boldsymbol{\Phi}}}}_{(B_2)} \cdot \underbrace{\frac{\partial \tilde{\boldsymbol{\Phi}}}{\partial \boldsymbol{\phi}}}_{(B_3)} \cdot \underbrace{\frac{\partial \boldsymbol{\phi}}{\partial \mathbf{s}}}_{(B_4)} \tag{32}$$

Table III briefly lists the meaning and matrix-size for the four terms in Equation (32). Details about the computational cost for each term are summarized in the following:

- (B_1) is geometry dependent and due to the small number of Δ-values (as the interface usually only covers small areas of the design space) generally computationally inexpensive.
- (B_2) has a band-structure as the smoothing operator is only applied within the filter radius R (cf. Equation (28)).
- (B_3) is computationally cheap as the support of the RBFs ϕ_j is limited by the radius of influence R_ϕ in Equation (27).
- (B_4) is a unity matrix as the jth RBF ϕ_j is only (linearly) dependent on the jth design variable s_j (cf. Equation (23)).

Equation (32) also identifies one of the disadvantages of this IBT: the sensitivities $\partial\boldsymbol{\Delta}/\partial\mathbf{s} = \partial\Delta_{(h,\alpha)}/\partial s_k$ only exist if $\Delta_{(h,\alpha)}$ exists. This means that the design can only grow across existing boundaries, that is, no new domains of solid material completely surrounded by fluid (islands) can emerge. Furthermore, it is not possible to create new holes within the solid domain. However, the inability to create new islands can be compensated by an initial design that has a sufficient number of separated solid regions. The creation of holes within the solid domain is insignificant

DOI: 10.1002/fld

for fluid optimization as this does not affect the flow solution. In structural optimization the issue of creating holes is usually handled by topological derivatives [30].

4.3. Evaluation of the LBM Jacobian (C)

The Jacobian of the LBM fixed-point system (9), $(\partial\mathbf{R}/\partial\mathbf{f})^{\mathrm{T}}$, can be expanded as

$$\left(\frac{\partial\mathbf{R}}{\partial\mathbf{f}}\right)^{\mathrm{T}}=\left(\frac{\partial\mathbf{M}}{\partial\mathbf{f}}\right)^{\mathrm{T}}-\mathbf{I} \tag{33}$$

where $(\partial\mathbf{M}/\partial\mathbf{f})^{\mathrm{T}}$ is a function of the operator $\mathbf{M}$, which advances the flow to the next time step and was introduced in Section 2. Analogously, $(\partial\mathbf{M}/\partial\mathbf{f})^{\mathrm{T}}$ can be separated into its components:

$$\left(\frac{\partial\mathbf{M}}{\partial\mathbf{f}}\right)^{\mathrm{T}}=\left(\frac{\partial\mathbf{\Pi}}{\partial\mathbf{f}}+\frac{\partial\mathbf{\Lambda}}{\partial\mathbf{f}}\right)^{\mathrm{T}}\circ\left(\frac{\partial\mathbf{\Omega}}{\partial\mathbf{f}}\right)^{\mathrm{T}} \tag{34}$$

Here, the Jacobians of the propagation operator $\mathbf{\Pi}$ and the collision operator $\mathbf{\Omega}$ have been described in detail in the authors' previous work [38]. At this point, only the Jacobian of the interpolation operator $\mathbf{\Lambda}$ will be discussed.

Considering the first of the two boundary interpolation functions, Equation (7), for $\Delta_{(h,\alpha)}<0.5$, the Jacobian can be written as:

$$\begin{aligned}\left(\frac{\partial\mathbf{\Lambda}}{\partial f_{(g,\beta)}}\right)^{\mathrm{T}}&=\left(\frac{\partial f_{(h,\alpha')^*}}{\partial f_{(g,\beta)}}\right)^{\mathrm{T}}\\&=\left(\frac{\partial(2\Delta_{(h,\alpha)}f_{(h,\alpha)}+(1-2\Delta_{(h,\alpha)})f_{(h^+,\alpha)})}{\partial f_{(g,\beta)}}\right)^{\mathrm{T}}\\&=\begin{cases}2\Delta_{(h,\alpha)} & \forall f_{(g,\beta)}=f_{(h,\alpha)}\\ 1-2\Delta_{(h,\alpha)} & \forall f_{(g,\beta)}=f_{(h^+,\alpha)}\\ 0 & \text{otherwise}\end{cases}\end{aligned} \tag{35}$$

The Jacobian for $\Delta_{(h,\alpha)}\geqslant 0.5$ can be obtained likewise.

As shown previously by the authors [39], the Jacobian of the propagation operator effectively shifts rows in the Jacobian of the collision operator. In a similar fashion, the Jacobian of the interpolation boundary condition (35) effectively shifts, scales, and adds rows in the Jacobian of the collision operator.

4.4. Delta sensitivities of the LBM fixed-point residual (E)

Considering the definition $\mathbf{M}=[\mathbf{\Pi}+\mathbf{\Lambda}](\mathbf{\Omega})$ and the involved operators, only the interpolation boundary operator $\mathbf{\Lambda}$ (Equations (7) and (8)) depends on $\Delta_{(h,\alpha)}$. Therefore, the derivative of the residual of the fixed-point problem (9) with respect to the geometry, $\partial\mathbf{R}/\partial\mathbf{\Delta}$, is given for the first interpolation function (7), that is, $\Delta_{(h,\alpha)}<0.5$ by

$$\begin{aligned}\left(\frac{\partial\mathbf{R}}{\partial\Delta_{(g,\beta)}}\right)=\left(\frac{\partial\mathbf{\Lambda}}{\partial\Delta_{(g,\beta)}}\right)&=\left(\frac{\partial f^*_{(h,\alpha')}}{\partial\Delta_{(g,\beta)}}\right)\\&=\left(\frac{\partial(2\Delta_{(h,\alpha)}f_{(h,\alpha)}+(1-2\Delta_{(h,\alpha)})f_{(h^+,\alpha)})}{\partial\Delta_{(g,\beta)}}\right)\\&=\begin{cases}2f_{(h,\alpha)}-2f_{(h^+,\alpha)} & \forall(g=h\wedge\alpha=\beta)\\ 0 & \text{otherwise}\end{cases}\end{aligned} \tag{36}$$

where g and β are subscripts to indicate the node location and velocity direction analogous to h and α. The derivative for $\Delta_{(h,\alpha)}\geqslant 0.5$ can be obtained likewise.

DOI: 10.1002/fld

5. NUMERICAL EXAMPLES

To illustrate the utility and features of the current approach for generalized fluid shape optimization, two numerical examples are studied. With the first example, the effect of algorithmic parameters (box constraints for design variables, smoothing radius and level set mesh coarseness) is analyzed, whereas the second example demonstrates the versatility of the current method. In both examples, we use a globally-convergent method of moving asymptotes (GCMMA) by Svanberg [57] as the optimization algorithm. The GCMMA is a dual algorithm that solves the optimization problem iteratively in the space of the dual variables. At each iteration an approximate, explicit, separable subproblem in the space of the primal variables is created and solved analytically. This algorithm is specifically suited for problems with large numbers of design variables and few constraints as on hand in the current study. Figure 12 illustrates the overall optimization process: based on the design variables the heights of the RBFs are assigned. The superposition of the RBFs leads to the level set function Φ, whose zero-level set defines the fluid–solid interface. Given the interface, the design is evaluated and a sensitivity analysis is performed. Based on the results from the analysis and sensitivity step the design variables are optimized, leading to new heights for the RBFs. If the convergence criteria are met, the algorithm terminates.

5.1. Pipe bend

The pipe bend problem, introduced by Borrvall and Petersson [6], has become a standard example for fluid topology optimization and was also studied in [11, 33]. The design domain is depicted in Figure 13, the circle with the dotted grid illustrates the fluid mesh. The objective is to minimize the difference in total pressure between the inlet and outlet, subject to a constraint that allows only 25% of the area to be fluid:

$$\begin{aligned} \min_{s_k} \quad & z = (p_{\text{in}} - p_{\text{out}}) \\ \text{s.t.} \quad & g = 0.25 - \frac{A_{\text{fluid}}}{L^2} \geqslant 0 \\ & s_{\min} \leqslant s_k \leqslant s_{\max} \end{aligned} \tag{37}$$

The total inlet and outlet pressures, p_{in} and p_{out}, are averaged over the inlet and outlet ports. The boundary conditions are a parabolic inlet velocity and a constant static pressure at the outlet. The domain boundaries are represented by 'no-slip' boundary conditions.

The optimization algorithm terminates, if constraints are satisfied and the absolute change in the objective value is less than 0.01 or if the number of iterations exceeds 400. While this pedestrian

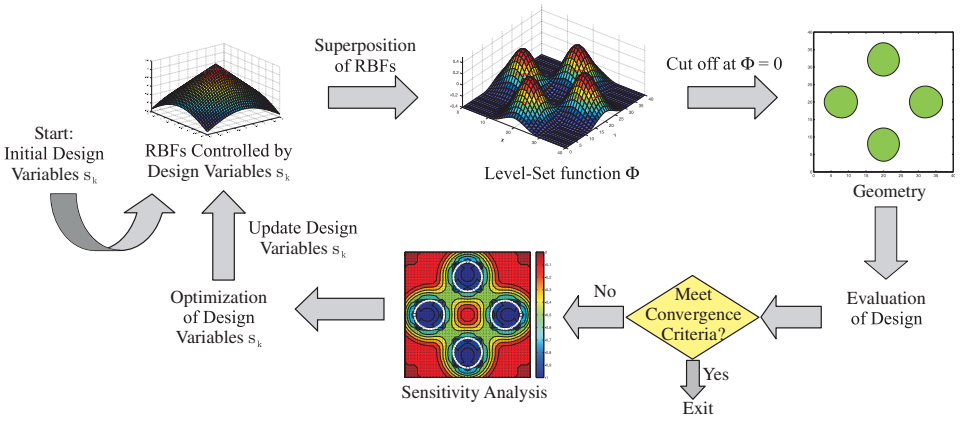

Figure 12. Optimization process.

DOI: 10.1002/fld

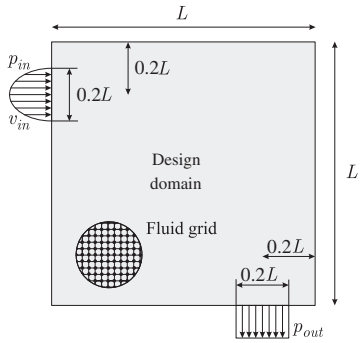

Figure 13. Design domain for the pipe bend.

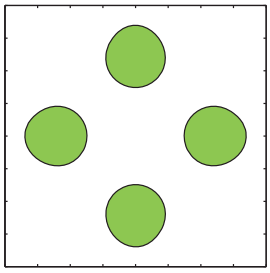

Figure 14. Initialization for the pipe bend.

Table IV. Parameters used for the pipe bend, if not stated differently.

Parameter type	Parameter	Standard value
Physical	Side length (L)	40
	Reynolds number (RE)	10
	Critical length (L_{crit})	9
	Dimensionless relaxation time (τ)	$\frac{1}{1.9}$
	Viscosity (v)	$\frac{1}{6}(2\tau-1)$
	Inlet velocity (v_{in})	$RE\cdot v/L_{\text{crit}}$
	Outlet pressure (p_{out})	$\frac{1}{3}$
Discretization	Fluid-domain mesh ($n\times n$)	41×41
	Level set mesh ($m\times m$)	41×41
	Fluid-domain gridsize (d)	$L/(n-1)$
	Level set gridsize (d_{LS})	$L/(m-1)$
Algorithmic	Relative smoothing radius (R_r)	5
	RBF support radius (R_ϕ)	$3d_{LS}$
	KS-factor (k)	20
	Lower/upper limit for s_k ($s_{\min}, s_{\max}$)	$-0.4d_{LS}$, $0.5d_{LS}$
	Stepsize (Δs)	$0.05\cdot(s_{\max}-s_{\min})d_{LS}$
	Number of subcycles	2

approach for monitoring the convergence does not guarantee that the optimality conditions are satisfied, numerical studies have shown that it is practical and sufficient to obtain visually converged results, that is, the geometry does not change noticeable even if more iterations are performed. Figure 14 shows the initial design for the pipe bend optimization problem, the Reynolds number

DOI: 10.1002/fld

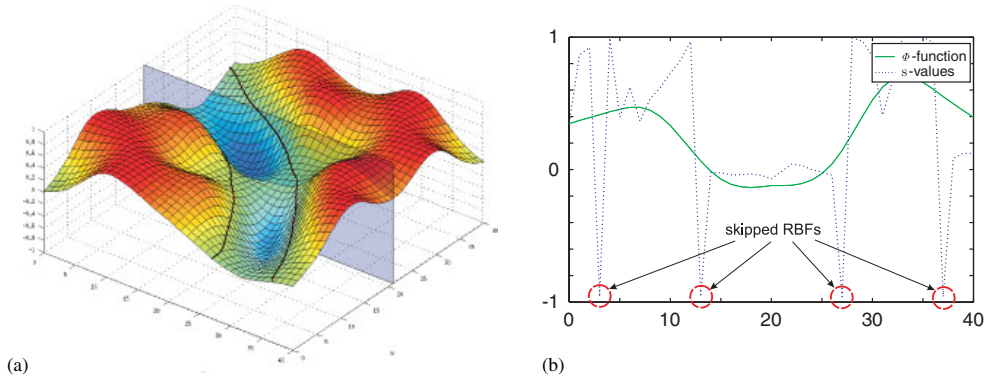

Figure 15. Influence of the limits for s_k $(s_{\min}, s_{\max})$ on the RBF-values: (a) Φ-function and (b) slice through Φ-function and corresponding s-values.

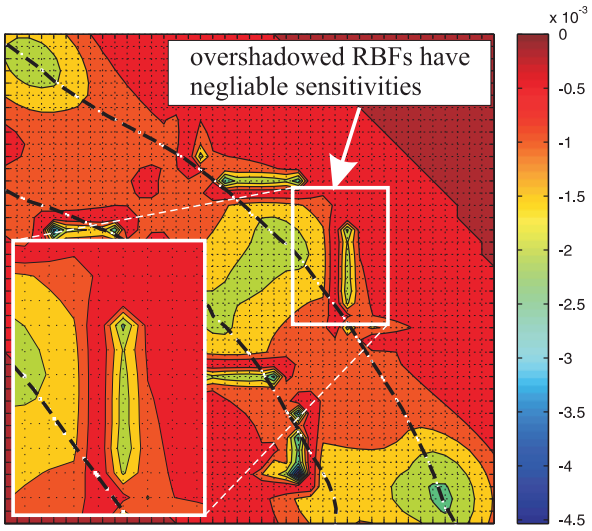

Figure 16. Sensitivities for overshadowed RBFs.

and critical length are given in Table IV. In the following we will study the effect of key algorithmic parameters on the optimization results. If not stated differently the parameter values listed in Table IV are used.

First we analyze the influence of the lower and upper limit for the design variables $(s_{\min}, s_{\max})$, which control the minimum and maximum height of the RBFs. Figure 15 shows an intermediate result where the upper and lower bounds are not chosen according to Equations (24) and (25) but set to $s_{\max} = 1, s_{\min} = -1$ ($d_{LS} = 1 \rightarrow$ Equations (24) and (25) are violated). The surface plot in Figure 15(a) depicts the Φ-function and a plane along which the surface is sliced. Figure 15(b) shows the Φ-function and s-values corresponding to the slice. As can be seen in Figure 15(b), there are several design variables that still have the same s-value at which they were initialized ($s = s_{\min} = -1$), that is, they did not change their value during the optimization process although the surrounding design variables have values $s \neq -1$. This problem occurs when RBFs are overshadowed by neighboring RBFs. As Figure 16 shows, overshadowed RBFs have negligible sensitivities. Although in the example in Figure 15 the skipped RBFs do not yield holes, there is a possibility

DOI: 10.1002/fld

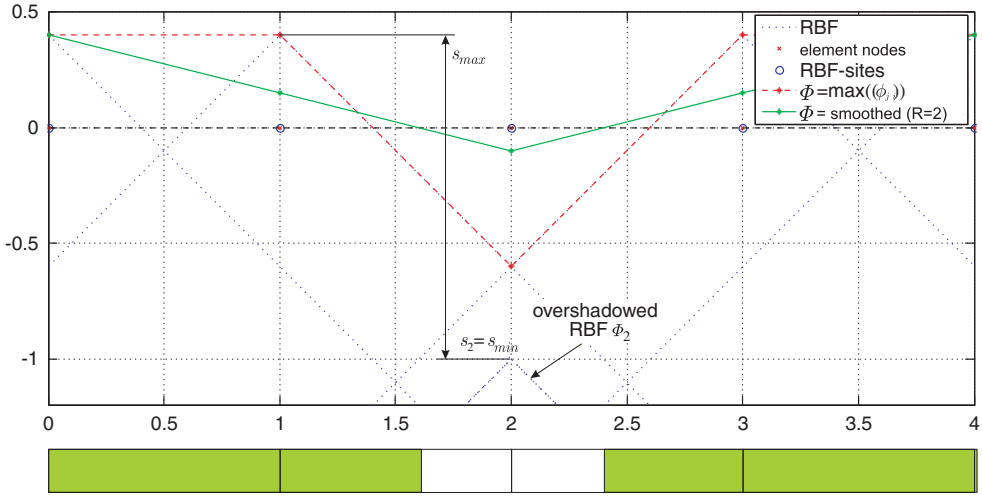

Figure 17. Overshadowed RBFs creating holes.

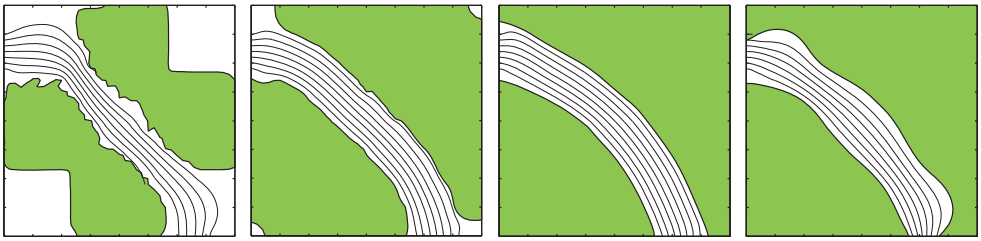

Figure 18. Different smoothing radii and the corresponding objective values of the optimum shape after i iterations (* indicates that constraint is still violated after design has converged): (a) $R_r = 0$: $i = 71^*$; $z = 11.55$; (b) $R_r = 2$: $i = 51^*$; $z = 6.91$; (c) $R_r = 5$: $i = 56$; $z = 6.50$; and (d) $R_r = 10$: $i = 35$; $z = 19.80$.

that holes occur that cannot be closed anymore. Figure 17 illustrates this problem for the 2D case: it is impossible to close the hole at the center, as the surrounding RBFs are already at their maximum and the overshadowed RBF Φ_2 has a negligible sensitivity; therefore, the optimizer will not modify $\Phi_2(s_2)$. This issue can be avoided by choosing the upper and lower bounds according to Equations (24) and (25).

As mentioned in Section 3.3, smoothing is crucial for the current approach. By modifying the relative smoothing radius R_r (see Equation (28)) the degree of smoothing can be controlled. Figure 18 shows a comparison between the optimum shapes for different values of R_r. Without smoothing, that is, $R_r = 0$, the boundaries along the channel are jagged. Kinks created by a very rough level set function hinder convergence to a feasible design. Increasing the radius to $R_r = 2$ improves the smoothness; however, the boundaries still show significant kinks. Further increasing the radius to $R_r = 5$ prevents kinks and creates smooth boundaries along the channel. A smoothing radius of $R_r = 10$ improves the local boundary smoothness even more; however, at the same time also impacts the global boundary shape. It can be seen in Figure 18 that a sufficiently large smoothing radius R_r is essential to guarantee smoothness of the boundaries. However, if the radius R_r is chosen too large, smoothing affects the global shape of the boundaries negatively.

Finally, we consider the influence of the coarseness of the level set mesh. Figure 19 shows a comparison between optimum (converged) designs for different refinements of the level set mesh.

DOI: 10.1002/fld

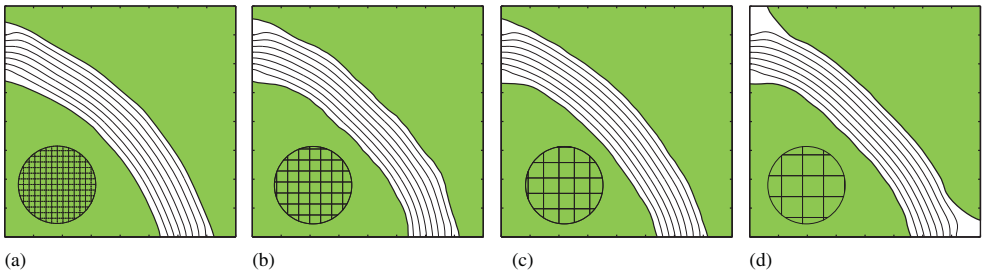

Figure 19. Different level set mesh coarseness (level set mesh densities shown in circles) and the corresponding objective values of the optimum shape after i iterations (* indicates that constraint is still violated after design has converged): (a) 41×41: $i=56$; $z=6.50$; (b) 21×21: $i=58$; $z=7.40$; (c) 15×15: $i=66$; $z=7.03$; and (d) 11×11: $i=59^*$; $z=7.18$.

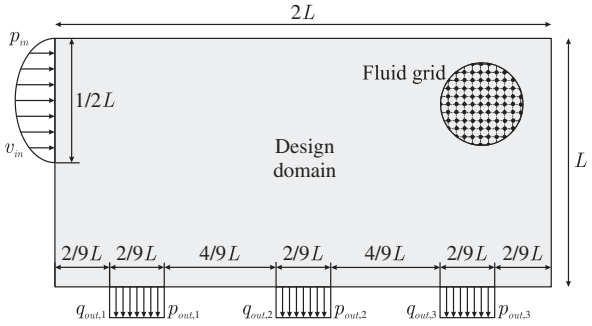

Figure 20. Design domain for the manifold.

In Figure 19(a) the level set mesh matches the fluid domain mesh, that is, one RBF in every LBM node, whereas in Figure 19(b), (c) and (d) the level set mesh is approximately 2, 2.7, and 4 times coarser than the fluid mesh, respectively. As the figure shows, it is possible to create reasonable channel-designs with level set meshes that are significantly coarser than the fluid mesh. Yet, if the level set mesh becomes too coarse, specific details cannot be described anymore. This issue can be observed at the upper left and lower right corners in Figure 19(d). Comparing Figure 19(a) and (c) shows that we can obtain very similar results when using only 225 (15×15) design variables instead of 1681 (41×41). This corresponds to a reduction of the design space dimension by over 86%.

5.2. *Manifold*

We study the optimal design of a manifold with one inlet and three outlets. Figure 20 shows the design domain for this problem; the circle with the dotted grid illustrates the fluid mesh. The objective is to minimize the difference in total pressure between the inlet and the outlets. The optimization is subjected to two constraints: the first one limits the maximum allowable fluid volume to 50% of the design domain and the second one requires the flow rate for each of the three outlets $q_{\text{out},i}$ to be $\frac{1}{3}$ of the inlet flow rate, q_{in}:

$$\min_{s_k} \quad z=\left(p_{\text{in}}-\sum_{i=1}^{3}p_{\text{out},i}\right)$$

$$\text{s.t.} \quad g_1=0.5-\frac{A_{\text{fluid}}}{2L^2}\geqslant 0$$

DOI: 10.1002/fld

$$g_2 = \sum_{i=1}^{3} (q_{\text{out},i} - \frac{1}{3} q_{\text{in}})^2 = 0 \tag{38}$$

$$s_{\min} \leqslant s_k \leqslant s_{\max}$$

The total inlet and outlet pressures, p_{in} and $p_{\text{out},i}$, are averaged over the inlet and outlet ports. The boundary conditions are a parabolic inlet velocity and a constant static pressure at the outlets. The domain boundaries are represented by 'no-slip' boundary conditions.

The optimization algorithm terminates if constraints are satisfied and the absolute change in the objective value is less than 0.01 or if the number of iterations exceeds 400. Figure 21 shows the initial design for the manifold optimization problem. The algorithmic parameters are chosen according to Table V. Figure 22 shows how the geometry evolves during the optimization process. As can be seen when comparing Figure 22(d)–(f), the basic shape of the channel is already obtained after 40 iterations. Until final convergence, however, 107 iterations are required. The evolution of the slender fin at the top left is the most time-consuming feature, as in this region, the objective and the mass constraint are strongly conflicting with each other. Note that the round shape of the fins next to outlets is due to the low Reynolds number. Despite the smoothing of the level set function, the current approach is still capable of creating sharp corners and cusps as is demonstrated by the small island in Figure 22(d) and the slender fin at the top left in Figure 22(f).

The graphs in Figure 23 illustrate the optimization progress quantitatively. The GCMMA algorithm performed one subcycle in about 90% of all iterations. The average number of fluid iterations

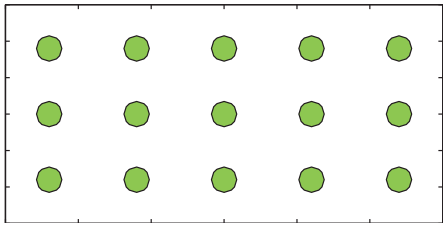

Figure 21. Initialization for the manifold.

Table V. Parameters used for the manifold.

Parameter type	Parameter	Standard value
Physical	Side length (L)	30
	Reynolds number (RE)	10
	Critical length (L_{crit})	9
	Dimensionless relaxation time (τ)	$\frac{1}{1.9}$
	Viscosity (v)	$\frac{1}{6}(2\tau - 1)$
	Inlet velocity (v_{in})	$RE \cdot v / L_{\text{crit}}$
	Outlet pressure (p_{out})	1/3
Discretization	Fluid-domain mesh ($n_x \times n_y$)	61×31
	Level set mesh ($m_x \times m_y$)	61×31
	Fluid-domain gridsize (d)	$L/(n_y - 1)$
	Level set gridsize (d_{LS})	$L/(m_y - 1)$
Algorithmic	Relative smoothing radius (R_r)	3.5
	RBF support radius (R_ϕ)	$3d_{LS}$
	KS-factor (k)	20
	Lower/upper limit for s_k ($s_{\min}, s_{\max}$)	$-0.4d_{LS}$, $0.5d_{LS}$
	Stepsize (Δs)	$0.025 \cdot (s_{\max} - s_{\min})$
	Number of subcycles	1

DOI: 10.1002/fld

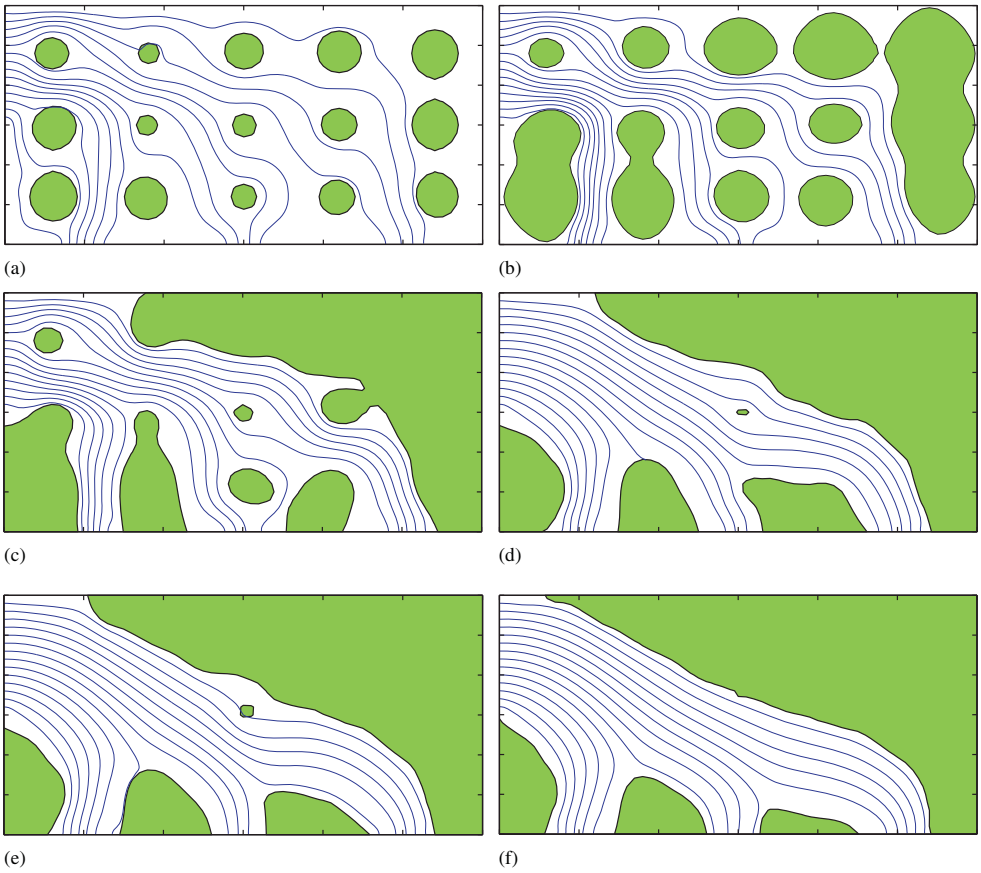

Figure 22. Evolution of the manifold geometry: (a) after 10 iterations: $z=11.09$, $g_1=0.72$, $g_2=0.05$; (b) after 20 iterations: $z=18.88$, $g_1=0.21$, $g_2=0.05$; (c) after 30 iterations: $z=11.88$, $g_1=0.00$, $g_2=0.03$; (d) after 40 iterations: $z=3.71$, $g_1=0.00$, $g_2=0.01$; (e) after 50 iterations: $z=3.12$, $g_1=0.00$, $g_2=0.01$; and (f) after 107 iterations: $z=2.71$, $g_1=0.00$, $g_2=0.00$.

to reach steady state was approximately 7300. The computational cost of the sensitivities was about 4 times higher than the cost for an analysis.

6. CONCLUSION

The present work has shown that the proposed geometric boundary representation, in combination with an explicit level set method, is well suitable for solving generalized fluid shape optimization problems. Our approach does not require finding appropriate porosity interpolation laws, it features higher spatial as well as temporal accuracy, and is applicable to transient problems. On the other hand, the proposed method has the disadvantage of not being capable of forming new domains of solid material that are completely surrounded by fluid, limiting the topological complexity of the final design. However, this problem can be mitigated by a proper initial design that has a sufficient number of separated solid regions. By appropriately choosing the upper and lower limits for the design variables it can be assured that the level set function evolves gradually past its boundaries without skipping over RBFs, preventing non-optimal holes in the design. Furthermore, it was shown that the geometric smoothing, which limits the spatial oscillations of the level set function Φ, is essential for obtaining reasonable results. For the pipe bend example, the geometric

DOI: 10.1002/fld

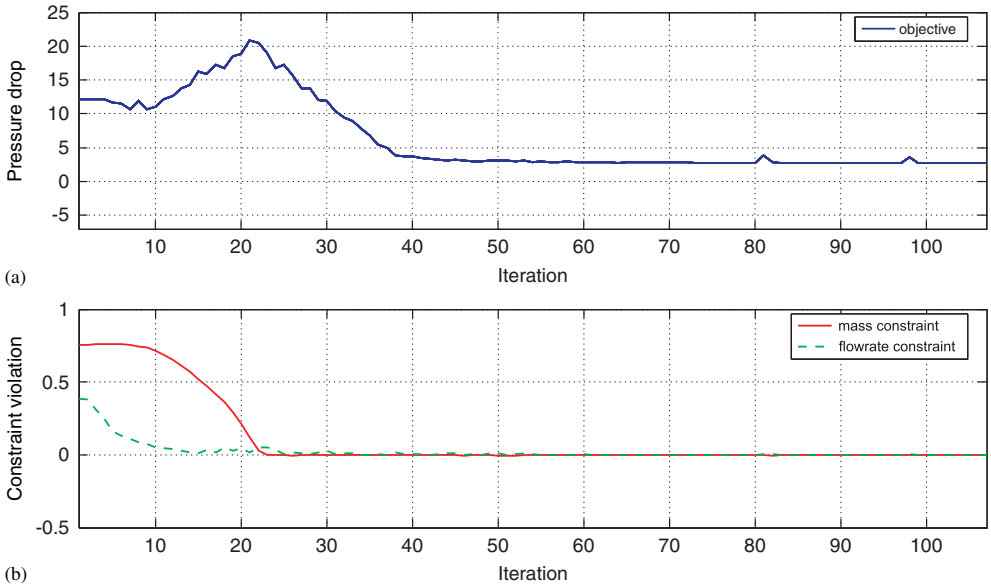

Figure 23. Objective and constraint values for the manifold: (a) history of objective values for manifold and (b) history of constraint violations for manifold.

boundary representation developed in this study yields the same results as the Brinkman approach. The manifold example illustrates the versatility of our approach for generalized fluid optimization problems.

ACKNOWLEDGEMENTS

The authors acknowledge the support of the National Science Foundation under grant DMI-0348759. The opinions and conclusions presented in this paper are those of the authors and do not necessarily reflect the views of the sponsoring organization.

REFERENCES

1. Bendsøe M, Sigmund O. *Topology Optimization*: *Theory*, *Methods and Applications*. Springer: Berlin, 2003.
2. Bruns T, Sigmund O, Tortorelli D. Numerical methods for the topology optimization of structures that exhibit snap-through. *International Journal for Numerical Methods in Engineering* 2002; **55**:1215–1237. DOI: 10.1002/nme.544.
3. Haber R, Bendsøe M. Problem formulation, solution procedures and geometric modeling: key issues in variable-topology optimization. *AIAA/USAF/NASA/ISSMO Symposium on Multidisciplinary Analysis and Optimization*, *No. AIAA-1998-4948 in Collection of Technical Papers. Pt. 3*. AIAA: New York, 1998.
4. Ramm E, Maute K, Schwarz S. Adaptive topology and shape optimization. *WCCM IV*, Buenos Aires, Argentina, 29 June–2 July 1998; 19–38.
5. Ramm E, Maute K, Schwarz S. Conceptual design by structural optimization. *EURO-C*, Badgastein, Austria, 31 March–3 April 1998; 896–897.
6. Borrvall T, Petersson J. Topology optimization of fluids in stokes flow. *International Journal for Numerical Methods in Fluids* 2003; **41**(1):77–107. DOI: 10.1002/fld.426.
7. Gersborg-Hansen A, Sigmund O, Haber R. Topology optimization of channel flow problems. *Structural and Multidisciplinary Optimization* 2005; **30**(3):181–192. DOI: 10.1007/s00158-004-0508-7.
8. Guest JK, Prévost JH. Topology optimization of creeping fluid flows using a Darcy–Stokes finite element. *International Journal for Numerical Methods in Engineering* 2006; **66**:461–484. DOI: 10.1002/nme.1560.
9. Othmer C. CFD topology and shape optimization with adjoint methods. *VDI Fahrzeug- und Verkehrstechnik*, *13. Internationaler Kongress*, *Berechnung und Simulation im Fahrzeugbau*, Würzburg, 2006. Available from: http://www.wire.tu-bs.de/mitarbeiter/cothmer/docs/vdi.pdf.

10. Othmer C, de Villiers E, Weller HG. Implementation of a continuous adjoint for topology optimization of ducted flows. *Eighteenth AIAA Computational Fluid Dynamics Conference*. AIAA: Miami, FL, 2007.
11. Pingen G, Evgrafov A, Maute K. Topology optimization of flow domains using the lattice Boltzmann method. *Structural and Multidisciplinary Optimization* 2007; **36**(6):507–524. DOI: 10.1007/s00158-007-0105-7.
12. Brinkman H. A calculation of the viscous force exerted by a flowing fluid on a dense swarm of particles. *Applied Scientific Research, Section A* 1947; **1**:27.
13. De Ruiter M, van Keulen F. Topology optimization using a topology description function. *Structural and Multidisciplinary Optimization* 2004; **26**(6):406–416. DOI: 10.1007/s00158-003-0375-7.
14. Raulli M, Maute K. Optimization of fully coupled electrostatic-fluid–structure interaction problems. *Computers and Structures* 2005; **83**:221–233.
15. Schwarz S, Maute K, Ramm E. Topology and shape optimization for elastoplastic structural response. *Computer Methods in Applied Mechanics and Engineering* 2001; **190**:2135–2155.
16. Succi S. *The Lattice Boltzmann Equation: For Fluid Dynamics and Beyond*. Oxford University Press: Oxford, 2001.
17. Hammer V, Olhoff N. Topology optimization of continuum structures subjected to pressure loading. *Structural and Multidisciplinary Optimization* 2000; **19**:85–92.
18. Maute K, Ramm E. Adaptive topology optimization. *Structural Optimization* 1995; **10**:100–112.
19. Pingen G. Optimal design for fluidic systems: topology and shape optimization with the lattice Boltzmann method. *Ph.D. Thesis*, University of Colorado at Boulder, 2008.
20. Allaire G, Jouve F, Toader AM. Structural optimization using sensitivity analysis and a level-set method. *Journal of Computational Physics* 2004; **194**:363–393. DOI: 10.1016/j.jcp.2003.09.032.
21. Wang SY, Wang MY. A moving superimposed finite element method for structural topology optimization. *International Journal for Numerical Methods in Engineering* 2006; **65**(11):1892–1922. DOI: 10.1002/nme.1527.
22. Mittal R, Gianluca I. Immersed boundary methods. *Annual Review of Fluid Mechanics* 2005; **37**:239–261. DOI: 10.1146/annurev.fluid.37.061903.175743.
23. Gerstenberger A, Wall W. An extended finite element method/Lagrange multiplier based approach for fluid–structure interaction. *Computer Methods in Applied Mechanics and Engineering* 2008; **197**:1699–1714.
24. Bouzidi M, Firdaouss M, Lallemand P. Momentum transfer of a lattice Boltzmann fluid with boundaries. *Physics of Fluids* 2001; **13**(11):3452–3459.
25. Sethian J, Wiegmann A. Structural boundary design via level set and immersed interface methods. *Journal of Computational Physics* 2000; **163**(2):489–528. DOI: 10.1006/jcph.2000.6581.
26. Wang MY, Wang X, Guo D. A level set method for structural topology optimization. *Computer Methods in Applied Mechanics and Engineering* 2003; **192**(1–2):227–246. DOI: 10.1016/S0045-7825(02)00559-5.
27. Xia Q, Wang MY, Wang S, Chen S. Semi-Lagrange method for level-set-based structural topology and shape optimization. *Structural and Multidisciplinary Optimization*, vol. 31. Springer: Berlin, Heidelberg, 2006; 419–429. DOI: 10.1007/s00158-005-0597-y.
28. Wei P, Wang MY. Parametric structural shape and topology optimization method with radial basis functions and level-set method. *Proceedings of IDETC/CIE 2006, ASME 2006 International Design Engineering Technical Conferences*, Philadelphia, U.S.A., 2006.
29. Luo Z, Tong L. A level set method for shape and topology optimization of large-displacement compliant mechanisms. *International Journal for Numerical Methods in Engineering* 2008; **76**(6):862–892. DOI: 10.1002/nme.2352.
30. De Ruiter M. Topology optimization using a topology description function approach. *Ph.D. Thesis*, Technische Universiteit Delft, 2005.
31. van Miegroet L, Duysinx P. Stress concentration minimization of 2d filets using x-fem and level set description. *Structural and Multidisciplinary Optimization* 2007; **33**(4–5):425–438. DOI: 10.1007/s00158-006-0091-1.
32. Cunha AL. A fully Eulerian method for shape optimization with application to Navier–Stokes flows. *Ph.D. Thesis*, Carnegie Mellon University, Pittsburgh, PA, September 2004.
33. Duan X, Ma Y, Zhang R. Optimal shape control of fluid flow using variational level set method. *Physics Letters A* 2008; **372**(9):1374–1379. DOI: 10.1016/j.physleta.2007.09.070.
34. Mohammadi B, Pironneau O. Theory and practice of optimal shape design. *European Journal of Computational Mechanics* 2008; **17**(1–2):13–30.
35. Pingen G, Waidmann M, Evgrafov A, Maute K. Application of a parametric level-set approach to topology optimization fluid with the Navier–Stokes and lattice Boltzmann equations. *WCSMO07*. ISSMO: Seoul, Korea, 21–25 May 2007.
36. Yu D, Mei R, Shyy W. A unified boundary treatment in lattice Boltzmann method. *APS Meeting Abstracts*, November 2002. J11+.
37. Chen S, Doolen GD. Lattice Boltzmann method for fluid flows. *Annual Review of Fluid Mechanics* 1998; **30**:329–364.
38. Pingen G, Evgrafov A, Maute K. Adjoint parameter sensitivity analysis for the hydrodynamic lattice Boltzmann method with applications to design optimization. *Computers and Fluids* 2009; **38**(4):910–923. DOI: 10.1016/j.compfluid.2008.10.002.
39. Pingen G, Waidmann M, Evgrafov A, Maute K. A parametric level-set approach for topology optimization of flow domains. *Structural and Multidisciplinary Optimization* 2009; DOI: 10.1007/s00/58-009-0405-1.

40. Geier M, Liu Z, Greiner A, Korvink J. Lattice Boltzmann based structural topology optimization of micro channels. *Second International Conference on Transport Phenomena in Micro and Nanodevices*, Barga, Italy, 2006.
41. Yang Z. Analysis of lattice Boltzmann boundary conditions. *Ph.D. Thesis*, Universität Konstanz, 2007.
42. Bouzidi M, Firdaouss M, Lallemand P. Momentum transfer of a Boltzmann-lattice fluid with boundaries. *Physics of Fluids* 2001; **13**(11):3452–3459.
43. Osher S, Sethian J. Fronts propagating with curvature dependent speed: algorithms based on Hamilton–Jacobi formulations. *Journal of Computational Physics* 1988; **79**:12–49.
44. Wang MY, Wang X. PDE-driven level sets, shape sensitivity and curvature flow for structural topology optimization. *Computer Modeling in Engineering and Sciences* 2004; **6**(4):373–395.
45. Burger M, Osher S. A survey on level set methods for inverse problems and optimal design. *European Journal of Applied Mathematics* 2005; **16**:263–301. DOI: 10.1017/S0956792505006182.
46. Sethian J, Smereka P. Level set methods for fluid interfaces. *Annual Review of Fluid Mechanics* 2003; **35**:341–372. DOI: 10.1146/annurev.fluid.35.101101.161105.
47. Wang MY, Wang S. Parametric shape and topology optimization with radial basis functions. *IUTAM Symposium on Topological Design Optimization of Structures*, *Machines and Materials*, Aalborg and Lyngby, Denmark, 2005; 13–22.
48. Buhmann M. *Radial Basis Functions*: *Theory and Implementations*. Cambridge University Press: Cambridge, 2003.
49. Mohammadi B. Global optimization, level set dynamics, incomplete sensitivity and regularity control. *International Journal of Computational Fluid Dynamics* 2007; **21**(2):61–68.
50. Sethian J. *Level Set Methods*. Cambridge University Press: Cambridge, 1996.
51. Jameson A, Martinelli L, Pierce NA. Optimum aerodynamic design using the Navier–Stokes equations. *Theoretical and Computational Fluid Dynamics* 1998; **10**:213–237.
52. Fung Y, Tong P. *Classical and Computational Solid Mechanics*. World Scientific Publishing: Singapore, 2001.
53. Kreisselmeier G, Steinhauser R. Systematic control design by optimizing a vector performance index. *International Federation of Active Controls Symposium on Computer Aided Design of Control Systems*, Zurich, Switzerland, 1979.
54. Sigmund O, Petersson J. Numerical instabilities in topology optimization: a survey on procedures dealing with checkerboards, mesh-dependencies and local minima. *Structural and Multidisciplinary Optimization* 1998; **16**(1):168–175.
55. Daoud F, Firl M, Bletzinger KU. Filter techniques in shape optimization with CAD-free parametrization. *Sixth World Congresses of Structural and Multidisciplinary Optimization*, Rio de Janeiro, Brazil, 2005.
56. Mei R, Yu D, Shyy W, Luo LS. Force evaluation in the lattice Boltzmann method involving curved geometry. *Physical Review E* 2002; **65**(4):041 203:1–041 203:14.
57. Svanberg K. A globally convergent version of MMA without linesearch. *Proceedings of the First World Congress of Structural and Multidisciplinary Optimization*, 28 May–2 June 1995; 9–16.

Appendix B

Publication [P2]: Topology Optimization of Flexible Micro-Fluidic Devices

Struct Multidisc Optim (2010) 42:495–516
DOI 10.1007/s00158-010-0526-6

RESEARCH PAPER

Topology optimization of flexible micro-fluidic devices

Sebastian Kreissl · Georg Pingen · Anton Evgrafov · Kurt Maute

Received: 10 September 2009 / Revised: 30 March 2010 / Accepted: 21 May 2010 / Published online: 12 June 2010

Abstract A multi-objective topology optimization formulation for the design of dynamically tunable fluidic devices is presented. The flow is manipulated via external and internal mechanical actuation, leading to elastic deformations of flow channels. The design objectives characterize the performance in the undeformed and deformed configurations. The layout of fluid channels is determined by material topology optimization. In addition, the thickness distribution, the distribution of active material for internal actuation, and the support conditions are optimized. The coupled fluid-structure response is predicted by a non-linear finite element model and a hydrodynamic lattice Boltzmann method. Focusing on applications with low flow velocities and pressures, structural deformations due to fluid-forces are neglected. A mapping scheme is presented that couples the material distributions in the structural and fluid mesh. The governing and the adjoint equations of the resulting fluid-structure interaction problem are derived. The proposed method is illustrated with the design of tunable manifolds.

Keywords Fluid-structure interaction · Hydrodynamic lattice Boltzmann method · Non-linear elasticity · Adjoint sensitivity analysis

Preliminary results of the work presented in this paper have been published in the proceedings of WCSMO-8, Lisbon, Portugal, 2009.

S. Kreissl · K. Maute (✉)
Center for Aerospace Structures,
University of Colorado at Boulder,
Boulder, CO, USA
e-mail: maute@colorado.edu

S. Kreissl
e-mail: kreissl@colorado.edu

G. Pingen
Department of Mechanical and Aerospace Engineering,
University of Colorado at Colorado Springs,
Colorado Springs, CO, USA
e-mail: gpingen@eas.uccs.edu

A. Evgrafov
Department of Mathematics,
Technical University of Denmark,
Lyngby, Denmark
e-mail: a.evgrafov@mat.dtu.dk

1 Introduction

This study focuses on topology optimization of dynamically tunable fluidic devices. The basic idea of the proposed design concept is to embed flow channels into a flexible structure that deforms in response to externally or internally applied mechanical loads. The primary goal is to optimize the layout of the elastically deforming fluid channels with respect to multiple objectives, characterizing the device in the deformed and undeformed configurations. To further enhance the device performance, the stiffness distribution, the layout of the actuation system, as well as the support conditions of the device are also optimized.

Topology optimization is a well established method for designing structural systems (Bendsøe and Sigmund 2003; Ramm et al. 1998a, b). For an overview of structural topology optimization the reader is referred to the manuscript by Bendsøe and Sigmund (2003). Topology optimization of flow problems was pioneered by Borrvall and Petersson (2003). In their initial study a Stokes flow model was employed. This approach has further been generalized in a number of ways (Andreasen et al. 2009; Gersborg-Hansen et al. 2005; Evgrafov 2006; Aage et al. 2008; Klimetzek

et al. 2006; Moos et al. 2004; Othmer et al. 2006; Othmer 2008). As an alternative to the Navier–Stokes flow model, Pingen et al. used the lattice Boltzmann method (LBM) to solve fluid topology optimization problems (Pingen 2008; Pingen et al. 2007a, b, 2009a, b).

Topology optimization of fluid-structure systems has hardly been studied so far. Guest and Prévost (2006) maximized the stiffness while simultaneously maximizing the fluid permeability of periodic materials. Although a fluid-structure interaction system was considered, no interaction between fluid and solid was taken into account in this study. Maute and Allen (2004) and Maute and Reich (2006) optimized the internal layout of structures accounting for coupling between flow and structural deformation. However, this approach only allows for changes of the shape but not the topology of the fluid–solid interface. Yoon (2009) recently introduced a monolithic formulation for topology optimization of fluid-structure interaction (FSI) problems. While this approach considers a fully coupled FSI system, it is limited to small structural deformations.

In this study we present a topology optimization method for FSI problems undergoing large elastic deformations. We focus on micro-fluidic devices with flow channels sandwiched between two elastically deforming structural layers. Owing to the low flow velocity in micro channels, the fluid pressure exerted on the structure is typically negligible in comparison to the stiffness of the structure. However, large deformations are needed to noticeably alter the flow due to mechanical actuation. Therefore, we consider only the effect of finite structural deformations on the flow field and disregard the influence of the fluid forces on the structural deformations, leading to a one-way structure-fluid coupling. We will show quantitatively with a numerical example that the fluid forces only have a negligible effect on the structural solution for the class of micro-fluidic devices considered in this study.

Following a standard material topology optimization approach, the geometry of the flow channels is described by a material distribution function. Additional optimization parameters are used to control the thickness distribution, the distribution of active material for internal actuation, and the support conditions of the device. The structural response is described by a non-linear finite element model using a total Lagrangian formulation. The flow is predicted by a hydrodynamic LBM operating on a fixed grid. The material distributions in the deforming structural mesh and fixed fluid mesh are coupled by a geometric mapping approach, as shown in Fig. 1. Contrary to a monolithic approach (Yoon 2009), the separate treatment of the fluid and structural domain allows to employ existing analysis modules: in the current study, an LBM fluid solver and a geometrically non-linear FEM structural solver. We consider optimization problems involving the fluid and structural

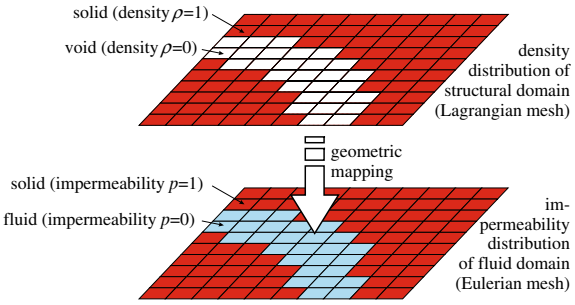

Fig. 1 Separate meshes for structural and fluid domain

behavior in the undeformed and deformed configuration at steady-state. These problems are cast into a multi-objective formulation and solved by a gradient based optimization algorithm computing the design sensitivities by an adjoint method.

In this paper we present an optimization method for a one-way coupled FSI problem using a material distribution approach to describe the geometry of the fluid and structural domains. We present details of the geometric mapping method that couples the material distribution in the fluid and structural meshes. We derive the adjoint of this system and discuss its computational complexity. The utility of the proposed approach is illustrated with three numerical examples. The remainder of the paper is organized as follows. In Sections 2 and 3 we describe the design and structural model. Section 4 outlines the basics of the LBM. This is followed by a description of the geometrical mapping from the structural domain into the fluid domain in Section 5. Section 6 describes the overall computational optimization procedure along with the sensitivity analysis. Finally, we demonstrate the key features of our approach with three 2-D numerical examples in Section 7. The results are summarized in Section 8.

2 Design models

Focusing on micro-fluidic devices, which are typically fabricated by micro-surface, bulk machining or layer deposition techniques, we consider structures that consist of multiple layers. In this paper, we focus on a three-layer design (see Fig. 2): the center layer houses the embedded fluid channels and is sandwiched between two structural layers, which provide structural support for the center layer and prevent evaporation and leakage.

To manipulate the design we consider four sets of optimization variables: (1) The layout of the flow channels in the center layer is described by a material distribution function. The material properties are defined via smooth interpolation functions depending on the optimization

Fig. 2 Structural system

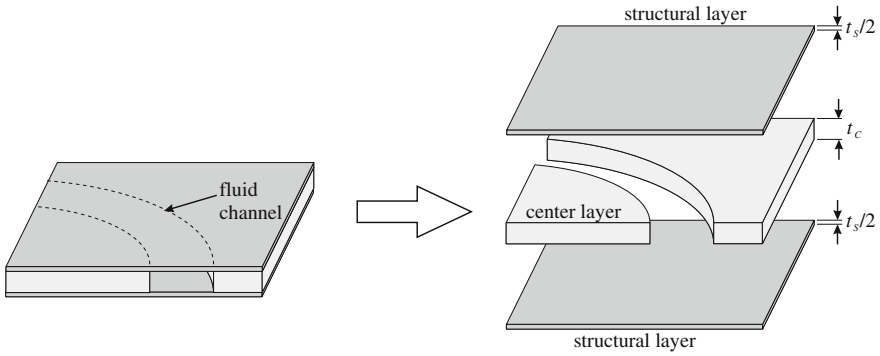

variables $s_m^i \in [0, 1]$. (2) The thickness distribution of the structural layers is defined by the optimization variables $s_t^i \in [0, 1]$. (3) The locations where the structural layers are attached to a ground structure are described by the distribution of the support stiffness which is defined by the optimization variables $s_s^i \in [0, 1]$. (4) The layout of active material embedded into the structural layers is described via the distribution of eigenstrains. In this study only isotropic eigenstrains ϵ_e are considered which are defined by the independent optimization variables $s_e^i \in [-1, 1]$. The four sets of optimization variables are combined into the design vector $\mathbf{s} = [\mathbf{s}_m\ \mathbf{s}_t\ \mathbf{s}_s\ \mathbf{s}_e]$.

By controlling the thickness of the structural layers via s_t^i we can tailor the stiffness independently from the layout of the layer that houses the fluid channels. This allows, for example, to stiffen areas beneath a flow channel or to soften areas beneath a solid center layer. To illustrate this issue, Fig. 3 shows the structural layout of a simple channel subject to a compressive load. The structure is fixed along the left and right edges. As the stiffness in the center layer along the channel is negligible, the pressure drop across the channel in the deformed configuration depends only on the stiffness of the structural layers, which can be controlled conveniently by the thickness. For practical applications, these thickness variations could be fabricated via layer deposition techniques (Kim et al. 2009) or 3D printing methods (Dimitrov et al. 2006).

The basic concept of varying the support stiffness is illustrated in Fig. 4. Imposing a large value for the support stiffness at a point, the structural displacements vanish and the point can be considered fixed (Babuška 1973). Manipulating the support stiffness has a similar but more pronounced effect compared to varying the thickness of the structural layers. While both alter the stiffness of the structure, their effect on the overall displacement field differs, as illustrated in Fig. 5. For example, increasing the value of the thickness variable s_t primarily reduces the deformation locally, within the stiffened region ($b^d \approx b^u$ in Fig. 5b). Increasing the support stiffness has a global effect and shields the left part of the structure from deforming ($a^d \approx a^u$ and $b^d \approx b^u$ in Fig. 5c). In practice this could be realized, for example via adhesive bonding techniques (Niklaus et al. 2006). Depending on the fabrication approach used to vary the thickness of the structural layers, the surface topography of the substrate may also have to be altered to allow bonding of the structural layer to the substrate.

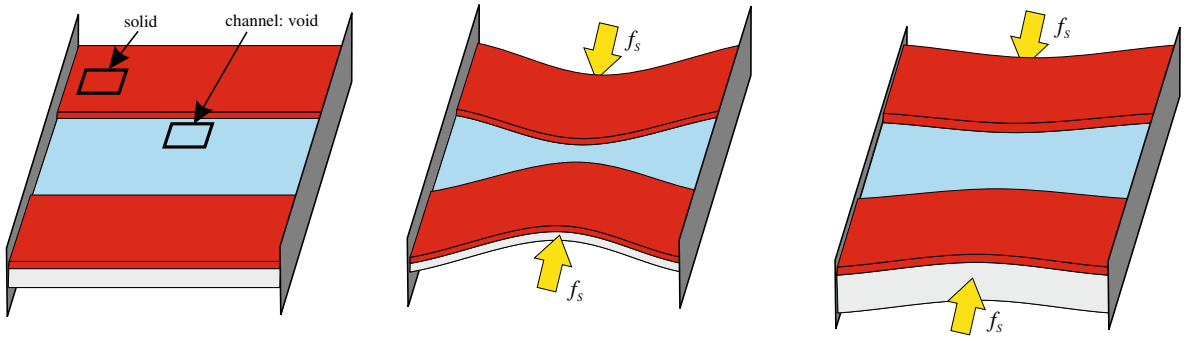

(a) Undeformed (b) Deformed: thin structural layer (c) Deformed: thick structural layer

Fig. 3 Influence of thickness of the structural layers on the stiffness (for visualization only the bottom structural layer is shown)

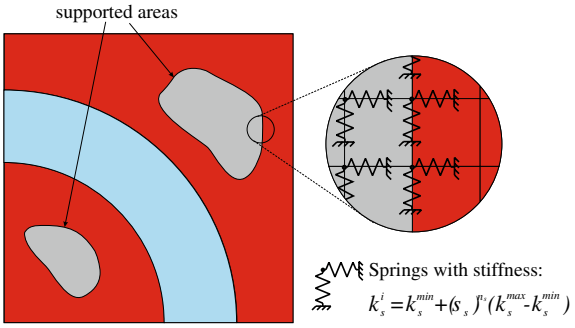

Fig. 4 Support layout (cp. Buhl 2002)

In particular in micro-fluidic applications, forces are conveniently generated by active materials embedded into the structural layers, such as piezo-ceramic or electro-active polymers (Bar-Cohen 2004; Zhang et al. 2005). Optimizing the layout of active materials in concert with the thickness of the structural layers and the distribution of the support stiffness allows fine-tuning of the structural deformations. The effect of active materials on the overall device is modeled by introducing eigenstrains into the constitutive equations of the structural layers.

3 Structural model

To alter low-speed flows, large changes of the channel geometry and thus large deformations of the structure are required. Therefore, the structural response is described by a geometrically non-linear finite element (FE) model. For the sake of simplicity, we assume a linear stress–strain relationship in this study. However, for a more realistic modeling of the structural response, especially when dealing with large strains, a non-linear stress–strain model would be more appropriate. We further assume that the thickness is much smaller than the in-plane dimensions of the structure and the structural response can be approximated by a plane-stress model.

The four sets of optimization variables defined previously are introduced into the structural FE model via interpolation functions, the corresponding interpolation parameters are summarized in Table 1. Following the standard notation in topology optimization, the density ρ^i and Young's modulus E_C^i of the center layer of the i-th element are defined by:

$$\rho^i = s_m^i \, \rho^{solid} \tag{1}$$

$$E_C^i = s_m^i \, E_C^{max} \tag{2}$$

The total Young's modulus of the layered structure is computed by weighting the Young's moduli of the layers with their thickness fractions:

$$E = E_C \left(\frac{t_C}{t}\right) + E_S \left(\frac{t_S}{t}\right) \quad \text{with } t = t_C + t_S \tag{3}$$

where t_C, t_S and E_S define thicknesses of the center layer, the structural layers and Young's modulus of the structural

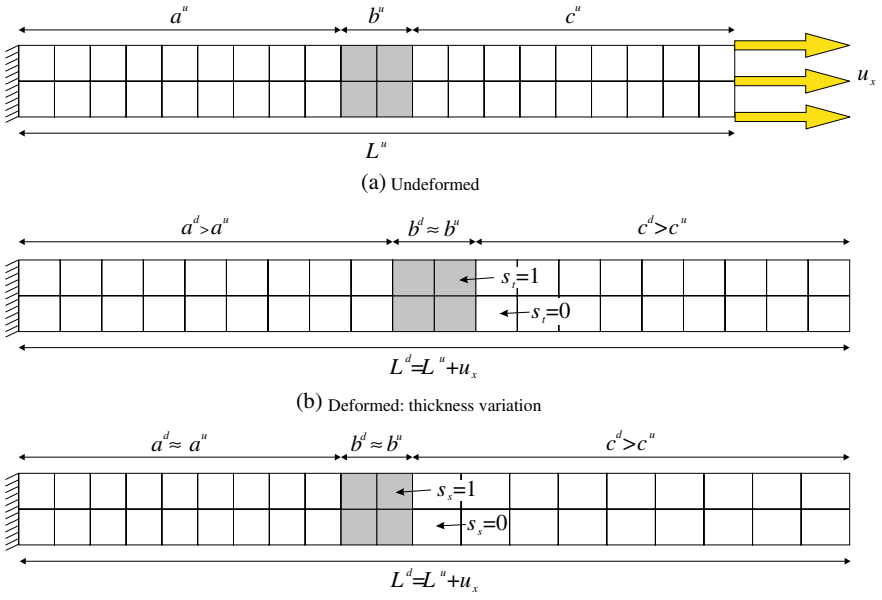

Fig. 5 Effect of thickness variation vs. support variation on structural displacement field

Table 1 Parameters for structural interpolation functions

Interpolated quantity	Parameter	Meaning
Density	ρ^i	Elemental density
	ρ^{solid}	Density of completely solid bulk material
Young's modulus	E_C^i	Elemental Young's modulus of center layer
	E_C^{max}	Maximum Young's modulus of center layer
Thickness	t_S^i	Elemental thickness of structural layers
	t_S^{min}	Minimum elemental thickness of structural layers
	t_S^{max}	Maximum elemental thickness of structural layers
Support stiffness	k_s^{min}	Minimum support stiffness
	k_s^{max}	Maximum support stiffness
Eigenstrain	ϵ_{eig}^{min}	Minimum eigenstrain
	ϵ_{eig}^{max}	Maximum eigenstrain

layers, respectively. The thickness of the structural layers for the i-th element is given by:

$$t_S^i = t_S^{min} + s_t^i \left(t_S^{max} - t_S^{min} \right) \tag{4}$$

where t_S^{min} and t_S^{max} are the minimum and maximum elemental thicknesses of the structural layer.

Following the work of Buhl (2002), a spring model with variable stiffness is used to smoothly vary the support conditions from 'moving freely' to 'fully clamped'. The spring stiffness k_s^i associated with the nodes of the i-th element are defined as:

$$k_s^i = k_s^{min} + s_s^i \left(k_s^{max} - k_s^{min} \right). \tag{5}$$

where k_s^{min} and k_s^{max} are the minimum and maximum support stiffnesses, respectively. A minimum support stiffness larger than zero is chosen to prevent rigid body motions and numerical ill-conditioning. For a value of $s_s^i = 1$ the support stiffness leads to negligible nodal displacements. Note that this approach acts only as a vehicle for determining the optimal locations for the supports and therefore the linear springs pose no inconsistency with the geometrically non-linear structural description.

The eigenstrains are interpolated linearly as follows:

$$\epsilon_e^i = s_e^i \, \epsilon_{eig}^{max} \tag{6}$$

The elemental eigenstrain ϵ_e^i enters the non-linear plane-stress formulation via the constitutive model assuming a linear elastic material behavior and an additive decomposition of the elastic and inelastic strains. The total nominal stress is defined e.g. in Belytschko et al. (2005):

$$\mathbf{P} = \mathbf{S} \cdot \mathbf{F}^T \quad \text{with} \quad \mathbf{S} = \mathbf{C} : \left(\mathbf{E} - \mathbf{E}^{eig} \right) \tag{7}$$

where $\mathbf{F}$ is the deformation gradient and $\mathbf{S}$ denotes the second Piola–Kirchhoff stress tensor. The stress depends on the material tensor $\mathbf{C}$, the total Green-Lagrange strain $\mathbf{E}$ and the inelastic isotropic eigenstrains $\mathbf{E}^{eig}$. The latter are defined as an explicit function of the optimization variables s_e via the interpolation (6):

$$\mathbf{E}^{eig} = \begin{bmatrix} \epsilon_e & 0 \\ 0 & \epsilon_e \end{bmatrix}. \tag{8}$$

From the total nominal stress we obtain the internal force $\mathbf{f}_S^{int}$, for example see Belytschko et al. (2005):

$$\mathbf{f}_S^{int} = \int_{A_0} \mathbf{B}_0^T \, \mathbf{P} \, t \, dA_0, \tag{9}$$

where A_0 is the area and $\mathbf{B}_0$ is the differential operator in the undeformed configuration.

The support stiffness leads to an additional force $\mathbf{f}_S^k$:

$$\mathbf{f}_S^k = \mathbf{K}_s \mathbf{u}, \quad \text{with } \mathbf{K}_s = k_s^i \mathbf{I} \tag{10}$$

where $\mathbf{K}_s$ is the stiffness matrix associated with the support layout, $\mathbf{u}$ are the displacements, and $\mathbf{I}$ is an identity matrix.

Given the internal forces, $\mathbf{f}_S^{int} + \mathbf{f}_S^k$ and the external loads, $\mathbf{f}_S^{ext}$, the structural residual $\mathbf{R}_S$ governing the static response is written as:

$$\mathbf{R}_S(\mathbf{u}, \mathbf{s}) = \mathbf{f}_S^{int}(\mathbf{u}, \mathbf{s}) + \mathbf{f}_S^k(\mathbf{u}, \mathbf{s}) - \mathbf{f}_S^{ext} = \mathbf{0}, \tag{11}$$

The above system of non-linear equations, (11), is solved by Newton's method.

4 Flow model

In this study we approximate the flow in the channels by a two-dimensional model assuming a uniform flow across the channel thickness. This approach neglects friction effects along the bottom of the channels and leads to approximations in predicting drag and pressure drop values. To capture the influence of no-slip conditions at the top and bottom layers, Borrvall and Petersson (2003) introduced an explicit approximation of the flow in thickness direction. As previous work by the authors on fluid topology optimization (Pingen et al. 2007a, b) has shown, the 2-D flow model leads to optimization results equivalent to the ones presented

in Borrvall and Petersson (2003). Therefore, the 2-D model is considered sufficient for the present study. However, it should be noted that in general the friction at the bottom/top of the channel may influence the flow solution.

Motivated by previous theoretical and numerical studies (Pingen 2008; Pingen et al. 2007a; Evgrafov et al. 2008), we choose a hydrodynamic LBM to predict the channel flow. The hydrodynamic LBM approximates the Navier–Stokes equations for low Mach number flows (Chen and Doolen 1998; Succi 2001; Yu et al. 2003). It can be derived from the Boltzmann transport equation which is typically discretized by an explicit finite difference scheme in space and time, constituting a two step time-marching process:

$$\text{Collision:}\quad \widetilde{f_\alpha}(\mathbf{x}_i,t) = f_\alpha(\mathbf{x}_i,t) - \frac{1}{\tau}\left[f_\alpha(\mathbf{x}_i,t) - f_\alpha^{eq}(\mathbf{x}_i,t)\right], \tag{12}$$

$$\text{Propagation:}\quad f_\alpha(\mathbf{x}_i+\delta t\mathbf{e}_\alpha, t+\delta t) = \widetilde{f_\alpha}(\mathbf{x}_i,t), \tag{13}$$

where $\mathbf{e}_\alpha$ is the velocity vector, f_α is the distribution function associated with the corresponding velocity $\mathbf{e}_\alpha$, $\mathbf{x}_i$ represents the location in physical space, $\mathbf{e}_\alpha\delta t$ is the lattice spacing, δt is the time step, $\tau = \lambda/\delta t$ is the dimensionless relaxation time, and $f^{eq} = f^{eq}(\bar{\rho}, \mathbf{w})$ is a Taylor series approximation of the Maxwell–Boltzmann equilibrium distribution. The macroscopic parameters (fluid density $\bar{\rho}$, velocity $\mathbf{w}$, pressure, and viscosity) can be evaluated via statistical moments of the distribution function f. Approximating the channel flows by a two-dimensional model, we use the D2Q9 lattice scheme (see e.g. Yu et al. 2003) in the current study.

To solve the topology optimization problem by gradient-based schemes, the LBM is augmented with the porosity model introduced by Spaid and Phelan (1997), providing a continuous transition from fluid to solid and vice versa. The macroscopic velocity $\mathbf{w}$ is rescaled during the collision step (12), leading to:

$$\tilde{\mathbf{w}}^j(t,\mathbf{x}) = \left(1 - p^j(\mathbf{x})^\kappa\right)\mathbf{w}^j(t,\mathbf{x}), \tag{14}$$

where $p^j(\mathbf{x})$ is the impermeability that is related to the porosity in the domain. The vector $\tilde{\mathbf{w}}(t,\mathbf{x})$ defines the scaled velocity through porous media, which is substituted into the equilibrium distribution function $f^{eq}(\bar{\rho}, \tilde{\mathbf{w}})$ in place of $\mathbf{w}$. Note, that the interpolation of the impermeability p^j is defined analogously to the interpolation of the structural density ρ^i: $p^j, \rho^i = 1$ corresponds to *solid* and $p^j, \rho^i = 0$ corresponds to *fluid*, respectively *void* for the structure. The impermeability distribution $p(\mathbf{x})$ in the flow model is a function of the material distribution $\rho(\mathbf{x})$ in the structural domain and the structural displacements, $\mathbf{u}$.

Numerical studies show that this porosity approach converges to a 0–1 distribution; best results were obtained for an exponent $\kappa \approx 3$ (Pingen et al. 2009a). Due to the element wise constant impermeability values, this approach results in stair-step boundaries. However, Pingen et al. (2009a) have shown in numerical studies that this porosity approach captures the flow characteristics—e.g. pressure drop, drag, etc.—sufficiently well, especially for the low Reynolds numbers considered in the current study.

In the current study we focus on steady-state flows which are described by the solution of the following fixed-point problem:

$$\mathbf{R}_F(\mathbf{f},\mathbf{s}) = \mathbf{M}(\mathbf{f},\mathbf{s}) - \mathbf{f} = \mathbf{0}, \tag{15}$$

where $\mathbf{R}_F$ denotes the fluid residual vector and $\mathbf{f}$ describes the fluid state. The operator $\mathbf{M}$ performs one collision (12) and one propagation (13), which corresponds to advancing the flow solution one time step by an explicit time integration scheme. We solve the fixed-point problem (15) by an explicit time-marching scheme advancing the flow until convergence toward steady-state. While this approach is memory efficient, it requires a relatively large number of time-steps to reach steady-state convergence.

5 Coupling structural and fluid domains

To couple the structural domain with the fluid domain a simple geometric mapping that transforms structural densities into fluid impermeabilities is employed. The basic concept is illustrated in Figs. 1 and 6. The structural densities, ρ^i, are defined on a deforming mesh using a Lagrangian formulation, whereas the impermeabilities, p^j, of the fluid are defined on a fixed mesh in an Eulerian formulation. The mapping is given by:

$$p^j\left(\rho^i, \mathbf{u}^i\right) = \frac{1}{A_F^j}\sum_{i=1}^{n_j}\left(\frac{\rho^i}{\rho^{solid}}A_{int}^{ij}\left(\mathbf{u}^i\right)\right). \tag{16}$$

The index i describes the structural elements that intersect with the j-th fluid element, A_{int}^{ij} is the intersection area between the i-th structural and the j-th fluid element, and A_F^j defines the area of the fluid element.

The impermeability of a fluid element p^j, (16), depends on (I) the densities of the underlying structural mesh, ρ^i, and (II) the deformation $\mathbf{u}^i$ of the Lagrangian mesh, as the mesh-geometry of the structural mesh affects the intersection areas A_{int}^{ij}. Note, that ρ^i defines the elemental structural density, cp. (1), in the undeformed configuration and is therefore, unlike the impermeability p^j, independent of the displacements $\mathbf{u}^i$.

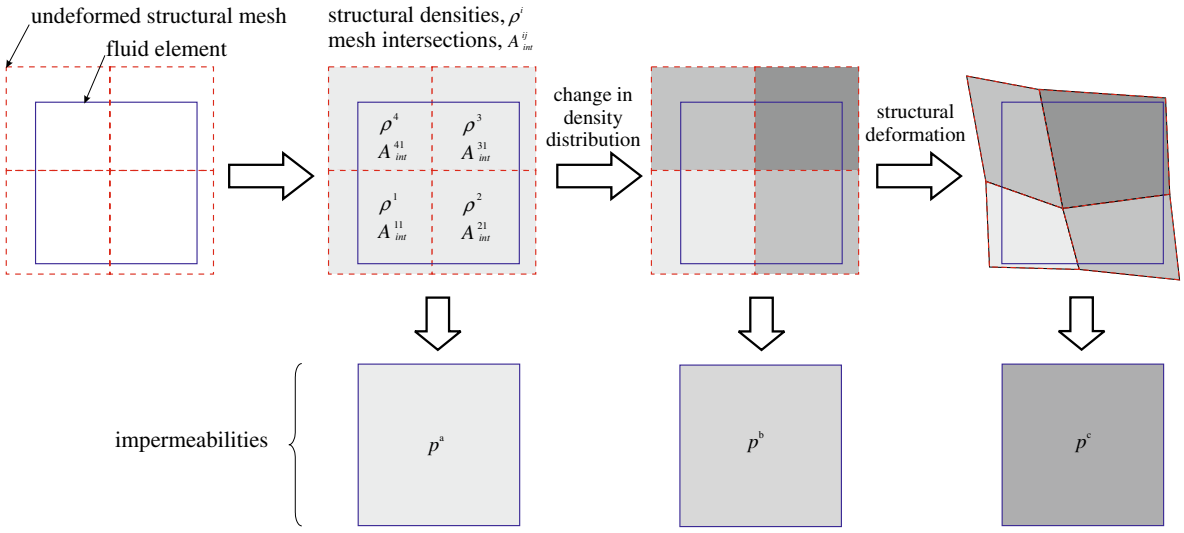

Fig. 6 Geometric mapping

6 Topology optimization of fluid-structure system

In this study we consider optimization problems of the following form:

$$\min_{\mathbf{s}} \; z = z\big(\mathbf{s}, \mathbf{u}^u(\mathbf{s}), \mathbf{f}^u(\mathbf{s}), \mathbf{u}^d(\mathbf{s}), \mathbf{f}^d(\mathbf{s})\big),$$
$$\text{s.t.} \begin{cases} \mathbf{s}, & \text{satisfy the design constraints,} \\ \mathbf{u}^{u,d}, & \text{solve (11) for given } \mathbf{s}, \\ \mathbf{f}^{u,d}, & \text{solve (15) for given } \mathbf{s}, \\ \mathbf{h}\big(\mathbf{s}, \mathbf{f}^{u,d}\big) = \mathbf{0}, & \text{the equality constraints,} \\ \mathbf{g}\big(\mathbf{s}, \mathbf{f}^{u,d}\big) \le \mathbf{0}, & \text{the inequality constraints,} \end{cases} \tag{17}$$

where z is a scalar performance functional constructed from a multi-objective formulation of the design problem; $\mathbf{s}$ is the vector of design variables, $\mathbf{u}$ is the displacement vector, $\mathbf{f}$ is the fluid state vector (cf. (12) and (13)) and $\mathbf{h}/\mathbf{g}$ are equality/inequality constraints, respectively. The superscripts 'u' and 'd' indicate the undeformed and deformed structural configuration. Typical objectives and constraints include pressure drop, drag, flow rate, energy loss, and mass.

6.1 Sensitivity analysis

The following discussion focuses on the sensitivity analysis of the design objective z, but can be applied analogously to design constraints. The derivative of the objective with respect to the design variables can be written as:

$$\frac{dz}{d\mathbf{s}} = \frac{\partial z}{\partial \mathbf{s}} + \left(\frac{\partial z}{\partial \mathbf{u}}\right)^T \frac{d\mathbf{u}}{d\mathbf{s}} + \left(\frac{\partial z}{\partial \mathbf{f}}\right)^T \frac{d\mathbf{f}}{d\mathbf{s}}. \tag{18}$$

The derivative of the displacements with respect to the design variables is computed from the derivative of the structural residual equation (11):

$$\frac{d\mathbf{R}_S}{d\mathbf{s}} = \frac{\partial \mathbf{R}_S}{\partial \mathbf{s}} + \frac{\partial \mathbf{R}_S}{\partial \mathbf{u}} \frac{d\mathbf{u}}{d\mathbf{s}} = \mathbf{0}. \tag{19}$$

Solving (19) for $d\mathbf{u}/d\mathbf{s}$ yields:

$$\begin{aligned} \frac{d\mathbf{u}}{d\mathbf{s}} &= -\underbrace{\left(\frac{\partial \mathbf{R}_S}{\partial \mathbf{u}}\right)^{-1}}_{\mathbf{K}_T} \frac{\partial \mathbf{R}_S}{\partial \mathbf{s}} \\ &= -{\mathbf{K}_T}^{-1} \left(\frac{\partial \mathbf{f}_S^{int}}{\partial \mathbf{s}} + \frac{\partial \mathbf{f}_S^{k}}{\partial \mathbf{s}} - \underbrace{\frac{\partial \mathbf{f}_S^{ext}}{\partial \mathbf{s}}}_{=0} \right), \end{aligned} \tag{20}$$

where $\mathbf{K}_T$ is the tangential stiffness matrix. Assuming that the external forces do not depend on the design variables, the term $\partial \mathbf{f}_S^{ext}/\partial \mathbf{s}$ vanishes. The partial derivative of the

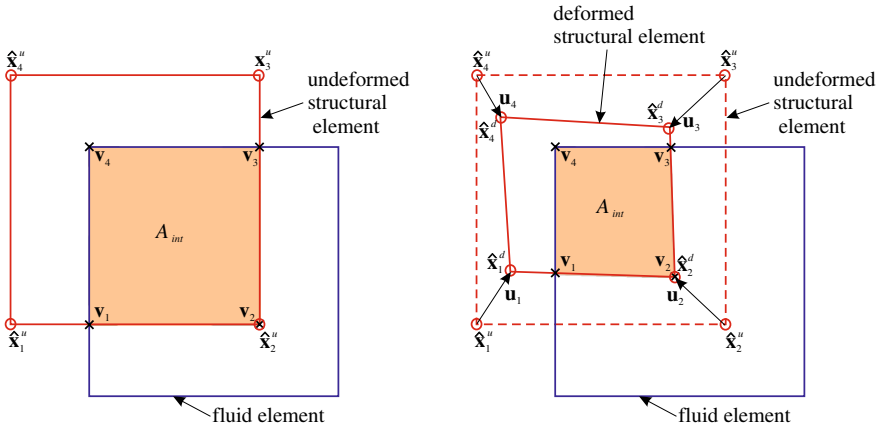

(a) Undeformed configuration

(b) Deformed configuration

Fig. 7 Intersection of structure and fluid mesh

internal force with respect to the design variables, $\partial \mathbf{f}_S^{int}/\partial \mathbf{s}$, is computed as (cp. (9)):

$$\begin{aligned}\frac{\partial \mathbf{f}_S^{int}}{\partial \mathbf{s}} &= \left[\frac{\partial \mathbf{f}_S^{int}}{\partial \mathbf{s}_m}, \frac{\partial \mathbf{f}_S^{int}}{\partial \mathbf{s}_t}, \frac{\partial \mathbf{f}_S^{int}}{\partial \mathbf{s}_s}, \frac{\partial \mathbf{f}_S^{int}}{\partial \mathbf{s}_e}\right] \\ &= \left[\int_A \mathbf{B}^T \frac{\partial \mathbf{P}}{\partial \mathbf{s}_m}\mathbf{t}\, dA, \int_A \mathbf{B}^T \left(\frac{\partial \mathbf{P}}{\partial \mathbf{s}_t}\mathbf{t} + \mathbf{P}\frac{\partial \mathbf{t}}{\partial \mathbf{s}_t}\right) dA, \right. \\ &\quad \left. \mathbf{0}, \int_A \mathbf{B}^T \frac{\partial \mathbf{P}}{\partial \mathbf{s}_e}\mathbf{t}\, dA\right]. \end{aligned} \tag{21}$$

For the term $\partial \mathbf{f}_S^k/\partial \mathbf{s}$ only the derivative with respect to the support design variables, $\mathbf{s}_s$, does not vanish (cp. (10)):

$$\frac{\partial \mathbf{f}_S^k}{\partial \mathbf{s}_s} = \frac{\partial \mathbf{K}_S}{\partial \mathbf{s}_s}\mathbf{u}, \tag{22}$$

where $\mathbf{K}_S$ is the global support-stiffness matrix.

Owing to the large number of optimization variables needed to resolve the geometry via a material distribution approach, we solve the above optimization problem using gradient based methods and compute the design sensitivities via an adjoint approach.

The derivative of the fluid state with respect to the design variables, $d\mathbf{f}/d\mathbf{s}$, is computed from the fluid residual equation (15):

$$\frac{d\mathbf{R}_F}{d\mathbf{s}} = \frac{\partial \mathbf{R}_F}{\partial \mathbf{s}} + \frac{\partial \mathbf{R}_F}{\partial \mathbf{f}}\frac{d\mathbf{f}}{d\mathbf{s}} + \frac{\partial \mathbf{R}_F}{\partial \mathbf{u}}\frac{d\mathbf{u}}{d\mathbf{s}} = 0. \tag{23}$$

Substituting (20) into (23) yields:

$$\begin{aligned}\frac{d\mathbf{f}}{d\mathbf{s}} &= -\underbrace{\left(\frac{\partial \mathbf{R}_F}{\partial \mathbf{f}}\right)^{-1}}_{\mathbf{J}_F}\left(\frac{\partial \mathbf{R}_F}{\partial \mathbf{s}} - \frac{\partial \mathbf{R}_F}{\partial \mathbf{u}}{\mathbf{K}_T}^{-1}\left(\frac{\partial \mathbf{f}_S^{int}}{\partial \mathbf{s}} + \frac{\partial \mathbf{f}_S^k}{\partial \mathbf{s}}\right)\right) \\ &\quad \text{with } \mathbf{p} = \mathbf{p}(\mathbf{u}, \mathbf{s}), \\ &= -\mathbf{J}_F^{-1}\frac{\partial \mathbf{R}_F}{\partial \mathbf{p}}\left(\frac{\partial \mathbf{p}}{\partial \mathbf{s}} - \frac{\partial \mathbf{p}}{\partial \mathbf{u}}{\mathbf{K}_T}^{-1}\left(\frac{\partial \mathbf{f}_S^{int}}{\partial \mathbf{s}} + \frac{\partial \mathbf{f}_S^k}{\partial \mathbf{s}}\right)\right), \end{aligned} \tag{24}$$

where the matrix $\mathbf{J}_F$ is the Jacobian of the fluid problem and the vector $\mathbf{p}$ defines the impermeabilities. Due to the large number of design variables, we employ the adjoint method in the following. Substituting (20) and (24) into the sensitivity equation (18) results in:

$$\begin{aligned}\frac{dz}{d\mathbf{s}} &= \frac{\partial z}{\partial \mathbf{s}} - \left(\frac{\partial z}{\partial \mathbf{u}}\right)^T {\mathbf{K}_T}^{-1}\left(\frac{\partial \mathbf{f}_S^{int}}{\partial \mathbf{s}} + \frac{\partial \mathbf{f}_S^k}{\partial \mathbf{s}}\right) \\ &\quad - \mathbf{a}_1 \times \frac{\partial \mathbf{R}_F}{\partial \mathbf{p}}\left(\frac{\partial \mathbf{p}}{\partial \mathbf{s}} + \frac{\partial \mathbf{p}}{\partial \mathbf{u}}{\mathbf{K}_T}^{-1}\left(\frac{\partial \mathbf{f}_S^{int}}{\partial \mathbf{s}} + \frac{\partial \mathbf{f}_S^k}{\partial \mathbf{s}}\right)\right), \end{aligned} \tag{25}$$

where $\mathbf{a}_1$ is the solution of the following adjoint equation:

$$\mathbf{a}_1 = \left(\frac{dz}{d\mathbf{f}}\right)^T {\mathbf{J}_F}^{-1}. \tag{26}$$

Table 2 Parameters for the interpolated quantities

Parameter	Value
Maximum Young's modulus of center layer (E_C^{max})	$5{\cdot}10^8$
Young's modulus of structural layers (E_S)	$5{\cdot}10^{10}$
Thickness of center layer (t_C)	0.5
Minimum thickness of structural layer (t_S^{min})	0.1
Maximum thickness of structural layer (t_S^{max})	2
Exponent for support stiffness interpolation (n_s)	3
Minimum support stiffness (k_s^{min})	$1{\cdot}10^{-4}$
Maximum support stiffness (k_s^{max})	$1{\cdot}10^{10}$
Maximum eigenstrain (ϵ_e^{max})	0.1

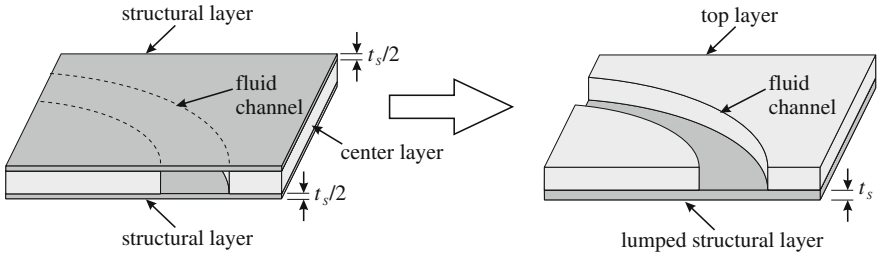

Fig. 8 Lumping two structural layers into one

The evaluation of $\partial \mathbf{R}_F/\partial \mathbf{p}$ and $dz/d\mathbf{f}$ in (25) and (26) has been described in Pingen et al. (2009a), the partial derivatives of the impermeabilities, $\partial \mathbf{p}/\partial \mathbf{s}$ and $\partial \mathbf{p}/\partial \mathbf{u}$, are discussed in Section 6.1.1. Rearranging (25) we get:

$$\frac{dz}{d\mathbf{s}} = \frac{\partial z}{\partial \mathbf{s}} - \mathbf{a}_1 \frac{\partial \mathbf{R}_F}{\partial \mathbf{p}} \frac{\partial \mathbf{p}}{\partial \mathbf{s}} + \mathbf{a}_2 \left(\frac{\partial \mathbf{f}_S^{int}}{\partial \mathbf{s}} + \frac{\partial \mathbf{f}_S^{k}}{\partial \mathbf{s}} \right), \tag{27}$$

where $\mathbf{a}_2$ is the solution to the second adjoint problem defined by:

$$\mathbf{a}_2 = \left(\mathbf{a}_1 \frac{\partial \mathbf{R}_F}{\partial \mathbf{p}} \frac{\partial \mathbf{p}}{\partial \mathbf{u}} - \left(\frac{\partial z}{\partial \mathbf{u}} \right)^T \right) {\mathbf{K}_T}^{-1}. \tag{28}$$

In the current study we do not consider objectives that depend directly on the design variables or the displacements. Therefore, the terms $\partial z/\partial \mathbf{s}$ in (27) and $\partial z/\partial \mathbf{u}$ in (28) vanish.

6.1.1 *Sensitivities of the fluid porosities*

As outlined in (16), the impermeabilities depend explicitly on variations in the structural density distribution, ρ^i, and the structural deformations, as the displacements $\mathbf{u}$ affect the intersection areas A_{int}^{ij}. The derivative of the impermeabilities with respect to the design variables is given by:

$$\frac{\partial p^j}{\partial \mathbf{s}^i} = \begin{cases} \dfrac{A_{int}^{ij}}{A_F^j \rho^{solid}} \dfrac{d\rho^i}{d\mathbf{s}^i} & \text{if } j\text{-th fluid element and } i\text{-th structural element intersect,} \\ 0 & \text{otherwise,} \end{cases} \tag{29}$$

where for the term $d\rho^i/d\mathbf{s}^i$ only the derivatives with respect to the material design variables, $\mathbf{s}_m^i$, do not vanish:

$$\frac{d\rho^i}{d\mathbf{s}_m^i} = \rho^{solid}. \tag{30}$$

The derivative of the impermeability with respect to the displacements is defined as follows:

$$\frac{\partial p^j}{\partial \mathbf{u}^i} = \begin{cases} \dfrac{\rho^i}{A_F^j \rho^{solid}} \dfrac{dA_{int}^{ij}}{d\mathbf{u}^i} & \text{if } j\text{-th fluid element and } i\text{-th structural element intersect,} \\ \mathbf{0} & \text{otherwise.} \end{cases} \tag{31}$$

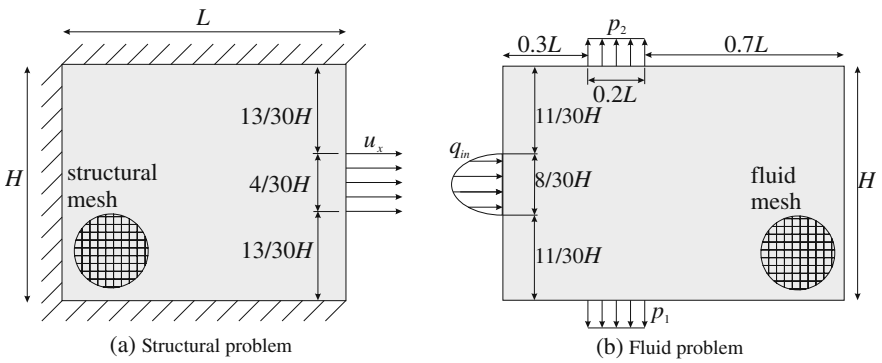

Fig. 9 Boundary conditions for the three-port manifold

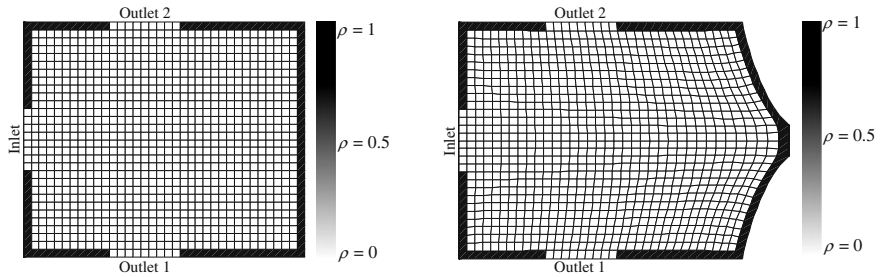

Fig. 10 Initial structural density distribution for the three-port manifold

(a) Undeformed state (b) Deformed state

The term $dA_{int}^{ij}/d\mathbf{u}^i$ can be expanded in the following way (cp. Fig. 7):

$$\frac{dA_{int}^{ij}}{d\mathbf{u}^i} = \underbrace{\frac{dA_{int}^{ij}}{d\mathbf{v}_k}}_{T_1} \underbrace{\frac{d\mathbf{v}_k}{d\hat{\mathbf{x}}_l}}_{T_2} \underbrace{\frac{d\hat{\mathbf{x}}_l}{d\mathbf{u}^i}}_{T_3}, \tag{32}$$

where T_1 defines the dependency of the intersection area A_{int}^{ij} on the vertices $\mathbf{v}_k$ of the polygon determining A_{int}^{ij}; T_2 characterizes the dependency of the polygon vertices on the position of the structural nodes $\hat{\mathbf{x}}_l$; T_3 describes the dependency of the nodes $\hat{\mathbf{x}}_l$ on the displacements $\mathbf{u}^i$ of the i-th structural element. Due to the definition of $\hat{\mathbf{x}}_l$, T_3 is simply a unity matrix in the deformed case and a zero-matrix in the undeformed case, respectively.

The adjoint sensitivity analysis has been validated through comparison with finite difference results.

7 Numerical examples

To illustrate the utility of the current approach we study the design of three tunable manifolds. The optimization problems are solved by the Globally-Convergent Method of Moving Asymptotes (GCMMA) of Svanberg (1995).

At each iteration in the optimization process we first solve the structural equilibrium equations for the deformed configuration. Then both, undeformed and deformed, material distributions are mapped onto the fluid mesh, leading to an undeformed and deformed fluid impermeability distribution. The flow solutions for both impermeability distributions are computed by advancing the flow in time until steady state convergence. The design criteria in the undeformed and deformed configurations are evaluated to obtain values of the objective function and constraints. The sensitivities are evaluated by the adjoint method using a direct solver for the linear systems, (26) and (28). The

Table 3 Objectives for the three-port manifold problem

Structural state	Outlet 1	Outlet 2
Undeformed	Maximize the mass flow, q_1^u	Minimize the mass flow, q_2^u
Deformed	Minimize the mass flow, q_1^d	Maximize the mass flow, q_2^d

Table 4 Parameters for the three-port manifold

Parameter type	Parameter	Value
Physical	Length (L)	36
	Height (H)	30
	Reynolds number (RE)	10
	Critical length (L_c)	9
	Dimensionless relaxation time (τ)	1/1.9
	Viscosity (v_F)	$\frac{1}{6}(2\tau - 1)$
	Inlet velocity (v_{in})	$RE \cdot v_F / L_c$
	Outlet pressure (p_{out})	1/3
	Prescribed external displacement (u_x)	$L/6$
	Poisson ratio (ν)	0.4
Discretization	Fluid-domain mesh ($n_x \times n_y$)	45×31
	Fluid-domain grid size	$L/(n_x - 1)$
	Structural-domain mesh ($m_x \times m_y$)	37×31
	Structural-domain grid size	$L/(m_x - 1)$
Algorithmic	Lower, upper limit for s^i (s^{min}, s^{max})	0, 1
	Step size (Δs)	$0.1(s^{max} - s^{min})$
	Number of GCMMA subcycles	2
Convergence	Tolerance for KKT conditions (ϵ_{kkt})	$1 \cdot 10^{-2}$
	Tolerance for design change (ϵ_s)	$2 \cdot 10^{-4}$
	Tolerance for constraint violation (ϵ_c)	$5 \cdot 10^{-3}$

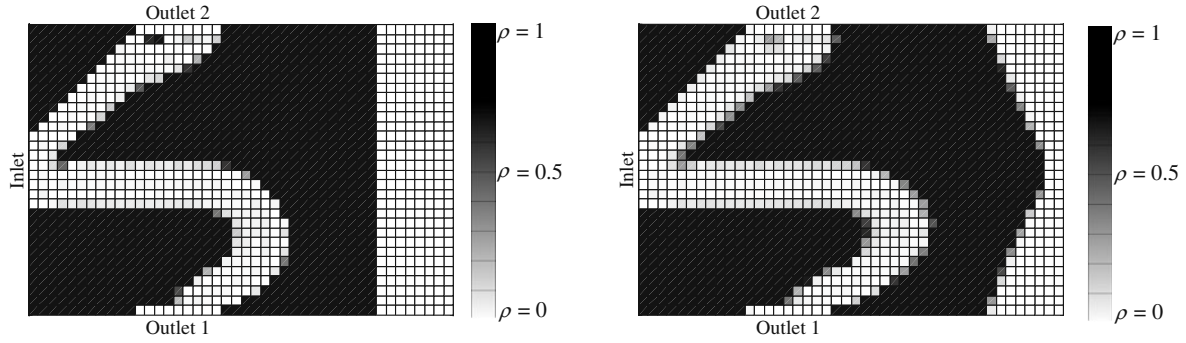

(a) Undeformed state (b) Deformed state

Fig. 11 Optimized impermeability distribution for the three-port manifold

convergence of the optimization process is monitored via the residual of the Karush–Kuhn–Tucker conditions $\mathbf{R}_{kkt}$, the design change $\|\Delta \mathbf{s}\|$, and the constraint violations. The following convergence criteria are defined:

$$\|\mathbf{R}_{kkt}\| < \epsilon_{kkt} \|\mathbf{R}_{kkt}\|_0, \tag{33}$$

$$\|\Delta \mathbf{s}\| < \epsilon_s \, N_s, \tag{34}$$

$$g_j < \epsilon_c, \tag{35}$$

where $\|\mathbf{R}_{kkt}\|_0$ is the norm of the residual of the initial design and N_s is the number of optimization variables. The tolerances ϵ_{kkt}, ϵ_s and ϵ_c for the three examples are defined in Tables 4, 8, and 9. For all three examples, we use the same interpolations linking abstract and physical design variables. The interpolation parameters are listed in Table 2. All values related to the flow solution in the following examples are in dimensionless lattice-units.

Using a 2-D approximation for the structural response and the flow allows us to simplify the three-layer model and lump the two structural layers into one. For this simplified model the center layer that houses the fluid channels becomes the top layer, which is connected to a single lumped structural layer. Figure 8 illustrates this simplified model.

7.1 Three-port manifold

In the first example, we consider a manifold that routes the flow from one inlet into two outlet ports. The goal of the design problem is to find the layout of the fluid channels and the thickness distribution of the structural layers such that the mass flow through the outlet ports can be controlled through an elastic deformation in response to a prescribed external displacement. In this example, internal actuation via eigenstrains is not considered and the supports are not altered in the optimization process. The boundary conditions for both the structural and the fluid problems are depicted in Fig. 9. The gridded circles illustrate the structural and fluid mesh, respectively. The structure is clamped along all edges except for the right one. The center of the latter is subjected to horizontal displacements $u_x = L/6$. The boundary conditions for the fluid model, Fig. 9b, are a parabolic inlet velocity distribution and a prescribed static pressure at both outlets. Note, that the fluid domain is 20% longer than the structural mesh. This ensures that the fixed fluid mesh covers the entire structural domain when the structure expands during deformation.

The initial density distributions in the undeformed and deformed configuration are illustrated in Fig. 10. We initialize the density distribution with $\rho = 1$ at the boundaries that are neither inlet nor outlet and $\rho = 0$ elsewhere. The thickness of the structural layer is uniformly initialized with $s_t^i = 0.5 \; \forall \, i$.

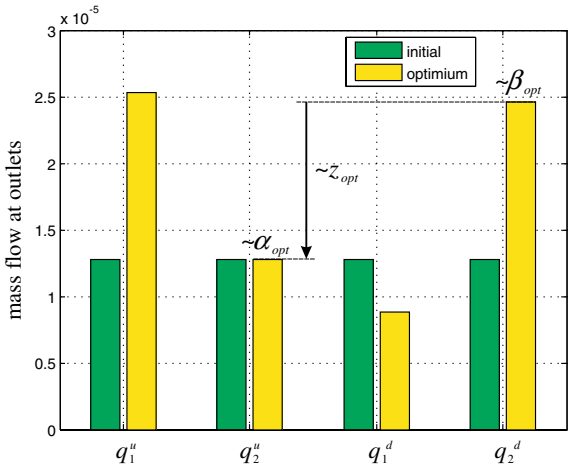

Fig. 12 Comparison between initial and optimized dynamic pressures at outlet 1 and 2 for the three-port manifold

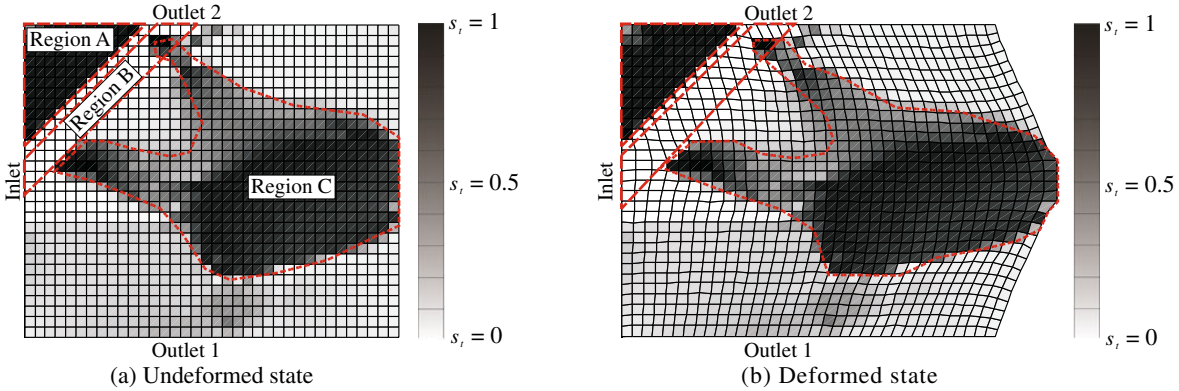

Fig. 13 Optimized relative thickness of structural layer for the three-port manifold

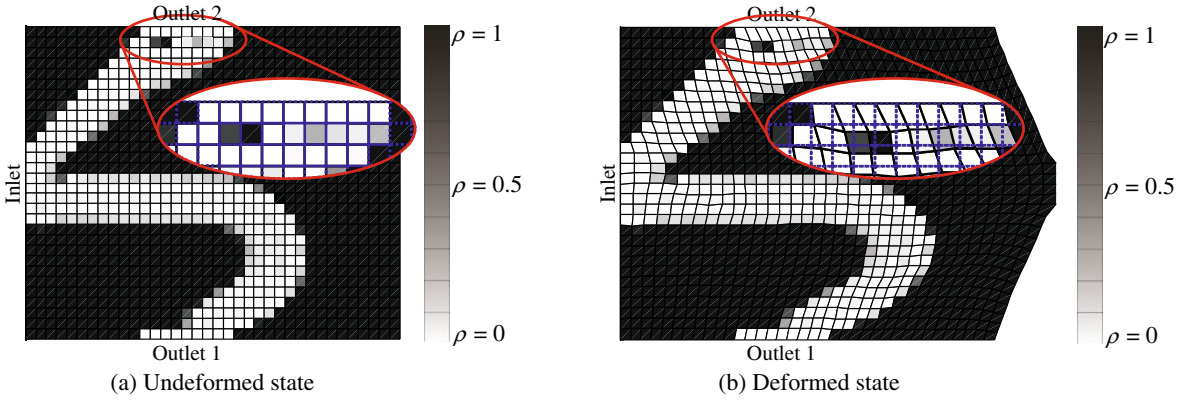

Fig. 14 Smearing effects due to mismatching meshes (Eulerian fluid mesh on Lagrangian density distribution)

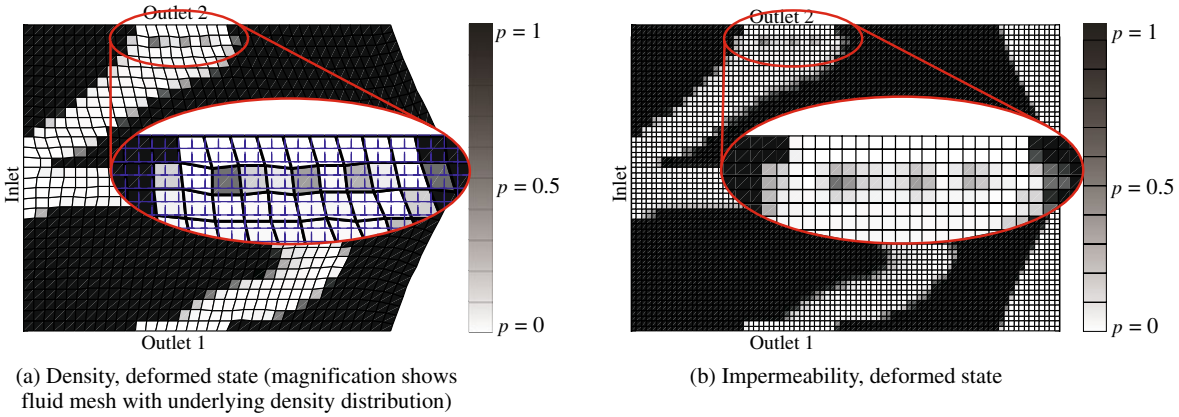

Fig. 15 Material layout after 274 iterations for refined fluid mesh

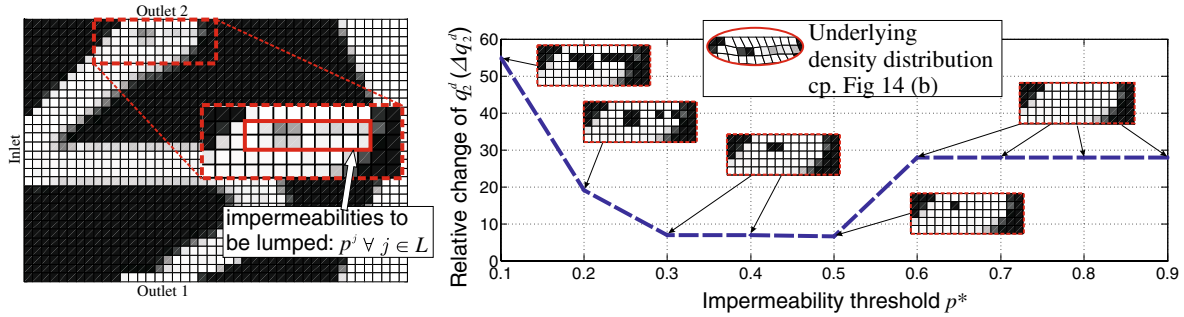

(a) Impermeability distribution in deformed state

(b) Relative change for Δq_2^d due to lumping of impermeabilities (rectangles show the lumped impermeability distributions for a given p^*)

Fig. 16 Lumping of intermediate impermeabilities and its effect

The design of a tunable manifold is formulated as a multi-criteria optimization problem. The goal is to find the layout of a flow-switch that guides the flow to one outlet in the undeformed configuration and to a second outlet in the deformed configuration. Specifically, the objective is to maximize the mass flow at the lower outlet in the undeformed state and minimize it in the deformed configuration. For the outlet at the top the goal is opposite: minimize the mass flow in the undeformed state and maximize it in the deformed configuration. These four objectives are listed in Table 3. The multiple objectives are treated via a bound formulation (Stadler 1988), which seeks a compromise between all objectives while avoiding that one objective is improved whereas another objective deteriorates significantly. The optimization problem can be written as follows:

$$
\begin{aligned}
&\min_{\mathbf{s}}\ z = \alpha - \beta,\\
&\text{s.t.}\ \ g_1 = q_1^u - \beta \geq 0,\\
&\qquad g_2 = \alpha - q_2^u \geq 0,\\
&\qquad g_3 = \alpha - q_1^d \geq 0,\\
&\qquad g_4 = q_2^d - \beta \geq 0,\\
&\qquad g_5 = 1.005 - \frac{(p_{in})^u}{\left(p_{in}^0\right)^u} \geq 0,\\
&\qquad g_6 = 1.005 - \frac{(p_{in})^d}{\left(p_{in}^0\right)^d} \geq 0,\\
&\qquad g_7 = \frac{1}{N_e}\sum_i^{N_e} \frac{\rho^i}{\rho^{solid}} - 0.75 \geq 0,\\
&s_m^{min} \leq s_m^i \leq s_m^{max},\\
&s_t^{min} \leq s_t^i \leq s_t^{max}.
\end{aligned}
\tag{36}
$$

where α and β are auxiliary variables. The mass flow is denoted by q. The subscripts indicate the outlet ports: '1' for the lower port and '2' for the upper port. The superscripts 'u' and 'd' refer to the undeformed and deformed configurations. The constraints g_5, g_6 ensure that the total inlet pressure is equal or less than 100.5% of the inlet pressure of the initial design (cf. Fig. 10). The mass constraint g_7 requires that at least 75% of the design domain is solid where N_e is the number of structural elements. The parameters for the three-port manifold example are summarized in Table 4. Due to the structure of (36), at every locally optimal solution the following equalities are satisfied:

$$\alpha = \max\left(q_2^u, q_1^d\right), \tag{37}$$

$$\beta = \min\left(q_1^u, q_2^d\right), \tag{38}$$

The optimization process converged in 418 iterations. While the thickness distribution converged rather fast, the density distribution showed a much slower convergence rate and hence required a large number of optimization steps. Figure 11 shows the optimized fluid channel. In the undeformed configuration, the bulk of the fluid flows through the lower outlet, as this flow path has a smaller pressure drop than the flow path to the upper port. In the deformed configuration the channel to the lower outlet port is stretched significantly. The additional length and curvature increases the pressure drop of the lower channel,

Table 5 Flow rates and objective for design with and without plug (cp. (37) and (38))

	With island	Without island
q_1^u	2.58×10^{-5}	$2.33 \times 10^{-5} \approx \beta$
q_2^u	$1.27 \times 10^{-5} \approx \alpha$	$1.74 \times 10^{-5} \approx \alpha$
q_1^d	9.34×10^{-6}	7.79×10^{-6}
q_2^d	$2.48 \times 10^{-5} \approx \beta$	3.15×10^{-5}
$z = \alpha - \beta$	-1.21×10^{-5}	-0.59×10^{-5}

Table 6 Norm of fluid forces, relative errors for solution with and without fluid forces

Norm of fluid forces	$\|\mathbf{f}_L^n\| = 9.3 \cdot 10^{-3}$
Relative error in displacements	$e_u = 3.7 \cdot 10^{-12}\%$
Relative error in impermeabilities	$e_p = 1.7 \cdot 10^{-12}\%$
Relative error in dynamic pressure	$e_z = -1.7 \cdot 10^{-9}\%$

reducing the mass flow, q_1^d, at the lower outlet. Moreover, Fig. 11b illustrates that the channel to the upper outlet widens under the structural deformation, increasing q_2^d.

A quantitative comparison between initial and optimized mass flows is shown in Fig. 12: three of the four mass flow rates are improved significantly compared to the initial design (cf. Table 3). However, the mass flow through the upper outlet in the undeformed configuration, q_2^u, hardly changed during the optimization.

Figure 13 displays the relative thickness of the structural layer. It shows that there are two regions in which the thickness of the structural layer is maximized, resulting in a stiffening of the corresponding structure. One is in the top left corner of the design domain (Region A), effectively stiffening the left edge of the channel to outlet 2. The region of the channel to outlet 2 (Region B) on the other hand has a minimum thickness. This thickness layout amplifies the widening of the channel to outlet 2 under deformation. The second region of high thickness values (Region C) connects the point of load incidence with the apex of the channel to outlet 1. Since the lower left of the design domain is weakened, this allows to further increase the length and curvature of this channel.

7.1.1 Influence of small features on the performance

The undeformed material distribution shows a small solid feature in front of the upper outlet, Fig. 11a. In the deformed configuration this feature is stretched. However, in the fluid model, the stretched feature is represented by intermediate impermeabilities. This brings up two questions: (I) is this feature an artifact that occurs owing to the chosen numerical representation? and (II) what are its benefits?

To answer (I) the mapping procedure is examined: in the undeformed configuration, the fluid and solid meshes are almost aligned, resulting in a mapping $p^j \approx \rho^i$, which leads to a mostly black and white impermeability distribution, see Fig. 11a. However, as the structure stretches, the Lagrangian solid mesh deforms while the Eulerian fluid mesh stays fixed, leading to a mismatch between the two meshes. This results in smeared-out and thus lower interface impermeabilities in the deformed state, Fig. 11b. Figure 14 illustrates this issue. The magnification depicts the density distribution on the Lagrangian mesh overlaid with the Eulerian fluid mesh. Figure 11b shows that in the deformed case two 'solid' densities, i.e. $\rho \approx 1$, get distributed over six fluid elements, hence the smearing.

In order to mitigate the smearing effect, the same problem was optimized using a twice as fine fluid mesh. Figure 15 shows both the density as well as the impermeability distribution for the refined fluid mesh after 274 iterations. As can be seen from Fig. 15, the finer fluid mesh effectively reduces the smearing effect, but does not prevent the formation of a solid feature in front of outlet 2.

To analyze the effect of the smeared out impermeabilities in the deformed configuration we lumped the intermediate impermeabilities into a discrete 0–1 distribution which is shown in Fig. 16. The intermediate impermeability distribution in Fig. 16a is compared with a lumped one, where the values for lumped impermeabilities, $\mathbf{p}_l$, are obtained from the following:

$$p_l^j = \begin{cases} 0 & \text{if } p^j \le p^* \quad \forall j \in L, \\ 1 & \text{if } p^j > p^* \quad \forall j \in L, \\ p^j & \qquad\quad \forall j \notin L, \end{cases} \tag{39}$$

where L is the list of 18 elements to be lumped. The relative change of the flow rate, Δq_2^d due to the lumping is defined as:

$$\Delta q_2^d = \frac{q_2^d(\mathbf{p}_l) - q_2^d(\mathbf{p})}{q_2^d(\mathbf{p})}, \tag{40}$$

where $\mathbf{p}$ and $\mathbf{p}_l$ define regular and the lumped impermeability distribution, respectively. Figure 16b shows the

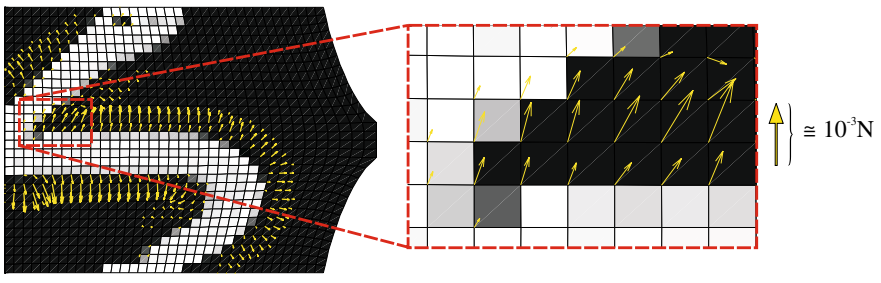

Fig. 17 Fluid forces acting of structure $\mathbf{f}_L^n$

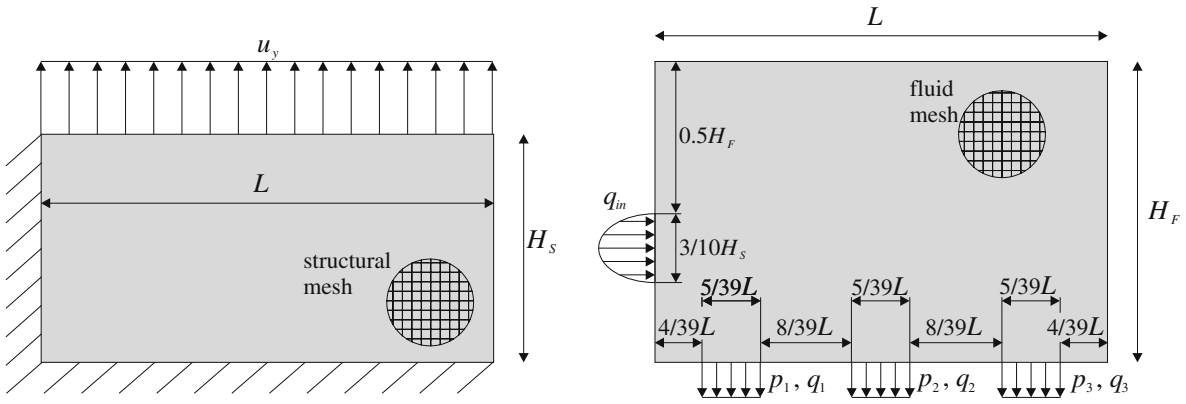

(a) Structural problem (b) Fluid problem

Fig. 18 Boundary conditions for the four-port manifold with external actuation

underlying density distribution (ellipse) as well as the corresponding lumped impermeabilities for different threshold values p^* (rectangles). As can be seen in the figure, an intermediate impermeability threshold of $0.3 \leq p* \leq 0.5$ leads to a small, $\approx$ 7%, change in the flow rate q_2^d. The lumped impermeability distribution for thresholds $0.3 \leq p^* \leq 0.4$ resemble the underlying densities the closest (two solid elements). Since the smeared impermeability distribution only differs by $\approx$ 7% from the discrete, and thus physically more meaningful distribution, we conclude that the geometric mapping produces physically consistent flow solutions/results for fluid problems with low Reynolds numbers as considered in this work.

After having demonstrated that the island is not an artifact, we analyze the benefits of this small feature. We compare the results from the original optimized design, as depicted in Fig. 11, with a design where the solid feature is removed, i.e. a lumped impermeability with a threshold of $p^* \geq 0.6$, cp. Fig. 16b. The quantitative results are listed in Table 5. The values show that the design without the island has twice as large of an objective value compared to the one with the island. The reason for this lies in the fact that without island, the flow rate for outlet 2 increases while at the same time the flow rate for outlet 1 decreases. This results in $q_1^u < q_2^d \rightarrow \beta = q_1^u$. Additionally, $\alpha \approx q_2^u$ is increased significantly due to the lower pressure drop when the island is removed. The combination of these effects results in an overall worsened objective when the feature is not present. This analysis shows that the performance of the optimized topology is due to both the geometry of the flow channels and the feature in front of the upper outlet.

Table 7 Constraints for the four-port manifold problem

Structural state	@ Outlet 1	@ Outlet 2	@ Outlet 3
Undeformed	$q_1^u = q_{in}^u/2$	$q_2^u = q_{in}^u/4$	$q_3^u = q_{in}^u/4$
Deformed	$q_1^d = q_{in}^d/3$	$q_2^d = q_{in}^d/3$	$q_3^d = q_{in}^d/3$

7.1.2 *Influence of the fluid forces on the structure*

The current study neglects the effect of the fluid forces on the structure, leading to a one-way structure-fluid coupling. In this subsection we demonstrate that the error resulting from this simplification is negligible for problems in which the structural displacements due to the fluid pressure are sufficiently small such that they do not affect the flow. This assumption holds for flows with low velocities and pressures and for bulky structures. As topology optimization methods may lead to slender features that might deform significantly even under low fluid pressures, this assumption needs to be verified for the resulting optimized design.

To analyze the influence of the fluid pressure on the structural deformation, we extend our approach described previously. Following a staggered coupling scheme, we compute the fluid pressure in the fluid model and map it onto the structural model leading to an additional external force term. The resulting structural deformations are imposed onto the fluid model as described in Section 5. To ensure proper convergence to steady state, the staggered scheme is repeated until the relative error in displacements, e_u^k, satisfies the following condition:

$$e_u^k = \frac{\left\| \mathbf{u}^k - \mathbf{u}^{k-1} \right\|}{\left\| \mathbf{u}^k \right\|} \leq 10^{-11}. \tag{41}$$

where k is the iteration index of the staggered scheme.

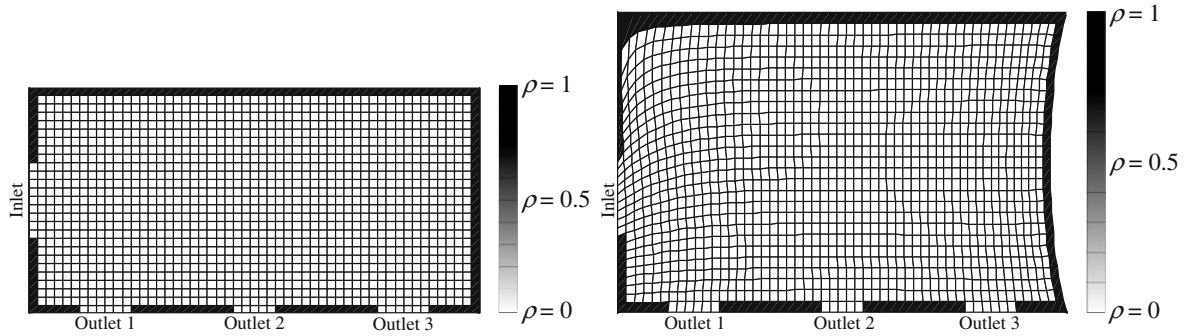

(a) Undeformed state (b) Deformed state

Fig. 19 Initial structural density distribution for the four-port manifold (material and thickness optimization)

Table 6 lists the relative errors of the fluid-structure response when the influence of the fluid forces on the structural deformations is ignored. The relative errors arising from the omission of the fluid forces is negligible as in the present example the fluid forces are insignificant in comparison to the structural stiffness. However, in cases where the structure is more flexible (e.g. long slender components) and/or the fluid velocities are higher, i.e. larger fluid forces, the effect of the fluid pressure on the structure may have to be considered.

Remark 1 The porosity model described in Section 4 can be employed to predict fluid forces $\mathbf{f}_E$ (where the subscript 'E' indicates that the force vector is defined on the Eulerian mesh). However, this approach results in forces not only at the fluid–solid interface but also within the solid domain. These non-physical forces occur due to the fact that porous material permits pressure gradients throughout the material. These pressure gradients in the porous material are still allowed to develop when $p = 1$ (solid), thus leading to forces within solid regions. To ensure that fluid forces only occur in the vicinity of the fluid–solid interface a scaled bounce-back boundary method is employed. For details on this method, the reader is referred to the work by Pingen et al. (2006).

Remark 2 Given the fluid forces, $\mathbf{f}_E$, the mapping described in Section 5 is used to transform $\mathbf{f}_E$ from the Eulerian mesh onto the Lagrangian mesh. This results in a fluid force vector $\mathbf{f}_L$, where the force acting on the i-th structural element is defined as:

$$f_L^i = \frac{1}{A_S^i} \sum_{j=1}^{n_i} \left(f_E^j A_{int}^{ji} \right). \tag{42}$$

This force is equally distributed to the nodes of the i-th structural element, which finally results in the vector of

Table 8 Parameters for the four-port manifold (material and thickness optimization)

Parameter type	Parameter	Value
Physical	Length (L)	48
	Height of fluid domain (H_F)	31
	Height of structural domain (H_S)	24
	Reynolds number (RE)	10
	Critical length (L_c)	9
	Dimensionless relaxation time (τ)	1/1.9
	Viscosity (ν_F)	$\frac{1}{6}(2\tau - 1)$
	Inlet velocity (v_{in})	$RE \cdot \nu_F / L_c$
	Outlet pressure (p_{out})	1/3
	Prescribed external displacement (u_y)	$0.25 H_S$
	Poisson ratio (ν)	0.4
Discretization	Fluid-domain mesh ($n_x \times n_y$)	49×32
	Fluid-domain grid size	$L/(n_x - 1)$
	Structural-domain mesh ($m_x \times m_y$)	53×27
	Structural-domain grid size	$L/(m_x - 1)$
Algorithmic	Lower, upper limit for s^i (s^{min}, s^{max})	0, 1
	Step size (Δs)	$0.05(s^{max} - s^{min})$
	Number of GCMMA subcycles	1
Convergence	Tolerance for KKT conditions (ϵ_{kkt})	$1 \cdot 10^{-7}$
	Tolerance for design change (ϵ_s)	$5 \cdot 10^{-3}$
	Tolerance for constraint violation (ϵ_c)	$5 \cdot 10^{-4}$

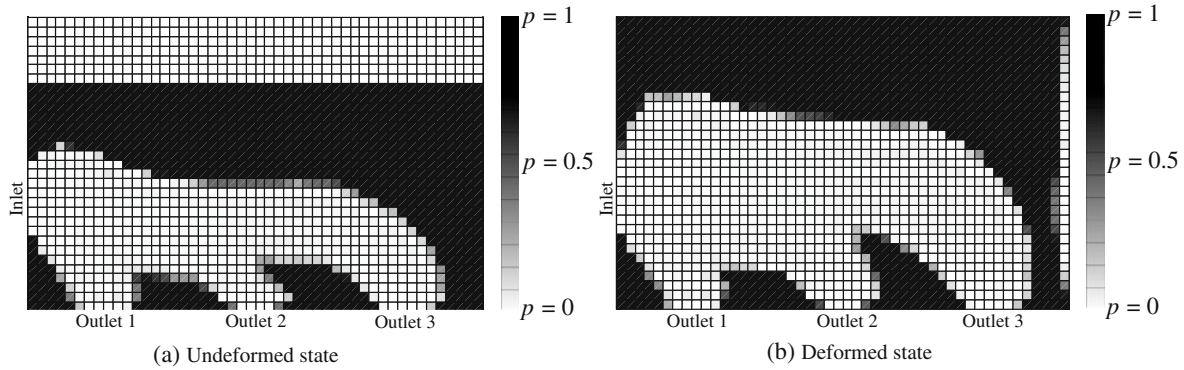

Fig. 20 Optimized impermeability distribution for the four-port manifold with external actuation

nodal fluid forces $\mathbf{f}_L^n$. This force vector $\mathbf{f}_L^n$ leads to structural deformations. The latter in return affects the intersection areas A_{int}^{ji} (cp. (42)), resulting in slightly different fluid forces f_L^i. Figure 17 shows the fluid forces, $\mathbf{f}_L^n$, in the structural domain. Note that the forces within the structural solid domain occur due to the mapping in (42).

7.2 Four-port manifold with external actuation

In the second example we optimize a system with one inlet and three outlet ports. As before, the goal of the design problem is to find the layout of the fluid channels and the thickness distribution of the structural layer such that the mass flow through the outlet ports can be controlled through an elastic deformation in response to an external prescribed displacement. Again, internal actuation and varying the support stiffness are not considered. The boundary conditions for both the structural and the fluid problem are depicted in Fig. 18. The gridded circles illustrate the structural and fluid mesh, respectively. The height of the fluid domain is approximately 25% higher than that of the structural domain. This ensures that the fixed fluid mesh covers the entire structural domain, even when the latter expands during deformation.

We minimize the difference in total pressure between the inlet and the outlets. Furthermore, we require for the undeformed configuration that the flow rate through outlet 1 (q_1^u) is $1/2$ of the inlet flow rate, q_{in}^u. The flow rates through the remaining two outlets, q_2^u and q_3^u, are required to be $1/4$ of the inlet flow rate. In the deformed configuration all three outlets, q_j^d, for $j = 1, \ldots, 3$, should have the same flow rate, i.e. $1/3$ of the inlet flow rate in the deformed configuration, q_{in}^d. Table 7 lists the flow rate constraints for the four-port manifold.

The structure is clamped on the left and lower edges. The upper edge is subjected to a prescribed displacement $u_y = 0.25 H_S$ in the vertical direction. The boundary conditions for the fluid model, Fig. 18b, are a parabolic inlet velocity and a prescribed static pressure of $p_{out} = 1/3$ at all three outlets.

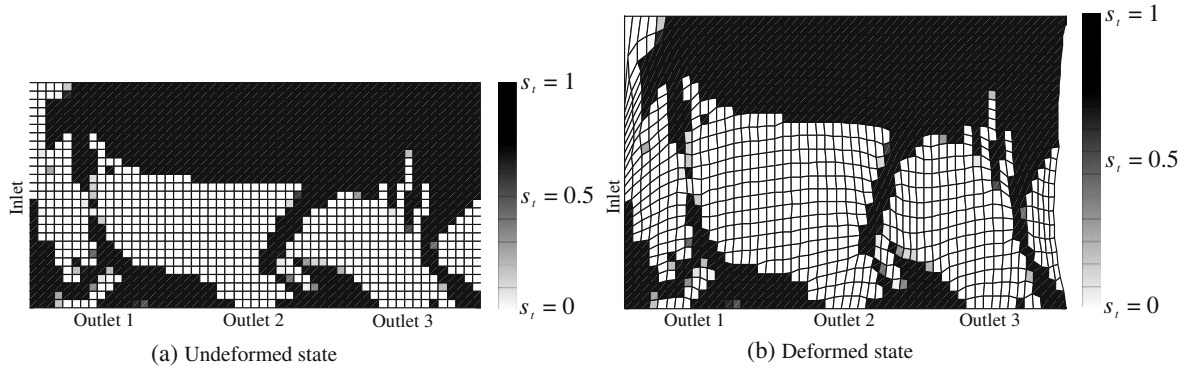

Fig. 21 Optimized relative substrate thickness for the four-port manifold with external actuation

The initial density distributions in the undeformed and deformed configurations are illustrated in Fig. 19. We initialize the density distribution with $\rho = 1$ at the boundary that is neither inlet nor outlet and $\rho = 0$ elsewhere. The substrate thickness is uniformly initialized with $s_t^i = 0.5 \,\forall\, i$.

The optimization problem is defined by the following set of equations:

$$
\begin{aligned}
\min_{\mathbf{s}} \; & z = p_{in}^u + p_{in}^d - \sum_{j=1}^{3} \left(p_j^u + p_j^d \right), \\
\text{s.t.} \; & g_1 = 0.005 - \left(q_{in}^u - \frac{1}{2} q_1^u \right)^2 - \left(q_{in}^u - \frac{1}{4} q_2^u \right)^2 \\
& \geq 0, \\
& g_2 = 0.005 - \left(q_{in}^d - \frac{1}{3} q_1^d \right)^2 - \left(q_{in}^d - \frac{1}{3} q_2^d \right)^2 \\
& \geq 0, \\
& g_3 = \frac{1}{N_e} \sum_{i}^{N_e} \frac{\rho^i}{\rho^{solid}} - 0.6 \geq 0, \\
& s_m^{min} \leq s_m^i \leq s_m^{max}, \\
& s_t^{min} \leq s_t^i \leq s_t^{max},
\end{aligned}
\tag{43}
$$

where, g_1 and g_2 describe the flow rate constraints and g_3 requires that at least 60% of the design domain has to be solid. Table 8 lists the parameters used for the four-port manifold example.

Figure 20 shows the optimized fluid channel, converged after 137 iterations. All three constraints are satisfied. In the undeformed configuration, the mass flow to the output ports 2 and 3 is limited by height of the horizontal main channel. When the structure undergoes deformation, the main channel widens, increasing the mass flow through outlet ports 2 and 3. Furthermore, the fin between outlet 2 and 3 deforms such that the channel to outlet 2 is widened and more flow is directed toward outlet 2. The increased mass flow through outlet 2 and 3 simultaneously leads to a decrease of the mass flow through outlet port 1.

Figure 21 illustrates the optimized relative substrate thickness. The thickness is mostly minimized in areas where the channel is located (cp. Fig. 20). This weakens the structure, allowing for a greater widening of the channel when deformed. The link slightly to the right of the center of the design domain stiffens the connection between the upper half of the design domain and the fin between outlet 2 and 3. When the structure is deformed, this link pulls the tip of the fin up and to the right, redirection the flow.

Table 9 Parameters for the four-port manifold (material, eigenstrain and support-layout optimization)

Parameter type	Parameter	Value
Physical	Length (L)	48
	Height of fluid domain (H_F)	24
	Height of structural domain (H_S)	24
	Reynolds number (RE)	10
	Critical length (L_c)	9
	Dimensionless relaxation time (τ)	1/1.9
	Viscosity (ν_F)	$\frac{1}{6}(2\tau - 1)$
	Inlet velocity (v_{in})	$RE \cdot \nu_F / L_c$
	Outlet pressure (p_{out})	1/3
	Prescribed external displacement	0
	Poisson ratio (ν)	0.4
Discretization	Fluid-domain mesh ($n_x \times n_y$)	49×25
	Fluid-domain grid size	$L/(n_x - 1)$
	Structural-domain mesh ($m_x \times m_y$)	53×27
	Structural-domain grid size	$L/(m_x - 1)$
Algorithmic	Lower, upper limit for s_m^i, s_s^i (s^{min}, s^{max})	0, 1
	Lower, upper limit for s_e^i (s_e^{min}, s_e^{max})	−1,1
	Step size (Δs)	$0.05(s^{max} - s^{min})$
	Number of GCMMA subcycles	1
Convergence	Tolerance for KKT conditions (ϵ_{kkt})	$1 \cdot 10^{-5}$
	Tolerance for design change (ϵ_s)	$1 \cdot 10^{-2}$
	Tolerance for constraint violation (ϵ_c)	$1 \cdot 10^{-5}$

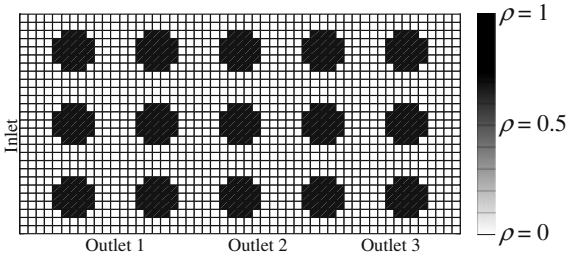

Fig. 22 Initial structural density distribution for the four-port manifold (material with internal actuation)

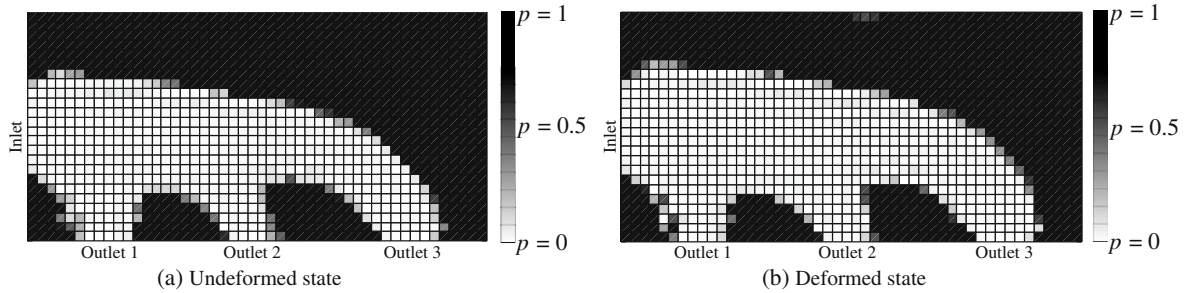

Fig. 23 Optimized impermeability distribution for the four-port manifold with internal actuation

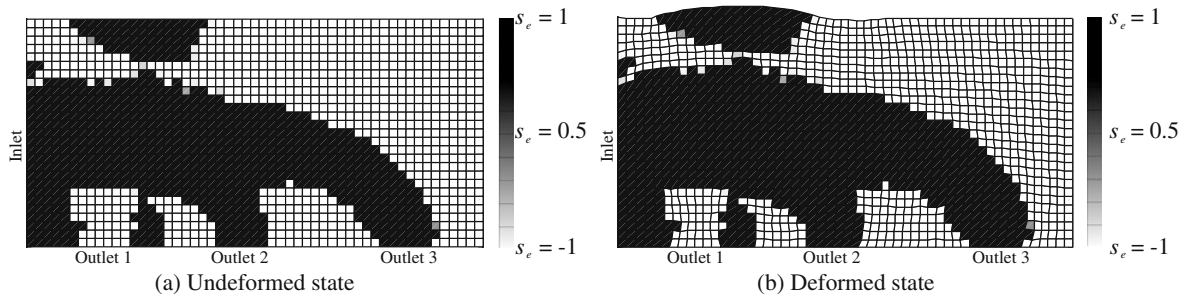

Fig. 24 Optimized eigenstrain for the four-port manifold with internal actuation

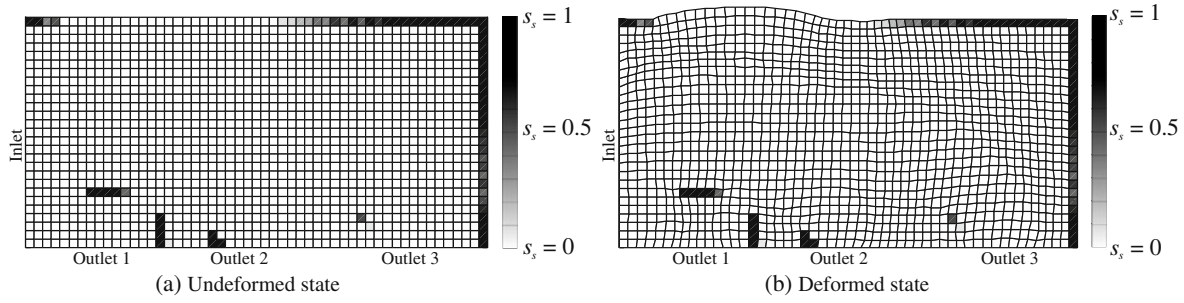

Fig. 25 Optimized support layout for the four-port manifold with internal actuation

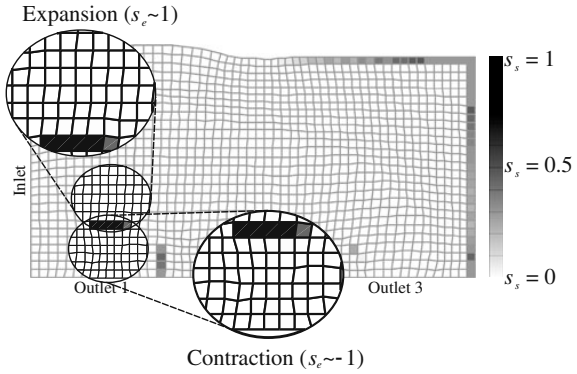

Fig. 26 Detail of optimized support layout in deformed configuration (cf. Figs. 24b and 25b)

7.3 Four-port manifold with internal actuation

The third example considers the same problem as in Section 7.2. However in this example we consider internal instead of external actuation and vary the eigenstrain distribution along with the support stiffness. The thickness is not altered. When employing eigenstrains, an adjustable support-layout is crucial to achieve large local deformations without requiring excessive eigenstrains. Since the system is no longer subjected to an external displacement and the displacements along the structural design domain are fixed, the dimensions of the fluid mesh are chosen such that they match the structural mesh. Table 9 lists the algorithmic parameters. To demonstrate the robustness of the current approach with respect to the initial design, we choose a different initialization for the density distribution, depicted in Fig. 22. The optimization problem is identical to the one defined in (43), but with box constraints on s_e^i and s_s^i instead of s_t^i. The eigenstrain design variables are uniformly initialized with $s_e^i = 10^{-4}$ and the support design with $s_s^i = 0.3$. The substrate thickness is fixed at $t = 1.05$, i.e. $s_t^i = 0.5$.

Figure 23 shows the optimized impermeability distribution after 179 iterations (converged) in the undeformed and deformed configuration. As can be seen from these figures, the channels to the outlet ports 2 and 3 (center and right) expand significantly in the deformed configuration, increasing the flow rates through these ports. On the other hand the channel to outlet port 1 contracts, which reduces the flow for outlet 1. The optimized eigenstrain distribution is illustrated in Fig. 24. It shows positive strains ($s_e^i = 1$: expansion) along the channels to the outlet ports 2 and 3 and negative strains ($s_e^i = -1$: contraction) around these channels, leading to a significant widening of the channels to the outlet ports 2 and 3. The area of the domain that coincides with the channel to outlet 1 shows negative strains, i.e. the channel to outlet 1 contracts.

The optimized support layout is depicted in Fig. 25. It shows that mainly the boundaries on the right and top edges are fixed, while the main bulk of the design space is unsupported. The small areas of high support stiffness within the interior of the domain are beneficial for the development of local areas of contraction/expansion, as depicted in Fig. 26. The elements with high support stiffness in between the two ellipses help to separate the area of contraction and expansion by bracing the structure.

8 Conclusions

An approach to topology optimization of FSI problems has been presented and applied to the multi-objective design optimization of dynamically tunable, elastically deforming micro fluidic devices. The proposed design method allows for optimizing the topology of the fluid channels in multi-layered structures, the thickness distribution of the structural layers, the layout of the active material, and the location of supports.

It was shown that for the class of problems considered in this paper, the structural deformations due to fluid forces are negligible in comparison to the deformations due to external and internal actuation. This allows considering only a one-sided structure-fluid coupling. As topology optimization gives only limited control over the resulting geometric features, the validity of this simplification should be verified for the resulting optimized design.

In order to alter the flow noticeably, large deformations are needed. Therefore, the structural response was modeled by a geometrically non-linear finite element model. To avoid issues due to large compressive loading, such as buckling, predominantly tensile loads have been considered in this study. However, compressive external and internal loads are expected to be particularly efficient in altering channel flows and remain to be studied in the future. The current study employs a linear stress–strain relation. To account for large strains a non-linear constitutive model such as a hyper-elastic model should be used. Due to the separate treatment of fluid and structural domain this could be easily incorporated in the existing framework.

In this study, a simple 2-D flow model has been considered. To capture the influence of bottom and top structural layers on the flow, refined fluid models need to be applied. Again this could be implemented without changing the overall computational framework. The fluid–solid interfaces are described via a porosity approach, which approximates the flow characteristics sufficiently well for low Reynolds number flows. However, for high Reynolds numbers, the stair-step interface geometry will likely cause problems.

The proposed method describes the structural deformations on a Lagrangian mesh and the flow is predicted on a

fixed Eulerian mesh. While in this paper a hydrodynamic lattice Boltzmann method was used, any finite element or finite volume flow solvers can be integrated into the proposed computational framework. The separation of structure and flow solver allows the use of standard analysis tools. In particular, it circumvents the need for fluid analysis methods capable of operating on moving meshes. However, a mapping method is needed to transform the structural density distribution into a impermeability distribution defining the layout in the undeformed and deformed configurations. In numerical studies the proposed simple geometric mapping approach was shown to be robust and computationally inexpensive.

Three numerical studies on the design of tunable manifolds have demonstrated that the proposed method is well suited for topology optimization of fluid-structure systems. While most micro-fluidic applications are dominated by low Reynolds number flows allowing for a one-sided FSI model, two-way coupling needs to be considered in general.

Acknowledgments The authors acknowledge the support of the National Science Foundation under grant DMI-0348759. The opinions and conclusions presented in this chapter are those of the authors and do not necessarily reflect the views of the sponsoring organization.

References

Aage N, Poulsen TH, Gersborg-Hansen A, Sigmund O (2008) Topology optimization of large scale Stokes flow problems. Struct Multidiscipl Optim 35(2):175–180. doi:10.1007/s00158-007-0128-0

Andreasen SC, Gersborg AR, Sigmund O (2009) Topology optimization of microfluidic mixers. Int J Numer Methods Fluids 61(5):498–513. doi:10.1002/fld.1964

Babuška I (1973) The finite element method with penalty (variational principle with penalty for finite element solution of model Poisson equation with homogeneous Dirichlet boundary conditions, noting convergence). Math Comput 27:221–228

Bar-Cohen Y (2004) Electroactive polymer (EAP) actuators as artificial muscles—reality, potential, and challenges. Bellingham SPIE—The International Society for Optical Engineering

Belytschko T, Liu WK, Moran B (2005) Nonlinear finite elements for continua and structures. Wiley, New York

Bendsøe MP, Sigmund O (2003) Topology optimization: theory, methods and applications. Springer, Heidelberg

Borrvall T, Petersson J (2003) Topology optimization of fluids in Stokes flow. Int J Numer Methods Fluids 41(1):77–107. doi:10.1002/fld.426

Buhl T (2002) Simultaneous topology optimization of structure and supports. Struct Multidiscipl Optim 23(5):336–346. doi:10.1007/s00158-002-0194-2

Chen S, Doolen GD (1998) Lattice Boltzmann method for fluid flows. Annu Rev Fluid Mech 30:329–364

Dimitrov D, Schreve K, de Beer N (2006) Advances in three dimensional printing–state of the art and future perspectives. Rapid Prototyping J 12(3):136–147

Evgrafov A (2006) Topology optimization of slightly compressible fluids. ZAMM 86(1):46–62. doi:10.1002/zamm.200410223

Evgrafov A, Pingen G, Maute K (2008) Topology optimization of fluid domains: kinetic theory approach. ZAMM 88(2):129–141. doi:10.1002/zamm.200700122

Gersborg-Hansen A, Sigmund O, Haber RB (2005) Topology optimization of channel flow problems. Struct Multidiscipl Optim 30(3):181–192. doi:10.1007/s00158-004-0508-7

Guest JK, Prévost JH (2006) Optimizing multifunctional materials: design of microstructures for maximized stiffness and fluid permeability. Int J Solids Struct 43(22–23):7028–7047. doi:10.1016/j.ijsolstr.2006.03.001

Kim H, Lee HBR, Maeng WJ (2009) Applications of atomic layer deposition to nanofabrication and emerging nanodevices. Thin Solid Films 517(8):2563–2580

Klimetzek FR, Paterson J, Moos O (2006) Autoduct: topology optimization for fluid flow. In: Proceedings of Konferenz für angewandte Optimierung. Karlsruhe, Germany

Maute K, Allen M (2004) Conceptual design of aeroelastic structures by topology optimization. Struct Multidiscipl Optim 27: 27–42

Maute K, Reich GW (2006) Integrated multidisciplinary topology optimization approach to adaptive wing design. AIAA J Aircr 43(1):253–263

Moos O, Klimetzek FR, Rossmann R (2004) Bionic optimization of air-guiding systems. In: Proceedings of SAE 2004 world congress & exhibition. Detroit, MI

Niklaus F, Stemme G, Lu J-Q, Gutmann RJ (2006) Adhesive wafer bonding. J Appl Phys 99(3):031101

Othmer C (2008) A continuous adjoint formulation for the computation of topological and surface sensitivities of ducted flows. Int J Numer Methods Fluids 58(8):861–877. doi:10.1002/fld.1770

Othmer C, Klimetzek T, Giering R (2006) Computation of topological sensitivities in fluid dynamics: cost function versatility. In: Proceedings of ECCOMAS CFD. Delft, Netherlands

Pingen G (2008) Optimal design for fluidic systems: topology and shape optimization with the lattice Boltzmann method. PhD thesis, University Of Colorado at Boulder

Pingen G, Evgrafov A, Maute K (2006) Towards the topology optimization of fluid-structure interaction problems with immersed boundary techniques. In: NSF design, service, and manufacturing grantees and research conference, St. Louis, Missouri

Pingen G, Evgrafov A, Maute K (2007a) Topology optimization of flow domains using the lattice Boltzmann method. Struct Multidiscipl Optim 36(6):507–524. doi:10.1007/s00158-007-0105-7

Pingen G, Waidmann M, Evgrafov A, Maute K (2007b) Application of a parametric level-set approach to topology optimization fluid with the Navier–Stokes and lattice Boltzmann equations. In: Proceedings of the 7th world congress of structural and multidisciplinary optimization, 21–25 May 2007, Seoul, Korea, ISSMO

Pingen G, Evgrafov A, Maute K (2009a) Adjoint parameter sensitivity analysis for the hydrodynamic lattice Boltzmann method with applications to design optimization. Comput Fluids 38(4):910–923. doi:10.1016/j.compfluid.2008.10.002

Pingen G, Waidmann M, Evgrafov A, Maute K (2009b) A parametric level-set approach for topology optimization of flow domains. Struct Multidiscipl Optim. doi:10.1007/s00158-009-0405-1

Ramm E, Maute K, Schwarz S (1998a) Adaptive topology and shape optimization. In: Proceedings of 4th world congress on computational mechanics, 29 June–2 July. Mendoza, Argentina, pp 19–38

Ramm E, Maute K, Schwarz S (1998b) Conceptual design by structural optimization. In: Proceedings of EURO-C, 31 March–3 April. Badgastein, Austria, pp 879–896

Spaid MAA, Phelan FR (1997) Lattice Boltzmann methods for modeling microscale flow in fibrous porous media. Phys Fluids 9(9):2468–2474

Stadler W (1988) Multicriteria optimization in engineering and in the sciences. Springer, Heidelberg

Succi S (2001) The lattice Boltzmann equation: for fluid dynamics and beyond. Oxford University Press, Oxford

Svanberg K (1995) A globally convergent version of MMA without linesearch. In: Proceedings of the first world congress of structural and multidisciplinary optimization, 28 May–2 June 1995, pp 9–16, Goslar, Germany

Yoon GH (2009) Topology optimization for stationary fluid-structure interaction problems using a new monolithic formulation. In: Proceedings of 8th world congress on structural and multidisciplinary optimization, Lisbon, Portugal

Yu D, Mei R, Luo LS, Shyy W (2003) Viscous flow computations with the method of lattice Boltzmann equation. Prog Aerosp Sci 39(5):329–367. doi:10.1016/S0376-0421(03)00003-4

Zhang XQ, Lowe C, Wissler M, Jahne B, Kovacs G (2005) Dielectric elastomers in actuator technology. Adv Eng Mater 7(5): 361–367

Appendix C

Publication [P3]: Topology Optimization for Unsteady Flow

INTERNATIONAL JOURNAL FOR NUMERICAL METHODS IN ENGINEERING
Int. J. Numer. Meth. Engng 2011; **87**:1229–1253
Published online 1 March 2011 in Wiley Online Library (wileyonlinelibrary.com). DOI: 10.1002/nme.3151

Topology optimization for unsteady flow

Sebastian Kreissl[1], Georg Pingen[2] and Kurt Maute[1,*,†]

[1]*Center for Aerospace Structures, University of Colorado at Boulder, Boulder, CO, U.S.A.*
[2]*Department of Engineering, Union University, Jackson, TN, U.S.A.*

SUMMARY

A computational methodology for optimizing the conceptual layout of unsteady flow problems at low Reynolds numbers is presented. The geometry of the design is described by the spatial distribution of a fictitious material with continuously varying porosity. The flow is predicted by a stabilized finite element formulation of the incompressible Navier–Stokes equations. A Brinkman penalization is used to enforce zero-velocities in solid material. The resulting parameter optimization problem is solved by a non-linear programming method. The paper studies the feasibility of the material interpolation approach for optimizing the topology of unsteady flow problems. The derivation of the governing equations and the adjoint sensitivity analysis are presented. A design-dependent stabilization scheme is introduced to mitigate numerical instabilities in porous material. The emergence of non-physical artifacts in the optimized material distribution is observed and linked to an insufficient resolution of the flow field and an improper representation of the pressure field within solid material by the Brinkman penalization. Two numerical examples demonstrate that the designs optimized for unsteady flow differ significantly from their steady-state counterparts. Copyright © 2011 John Wiley & Sons, Ltd.

Received 20 September 2010; Revised 5 January 2011; Accepted 11 January 2011

KEY WORDS: Navier–Stokes flow; Brinkman penalization; finite element formulation; stabilization; adjoint sensitivity analysis; non-linear programming

1. INTRODUCTION

A broad class of fluidic systems is dominated by unsteady flows, such as systems involving accelerating/decelerating flows, time-varying boundary conditions, and dynamic instabilities. Specific examples include unsteady flows due to the opening/closing of valves, pulsating flows due oscillatory inflow conditions in pumps, and vortex shedding [1–4]. In such cases, using steady-state flow models in the design process may lead to sub-optimal solutions; instead the unsteady nature of the flow needs to be considered. In this paper, we present a methodology to optimally design the layout and shape for unsteady flow problems.

In contrast to the large body of work on optimizing flow problems under steady-state conditions [5, 6], there are only few studies on design optimization methods considering unsteady flows. For example, Mani and Mavriplis [7] considered unsteady effects of compressible flows for design optimization. Homescu *et al.* [8] applied optimization strategies to suppress vortex shedding of a flow around a cylinder. Rumpfkeil and Zingg [9, 10] optimized the shape of an airfoil along with control parameters for unsteady external flows.

*Correspondence to: Kurt Maute, Center for Aerospace Structures, University of Colorado at Boulder, Boulder, CO, U.S.A.
†E-mail: maute@colorado.edu

Figure 1. Shape vs topology optimization of a channel: (a) initial design; (b) shape-optimized design; and (c) topology-optimized design.

The above-mentioned studies all focus on shape optimization problems that are limited to changes in the shape of boundaries present in the initial design, as shown in Figure 1. Shape optimization is well suited to fine-tune an existing close-to-optimal design. To find conceptually novel designs without the need for a well-defined initial guess, topology optimization has shown great promise as an engineering design tool [11]. The underlying idea of topology optimization is to describe the geometry of a body via its material distribution. By varying the material distribution the geometry of the design can be altered conceptually, i.e. fluid/solid interfaces can be created or merged, see Figure 1(c). To allow for a smooth transition between fluid and solid states, a fictitious material with continuously varying porosity is typically introduced.

Fluid topology optimization was pioneered by Borrvall and Petersson [12] for Stokes flows. Guest and Prévost [13] conducted fluid topology optimization using a Darcy–Stokes flow model. Challis and Guest [14] used a level set parameterization of the material distribution to solve Stokes flow problems. The work on Stokes models was extended to Navier–Stokes (NS) models [15–18]. Othmer *et al.* optimized the layout of 3D airduct manifolds for automotive applications employing an incompressible NS model [19, 20]. As an alternative to the NS flow model, Pingen *et al.* used the lattice Boltzmann method (LBM) for solving fluid topology optimization problems [21, 22]. Kreissl *et al.* [23] employed the LBM in combination with a level set-based geometric interface representation for generalized shape optimization of fluids.

So far topology optimization has only been applied to steady-state fluid problems, although a wide range of engineering applications involves unsteady flows. Furthermore, optimization strategies based on steady-state flow models are generally limited to small Reynolds numbers. At higher Reynolds numbers, even if a steady-state flow solution exists for the initial and optimum design, unsteady flow may be present in intermediate designs that are generated in the course of the optimization process. In this case, the inability of describing unsteady flows by steady-state models often prevents the optimization process to converge [22]. To consider a broader class of flow problems, unsteady flow models need to be integrated into optimization methods.

The current study focuses on the topology optimization of fluidic devices with unsteady flows, i.e. the flow is assumed to vary over time and is not necessarily limited to oscillatory variations. The flow response is predicted by a streamline-upwind/Pedrov–Galerkin (SUPG), pressure-stabilizing/Pedrov–Galerkin (PSPG) finite element (FE) formulation of the incompressible NS equations [24] and an implicit time integration scheme. Following a fictitious material approach the elemental porosities are treated as design variables. Flow through porous material is modeled via a Brinkman penalization, which enforces zero-velocities in solid material [25].

The optimization problems of interest can be written in time-discrete form as follows:

$$\begin{aligned}
\min_{s} \quad & Z(\mathbf{f}^0,\ldots,\mathbf{f}^{N_t},\mathbf{s}) \;= \mathscr{Z}\left(\sum_{n=0}^{N_t} z^n(t^n,\mathbf{f}^n,\mathbf{s})\right),\\
\text{s.t.} \quad & H_j(\mathbf{f}^0,\ldots,\mathbf{f}^{N_t},\mathbf{s}) = \mathscr{H}_j\left(\sum_{n=0}^{N_t} h_j^n(t^n,\mathbf{f}^n,\mathbf{s})\right)=0 \quad \forall j=1,\ldots,N_h, \qquad (1)\\
& G_j(\mathbf{f}^0,\ldots,\mathbf{f}^{N_t},\mathbf{s}) = \mathscr{G}_j\left(\sum_{n=0}^{N_t} g_j^n(t^n,\mathbf{f}^n,\mathbf{s})\right)\geqslant 0 \quad \forall j=1,\ldots,N_g,
\end{aligned}$$

DOI: 10.1002/nme

where $\mathbf{s}$ is the vector of design variables and $\mathbf{f}^n$ is the vector of fluid-state variables satisfying the discretized governing equations $\mathbf{R}^n_{\text{dyn}}$ at the time steps $n=0,\ldots,N_t$. The objective Z is a differentiable function $\mathscr{Z}$ that depends on the sum of the contributions, z^n, from all time steps. The equality and inequality constraints are denoted by H_j and G_j, respectively, and have the same functional form as Z. The above parameter optimization problem (1) is solved by a non-linear programming method. The gradients of objective and constraints are computed by an adjoint method.

The key challenges of the optimization approach outlined above include (a) the accuracy and stability of the numerical fluid model in dependence of the material layout and (b) the costs of computing the flow and adjoint solutions accumulated over the optimization process. While the latter aspect deserves attention especially for large numerical models, this study focuses on the interplay between describing the geometry via a Brinkman penalization and the flow prediction. Usually, the Brinkman penalization is used to approximate flow through porous material. In topology optimization, we seek to enforce zero-velocities in solid material, i.e. in regions where the solid volume fraction is one. For optimization problems at steady-state conditions and very low Reynolds numbers ($Re\approx 1$), using a Brinkman approach has shown satisfying results. In this study, we consider unsteady flows at Reynolds numbers between 100 and 1000. For such problems we will show that the Brinkman approach can suffer from numerical instabilities and may lead to non-physical artifacts in the optimized material layout. These issues are due to (a) a detrimental interaction between the SUPG-stabilization technique and the Brinkman term, (b) an insufficient spatial resolution of the flow fields, in particular within porous regions, and (c) the improper representation of pressure fields in solid material by the Brinkman approach.

In this paper, we will discuss these numerical issues and propose methods to mitigate them. In Section 2 the stabilized FE formulation of the incompressible NS equations with Brinkman penalization is outlined. The features of the Brinkman approach in the context of topology optimization are studied in Section 3. Section 4 presents the adjoint sensitivity analysis. In Section 5 the key features of the proposed approach are demonstrated with two 2D numerical examples. The main results are summarized in Section 6.

2. FINITE ELEMENT-BASED INCOMPRESSIBLE NAVIER–STOKES FORMULATION

For a given design, the unsteady flow field is predicted by an FE formulation of the incompressible NS equations:

$$\text{Momentum equation:}\quad \hat{\rho}\left(\frac{\partial \hat{v}_i}{\partial \hat{t}}+\frac{\partial \hat{v}_i}{\partial \hat{x}_j}\hat{v}_j\right)+\hat{\alpha}\hat{v}_i=\frac{\partial \hat{\sigma}_{ij}}{\partial \hat{x}_j}+\hat{f}_i^B, \tag{2}$$

$$\text{Incompressibility condition:}\quad \frac{\partial \hat{v}_i}{\partial \hat{x}_i}=0, \tag{3}$$

where $\hat{\rho}$, $\hat{v}$, $\hat{t}$ describe the dimensional density, velocity, and time, respectively. The subscripts i, j define the spatial directions. The external body forces are denoted by $\hat{f}_i^B$; for the sake of brevity $\hat{f}_i^B$ is assumed to be zero and dropped in the following derivations. The stress tensor $\hat{\sigma}_{ij}$ is defined as

$$\hat{\sigma}_{ij}=-\hat{p}\delta_{ij}+2\hat{\mu}\frac{1}{2}\left(\frac{\partial \hat{v}_i}{\partial \hat{x}_j}+\frac{\partial \hat{v}_j}{\partial \hat{x}_i}\right), \tag{4}$$

where $\hat{p}$ and $\hat{\mu}$ describe the dimensional pressure and dynamic viscosity. The Brinkman term, $\hat{\alpha}\hat{v}_i$, scales the velocities based on the design-dependent scalar $\hat{\alpha}$ that characterizes the local porosity. Details on the Brinkman method will be presented in Section 3.

DOI: 10.1002/nme

After integration by parts of $\partial\hat{\sigma}_{ij}/\partial\hat{x}_j$ and transformation to non-dimensional variables, the weak form of the governing Equations (2) and (3) can be written as follows:

$$\underbrace{\int_\Omega w_i \rho \frac{\partial v_i}{\partial t}\,\mathrm{d}\Omega}_{\text{inertia}} + \underbrace{\int_\Omega w_i \rho \frac{\partial v_i}{\partial x_j} v_j\,\mathrm{d}\Omega}_{\text{convective}} - \underbrace{\int_\Omega \frac{1}{2}\left(\frac{\partial w_i}{\partial x_j}+\frac{\partial w_j}{\partial x_i}\right) p\delta_{ij}\,\mathrm{d}\Omega}_{\text{pressure}}$$
$$+ \underbrace{\int_\Omega \frac{1}{2}\left(\frac{\partial w_i}{\partial x_j}+\frac{\partial w_j}{\partial x_i}\right) 2\mu\frac{1}{2}\left(\frac{\partial v_i}{\partial x_j}+\frac{\partial v_j}{\partial x_i}\right)\mathrm{d}\Omega}_{\text{shear}} + \underbrace{\int_\Omega w_i \alpha v_i \Omega}_{\text{Brinkman}} + \underbrace{\int_\Omega q\frac{\partial v_i}{\partial x_i}\,\mathrm{d}\Omega}_{\text{continuity}}$$
$$- \underbrace{\int_\Gamma w_i n_j\left(-p\delta_{ij}+2\mu\frac{1}{2}\left(\frac{\partial v_i}{\partial x_j}+\frac{\partial v_j}{\partial x_i}\right)\right)\mathrm{d}\Gamma}_{\text{boundary}} = 0, \tag{5}$$

where w_i is a velocity test function and q a pressure test function. The non-dimensional dynamic viscosity is defined as

$$\mu = \frac{\hat{\mu}}{\hat{L}_{\text{ref}}\hat{v}\hat{\rho}} = \frac{1}{Re}, \tag{6}$$

where $\hat{L}_{\text{ref}}$, $\hat{v}$, $\hat{\rho}$ are the dimensional reference length, reference velocity, reference density and Re is the Reynolds number. The nodal static residual vector of the volume terms is defined as:

$$\mathbf{R}_s^\Omega = \left\{ \begin{array}{c} \displaystyle\int_\Omega \left(w_i \rho\left(\frac{\partial v_i}{\partial x_j} v_j\right) + \frac{1}{2}\left(\frac{\partial w_i}{\partial x_j}+\frac{\partial w_j}{\partial x_i}\right)\sigma_{ij} + w_i \alpha v_i \right)\mathrm{d}\Omega \\ \displaystyle\int_\Omega q\frac{\partial v_i}{\partial x_i}\,\mathrm{d}\Omega \end{array} \right\} \in \Re^{3\times 1}. \tag{7}$$

The contribution from the boundary term to the nodal static residual is given by:

$$\mathbf{R}_s^\Gamma = \left\{ \begin{array}{c} \displaystyle\int_\Gamma w_i n_j\left(-p\delta_{ij}+2\mu\frac{1}{2}\left(\frac{\partial v_i}{\partial x_j}+\frac{\partial v_j}{\partial x_i}\right)\right)\mathrm{d}\Gamma \\ 0 \end{array} \right\} \in \Re^{3\times 1}. \tag{8}$$

Based on Equations (7) and (8), the elemental static residual can be written as

$$\mathbf{R}_s^e = \mathfrak{A}(\mathbf{R}_s^\Omega + \mathbf{R}_s^\Gamma), \tag{9}$$

where $\mathfrak{A}$ defines an assembly operator. The contribution from the inertia term will be considered later. In this study, the velocity and pressure fields are approximated piecewise linearly by a bilinear, equal-order-interpolation, four-node velocity–pressure Q1Q1-element [24].

2.1. Stabilization

The standard Galerkin FE formulation of the incompressible flow equations suffers from two forms of numerical instabilities [26]: (I) *velocity oscillations* due to the advective term in the NS equation, and (II) *pressure oscillations* in the case of an inappropriate combination of interpolation functions for the velocity and the pressure [24]. Since the Q1Q1-element uses the same interpolation order for velocity and pressure, both instabilities have to be addressed. We employ the SUPG formulation to prevent spurious node-to-node oscillations in the velocity field (I) [24]. To inhibit pressure oscillations (II), the PSPG scheme is used.

DOI: 10.1002/nme

The SUPG and PSPG stabilization parameters are computed following the work by Tezduyar *et al.* [24]

$$\tau_{\mathrm{SUPG}} = \frac{h}{2\|\mathbf{v}^{\mathrm{gp}}\|} r(Re_v), \tag{10}$$

$$\tau_{\mathrm{PSPG}} = \frac{h^{\#}}{2\|\mathbf{V}\|} r(Re_V^{\#}), \tag{11}$$

where $\mathbf{v}^{\mathrm{gp}}$ is the local velocity, defined at every Gauss-integration-point, $\|\mathbf{V}\|$ is the norm of the so-called 'global scaling velocity' [24] which is set to a constant value of 10^{-6}. Based on those local velocities, the elemental Reynolds numbers Re_v and $Re_V^{\#}$ are defined as

$$Re_v = \frac{\|\mathbf{v}^{\mathrm{gp}}\| h}{2\nu}, \tag{12}$$

$$Re_V^{\#} = \frac{\|\mathbf{V}\| h^{\#}}{2\nu}, \tag{13}$$

where ν describes the kinematic viscosity. The 'element lengths', h and $h^{\#}$, are computed by:

$$h = 2\left(\sum_{a=1}^{4} \left| \frac{\mathbf{v}^a}{\|\mathbf{v}^a\|} \cdot \nabla N_a \right| \right)^{-1}, \tag{14}$$

$$h^{\#} = 2\sqrt{\frac{A_e}{\pi}}. \tag{15}$$

In Equations (14) and (15), N_a is the shape function associated with node a and A_e is the area of the element. The function $r(Re)$ used in Equations (10) and (11) is defined as:

$$r(Re) = \begin{cases} Re/3 & \text{if } 0 \leqslant Re \leqslant 3, \\ 1 & \text{if } Re > 3. \end{cases} \tag{16}$$

The graph in Figure 2 illustrates the dependency of the SUPG-stabilization parameter τ_{SUPG} on the velocity for a given streamline element length h, cp. Equation (10). Owing to the structure of the function $r(Re)$, Equation (16), the velocity cancels out for elemental Reynolds numbers

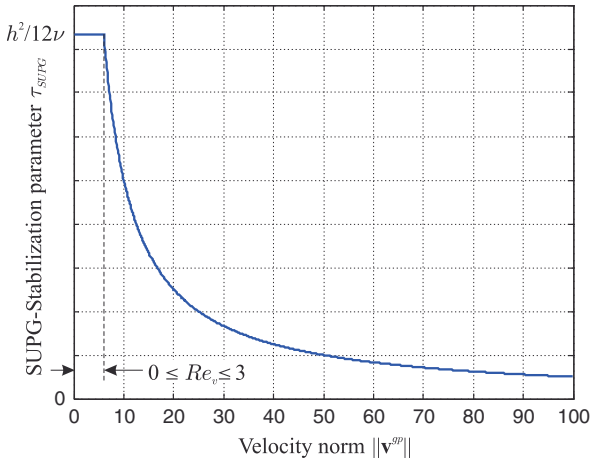

Figure 2. SUPG-stabilization parameter τ_{SUPG}.

DOI: 10.1002/nme

less than three, hence $\tau_{\mathrm{SUPG}}=h^2/12v$ for $0\leqslant Re_v\leqslant 3$. For elemental Reynolds numbers larger than three, $r(Re_v)=1$ and therefore $\tau_{\mathrm{SUPG}}=h/(2\|\mathbf{v}^{\mathrm{gp}}\|)$ for $Re_v>3$.

Given the stabilization parameters τ_{SUPG} and τ_{PSPG}, Equation (5) is modified by adding a stabilization term:

$$\int_\Omega \left(w_i \rho \left(\frac{\partial v_i}{\partial t} + \frac{\partial v_i}{\partial x_j} v_j \right) + \frac{1}{2} \left(\frac{\partial w_i}{\partial x_j} + \frac{\partial w_j}{\partial x_i} \right) \sigma_{ij} + w_i \alpha v_i + q \frac{\partial v_i}{\partial x_i} \right) \mathrm{d}\Omega - \int_\Gamma w_i n_j \sigma_{ij} \, \mathrm{d}\Gamma$$

$$+ \sum_{e=1}^{n_{el}} \int_{\Omega_e} \frac{1}{\rho} \left(\tau_{\mathrm{SUPG}} \rho \frac{\partial w_i}{\partial x_j} v_j + \tau_{\mathrm{PSPG}} \frac{\partial q}{\partial x_i} \right) \left(\rho \left(\frac{\partial v_i}{\partial t} + \frac{\partial v_i}{\partial x_j} v_j \right) - \frac{\partial \sigma_{ij}}{\partial x_i} + \alpha v_i \right) \mathrm{d}\Omega = 0. \quad (17)$$

The elemental static residual vector of the stabilized system can be derived analogous to Equations (5)–(9) and the contribution from the stabilized inertia term will be discussed below.

2.2. Time integration

The temporal evolution of the flow fields is predicted by an implicit time-marching scheme. For the sake of simplicity, a standard backward Euler scheme is considered here. The time derivative of the fluid-state vector $\mathbf{f}$ is approximated as follows:

$$\dot{\mathbf{f}} = \frac{\mathbf{f}^n - \mathbf{f}^{n-1}}{\Delta t} \quad \text{with } \mathbf{f}^0 = \bar{\mathbf{f}}, \quad (18)$$

where the superscript n indicates the time step, Δt is the time step size, and $\bar{\mathbf{f}}$ is the initial condition. The dynamic residual is computed as

$$\begin{aligned} \mathbf{R}^0_{\mathrm{dyn}} &= \mathbf{f}^0 - \bar{\mathbf{f}}, \\ \mathbf{R}^n_{\mathrm{dyn}} &= \mathbf{M}^n \dot{\mathbf{f}} + \mathbf{R}^n_s \quad \forall n = 1, \ldots, N_t, \end{aligned} \quad (19)$$

where $\mathbf{R}^n_s$ is the static residual. The mass matrix collects the contributions of the inertia terms in Equations (5) and (17), respectively.

3. BRINKMAN PENALIZATION FOR NAVIER–STOKES FLOW

In topology optimization the geometry of a body is typically defined via its material distribution. For fluid topology optimization, the most common approach is to enforce the boundary conditions along the fluid–solid interface and within the solid via a Brinkman penalization. In contrast to methods using the Brinkman approach to approximate flow through real porous material, here a fictitious porous material is used as a vehicle for continuously interpolating between fluid and solid states in the course of the optimization process. For flow problems, the optimization process converges typically to material distributions composed of mostly fluid and solid states. Thus, the Brinkman penalization should (a) represent the correct flow fields in the fluid and solid regions and (b) lead to a smooth transition of flow fields as the porosity is changing.

The porosity of the material is represented by the scalar α in the non-dimensional form of the NS equations, Equation (5), and can be thought of as a measure of the impermeability of the material: for a value of $\alpha \gg 1$, i.e. high impermeability (solid material), the velocity v_i vanishes in order for Equation (5) to be satisfied. Contrary, for a value of $\alpha = 0$, i.e. zero impermeability (fluid material), the Brinkman term vanishes, leading to the standard incompressible NS formulation.

Gersborg-Hansen *et al.* [15] employed an analogous velocity penalization. However, in their study the scalar α is based on the lubrication approximation and controls the distance between two plates separated by fluid. In addition to the Brinkman term, Seo [27] also used an impermeability-dependent viscosity for the material interpolation. Following the work by Borrvall and Peterson [12], the current study chooses a convex interpolation function α

$$\alpha(s) = \overline{\alpha} + (\underline{\alpha} - \overline{\alpha}) s \frac{1 + p_\alpha}{s + p_\alpha} \quad \text{with } 0 \leqslant s \leqslant 1, \quad (20)$$

DOI: 10.1002/nme

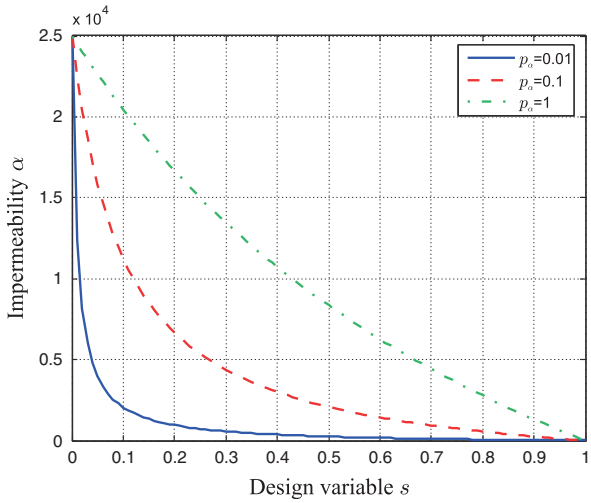

Figure 3. Impermeability interpolation.

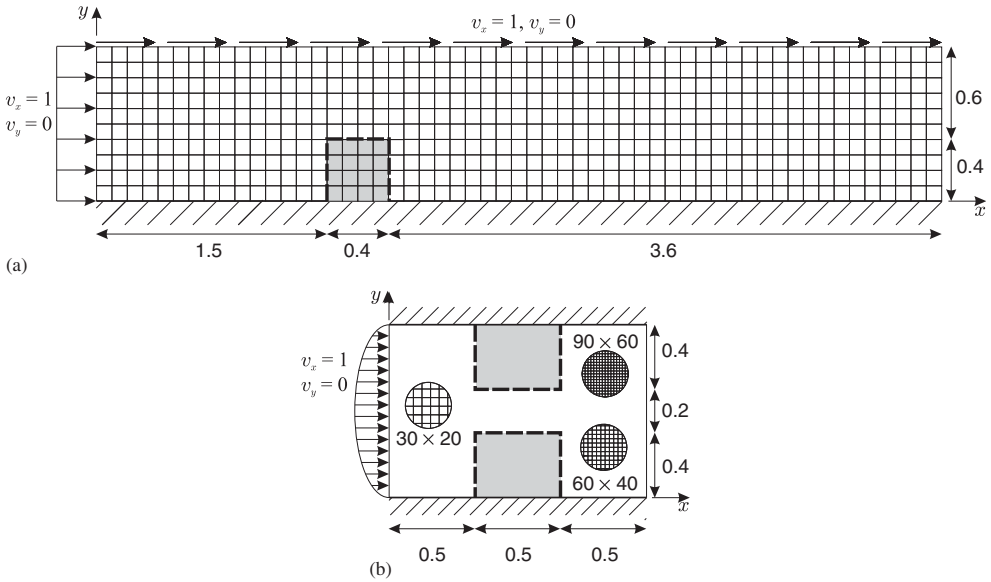

Figure 4. Example configurations considered in the following studies (dashed lines indicate fluid–solid interfaces): (a) step [28, 29] and (b) necking.

where $\underline{\alpha}$, $\overline{\alpha}$ are the lower and upper limits, s defines the optimization variable, and p_α is a penalty parameter that allows to control the amount of elements with intermediate impermeabilities in the optimal design. For large p_α-values the interpolation becomes more linear cp. Figure 3, leading to less intermediate impermeabilities (‘gray’ elements) [12].

In the following subsection, we will discuss the suitability of the Brinkman approach for topology optimization of unsteady flows. We will illustrate various aspects with two examples shown in Figure 4. The dashed lines indicate the fluid–solid interface. The gray areas, indicating solid material, will be represented either by a Brinkman approach or by a body-fitted mesh; in the latter case, the gray areas are not part of the computational domain. The inflow conditions for

DOI: 10.1002/nme

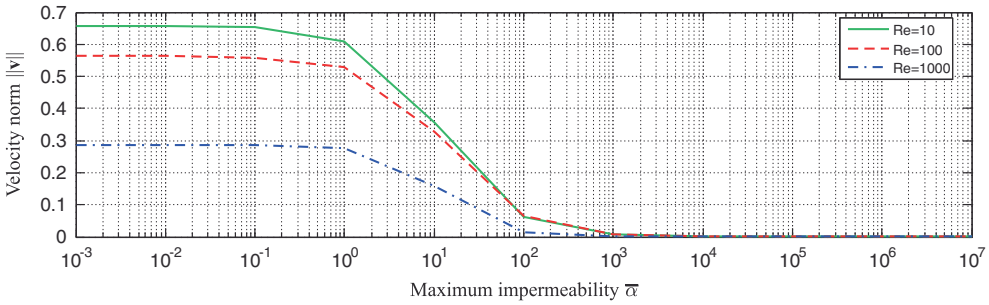

Figure 5. Velocity penalization, with $\underline{\alpha}=0$ and varying $\overline{\alpha}$ (based on configuration in Figure 4(a)).

the step problem in Figure 4(a) are a plug flow in the x-direction at the left edge and prescribed velocities along the top edge. For this example, we only consider one mesh with 55 elements in the x-direction and 10 elements in the y-direction. The inflow condition for the necking example in Figure 4(b) is a parabolic velocity profile. We will consider constant and time-varying inlet velocities. For this example different levels of mesh refinement are considered, indicated by the gridded circles in Figure 4(b). Both problems have traction-free outlet conditions [30].

3.1. Velocity penalization

The flow velocities within solid material and along the fluid/solid interface need to vanish. To study the ability of the Brinkman approach to enforce these conditions, we consider the step example depicted in Figure 4(a) and compute the flow solution for $Re=10$, $Re=100$, and $Re=1000$ after three time steps with $v_{\text{in}}=1$ and $\Delta t=0.1$. We vary the impermeability α, which is uniform in the porous domain, i.e. within the step. The velocity norm at the center of the gray area is plotted over the impermeability α in Figure 5. Note that the results are presented in non-dimensional form. The graphs illustrate that values of $\alpha\approx 10^4$ are necessary to drive the velocity norm $\|\mathbf{v}\|<10^{-3}$. Borrvall and Petersson [12] as well as Khadra *et al.* [31] propose a maximum impermeability $\overline{\alpha}$ that is dependent on the Reynolds number. However, the graphs in Figure 5 suggest that for all three Reynolds numbers a maximum impermeability of $\alpha>10^4$ is sufficient to enforce the zero-velocity condition. Therefore, we choose a Reynolds number-independent maximum impermeability of $\overline{\alpha}=2.5\times 10^4$ for the examples studied in this paper; the lower limit is set to $\underline{\alpha}=0$.

3.2. Treatment of pressure field in solid material

As can be seen from the momentum equation (2), the Brinkman approach only penalizes velocities but does not explicitly control the pressure. Therefore, the pressure is continuous across the solid material, cp. [28]. We revisit the example problem in Figure 4(b) to illustrate this issue and compare the pressure for a body-fitted and for a Brinkman-based configuration. The graphs in Figure 6 plot the pressure along $y=1/2$ and $y=3/4$ for two levels of mesh refinement. The graphs for the body-fitted and Brinkman-based configuration show a qualitative agreement. Note that no pressure values are computed in solid domain when using a body-fitted mesh. Comparing Figure 6(a) and (b) indicates that the difference between the Brinkman and the body-fitted configuration decreases as the mesh is refined. Furthermore, the figures illustrate that within the (porous) solid domain, the Brinkman approach leads to a continuous pressure distribution.

For modeling flow through porous material with a solid volume fraction of less than one the pressure field in the porous region can be considered physical. However, the current study uses the porosity approach only as a vehicle. Ideally, the solid material should be completely impermeable for both convective mass transport and pressure diffusion. The inability of the Brinkman approach to prevent pressure diffusion may lead to errors in the flow prediction. In the context of topology optimization and depending on the setup of the optimization problem, we observed that erroneous

DOI: 10.1002/nme

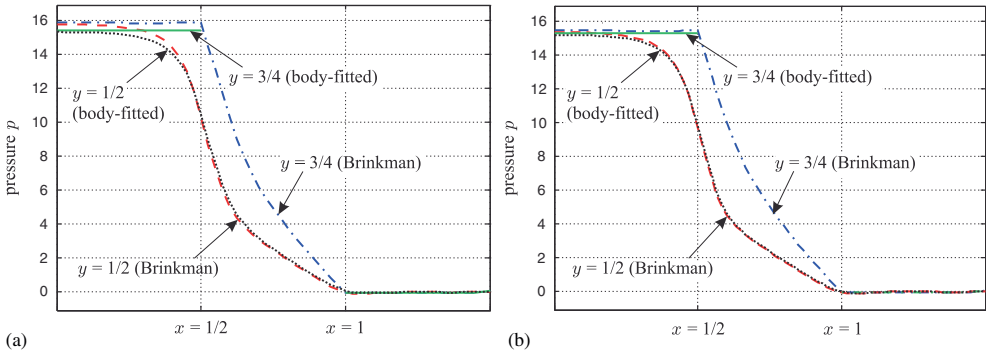

Figure 6. Pressure gradient in solid material (based on configuration in Figure 4(b)): (a) 60×40 mesh and (b) 90×60 mesh.

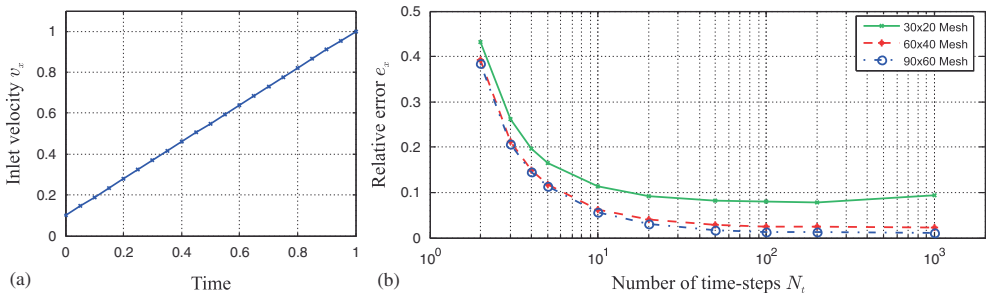

Figure 7. Error between porous boundary representation and body-fitted mesh (based on configuration in Figure 4(b)): (a) inlet velocity ramp (here $N_t = 20$) and (b) error.

pressure fields within the solid domains may lead to non-physical artifacts in the final design, especially if the computational mesh is coarse. This issue will be revisited in Section 5.3.

3.3. Temporal and spatial refinement

For topology optimization of steady-state flows at very low Reynolds numbers, $Re \approx 1$, the accuracy of the Brinkman penalization has been verified in numerous studies [12, 13, 21]. Here, we study the spatial and temporal accuracy of the Brinkman penalization for unsteady flow problems. We compare the results of a porosity-based geometry representation with those of a body-fitted mesh for different time step sizes Δt and grid sizes Δx.

We consider the necking problem depicted in Figure 4(b). The inlet velocity is ramped up from $v_x = 0.1$ to $v_x = 1$ over a period of $T = 1$, see Figure 7(a). The maximum inlet velocity corresponds to a Reynolds number of $Re = 100$. For the porosity-based design, we set the impermeability of the solid elements to $\alpha = \overline{\alpha}$ and the remainder to $\underline{\alpha}$. We study three levels of mesh refinement: $nx \times ny = 30 \times 20$, 60×40, and 90×60, where nx, ny is the number of elements in the x-direction and y-direction, respectively. Keeping the overall simulation time constant, $T = N_t \cdot \Delta t = 1$, we consider different time step sizes $\Delta t = 1/N_t$ by changing the number of time steps N_t. We monitor the x-velocity of the porosity-based configurations, $\mathbf{v}_x^{pN_t}$, at all N_t time steps and compute the error relative to the solution using a body-fitted mesh with highest temporal resolution ($N_t = 1000$), $\mathbf{v}_x^{b1k}$:

$$e_x(N_t) = \frac{\sum_{n=1}^{N_t} \left\| \mathbf{v}_x^{pN_t}\left(n\frac{T}{N_t}\right) - \mathbf{v}_x^{b1k}\left(n\frac{T}{N_t}\right) \right\|}{\sum_{n=1}^{N_t} \left\| \mathbf{v}_x^{b1k}\left(n\frac{T}{N_t}\right) \right\|} 100 \quad \text{for } N_t = 2, 3, 4, 5, 10, 50, 100, 200, 1000. \tag{21}$$

DOI: 10.1002/nme

The relative error e_x is plotted over the number of time steps N_t for different spatial resolutions in Figure 7(b). As the number of time steps N_t increases, i.e. Δt decreases, the relative error between the porous and the body-fitted representation decreases. The graphs further illustrate that relative error decreases as the mesh is refined. The reduction in the error due to the spatial refinement becomes more pronounced when smaller time steps are used.

This study suggests that in the context of topology optimization the employed Brinkman approach is well suited to predict the flow fields of unsteady flow problems. However, small time steps and a refined mesh are necessary to obtain accurate results. Note that the (porous) solid domain in the present example is rather bulky and therefore the inability of the Brinkman approach to prevent pressure diffusion through solid material does not lead to noticeable errors.

3.4. Brinkman penalization and SUPG stabilization

The presence of the Brinkman term in the stabilized FE formulation of the incompressible NS equations leads to two interesting numerical phenomena: (a) a 'stabilizing' effect that unlike e.g. SUPG stabilization leads to incorrect flow predictions and (b) the occurrence of numerical instabilities in porous regions for which we present a remedy.

In numerical studies, we have observed that the contribution from a Brinkman term with $\alpha > 0$ can be sufficient for suppressing velocity oscillations even when no SUPG stabilization is applied. However, we will show with an example that this, unlike the SUPG stabilization, may drastically change the physics of the system. We revisit the step example depicted in Figure 4(a) considering a steady-state flow at a Reynolds number of $Re = 250$, cp. [29, 32]. A comparison between the x-velocities (I) without SUPG stabilization and without Brinkman penalization ($\tau_{\mathrm{SUPG}} = 0, \alpha = 0$), (II) without SUPG stabilization and with Brinkman penalization ($\tau_{\mathrm{SUPG}} = 0, \alpha = 1$) as well as (III) with SUPG stabilization and without Brinkman penalization ($\tau_{\mathrm{SUPG}} \neq 0, \alpha = 0$) is depicted in Figure 8.

The graph for case (I) shows velocity oscillations in the area in front of the step. These oscillations can be suppressed by adding a Brinkman penalization with $\alpha = 1$ for all elements, case (II). Finally, the graph for case (III) shows the x-velocity for a SUPG-stabilized system without Brinkman penalization. Comparing the velocities for (II) and (III) demonstrates that velocity oscillations can be suppressed by a Brinkman term; however, the resulting solution differs significantly from the actual physical solution, case (III). Therefore, the Brinkman penalization should not be used to 'stabilize' the flow equations, for example by choosing a large value for the lower limit, $\underline{\alpha}$, in Equation (20).

According to Seo [27], who conducted topology optimization for steady-state flows, large impermeabilities can result in localized velocity oscillation at the fluid–solid interface. Numerical studies conducted by the authors confirmed these issues: for a non-zero Brinkman term the flow solution diverges if the stabilization parameters are computed according to Equations (10) and (11). To investigate this phenomenon we revisit the porosity-based configuration depicted in Figure 4(b),

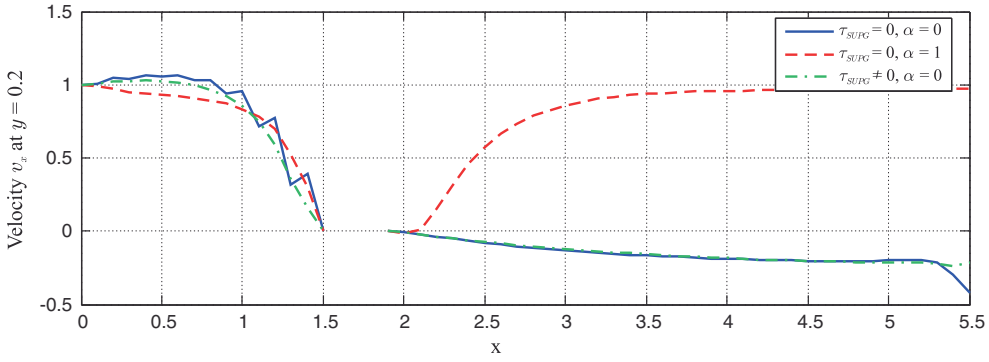

Figure 8. Stabilizing effect of τ_{SUPG} and α; the results are computed for configuration in Figure 4(a).

DOI: 10.1002/nme

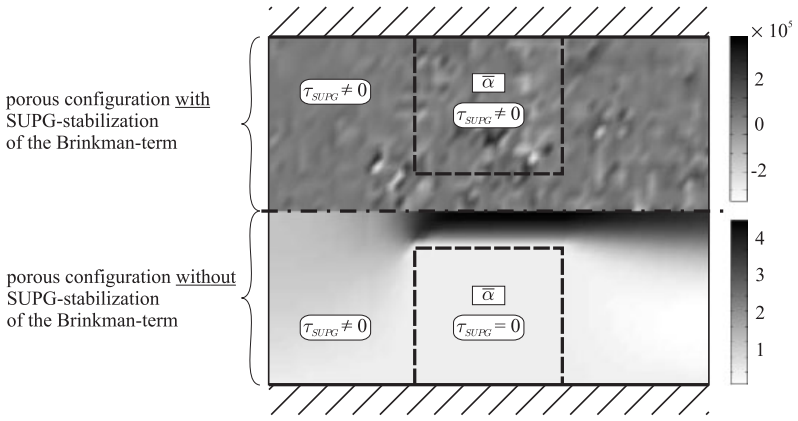

Figure 9. Contours of horizontal velocity v_x with and without SUPG stabilization of the Brinkman term, cp. Figure 4(b) with 60×40 mesh.

for a steady-state flow with $Re = 100$. The solution diverges if the stabilization is computed according to Equation (17). However, the solution converges if the Brinkman term is not SUPG-stabilized, cp. Figure 9. This observation suggests that the divergence is related to the SUPG stabilization of the Brinkman term.

As an alternative to simply removing the Brinkman term from the SUPG-residual, which leads to a mathematically inconsistent formulation, we introduce an impermeability-dependent 'SUPG-switch', $c_{\mathrm{SUPG}}(\alpha)$. This switch cancels the SUPG stabilization if the impermeability exceeds a threshold while ensuring a mathematically consistent system. Replacing τ_{SUPG} in Equation (17) with the product

$$\tau^*_{\mathrm{SUPG}} = c_{\mathrm{SUPG}}(\alpha)\tau_{\mathrm{SUPG}} \tag{22}$$

effectively mitigates the convergence issues due to velocity oscillations. This 'SUPG-switch', $c_{\mathrm{SUPG}}(\alpha)$, should not be confused with the switch $r(Re)$ in Equation (16): both are necessary for the solution to converge. To guarantee the differentiability of the 'SUPG-switch' with respect to the design variables, a smoothened Heaviside-function is employed for $c_{\mathrm{SUPG}}(\alpha)$

$$c_{\mathrm{SUPG}}(\alpha) = \begin{cases} 1 & \text{if } \alpha < \alpha_t, \\ 0.5 + 0.5 \sin\left(\left(\dfrac{\alpha_t - \alpha}{\alpha_{\mathrm{bw}}} + 0.5\right)\pi\right) & \text{if } \alpha_t \leqslant \alpha \leqslant \alpha_t + \alpha_{\mathrm{bw}}, \\ 0 & \text{if } \alpha > \alpha_t + \alpha_{\mathrm{bw}}, \end{cases} \tag{23}$$

where α_t defines the impermeability threshold and α_{bw} the bandwidth of the smoothened Heaviside-function, cp. Figure 10. We achieved the best results with small values for both α_t and α_{bw}: $\alpha_t = \alpha_{\mathrm{bw}} = 10^{-4}$.

To illustrate the effect of the impermeability-dependent 'SUPG-switch', $c_{\mathrm{SUPG}}(\alpha)$, we analyze the step problem depicted in Figure 4(a) considering a steady-state flow at a Reynolds number of $Re = 250$ [32]. The solid domain in Figure 4(a) is assigned an intermediate impermeability of $\alpha = 100$, the remainder of the domain is 100% fluid, i.e. $\alpha = \underline{\alpha} = 0$. The graphs in Figure 11 show a comparison of the velocity in the x-direction, v_x, for (I) the body-fitted mesh, (II) a porosity-based configuration with a constant $c_{\mathrm{SUPG}} = 1$, i.e. τ_{SUPG} is not rescaled and (III) a porosity-based configuration with an impermeability-dependent $c_{\mathrm{SUPG}} = c_{\mathrm{SUPG}}(\alpha)$. As can be seen from the graphs, v_x oscillates when τ_{SUPG} is not adjusted to the impermeability. Contrary, if τ_{SUPG} is scaled down with an impermeability-dependent $c_{\mathrm{SUPG}}(\alpha)$ according to Equation (22), the oscillations are mitigated significantly.

DOI: 10.1002/nme

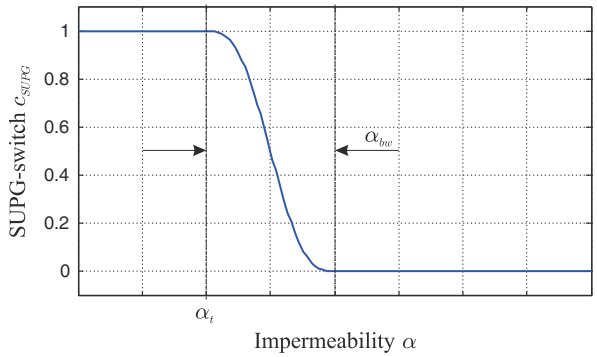

Figure 10. Smoothed Heaviside-function for c_{SUPG}.

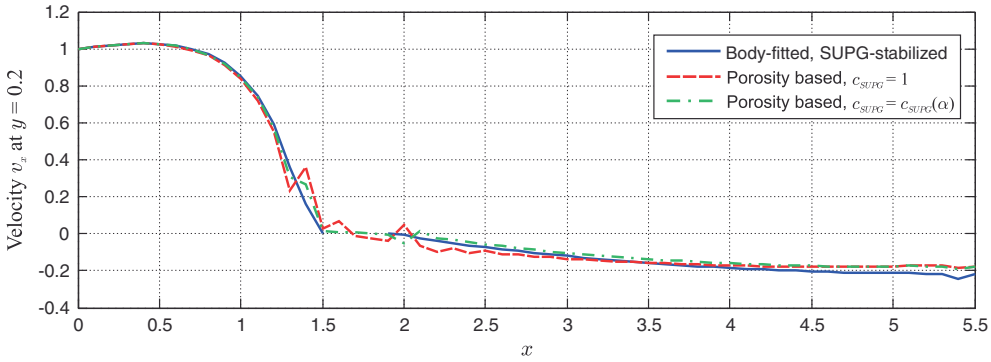

Figure 11. Comparison between velocities with constant c_{SUPG} and impermeability-dependent $c_{\mathrm{SUPG}}(\alpha)$ (based on configuration in Figure 4(a)).

4. ADJOINT SENSITIVITY ANALYSIS

The gradients of objective and constraints with respect to the design variables are computed by an adjoint sensitivity analysis. In the following we specifically consider the functional form of the objectives and constraints, defined in the optimization problem, Equation (1). For the sake of brevity, the adjoint formulation of the sensitivity equation will be derived only for the objective, Z. The sensitivity equations for the constraints can be developed analogously.

For compactness, we combine the quantities at discrete times to column vectors:

$$\begin{aligned} \tilde{\mathbf{z}} &= [z^0, \ldots, z^{N_t}]^{\mathrm{T}}, \\ \tilde{\mathbf{R}}_{\mathrm{dyn}} &= [\mathbf{R}^0_{\mathrm{dyn}}, \ldots, \mathbf{R}^{N_t}_{\mathrm{dyn}}]^{\mathrm{T}}, \\ \tilde{\mathbf{f}} &= [\mathbf{f}^0, \ldots, \mathbf{f}^{N_t}]^{\mathrm{T}}. \end{aligned} \tag{24}$$

Using this notation, the derivative of the objective Z, cp. Equation (1), with respect to the design variable s_k can be written as:

$$\frac{\mathrm{d}Z}{\mathrm{d}s_k} = \frac{\partial \mathscr{Z}}{\partial s_k} + \left(\frac{\partial \mathscr{Z}}{\partial \tilde{\mathbf{z}}}\right)^{\mathrm{T}} \left(\frac{\partial \tilde{\mathbf{z}}}{\partial s_k} + \left(\frac{\partial \tilde{\mathbf{z}}}{\partial \tilde{\mathbf{f}}}\right) \frac{\mathrm{d}\tilde{\mathbf{f}}}{\mathrm{d}s_k}\right). \tag{25}$$

DOI: 10.1002/nme

The derivative of the fluid state with respect to the design variables, $d\tilde{\mathbf{f}}/ds_k$ is computed from the total derivative of the residual equation:

$$\frac{\mathrm{d}\tilde{\mathbf{R}}_{\mathrm{dyn}}}{\mathrm{d}s_k}=\frac{\partial\tilde{\mathbf{R}}_{\mathrm{dyn}}}{\partial s_k}+\frac{\partial\tilde{\mathbf{R}}_{\mathrm{dyn}}}{\partial\tilde{\mathbf{f}}}\frac{\mathrm{d}\tilde{\mathbf{f}}}{\mathrm{d}s_k}=\mathbf{0}. \tag{26}$$

Solving Equation (26) for $\mathrm{d}\tilde{\mathbf{f}}/\mathrm{d}s_k$ and substituting the result into Equation (25) yields

$$\frac{\mathrm{d}Z}{\mathrm{d}s_k}=\frac{\partial\mathscr{Z}}{\partial s_k}+\left(\frac{\partial\mathscr{Z}}{\partial\tilde{\mathbf{z}}}\right)^{\mathrm{T}}\left(\frac{\partial\tilde{\mathbf{z}}}{\partial s_k}-\left(\frac{\partial\tilde{\mathbf{z}}}{\partial\tilde{\mathbf{f}}}\right)\left(\frac{\partial\tilde{\mathbf{R}}_{\mathrm{dyn}}}{\partial\tilde{\mathbf{f}}}\right)^{-1}\frac{\partial\tilde{\mathbf{R}}_{\mathrm{dyn}}}{\partial s_k}\right), \tag{27}$$

where we can identify the following adjoint problem:

$$\left(\frac{\partial\tilde{\mathbf{R}}_{\mathrm{dyn}}}{\partial\tilde{\mathbf{f}}}\right)^{\mathrm{T}}\tilde{\boldsymbol{\lambda}}=-\left(\frac{\partial\tilde{\mathbf{z}}}{\partial\tilde{\mathbf{f}}}\right)^{\mathrm{T}}\frac{\partial\mathscr{Z}}{\partial\tilde{\mathbf{z}}}. \tag{28}$$

For the zeroth step, $n=0$, the derivatives of the dynamic residual vector with respect to the state vectors $\partial\mathbf{R}^0_{\mathrm{dyn}}/\partial\mathbf{f}^j$ are given by:

$$\frac{\partial\mathbf{R}^0_{\mathrm{dyn}}}{\partial\mathbf{f}^j}=\begin{cases}\mathbf{I} & \forall\, j=0,\\ \mathbf{0} & \forall\, j=1,\ldots,N_t.\end{cases} \tag{29}$$

For the nth step, $n>0$, the derivatives $\partial\mathbf{R}^n_{\mathrm{dyn}}/\partial\mathbf{f}^j$ yield:

$$\frac{\partial\mathbf{R}^n_{\mathrm{dyn}}}{\partial\mathbf{f}^j}=\begin{cases}-\dfrac{\mathbf{M}^n}{\Delta t}\equiv\mathbf{C}^n & \forall\ j=n-1,\\ \dfrac{\mathbf{M}^n}{\Delta t}+\dfrac{\partial\mathbf{R}^n_s}{\partial\mathbf{f}^n}\equiv\mathbf{D}^n & \forall\ j=n,\\ \mathbf{0} & \forall\ j\in\{1,\ldots,N_t\}\backslash\{n-1,n\}.\end{cases} \tag{30}$$

Rewriting Equations (28)–(30) in matrix notation, leads to the following adjoint system:

$$\underbrace{\begin{bmatrix}\mathbf{I} & [\mathbf{C}^0]^{\mathrm{T}} & & & \\ & [\mathbf{D}^1]^{\mathrm{T}} & [\mathbf{C}^1]^{\mathrm{T}} & & \\ & & [\mathbf{D}^2]^{\mathrm{T}} & \ddots & \\ & & & \ddots & [\mathbf{C}^{N_t-1}]^{\mathrm{T}} \\ & & & & [\mathbf{D}^{N_t}]^{\mathrm{T}}\end{bmatrix}}_{\mathbf{A}^{\mathrm{T}}}\underbrace{\begin{pmatrix}\boldsymbol{\lambda}^0\\ \boldsymbol{\lambda}^1\\ \boldsymbol{\lambda}^2\\ \vdots\\ \boldsymbol{\lambda}^{N_t}\end{pmatrix}}_{\tilde{\boldsymbol{\lambda}}}=-\begin{pmatrix}(\partial z^0/\partial\mathbf{f}^0)^{\mathrm{T}}\,(\partial\mathscr{Z}/\partial z^0)\\ (\partial z^1/\partial\mathbf{f}^1)^{\mathrm{T}}\,(\partial\mathscr{Z}/\partial z^1)\\ (\partial z^2/\partial\mathbf{f}^2)^{\mathrm{T}}\,(\partial\mathscr{Z}/\partial z^2)\\ \vdots\\ (\partial z^{N_t}/\partial\mathbf{f}^{N_t})^{\mathrm{T}}\,(\partial\mathscr{Z}/\partial z^{N_t})\end{pmatrix}. \tag{31}$$

As the matrix $\mathbf{A}^{\mathrm{T}}$ is band structured with a single block at the end of the diagonal this system can be solved conveniently backwards in time starting from time step N_t. Given the adjoint solution $\tilde{\boldsymbol{\lambda}}$, the derivative of the objective with respect to the design variable s_k can be determined as follows:

$$\frac{\mathrm{d}Z}{\mathrm{d}s_k}=\frac{\partial\mathscr{Z}}{\partial s_k}+\left(\frac{\partial\mathscr{Z}}{\partial\tilde{\mathbf{z}}}\right)^{\mathrm{T}}\frac{\partial\tilde{\mathbf{z}}}{\partial s_k}+(\tilde{\boldsymbol{\lambda}})^{\mathrm{T}}\frac{\partial\tilde{\mathbf{R}}_{\mathrm{dyn}}}{\partial s_k}. \tag{32}$$

For solving the optimization problems presented in Section 5 we store the fluid states in-core at all time steps when solving the forward problem. The sub-matrices $\mathbf{C}^n$ and $\mathbf{D}^n$ are recomputed for every time step in the adjoint sensitivity analysis. Strategies for reducing the memory requirements

DOI: 10.1002/nme

and for lowering the computational costs for the adjoint sensitivity analysis were studied, for example, by Rumpfkeil and Zingg [9, 10] and Hinze *et al.* [33].

5. NUMERICAL EXAMPLE: DIFFUSER FOR UNSTEADY INLET CONDITIONS

The utility and key features of the proposed topology optimization approach for unsteady flow problems are illustrated with two numerical examples. In both examples the system is subjected to an unsteady inflow condition with the fluid initially being at rest, i.e. the initial conditions are design independent.

The parameter optimization problem is solved using the Globally Convergent Method of Moving Asymptotes (GCMMA) of Svanberg [34]. The GCMMA is a dual algorithm that solves the optimization problem iteratively in the space of the dual variables. At each iteration an approximate, explicit, separable subproblem in the space of the primal variables is created and solved analytically. This algorithm is specifically suited for problems with large numbers of design variables and few constraints. In the following, the GCMMA is considered converged, if the constraints are satisfied and the relative change in the design variables, Δ_s, is sufficiently small, i.e.

$$\frac{\|\mathbf{s}^{m-1}-\mathbf{s}^{m}\|}{\|\mathbf{s}^{m-1}\|}<\Delta_s, \tag{33}$$

where the superscript m defines the iteration number of the optimization process. The parameter settings for the GCMMA used in the following are listed in Table I. The initial design domain is set to 100% fluid, i.e. $s_k=1\ \forall k=1,\ldots,N_s$.

5.1. Diffuser design for steady-state and unsteady flows

The diffuser problem, shown in Figure 12, was introduced by Borrvall and Petersson [12] and has been studied frequently for steady-state flow conditions [14, 21]. The objective is to minimize the

Table I. GCMMA parameters.

Parameter	Value
Step size (Δs)	0.1
Initial adaptation of asymptotes	0.5
Adaptation of asymptotes	0.7
Scaling factor for constraint violation	10^2
Maximum number of sub-cycles	1
Relative change in optimization variables	$\Delta_s=10^{-5}$

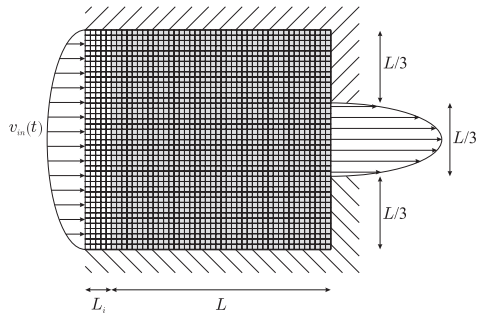

Figure 12. Computational domain for diffuser problem (design domain is highlighted by gray elements).

DOI: 10.1002/nme

difference in total pressure between the inlet and outlet, i.e. minimize the dissipation, subject to a constraint that limits the maximum area of the design space that can be occupied by fluid to 50%

$$\begin{aligned} \min_{\mathbf{s}} \quad & Z_{ss} = (p_{\text{in}}^{\text{tot}} - p_{\text{out}}^{\text{tot}}), \\ \text{s.t.} \quad & g = 0.5 - \frac{1}{N_s} \sum_{k=1}^{N_s} s_k \geqslant 0, \\ & s_{\min} \leqslant s_k \leqslant s_{\max} \quad \forall k = 1, \ldots, N_s, \end{aligned} \tag{34}$$

where N_s is the number of design variables.

In the original problem formulation, inlet and outlet pressure are computed at steady state. Considering an unsteady flow, we define the objective as the difference in total pressure, averaged over all time steps:

$$\min_{\mathbf{s}} Z_{us} = \frac{1}{N_t} \sum_{n=1}^{N_t} (p_{\text{in}}^{\text{tot}}(t^n) - p_{\text{out}}^{\text{tot}}(t^n)). \tag{35}$$

In both formulations, the total inlet and outlet pressures, $p_{\text{in}}^{\text{tot}}$ and $p_{\text{out}}^{\text{tot}}$, are averaged spatially over the inlet and outlet ports.

In Figure 12, the design domain is highlighted in gray. In order to resolve the unsteady flow close to the inlet, we add five layers of fluid elements to the computational domain, which are not part of the design domain. At the domain boundaries no-slip boundary conditions are imposed. The outlet is modeled as traction-free. At the inlet a time-varying parabolic velocity distribution is enforced. Figure 13 shows the evolution of the maximum inlet velocity, v_{in}, over time. The signal contains two components, a sinusoidal-shaped ramp and a constant plateau:

$$v_{\text{in}} = \begin{cases} \sin\left(\dfrac{\pi}{2T_R} t_n\right)^2 & \forall t_0 < t_n \leqslant T_R, \\ 1 & \forall T_R < t_n \leqslant T_R + T_P, \end{cases} \tag{36}$$

Smaller values for the times T_R and T_P will lead to more rapid signal changes, resulting in an increased flow unsteadiness.

In the following, we study the diffuser problem for increasing inlet velocities. The maximum inlet velocities correspond to Reynolds numbers $Re = 100$ and $Re = 1000$. The model and algorithmic

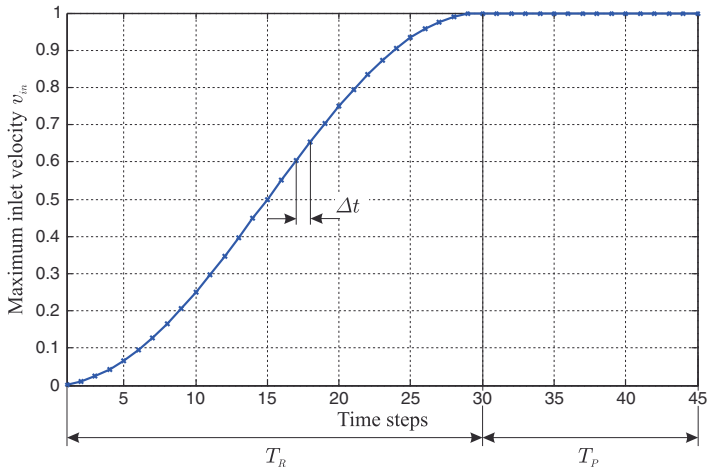

Figure 13. General inlet velocity signal for diffuser problem (here: $T_R = 30\Delta t$, $T_P = 15\Delta t$).

DOI: 10.1002/nme

Table II. Non-dimensional flow parameters for diffuser example (with $Re = Lv_{\text{in}}\rho/\mu$).

Flow parameter	Value
Inlet length (L)	1
Reference length (L_{ref})	L
Inlet clearance (L_i)	5/47
Maximum inlet velocity ($\max(v_{\text{in}})$)	1
Dynamic viscosity (μ)	$1/Re$
Density (ρ)	1
Time step for transient analysis (Δt)	10^{-4}
Time step for steady-state analysis (Δt_∞)	10^4

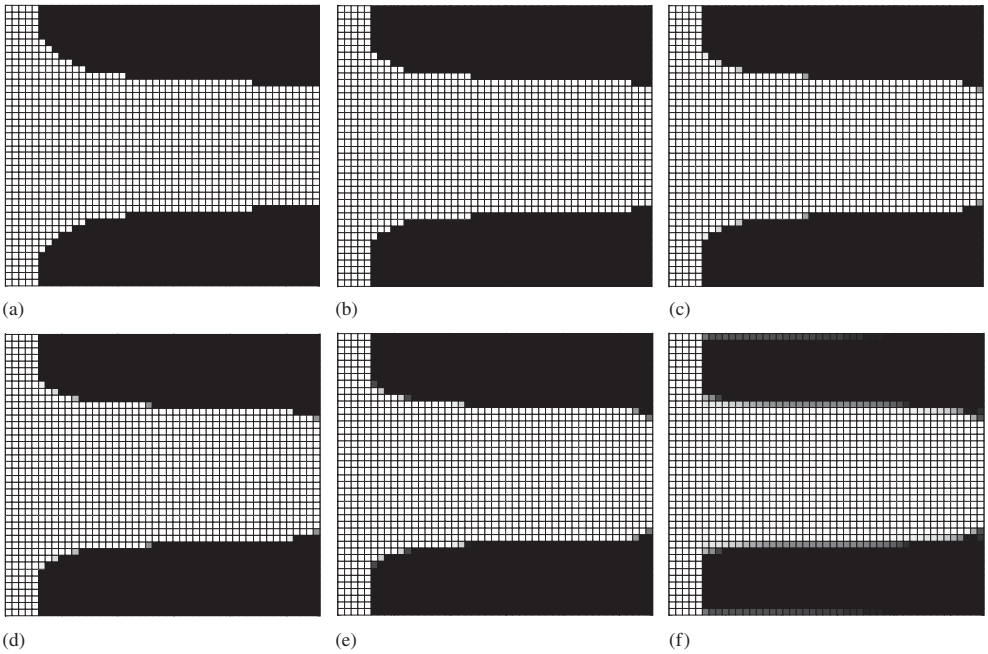

Figure 14. Optimized diffuser designs for various inlet velocity signals (m indicates the number of iterations until convergence): (a) steady-state, $m=31$, $T_R=0$, $T_P=3\Delta t_\infty$; (b) unsteady, $m=29$, $T_R=30\Delta t$, $T_P=30\Delta t$; (c) unsteady, $m=28$, $T_R=30\Delta t$, $T_P=15\Delta t$; (d) unsteady, $m=29$, $T_R=60\Delta t$, $T_P=0$; (e) unsteady, $m=60$, $T_R=30\Delta t$, $T_P=0$; and (f) unsteady, $m=55$, $T_R=15\Delta t$, $T_P=0$.

parameters for these studies are listed in Table II. The penalty for intermediate impermeabilities, p_α, is set to 0.1.

5.2. *Optimization results for* $Re=100$

First, we compare the optimization results for unsteady flow conditions with the steady-state design. Here, the computational domain is discretized by 47×42 elements with 42×42 elements within the design domain. We vary the time period T_R over which the inlet velocity is ramped up and T_P during which the velocity is held constant.

The optimized diffuser designs for steady-state conditions and for different unsteady input signals are depicted in Figure 14. As T_R and T_P decrease, i.e. the problem becomes more unsteady, the optimized designs differ increasingly from the steady-state solution in Figure 14(a). In the most unsteady case, Figure 14(f), the channel walls are almost horizontal with a pronounced necking

DOI: 10.1002/nme

Table III. Quantitative results for diffuser problem.

Time signal for inlet velocity ($v_{\text{in}}(t_i)$)	Design in Figure 14	Objective for steady-state design (Z_{ss})	Objective for unsteady design (Z_{us})	Relative improvement $((Z_{us}-Z_{ss})/Z_{ss})$
$T_R=0,\ T_P=3\Delta t_\infty$	(a)	95.95	100.70	—
$T_R=30\Delta t,\ T_P=30\Delta t$	(b)	10.63×10^3	10.58×10^3	−0.47%
$T_R=0,\ T_P=3\Delta t_\infty$	(a)	95.95	104.21	—
$T_R=30\Delta t,\ T_P=15\Delta t$	(c)	14.07×10^3	14.00×10^5	−0.47%
$T_R=0,\ T_P=3\Delta t_\infty$	(a)	95.95	103.93	—
$T_R=60\Delta t,\ T_P=0$	(d)	10.48×10^3	10.42×10^5	−0.64%
$T_R=0,\ T_P=3\Delta t_\infty$	(a)	95.95	112.67	—
$T_R=30\Delta t,\ T_P=0$	(e)	20.33×10^3	20.67×10^5	−1.31%
$T_R=0,\ T_P=3\Delta t_\infty$	(a)	95.95	246.80	—
$T_R=15\Delta t,\ T_P=0$	(f)	37.87×10^3	36.40×10^3	−3.87%

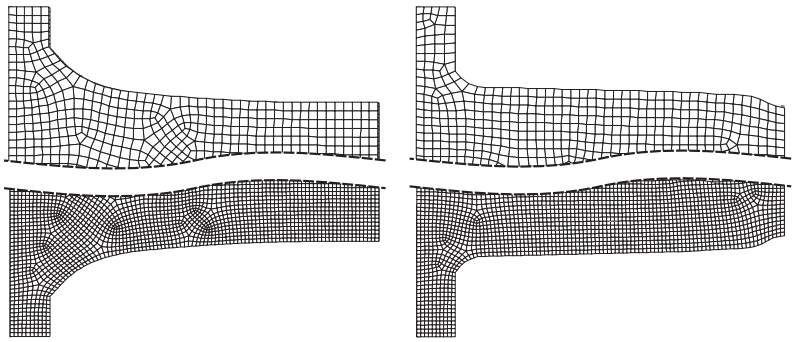

Figure 15. Body-fitted meshes for optimized diffuser designs: (a) steady-state design, cp. Figure 14(a) (886 elements/4296 elements) and (b) unsteady design, cp. Figure 14(f) (903 elements/4044 elements).

at the outlet. We compare the performance of the steady-state design for unsteady flow conditions against the performance of the unsteady solutions in Table III. The objective values confirm that a design performs better when subject to the inlet signal that it was optimized for. Furthermore, Table III shows that the performance of the steady-state design deteriorates as the flow conditions become more unsteady.

To verify the accuracy of the performance predictions, we compare the results of the uniform mesh using the Brinkman penalization against the ones of body-fitted meshes. We analyze the transient response of the steady-state design, Figure 14(a), and the unsteady design, Figure 14(f), for $T_R=15\Delta t$, $T_P=0$. Body-fitted meshes with two different levels of mesh refinement are shown in Figure 15. The mesh density of the coarse meshes, which contain about 900 elements, is comparable to the uniform mesh used in combination with the Brinkman approach. The fine body-fitted meshes contain about 4000 elements. A transient flow analysis with the coarse body-fitted meshes leads to an objective of $Z=37.33\times10^3$ for the steady-state design and $Z=36.67\times10^3$ for the unsteady design, both results agreeing well with the Brinkman-based prediction, listed in Table III. The refined body-fitted meshes yield slightly increased objective values: $Z=41.73\times10^3$ for the steady-state design and $Z=40.47\times10^3$ for the unsteady design. However, these results confirm that the unsteady design outperforms the steady-state design under unsteady flow conditions.

DOI: 10.1002/nme

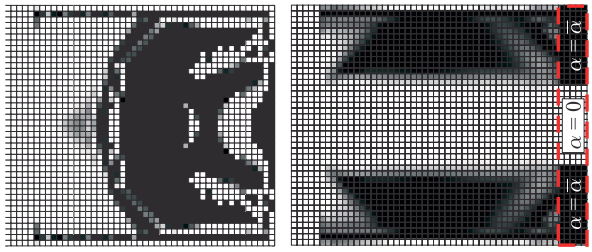

(a) (b)

Figure 16. Optimized design for $Re = 1000$: (a) 47×42 mesh, $N_s = 42^2$, $m = 100$ and (b) 52×42, $N_s = 42^2$, $m = 45$ additional non-design layer around outlet.

5.3. *Optimization results for* $Re = 1000$

Focusing on the most unsteady inlet velocity signal considered above, Figure 14(f), we consider the diffuser problem for a Reynolds number of $Re = 1000$. Using the same discretization of the computational domain as previously, i.e. 47×42 elements, the material distribution after 100 iterations is depicted in Figure 16(a). Although the objective has dropped significantly at this point in the optimization process, the material distribution contains many unexpected features, such as the plug in front of the outlet. In the following subsections, we will show that the emergence of these non-physical design features is partially due to the setup of the optimization problem but predominantly caused by an insufficiently refined mesh.

5.3.1. Influence of setup of optimization problem. As pointed out earlier, the Brinkman approach does not prevent pressure diffusion through solid areas and predicts a non-physical pressure field within solid regions. In the design of Figure 16(a) solid material is placed in front of the outlet where the average (non-physical) pressure contributes to the objective. To ensure that the outlet pressure is measured within a reasonably developed flow we add an additional layer of elements next to the outlet. In the fluid region of this layer the impermeability is set to $\alpha = 0$, in the solid region $\alpha = \overline{\alpha}$.

For a mesh with an identical grid size but with an additional layer of non-design domain next to the outlet, 52×42 elements, the optimized material distribution is shown in Figure 16(b). While adding a non-design layer leads to a more reasonable design the material distributions still exhibit unexpected artifacts.

5.3.2. Influence of mesh refinement. In the following we will show that as the Reynolds number increases finer meshes are needed to discretize the flow field. While this requirement is rather typical for flow problems we will illustrate that the level of refinement is mainly driven by the need to capture the flow fields of intermediate designs characterized by material distributions with spatially varying porosities.

First, we compare the total pressure for the designs in Figures 14(f), which is optimized for $Re = 100$, and 16(a), that is the material distribution with many artifacts, after the last time step. The inlet velocity signal is the same as for the problem shown in Figure 14(f). We consider two Reynolds numbers: $Re = 100$ and $Re = 1000$, and different levels of mesh refinement. The results are depicted in Figure 17: the top half of the figures shows the material distribution and the bottom half shows the total pressure fields. The total pressure in the horizontal direction at the center of the domain is plotted in the diagrams below the contour plots.

Using a 47×42 mesh, the pressure field for the design in Figure 14(f) is qualitatively very similar for both Reynolds numbers, cp. Figures 17(a) and (d). As expected the pressure decreases from inlet to outlet port. For $Re = 100$ and a 47×42 mesh, the total pressure field for the non-physical design is depicted in Figure 17(b): again the maximum total pressure occurs at the inlet, the minimum at the outlet. However, for $Re = 1000$ the 47×42 mesh predicts a completely different, incorrect pressure field, Figure 17(c): the total pressure at the outlet is higher than at the inlet,

DOI: 10.1002/nme

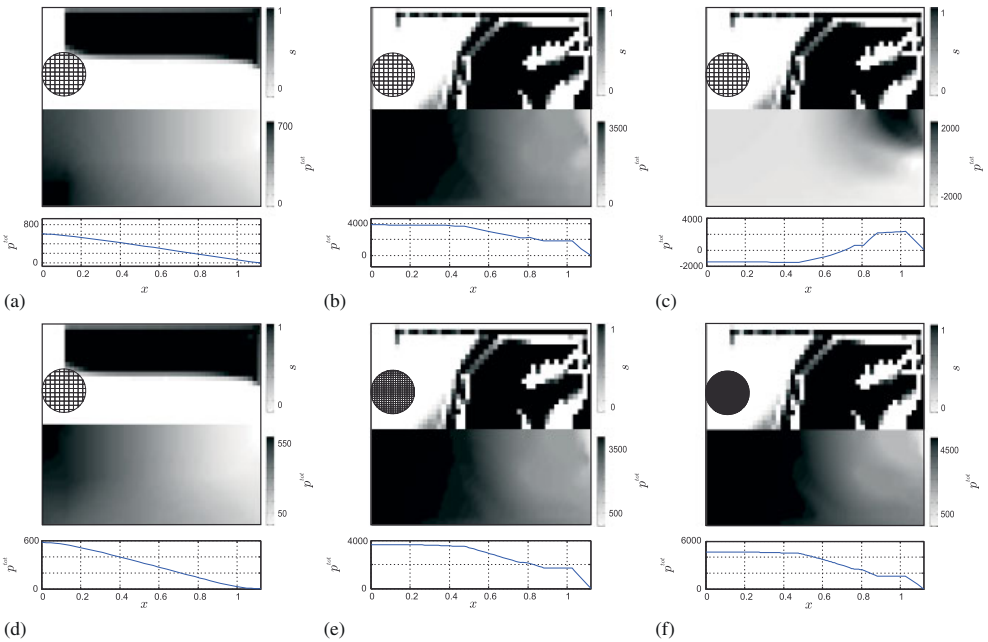

Figure 17. Total pressure contours for designs in Figures 14(f) and 16(a): (a) $Re=100$, 47×42 mesh; (b) $Re=100$, 47×42 mesh; (c) $Re=1000$, 47×42 mesh; (d) $Re=1000$, 47×42 mesh; (e) $Re=1000$, 94×84 mesh; and (f) $Re=1000$, 188×168 mesh.

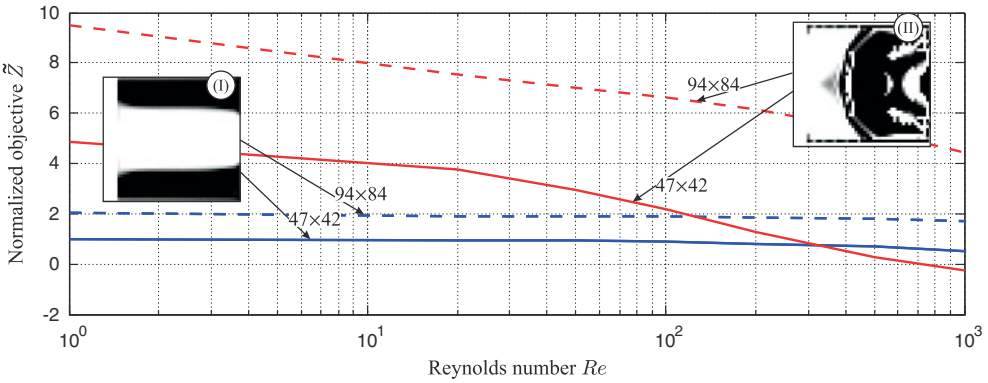

Figure 18. Influence of Reynolds number on objective on designs depicted in Figures 14(f) and 16(a).

leading to an improved, negative objective. Refining the mesh cures the incorrect flow prediction, cp. Figures 17(e) and (f).

To understand the influence of Reynolds number and mesh refinement on the prediction of flow field and objective, we compare the objectives of: (I) the diffuser optimized for $Re=100$, cp. Figure 14(f), and (II) the non-physical design of Figure 16(a). Both designs are studied for different Reynolds numbers, $1\leqslant Re\leqslant1000$, and for different levels of mesh refinement. Note, we only refine the mesh to improve the approximation of the flow field but leave the resolution of the material distributions unchanged. For each Reynolds number the objective is normalized $\tilde{Z}=Z/Z_0$, where Z_0 is the objective of case (I) for a Reynolds number of $Re=1$ and a 47×42 mesh.

Figure 18 illustrates that for low Reynolds numbers, the design (I) has a lower objective than design (II). However, as the Reynolds number increases, predictions based on the 47×42 mesh suggest that

DOI: 10.1002/nme

design (II) has a lower objective than design (I). At $Re>800$ the objective of design (II) even becomes negative, clearly indicating that the flow prediction is incorrect. As the meshes are refined, design (I) outperforms (II) over the entire Reynolds number range considered which is consistent with what one would expect given the material layout. This study demonstrates that higher Reynolds numbers require refined meshes in order to predict the flow fields correctly. If the mesh is too coarse the optimizer 'utilizes' the deficiency of the model, which might lead to artifacts.

Note that even a coarse mesh predicts the objective well for the design (I), cp. Figure 17(a), over the entire range of Reynolds numbers considered above. Thus, a refined mesh for higher Reynolds numbers is not necessarily warranted by the near-optimum design. The following numerical experiment will show that refined meshes are needed to accurately predict the flow fields for material distributions with strongly varying porosities, i.e. large differences in impermeability between neighboring elements.

Starting from a homogeneous porosity distribution, we gradually increase the contrast in impermeability variation until we recover the non-physical design of Figure 16(a). The design variables are interpolated as follows:

$$\hat{s}_k = 0.5 + f_s(s_k - 0.5) \quad \forall k = 1, \ldots, N_s, \quad 0 \leqslant f_s \leqslant 1, \tag{37}$$

where $\hat{s}_k$ is the value of the optimization variables corresponding to the non-physical design and f_s is a blending factor that controls the variation of $\hat{s}_k$. We compute the objective values as the blending factor is increased for two levels of mesh refinement at $Re = 1000$.

The results of this study are depicted in Figure 19 and show the dependency of the scaled objective $\hat{Z} = Z/Z^*$, where $Z^* = Z(f_s = 0)$ for the 47×42 mesh. Using the 47×42 mesh, the objective decreases for increasing impermeability variation while for the fine mesh the trend is opposite. These results show that an insufficiently refined mesh is not able to capture the correct flow characteristic as the porosity variation increases. This may cause the emergence of non-physical artifacts in the optimized material distributions.

To demonstrate that mesh refinement remedies the emergence of non-physical artifacts, the diffuser design problem is solved for increasingly fine meshes. The optimized material distributions are shown in Figures 20(a) and (b). Even without adding an additional non-design layer along the outlet the material distribution converges to intuitively reasonable designs as the mesh is refined.

In the above mesh refinement study we simultaneously increased the resolution of the material distribution and the flow field. To show that the formation of artifacts is due to insufficient resolution of the flow field, we optimize the 94×84 mesh with a four times coarser approximation of the material distribution, i.e. one design variable controls the impermeability of four fluid elements. The optimized design is shown in Figure 20(c), which agrees well with the one in Figure 20(b).

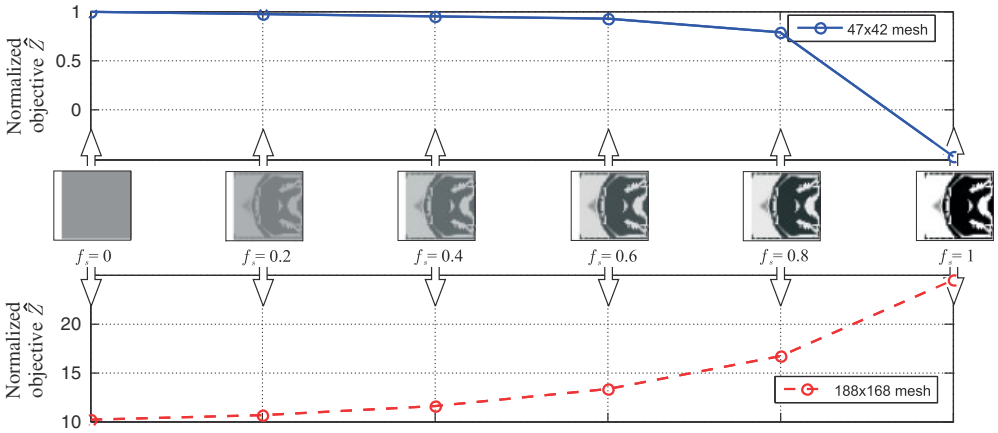

Figure 19. Influence of impermeability variation on objective at $Re = 1000$ for design depicted in Figure 16(a).

DOI: 10.1002/nme

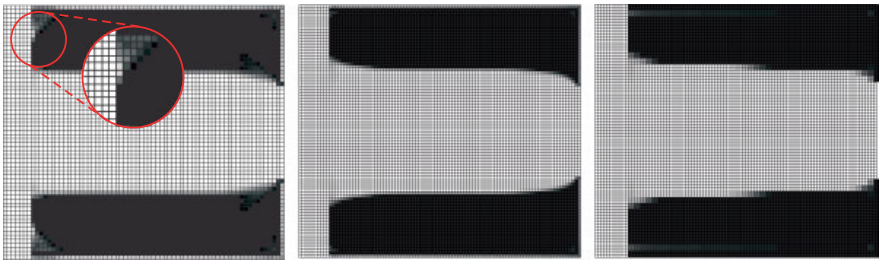

(a) (b) (c)

Figure 20. Optimized diffuser designs for $Re=1000$ (N_s defines the number of design variables, m the number of iterations until convergence): (a) 70×63 mesh, $N_s=63^2$, $m=112$; (b) 94×84 mesh, $N_s=84^2$, $m=41$; and (c) 94×84 mesh, $N_s=42^2$, $m=51$.

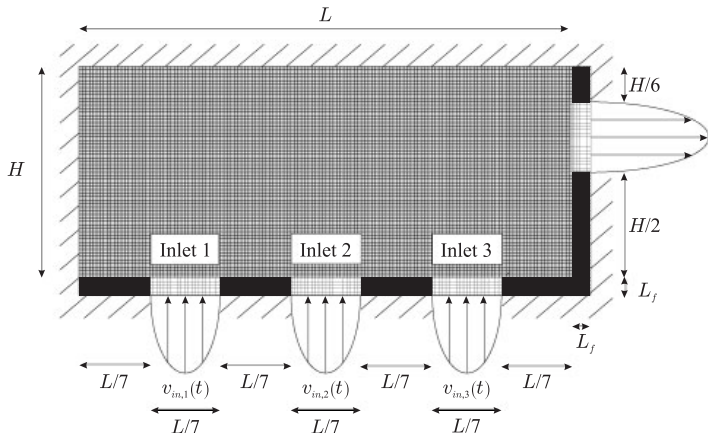

Figure 21. Design domain for manifold.

This comparison suggests that most importantly a sufficient resolution of the flow field is necessary to prevent the formation of non-physical design features.

5.4. *Manifold for oscillating inlet velocities*

The second example is concerned with the design of a manifold connecting three inlet ports and one outlet port. The inlet velocities are defined by phase shifted, sinusoidal half-waves. The goal is to minimize the maximum total pressure drop between the inlet and outlet ports.

The computational domain is depicted in Figure 21. The gray area indicates the design domain. The initial design domain is set to 100% fluid, i.e. $s_k=1\ \forall\ k=1,\ldots,N_s$. The domain boundaries are represented by a stick condition. The outlet is modeled as traction-free. A parabolic velocity profile is prescribed along the inlet ports. The evolution of the three inlet velocities is graphed in Figure 22. As in the previous example, each signal consists of two components, a non-linear sinusoidal half-wave and a constant part:

$$v_{in,1}(t^n)=\begin{cases}(1-v_\varepsilon)\sin(\omega t^n)^2+v_\varepsilon & \text{if } t^n\leqslant 27\times10^{-4},\\ 0 & \text{else,}\end{cases} \tag{38}$$

$$v_{in,2}(t^n)=\begin{cases}(1-v_\varepsilon)\sin(\omega t^n)^2+v_\varepsilon & \text{if } 18\times10^{-4}<t^n\leqslant 44\times10^{-4},\\ 0 & \text{else,}\end{cases} \tag{39}$$

DOI: 10.1002/nme

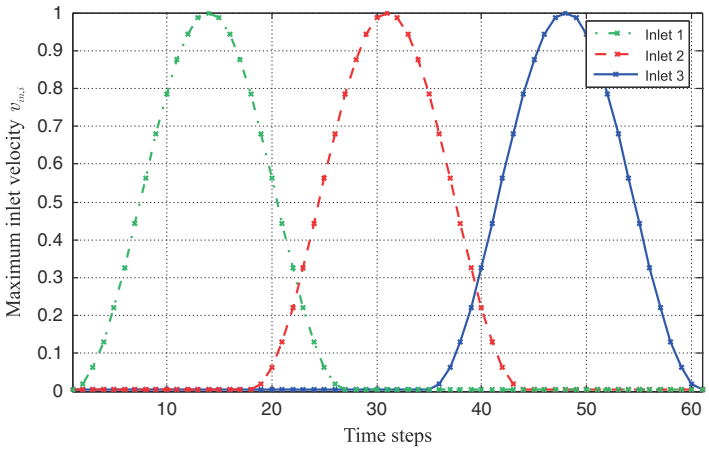

Figure 22. Inlet velocity signals for manifold problem.

$$v_{in,3}(t^n) = \begin{cases} (1-v_\varepsilon)\sin(\omega t^n)^2 + v_\varepsilon & \text{if } 35\times10^{-4} < t^n \leqslant 61\times10^{-4}, \\ 0 & \text{else}, \end{cases} \tag{40}$$

where v_ε is a small minimum velocity, which was set to 5×10^{-5} and $\omega = \pi/27$, defines the frequency of the sine-waves.

The objective is to minimize the maximum total pressure drop from the inlets to the outlet over the entire simulation time, $T = N_t \Delta t$. To guarantee differentiability of the objective function with respect to the design variables, a Kreisselmeier–Steinhauser (KS) function is used to extract the maximum [35]. The optimization problem is subject to a constraint that allows 50% of the design domain to be fluid

$$\begin{aligned} \min_{\mathbf{s}} \quad & Z = \frac{1}{k}\log\left(\sum_{n=1}^{N_t} e^{kz(t^n)}\right), \quad \text{with } z(t^n) = p_{\text{in}}^{\text{tot}}(t^n) - p_{\text{out}}^{\text{tot}}(t^n), \\ \text{s.t.} \quad & g = 0.5 - \frac{1}{N_s}\sum_{k=1}^{N_s} s_k \geqslant 0, \\ & s_{\min} \leqslant s_k \leqslant s_{\max} \quad \forall\ k = 1, \ldots, N_s, \end{aligned} \tag{41}$$

where the KS-factor k is set to 3. Numerical studies have shown that the results are insensitive to the value of the KS-factor for $3 \leqslant k \leqslant 10$. The total inlet and outlet pressures, $p_{\text{in}}^{\text{tot}}(t^n)$ and $p_{\text{out}}^{\text{tot}}(t^n)$, are averaged over the inlet and outlet ports.

The computational domain is discretized with 145×65 elements, including five layers of elements at the bottom and right that are not part of the design domain. The Reynolds number is set to $Re = 100$ with respect to the outlet width. The flow and algorithmic parameters are listed in Table IV. The penalty for intermediate impermeabilities, p_α is set to 0.2.

In Figure 23, we show the optimized designs for steady-state conditions, i.e. all three inlet velocities are kept constant, at $v_{\text{in}} = 1$, and for pulsating inlet flows. While the overall layout is the same for both designs, the shape of the channels differs significantly: in the steady-state design, Figure 23(a), the channel connecting inlet 1 (bottom left) and the outlet is the longest and therefore has a high pressure drop. Similarly, the channel connecting inlet 3 (bottom right) and the outlet has a low pressure drop. Since the objective of the unsteady optimization is to minimize the maximum pressure drop, the unsteady design has a widened channel from inlet 1 to the outlet. In order to satisfy the area constraint, the remaining two channels have to be narrowed.

Note that optimizing the manifold over two repeating cycles of pulsating inflows leads to the same geometry for the single cycle design shown in Figure 23(b).

DOI: 10.1002/nme

Table IV. Non-dimensional flow parameters for manifold example (with $Re = L v_{\text{in}} \rho / \mu$).

Flow parameter	Value
Manifold length (L)	1
Manifold height (H)	$3L/7$
Reference length (L_{ref})	$H/3$
Maximum inlet velocity ($\max(v_{\text{in},i})$)	1
Dynamic viscosity (μ)	$1/Re$
Density (ρ)	1
Time step for transient analysis (Δt)	10^{-4}
Time step for steady-state analysis (Δt_{∞})	10^{4}

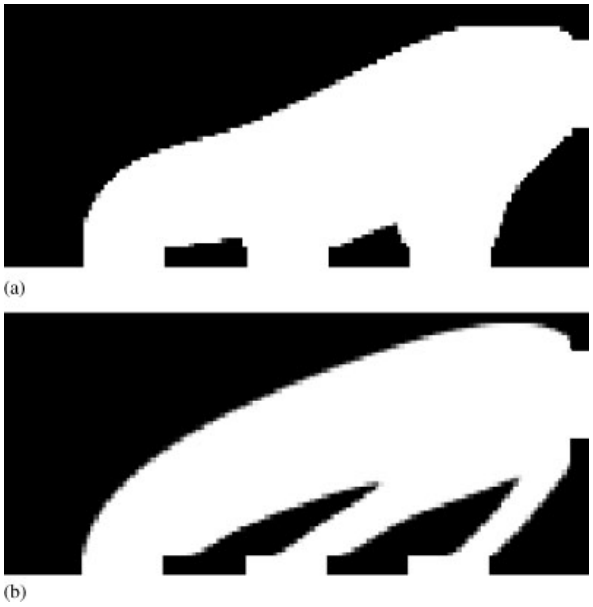

Figure 23. Optimized manifold designs: (a) steady-state design, $m=200$ and (b) unsteady-state design, $m=97$.

To compare the performance of the two designs under unsteady flow conditions, we perform a transient flow simulation for the steady-state design. In Figure 24, we plot the total pressure drop over time, for both steady-state and unsteady design. The comparison shows that through the unsteady optimization, the maximum pressure drop could be reduced from a value of ≈ 15.83 to ≈ 14.93 which corresponds to an improvement of $\approx 5.7\%$.

6. CONCLUSIONS

This study has presented a computational approach for optimizing the layout and shape of unsteady flow problems governed by the incompressible NS equations. A material distribution approach was used to describe the geometry. The boundary conditions at the fluid–solid interface were imposed via a Brinkman penalization. An impermeability-dependent SUPG-stabilization technique was introduced that effectively prevents velocity oscillations in porous material.

The emergence of non-physical artifacts was observed for unsteady flows at higher Reynolds numbers. This issue was linked to insufficient resolutions of the flow field and erroneous pressure

DOI: 10.1002/nme

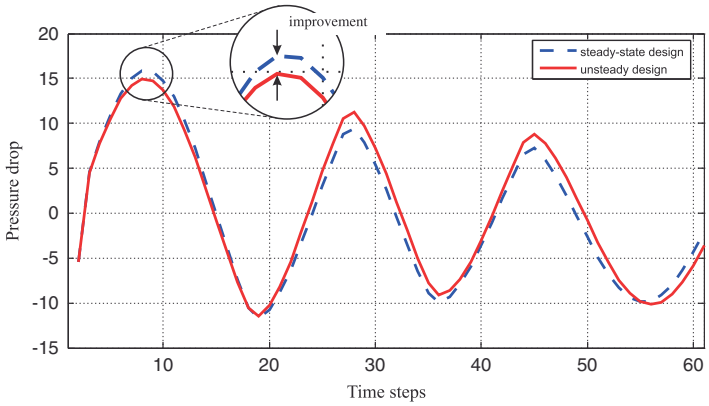

Figure 24. Comparison of pressure drop history for optimal designs, both for unsteady input signals, cp. Equations (38)–(40).

field predictions within solid regions. Physically meaningful designs were obtained by using sufficiently refined meshes. As the Brinkman approach does not prevent pressure diffusion through solid material, a non-physical pressure field is predicted within solid regions. Therefore, design criteria that are functions of the fluid pressure should be evaluated only over non-design regions guaranteed not to contain solid material. The inability of the Brinkman approach to prevent pressure diffusion through solid areas may also affect the overall accuracy of the flow predictions and thus the optimization results. Issues due to this deficiency were not observed in the examples considered in this study but may occur in other design problems. To avoid the difficulties caused by the Brinkman approach, a geometric boundary representation and immersed boundary techniques may be considered [23].

With two numerical examples we have illustrated that optimum unsteady designs differ increasingly from the corresponding steady-state designs as the problem becomes more unsteady. The performance of steady-state designs deteriorates as the flow varies more rapidly in time. While we have identified and addressed several key issues regarding the application of the Brinkman penalization to topology optimization, only 2D problems with Reynolds numbers up to $Re = 1000$ were studied. The proposed formulations and numerical methods can be easily extended onto 3D problems and are applicable to flows with larger Reynolds numbers. However, the stringent requirements on mesh refinement and the associated numerical cost for forward and sensitivity analysis are expected to limit the range of optimization problems that can be solved with the proposed method. Techniques for reducing the computational costs of both forward and sensitivity analysis need to be considered for 3D problems and higher Reynolds number flows.

ACKNOWLEDGEMENTS

The authors acknowledge the support of the National Science Foundation under grant CMMI-0729520. The opinions and conclusions presented in this chapter are those of the authors and do not necessarily reflect the views of the sponsoring organization.

REFERENCES

1. Azoury PH. *Engineering Applications of Unsteady Flow*. Wiley: New York, 1992.
2. Thorley ARD. *Fluid Transients in Pipeline Systems*. D & L George Ltd.: Hertfordshire, U.K., 2004.
3. Fox JA. *Transient Flow in Pipelines, Open Channels and Sewers*. Ellis Horwood Limited: Chichester, U.K., 1989.
4. Miller JA, Telionis DP. *International Symposium on Nonsteady Fluid Dynamics*. The American Society of Engineers, 1990.
5. Gunzburger MD. *Advances in Design and Control*. SIAM: Philadelphia, PA, 2003.

DOI: 10.1002/nme

6. Mohammadi B, Pironneau O. *Applied Shape Optimization for Fluids*. Oxford University Press: Oxford, 2001.
7. Mani K, Mavriplis DJ. Unsteady discrete adjoint formulation for two-dimensional flow problems with deforming meshes. *AIAA Journal* 2008; **46**(6):1351–1364.
8. Homescu C, Navon IM, Li Z. Suppression of vortex shedding for flow around a circular cylinder using optimal control. *International Journal for Numerical Methods in Fluids* 2002; **38**(1):43–69.
9. Rumpfkeil MP, Zingg DW. The optimal control of unsteady flows with a discrete adjoint method. *Optimization and Engineering* 2010; **11**(1):5–22.
10. Rumpfkeil MP, Zingg DW. Unsteady optimization using a discrete adjoint approach applied to aeroacoustic shape design. *The 46th AIAA Aerospace Sciences Meeting and Exhibit*, Reno, NV, 2008.
11. Bendsøe MP, Sigmund O. *Topology Optimization*: *Theory*, *Methods and Applications*. Springer: Berlin, 2003.
12. Borrvall T, Petersson J. Topology optimization of fluids in Stokes flow. *International Journal for Numerical Methods in Fluids* 2003; **41**(1):77–107.
13. Guest JK, Prévost JH. Topology optimization of creeping fluid flows using a Darcy–Stokes finite element. *International Journal for Numerical Methods in Engineering* 2006; **66**:461–484.
14. Challis V, Guest JK. Level set topology optimization of fluids in Stokes flow. *International Journal for Numerical Methods in Engineering* 2009; **79**(10):1284–1308.
15. Gersborg-Hansen A, Sigmund O, Haber RB. Topology optimization of channel flow problems. *Structural and Multidisciplinary Optimization* 2005; **30**(3):181–192.
16. Okkels F, Olesen LH, Bruus H. Applications of topology optimization in the design of micro- and nanofluidic systems. *NSTI—Nanotechnology*, vol. 1, 2005; 575–578.
17. Olesen LH, Okkels F, Bruus H. A high-level programming-language implementation of topology optimization applied to steady-state Navier–Stokes flow. *International Journal for Numerical Methods in Engineering* 2006; **65**(7):975–1001.
18. Evgrafov A, Pingen G, Maute K. Topology optimization of fluid domains: kinetic theory approach. *ZAMM—Zeitschrift für Angewandte Mathematik und Mechanik* 2008; **88**(2):129–141.
19. Othmer C. CFD topology and shape optimization with adjoint methods. *VDI Fahrzeug- und Verkehrstechnik*, *13. Internationaler Kongress*, *Berechnung und Simulation im Fahrzeugbau*. Würzburg: Germany, 2006.
20. Othmer C, de Villiers E, Weller HG. Implementation of a continuous adjoint for topology optimization of ducted flows. *The 18th AIAA Computational Fluid Dynamics Conference*. AIAA: Miami, FL, 2007.
21. Pingen G, Evgrafov A, Maute K. Topology optimization of flow domains using the lattice Boltzmann method. *Structural and Multidisciplinary Optimization* 2007; **36**(6):507–524.
22. Pingen G, Waidmann M, Evgrafov A, Maute K. A parametric level-set approach for topology optimization of flow domains. *Structural and Multidisciplinary Optimization* 2009; **41**(1):117–131. DOI: 10.1007/s00158-009-0405-1.
23. Kreissl S, Pingen G, Maute K. An explicit level-set approach for generalized shape optimization of fluids with the lattice Boltzmann method. *International Journal for Numerical Methods in Fluids* 2009. Available online: DOI: 10.1002/fld.2193.
24. Tezduyar TE, Mittal S, Ray SE, Shih R. Incompressible flow computations with stabilized bilinear and linear equal-order-interpolation velocity–pressure elements. *Computer Methods in Applied Mechanics and Engineering* 1992; **95**:221–242.
25. Brinkman HC. A calculation of the viscous force exerted by a flowing fluid on a dense swarm of particles. *Applied Scientific Research*, *Section A* 1947; **1**:27.
26. Franca L. Incompressible flows based upon stabilized methods. *Technical Report*, Denver, CO, U.S.A., 1993.
27. Seo JH. Optimal design of material microstructure for convective heat transfer in a solid–fluid mixture. *Ph.D. Thesis*, University of Michigan at Ann Arbor, 2009.
28. Angot P, Bruneau C-H, Fabrie P. A penalization method to take into account obstacles in viscous flows. *Numerische Mathematik* 1999; **81**:497–520.
29. Brooks AN, Hughes TJR. Streamline upwind/Petrov–Galerkin formulations for convection dominated flows with particular emphasis on the incompressible Navier–Stokes equations. *Computer Methods in Applied Mechanics and Engineering* 1982; **32**(1–3):199–259.
30. Tezduyar TE, Shih R. Numerical experiments on downstream boundary of flow past a cylinder. *Journal of Engineering Mechanics* 1991; **117**(4):854–871.
31. Khadra K, Angot P, Parneix S, Caltagirone JP. Fictitious domain approach for numerical modelling of Navier–Stokes equations. *International Journal for Numerical Methods in Fluids* 2000; **34**(8):651–684.
32. Wall WA. Fluid–struktur-interaktion mit stabilisierten finiten elementen. *Ph.D. Thesis*, Universität Stuttgart, 1999 (in German).
33. Hinze M, Walther A, Sternberg J. An optimal memory-reduced procedure for calculating adjoints of the instationary Navier–Stokes equations. *Optimal Control Applications and Methods* 2006; **27**(1):19–40.
34. Svanberg K. A globally convergent version of MMA without linesearch. *Proceedings of the First World Congress of Structural and Multidisciplinary Optimization*, 28 May–2 June 1995. Goslar: Germany, 1995; 9–16.
35. Kreisselmeier G, Steinhauser R. Systematic control design by optimizing a vector performance index. *International Federation of Active Contrals Symposium on Computer Aided Design of Control Systems*. Zurich: Switzerland, 1979.

Appendix D

Publication [P4]: Fluid Topology Optimization Based on the Extended Finite Element Method [1]

[1] Submitted to Structural And Multidisciplinary Optimization on September 24th 2011

Fluid Topology Optimization Based on the Extended Finite Element Method

Sebastian Kreissl*, and Kurt Maute†

Abstract

This study focuses on finding the optimal layout of fluidic devices subjected to incompressible flow at low Reynolds numbers. The proposed approach uses a levelset method to describe the fluid-solid interface geometry. The flow field is modeled by the incompressible Navier-Stokes equations and discretized by the extended finite element method (XFEM). The no-slip condition along the fluid-solid interface is enforced via a stabilized Lagrange multiplier method. Unlike the commonly used porosity approach, the XFEM approach does not rely on a material interpolation, which allows for more flexibility in formulating the design problems. Further, it mitigates shortcomings of the porosity approach, such as: spurious pressure diffusion through solid material, large sensitivity of the accuracy of the boundary enforcement with respect to the model parameters - which may affect the optimization results, and poor boundary resolution. Numerical studies verify that the proposed method is able to recover optimization results obtained with the porosity approach. Further, it is demonstrated that the XFEM approach yields physical results for problems that cannot be solved with the porosity approach.

KEY WORDS: Extended finite element method, levelset method, Navier-Stokes, stabilized Lagrange multiplier method, adjoint sensitivity analysis, nonlinear programming.

1 Introduction

This study focuses on a methodology for optimizing the geometry of fluidic devices. The flow field is described via the incompressible Navier-Stokes equations at low Reynolds numbers. The commonly used material interpolation approach [1], which introduces a fictitious porous material

*Center for Aerospace Structures, University of Colorado at Boulder, Boulder, CO, USA, kreissl@colorado.edu

†Corresponding author, Center for Aerospace Structures, University of Colorado at Boulder, Boulder, CO, USA, maute@colorado.edu

has proven to work well for simple fluid optimization problems, such as problems involving steady-state flow [2] and problems aiming to minimize the dissipated energy. However, for more complex problems, e.g. coupled fluid-structure systems [3, 4] or transient flow problems [5, 6] the material interpolation approach has shown shortcomings. These shortcomings include the need for a tailored interpolation model in combination with an adequate objective as well as mass constraint for driving the design to a 0-1 material distribution. Further, the interpolation approach may yield erroneous flow fields, caused by pressure diffusing through 'solid' material if the mesh is not sufficiently fine [5]. To overcome these issues, this study introduces a geometric boundary representation combining a parametric levelset method to capture the evolution of the interface during the optimization process and an extended finite element method (XFEM) for predicting the flow field.

The common approach for both structural and fluid topology optimization is to employ a material distribution function, where the material properties - typically constant within one element - are controlled directly by the design variables [1, 7]. In this case, the material distribution is usually relaxed: instead of only allowing for discrete materials such as fluid or solid, intermediate material states - described by an interpolation model are introduced [7]. This continuous transition facilitates the use of gradient based optimization algorithms.

As an alternative to the elemental parameterization of the material distribution, levelset methods have recently gained popularity [8, 9]. The levelset field can either be mapped onto material properties [10] or into a geometric interface description [11]. In levelset-based optimization schemes, the levelset field is typically advanced by solving the Hamilton-Jacobi equation (HJE), where the steady-state solution of the HJE defines the solution of the optimization problem [12]. Alternatively, the levelset field can directly be controlled by the design variables [13], which allows the resulting parameter optimization problem to be solved by nonlinear programming methods.

The levelset method has recently become popular for fluid optimization problems: Cunha [14] used levelsets for solving inverse problems involving a stationary, viscous, incompressible flow. Mohammadi [15] employed levelsets for shape optimization of supersonic applications using an Euler flow model. Pingen et al. [16] have presented a levelset method for the optimization of flow problems using a hydrodynamic Lattice Boltzmann (LB) fluid solver. Challis and Guest have applied a levelset method [9] to solve Stokes flow optimization problems. Duan et al. [17, 18, 19] applied a levelset method to solve fluid optimization problems for Stokes- and Navier-Stokes-flows.

The common approach for using levelsets for fluid optimization is to map the levelset field into a porosity distribution: either a discrete [9] or a continuous one [10], see Figs. 1a and b. Note that in these cases, the 'solid' elements are still considered in the computational analysis. Alternatively, Zhou and Li remeshed the fluid domain based on the interface location [20], Fig. 1c. In a previous study, the authors have employed a levelset method in combination with an LB solver and a geometric boundary representation that enforces no-slip conditions along the fluid-solid interface [11]. The non-matching interface intersects the mesh, dividing the design domain into a solid and a fluid

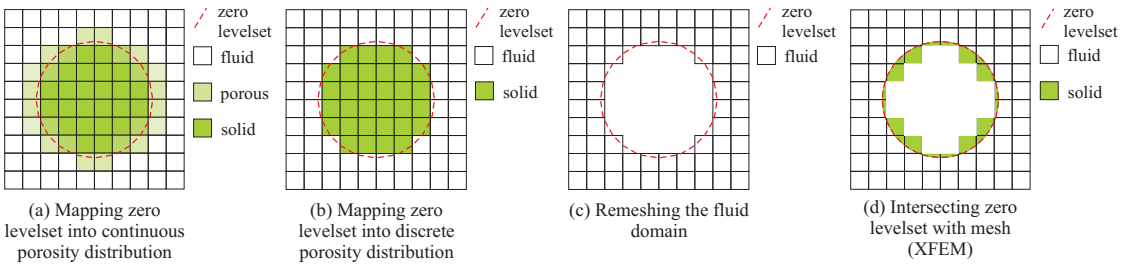

Figure 1: Boundary enforcement in levelset based fluid topology optimization.

part, bypassing the need for a fictitious material model, Fig. 1d. In this case, non-intersected solid elements are omitted from the computational analysis.

The approach presented here follows a similar idea as [11], but instead of using an LB method a more common finite element formulation of the steady-state incompressible Navier-Stokes equations is chosen. The latter are given by:

$$\text{Momentum equation:} \quad \hat{\rho}\frac{\partial \hat{v}_i}{\partial \hat{x}_j}\hat{v}_j = \frac{\partial \hat{\sigma}_{ij}}{\partial \hat{x}_j} + \hat{f}_i^B, \tag{1}$$

$$\text{Incompressibility condition:} \quad \frac{\partial \hat{v}_i}{\partial \hat{x}_i} = 0, \tag{2}$$

where $\hat{\rho}$ and $\hat{v}_i$ describe the dimensional density and velocity, respectively. The subscripts i, j define the spatial directions. The external body forces are denoted by $\hat{f}_i^B$. The stress tensor $\hat{\sigma}_{ij}$ is defined as:

$$\hat{\sigma}_{ij} = -\hat{p}\delta_{ij} + 2\hat{\mu}\frac{1}{2}\left(\frac{\partial \hat{v}_i}{\partial \hat{x}_j} + \frac{\partial \hat{v}_j}{\partial \hat{x}_i}\right), \tag{3}$$

where $\hat{p}$ and $\hat{\mu}$ describe the dimensional pressure and dynamic viscosity, respectively.

For fluid topology optimization, the force term $\hat{f}_i^B$ in the momentum equation (1) is commonly augmented with a Brinkman term, αv_i, penalizing the velocities [21]. The scalar α can be interpreted as an impermeability measure, with the velocity v_i vanishing for increasing α-values. The Brinkman approach is commonly used to model flow through porous media and adequately predicts flow and pressure fields for impermeabilities $\alpha > 0$. However, in material interpolation based fluid topology optimization, the porosity is only a vehicle. Ideally, the solid material should be completely impermeable for both convective mass transport and pressure diffusion. Since the Brinkman approach cannot prevent pressure diffusion for practical model parameters, cp. [5, 22], it may lead to errors in the flow prediction. As we will demonstrate below, erroneous pressure fields may lead to non-physical results during the optimization process.

In structural as well as fluid optimization, using fictitious porous material models requires penalizing intermediate densities such that the material distribution converges to a 0-1 solution. However,

in most cases a suitable combination of material interpolation scheme, objective function, and constraints are needed to obtain an adequate penalization effect. For structural topology optimization problems, a volume constraint is typically needed to penalize intermediate densities when optimizing the stiffness using the Solid Isotropic Material with Penalisation (SIMP) approach [7]. In fluid topology optimization, most often the dissipated energy in the system is minimized and the impermeability is interpolated as a nonlinear function of the optimization variables. Similar to structural problems, the formulation of the optimization problem needs to be augmented by an auxiliary volume constraint, such that the optimization process converges to a 0-1 solution. Furthermore, for optimization problems aiming at improving multiple functionalities and/or involving multiple physical phenomena it becomes increasingly difficult to define consistent interpolation models.

To avoid the disadvantages of the Brinkman penalization approach, we present a topology optimization method that combines a levelset description of the fluid-solid interface geometry and an extended finite element formulation of the flow problem. The basic concept of XFEM is to capture discontinuities in the solution within an intersected element by enriching the shape functions and enforcing the interface conditions along the intersection. XFEM was originally developed to model discontinuous displacement fields in crack propagation problems in solid mechanics [23, 24, 25, 26]. Miegroet and Duysinx [27] as well as Wei et al. [28] have applied levelsets based XFEM for optimizing linear elastic structures. Wang and Wang [29] applied a superimposed FEM (SFEM) for structural topology optimization which employs a locally refined mesh around the interface that is mapped onto a coarser global mesh. Recently, XFEM has also been applied to flow problems involving discontinuities: Chessa and Belytschko [30] as well as Sauerland and Fries [31] studied two phase flows using XFEM. Gerstenberger and Wall have applied XFEM to solve fluid-structure-interaction problems [32, 33].

For flow topology optimization, XFEM allows to model and optimize the flow field on a fixed grid, bypassing the need for a material interpolation scheme. The boundary condition can be enforced along the fluid-solid interface with great accuracy, effectively improving the resolution of the interface geometry and overcoming the stair-step approximation of material distribution approaches c.p. Fig. 1a and b. As the governing equations are only evaluated over the flow domain, the XFEM approach does not suffer from spurious pressure diffusion through solid, and reduces the computational cost since non-intersected solid elements are automatically omitted from the analysis process. Despite these interesting features, XFEM has not yet been integrated into a fluid topology optimization method.

The remainder of this paper is structured as follows: In Section 2, we outline the finite element formulation of the incompressible Navier-Stokes equations, in Section 3 the levelset method employed in this study is described. Section 4 details the extended finite element method with particular focus on the enforcement of boundary conditions along the fluid-structure interface. In Section 5 we

describe the class of optimization problems considered in this study. The properties of the proposed approach are demonstrated by three numerical examples in Section 6. The paper is summarized in Section 7.

2 Finite Element Formulation of the Incompressible Navier-Stokes Equations

The weak form of the steady-state incompressible Navier-Stokes equations (1)-(2) can be written with non-dimensional variables as follows:

$$R = \int_\Omega w_i \rho \frac{\partial v_i}{\partial x_j} v_j d\Omega - \int_\Omega \frac{1}{2}\left(\frac{\partial w_i}{\partial x_j} + \frac{\partial w_j}{\partial x_i}\right) p\delta_{ij} d\Omega + \int_\Omega \frac{1}{2}\left(\frac{\partial w_i}{\partial x_j} + \frac{\partial w_j}{\partial x_i}\right) 2\mu \frac{1}{2}\left(\frac{\partial v_i}{\partial x_j} + \frac{\partial v_j}{\partial x_i}\right) d\Omega + \int_\Omega q \frac{\partial v_i}{\partial x_i} d\Omega - \int_\Gamma w_i n_j \left(-p\delta_{ij} + 2\mu \frac{1}{2}\left(\frac{\partial v_i}{\partial x_j} + \frac{\partial v_j}{\partial x_i}\right)\right) d\Gamma = 0, \quad (4)$$

where R is a residual, w_i a velocity test function and q a pressure test function. Note, the divergence of the stress tensor, $\partial\hat{\sigma}_{ij}/\partial\hat{x}_j$ in Eq. (1), has been integrated by parts. The non-dimensional dynamic viscosity can be defined as:

$$\mu = \frac{\hat{\mu}}{\hat{L}_{ref}\hat{v}\hat{\rho}} = \frac{1}{Re}, \quad (5)$$

where $\hat{L}_{ref}$, $\hat{v}$, $\hat{\rho}$ are the dimensional reference length, reference velocity, reference density and Re is the Reynolds number.

In this study, the weak form of the incompressible Navier-Stokes equations (4) is discretized by four-node finite elements, i.e. the velocity and pressure fields are approximated piecewise by bi-linear, equal-order interpolations. To avoid numerical instabilities we employ an SUPG/PSPG-stabilization scheme [34].

3 Levelset method

The levelset method, first developed by Osher and Sethian [35], uses a 3-dimensional function Φ to describe the interface within a 2-dimensional space, Fig. 2. The interface Γ_i is implicitly defined through the zero levelset:

$$\Gamma_i = \{\mathbf{x} : \Phi(\mathbf{x}) = 0\}. \quad (6)$$

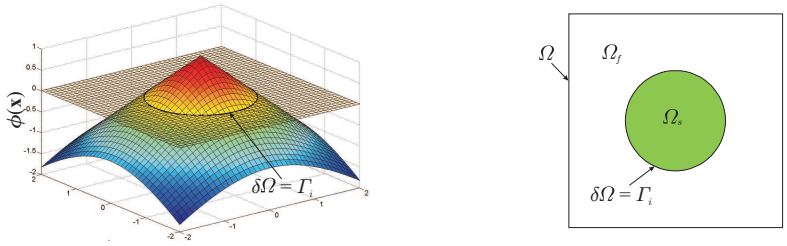

Figure 2: Interface Γ_i implicitly defined through $\Phi(\mathbf{x}) = 0$.

The value of the scalar function Φ defines whether a point at $\mathbf{x}$ is fluid (Ω_f), solid (Ω_s) or located on the fluid-structure interface Γ_i:

$$\Phi(\mathbf{x}) < 0 \qquad \forall\ \mathbf{x} \in \Omega_f, \tag{7}$$

$$\Phi(\mathbf{x}) = 0 \qquad \forall\ \mathbf{x} \in \delta\Omega = \Gamma_i, \tag{8}$$

$$\Phi(\mathbf{x}) > 0 \qquad \forall\ \mathbf{x} \in \Omega_s. \tag{9}$$

In the proposed approach, the levelset field is discretized by finite elements with the same resolution as the flow solution. As we have shown in a previous study on fluid optimization, smoothing is necessary to limit the spatial oscillations of the interface [11]. Therefore each nodal levelset value Φ_i is defined as function of a set of nodal design variables $\mathbf{s}_i$:

$$\Phi_i = \Phi_i\left(\mathbf{s}_i\right), \text{with } \mathbf{s}_i = \left[s_j, s_k, \ldots\right]. \tag{10}$$

The levelset field is smoothed by a distance based filter following the ideas of Sigmund and Petersson [36] as well as Daoud et al. [37]:

$$\Phi_i = \frac{\sum_j \left(r^s h - d_{ij}\right) s_j}{\sum_{i,j} \left(r^s h - d_{ij}\right)} \quad \forall\ j : d_{ij} \leq r^s h, \tag{11}$$

where d_{ij} is the distance between the i-th and the j-th node, r^s is the relative smoothing radius and h denotes the edge length of one element. The nodal levelset values, Φ_i, define the interface Γ_i as shown in Fig. 3.

For the optimization problems considered in this study, the interface geometry is varied by manipulating the levelset field in the optimization process. The interface geometry is only dependent on the design variables that lie within a band of width $2r^s$ around the interface, c.p. Eq. (11). Design variables outside of this band have zero sensitivities. Therefore the design can only grow across existing boundaries, i.e. boundaries can merge, but no new domains of solid material completely surrounded by fluid (islands) can develop. Likewise it is not possible to create new holes in the solid domain. However, the inability to create new islands can be compensated by an initial design that has a sufficient number of separated solid regions. The creation of holes within the solid

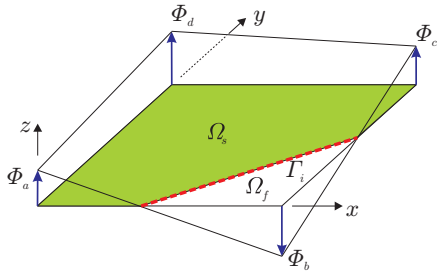

Figure 3: Determining the interface position, based on the nodal Φ_i-values.

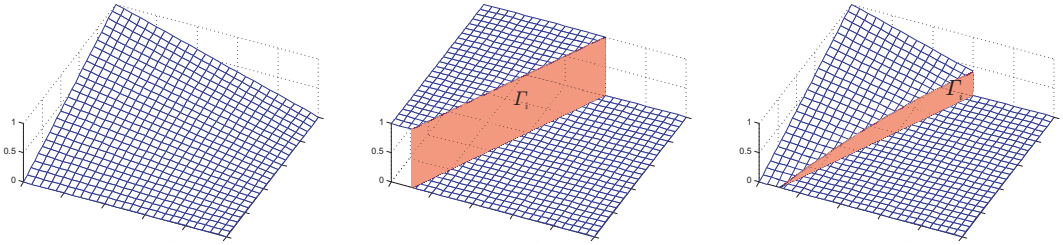

(a) Standard shape function, N

(b) Heaviside enrichment function, ψ

(c) Product of standard shape and enrichment function, $N\psi$

Figure 4: Regular bilinear shape function and Heaviside enrichment function.

domain is insignificant for fluid optimization as these do not affect the flow solution. In structural optimization the issue of creating holes is usually handled by topological derivatives [38, 39].

4 Extended Finite Element Method

The basic concept of XFEM is to enrich the shape functions which allows to model discontinuities in the solution within an intersected element across the interface Γ_i. In the current study, a Heaviside function is chosen for the enrichment, such that the velocity and pressure fields can be set to zero in the solid, c.p. Fig. 4:

$$f(\mathbf{x}) = \sum_i N_i(\mathbf{x}) \left(\tilde{f}_i(\mathbf{x}) + \psi(\mathbf{x}) \bar{f}_i(\mathbf{x}) \right) \quad \text{with } \psi(\mathbf{x}) = \begin{cases} 1 \; \forall \; \mathbf{x} \in \Omega_f, \\ 0 \; \forall \; \mathbf{x} \in \Omega_s, \end{cases} \tag{12}$$

where $N_i(\mathbf{x})$ is the standard shape function and $\psi(\mathbf{x})$ is the enrichment function; $\tilde{f}_i$ denotes regular and $\bar{f}_i$ enriched degrees of freedom; Ω_f and Ω_s distinguish the fluid and the solid domain.

To enforce the stick condition along the fluid-solid interface,

$$\mathbf{v}(\mathbf{x}) = \hat{\mathbf{v}} \equiv \mathbf{0} \quad \forall \; \mathbf{x} \; \in \; \Gamma_i, \tag{13}$$

we follow the idea of Gerstenberger and Wall who introduced an additional stress field as the Lagrange multiplier for enforcing the boundary condition along the fluid-solid interface [33].

Starting from the weak form of the incompressible Navier-Stokes equations (4), the residual R is augmented as follows:

$$R - \underbrace{\int_{\Gamma_i} \gamma_{ij} n_j \left(v_i - \hat{v}_i\right) d\Gamma_i}_{\text{constraint term}} - \underbrace{\int_{\Gamma_i} w_i \sigma_{ij}^L n_j d\Gamma_i}_{\text{Lagrange multiplier term}} - k \underbrace{\int_{\Omega_f} \gamma_{ij} \left(\frac{1}{2\mu}\left(\sigma_{ij} + p\delta_{ij}\right) - \epsilon_{ij}^L\right) d\Omega_f}_{\text{consistency term}} = 0, \quad (14)$$

where σ_{ij}^L is the assumed stress field which - multiplied with the normal n_j - functions as a Lagrange multiplier. The test function corresponding to σ_{ij}^L is denoted by γ_{ij}. The tensor ϵ_{ij}^L is the strain rate based on σ_{ij}^L, defined as:

$$\epsilon_{ij}^L = \frac{1}{2\mu}\left(\sigma_{ij}^L + \delta_{ij} p\right). \quad (15)$$

In Eq. (14), the first term enforces the constraint, the second one corresponds to the Lagrange multiplier, $\lambda_i = \sigma_{ij} n_j$, and the third term couples the Lagrange multiplier with the flow solution. Choosing a discontinuous Lagrange multiplier space allows for eliminating the Lagrange multiplier degrees of freedom on an elemental level. Thus the interface condition is enforced without introducing additional unknowns.

In this study we chose constant shape function for both γ_{ij} and σ_{ij}^L. In addition we introduce the scaling factor k in the compatibility term in Eq. (14). Setting k to zero, leads to a classical Lagrange multiplier formulation, which would either require finding an appropriate Lagrange multiplier space or stabilizing the Lagrange multipliers, both of which are challenging tasks [33]. While increasing k improves the numerical stability, it leads to a less accurate enforcement of the boundary condition. In the original work of Gerstenberger and Wall k is set to one. Due to the structure of the compatibility term, boundary conditions are less strongly enforced as the Reynolds number, c.p. Eq. (5), and the elemental fluid area increase. Therefore, we define the scaling parameter k as follows:

$$k = \eta \frac{\Omega^e - \Omega_f^e}{\Omega^e}, \quad (16)$$

where Ω_f^e defines the fluid area and Ω^e the total area of one element. The scalar η depends on the Reynolds number and the spatial discretization. For further details on this XFEM approach, the reader is referred to [33].

5 Optimization Problem

The optimization problems of interest can be written as follows:

$$\begin{aligned} &\min_{\mathbf{s}} \; z\left(\mathbf{s}, \mathbf{f}\left(\mathbf{s}\right)\right), \\ &\text{s.t.} \begin{cases} \mathbf{s}, & \text{satisfy the design constraints,} \\ \mathbf{f}, & \text{solves the governing equations for given } \mathbf{s}, \\ \mathbf{h}\left(\mathbf{s}, \mathbf{f}\right) = \mathbf{0}, & \text{satisfy the equality constraints,} \\ \mathbf{g}\left(\mathbf{s}, \mathbf{f}\right) \leq \mathbf{0}, & \text{satisfy the inequality constraints,} \end{cases} \end{aligned} \tag{17}$$

where z is a particular performance (objective) functional, $\mathbf{s}$ is the vector of design variables, $\mathbf{f}$ is the vector of fluid states and $\mathbf{h}, \mathbf{g}$ are equality, inequality constraints, respectively. Typical objectives and constraints include pressure drop, drag, flow rate, energy loss, and volume. The geometry, and thus the performance, of the current design is given via the zero levelset, which is controlled via the design variables, c.p. Eqs. (10)–(11). The parameter optimization problem (17) is solved by a nested loop approach using a gradient-based optimization method.

Due to the large number of design variables defining the nodal levelset values, the gradients of objective (and constraints) are computed by an adjoint formulation:

$$\frac{dz}{ds_k} = \frac{\partial z}{\partial s_k} - \boldsymbol{\lambda}^T \frac{\partial \mathbf{R}}{\partial s_k}, \tag{18}$$

where $\boldsymbol{\lambda}$ is the solution to the adjoint problem:

$$\frac{\partial \mathbf{R}}{\partial \mathbf{f}} \boldsymbol{\lambda} = \frac{\partial z}{\partial \mathbf{f}}. \tag{19}$$

6 Numerical Examples

To demonstrate the utility of the proposed approach for optimizing the geometry of two-dimensional incompressible flow problems at steady-state, three numerical examples are studied. The first example shows the ability of the proposed approach to reproduce results found by the Brinkman penalization method. Examples two and three illustrate the advantage of the proposed XFEM approach over the Brinkman penalization method.

All examples are solved by the Globally-Convergent Method of Moving Asymptotes (GCMMA) [40]. The GCMMA is a dual algorithm that solves the optimization problem iteratively in the space of the dual variables. At each iteration an approximate, explicit, separable subproblem in the space of the primal variables is constructed and solved analytically. This algorithm is specifically suited for problems with large numbers of design variables and few constraints as it is the case in the current study. For all examples we use the GCMMA parameters listed in Tab. 1. The step size

Parameter	Value
initial adaptation of asymptotes	0.5
adaptation of asymptotes	0.7
maximum number of sub-cycles	0

Table 1: GCMMA parameters used for all examples.

for the optimization variables, Δs and the constraint penalty, p_g, are specified for every example separately. We monitor the convergence of the optimization process by (a) the norm of the residual of the Karush-Kuhn-Tucker (KKT) conditions R^{KKT} [41] and (b) the change in the design variables d^s between two consecutive design iterations:

$$d^s = \frac{\|\mathbf{s}_n - \mathbf{s}_{n-1}\|}{\|\mathbf{s}_{n-1}\|}. \tag{20}$$

Depending on the optimization problem, we use one or both of the following criteria for determining convergence:

$$R^{KKT} < \epsilon^{KKT}, \tag{21}$$

$$d^s < \epsilon^d. \tag{22}$$

The nonlinear flow problem (14) is solved via Newton's method. The latter is considered converged if:

$$\frac{\|\mathbf{R}\|}{\|\mathbf{R}_0\|} \leq 10^{-3}, \tag{23}$$

where $\|\mathbf{R}_0\|$ and $\|\mathbf{R}\|$ define the norm of the total initial and total current residual vector, respectively. For all problems studied in the following, the scalar η in Eq. (16) is set to 1.

6.1 Pipe-bend

The pipe-bend problem, studied in [1, 17, 42] is a standard example for fluid topology optimization. The design domain as well as the initial design are depicted in Figs. 5a and 5b. The objective is to minimize the difference in total pressure, $p^{tot} = 1/2\rho \|\mathbf{v}\|^2 + p$, between the inlet and outlet, subject to a constraint that allows only 25% of the area to be fluid:

$$\begin{aligned} \min_{s_k} \quad & z = (p_{in}^{tot} - p_{out}^{tot}), \\ \text{s.t.} \quad & g = 0.25 - \frac{A_{fluid}}{L^2} \geq 0, \\ & s_{min} \leq s_k \leq s_{max}. \end{aligned} \tag{24}$$

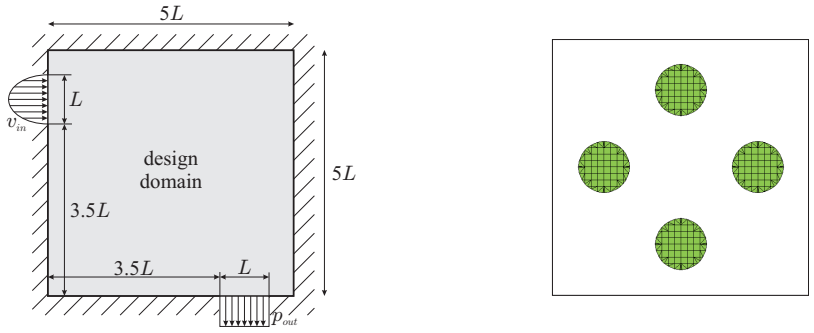

(a) Design domain (b) Initialization

Figure 5: Pipe-bend example.

The total inlet and outlet pressures, p_{in}^{tot} and p_{out}^{tot}, are averaged over the inlet and outlet ports. The boundary conditions, depicted in Fig. 5a, are a parabolic inlet velocity, v_{in}, and a constant static pressure at the outlet, p_{out}. The domain boundaries are represented by a 'no-slip' condition. The computational domain is discretized by 40×40 elements. The initial design is given as four circular regions of solid, Fig. 5b. The parameter settings for this example are listed in Tab. 2.

In order to guarantee proper flow through the inlet and outlet ports, the levelset values coinciding with the nodes on the inlet and outlet are fixed at $\Phi_i = -1$ and are omitted from the smoothing operation defined in Eq. (11). The same treatment of inlet and outlet ports is applied to the examples below.

The optimized geometry is depicted in Fig. 6a. For comparison we optimize the problem (24) using the porosity approach for two different levels of mesh refinement: 40×40 and 80×80 elements. In case of the porosity approach, the material distribution defines the impermeability in the Brinkman term. Following the work by Borrvall and Peterson [1], a convex interpolation function is chosen for the impermeability α:

$$\alpha\left(s\right) = \alpha_{\max} + \left(\alpha_{\min} - \alpha_{\max}\right) s \frac{1 + p_\alpha}{s + p_\alpha} \quad \text{with } 0 \leq s \leq 1, \tag{25}$$

where $\alpha_{\min} = 0$ is the lower, $\alpha_{\max}$ the upper limit and s defines the optimization variable. The scalar p_α is a penalty parameter that allows controlling the amount of elements with intermediate impermeabilities in the optimal design [1].

Figures 6b and 6c show the zero-levelset of the optimized XFEM geometry on top of the optimized porosity distribution. Both designs agree well with the one obtained from the XFEM based optimization. Figure 6b illustrates that - for the same mesh density - the proposed XFEM approach has higher boundary resolution compared to the porosity approach. When employing the porosity approach, we observed that both the constraint penalty p_g and the interpolation penalty p_α have a strong influence on the resulting optimized geometry.

Parameter type	**Parameter**	**Value**
nondim. flow parameters	max. inlet velocity, $\max(v_{in})$	1.5
	outlet pressure, p_{out}	1
	density, ρ	1
	reference length, L	1
	Reynolds number, Re	100
optimization parameters (XFEM approach)	optimizer step size, Δs	0.04
	constraint penalty, p_g	50
	relative smoothing radius, r^s	4.5
	KKT threshold, ϵ^{KKT}	$3 \cdot 10^{-3}$
optimization parameters (porosity approach 40×40)	optimizer step size, Δs	0.05
	constraint penalty, p_g	2
	interpolation penalty, p_α	0.001
	KKT threshold, ϵ^{KKT}	2
	design change threshold, ϵ^d	10^{-9}
	max. impermeability, $\alpha_{\max}$	$2.5 \cdot 10^4$
optimization parameters (porosity approach 80×80)	optimizer step size, Δs	0.05
	constraint penalty, p_g	5
	interpolation penalty, p_α	0.001
	KKT threshold, ϵ^{KKT}	0.5
	design change threshold, ϵ^d	10^{-11}
	max. impermeability, $\alpha_{\max}$	$2.5 \cdot 10^4$

Table 2: Parameter settings for pipe-bend.

6.2 U-bend

Drawbacks of the porosity approach are its inability to prevent pressure diffusion through solid material [5, 22] and its high sensitivity of the accuracy of the boundary enforcement with respect to model parameters. To investigate these phenomena we define the problem depicted in Fig. 7a. It includes a solid region (black) and a fluid region (white) both of which are not part of the design domain that is highlighted in grey color. The inlet has a prescribed parabolic velocity profile, v_{in}, and the outlet a prescribed static pressure, p_{out}. The computational domain is discretized by 40×60 elements. Table 3 lists the parameters defining this problem.

The goal of this optimization problem is to minimize the pressure drop from the inlet to the outlet

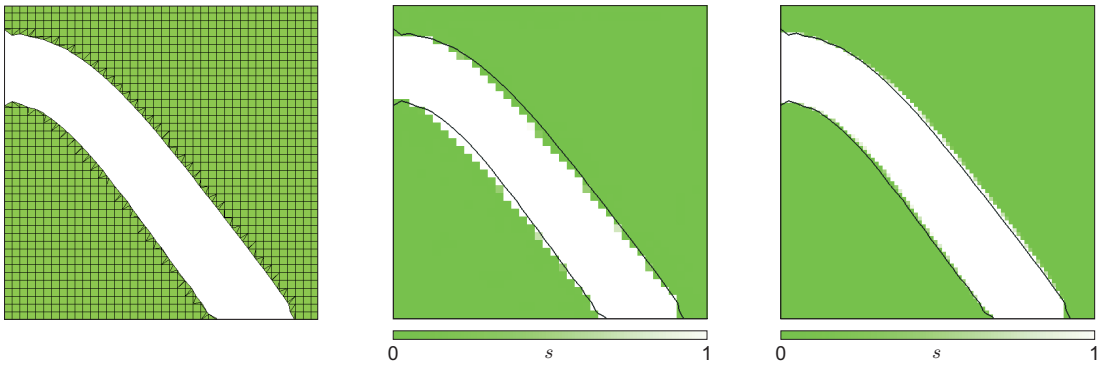

(a) XFEM (40×40 mesh)

(b) Zero levelset on 40×40 porosity distribution

(c) Zero levelset on 80×80 porosity distribution

Figure 6: Optimized pipe-bend geometries.

subjected to a volume constraint:

$$\begin{aligned} \min_{s_k} \quad & z = (p_{in}^{tot} - p_{out}^{tot}), \\ \text{s.t.} \quad & g = 0.5 - \frac{A_{fluid}}{HW} \geq 0, \\ & s_{min} \leq s_k \leq s_{max}. \end{aligned} \tag{26}$$

The total inlet and outlet pressures, p_{in}^{tot} and p_{out}^{tot}, are averaged over the inlet and outlet ports. We consider two different Reynolds numbers: $Re = 0.1$ and $Re = 10$. Using the porosity approach, the fluid non-design-domain is modeled via perfectly permeable material, i.e. $\alpha = 0$ and the solid non-design-domain by an impermeable material with $\alpha = \alpha_{max}$. Note that for the porosity approach even elements that are 100% solid, i.e. $\alpha = \alpha_{max}$ are part of the computational domain, whereas in the XFEM case non-intersected solid elements are not considered in the computation of the flow field.

The initial design for both the XFEM and the porosity based optimization are depicted in Fig. 7a. To assess the accuracy of the pressure fields of these two initial geometries, we create a body-fitted mesh by excluding the solid regions. The body-fitted mesh is considered converged at about 160×240 elements. We compare the error of the XFEM and the porosity approach relative to the body-fitted mesh:

$$e_r^{\square} = \frac{\max\left(\mathbf{p}^b\right) - \max\left(\mathbf{p}^{\square}\right)}{\max\left(\mathbf{p}^b\right)} \cdot 100, \tag{27}$$

where $\mathbf{p}^b$ is the pressure field based on the body-fitted mesh; $\mathbf{p}^{\square}$ refers to pressure field of the porosity based approach ($\square = p$) or the XFEM approach ($\square = x$), respectively. We consider three levels of mesh refinement for both the porosity and the XFEM approach: $nx \times ny \in [40 \times 60, 80 \times 120, 160 \times 240]$, where nx and ny are the number of elements along the edges in x- and y-direction. Furthermore, we consider three values for the maximum impermeability:

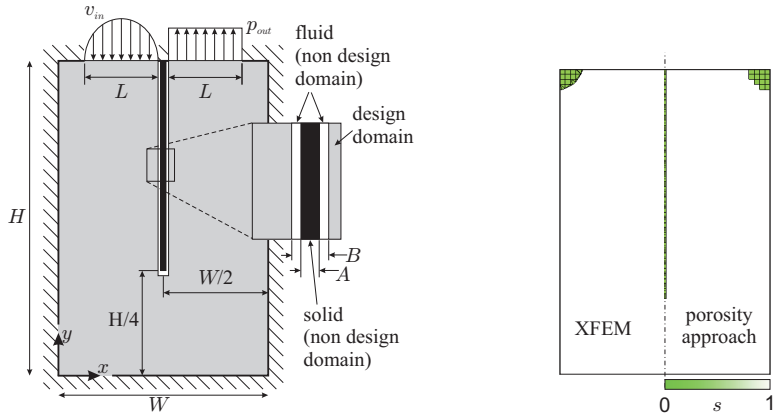

(a) Design domain (b) Initialization

Figure 7: U-bend example.

$\alpha_{\max} \in \left[2.5 \cdot 10^4, 2.5 \cdot 10^5, 2.5 \cdot 10^6\right]$. Since the derivative $d\alpha/ds$ is proportional to the negative of $\alpha_{\max}$, the absolute value of the sensitivities becomes large for $\alpha_{\max} \gg 1$. As a result, even small changes in the design variable, Δs, yield large changes in the impermeability $\Delta\alpha$. As observed in a previous study by the authors [5], large differences in the impermeability between neighboring elements lead to non-physical flow fields if the mesh is not sufficiently fine.

The corresponding error values for $Re = 0.1$ are listed in Tab. 4. The results indicate that increasing the maximum impermeability improves the accuracy of the pressure field. However, even the finest considered mesh with $\alpha_{\max} = 2.5 \cdot 10^6$ still yields an error of $e_r^p = -18.53\%$. Contrary, the error of the XFEM approach converges towards zero as the mesh is refined: $e_r^x = 0.35\%$ for the finest mesh resolution.

Using the XFEM approach for solving the optimization problem (26) yields the geometries depicted in Fig. 8: for both considered Reynolds numbers an intuitive design is obtained.

Figure 9 shows the optimized geometries when a porosity approach is used to solve the optimization problem (26). Using a maximum porosity of $\alpha_{\max} = 2.5 \cdot 10^4$ for the low Reynolds number $Re = 0.1$, diffusion dominated case, yields the design depicted in Fig. 9a. The velocity streamlines indicate a mass flow through the slender solid member caused by pressure diffusion through solid material. Comparing the pressure field along a horizontal line at $y = 0.9H$ for both the initial and the optimized geometry in Fig. 10 illustrates the error in the pressure field predicted by the porosity approach. As the solid member does not prevent pressure diffusion, the pressure on the inlet side is significantly lower for porous case than for the XFEM one. Increasing the maximum impermeability, Figs. 9b and 9c, remedies this issue. For the convection dominated case, $Re = 10$, a maximum impermeability of $\alpha_{\max} = 2.5 \cdot 10^4$ is sufficient to prevent pressure diffusion, Fig, 9d. As $\alpha_{\max}$

Parameter type	Parameter	Value
nondim. flow parameters	height, H	1
	width, W	2W/3
	reference length, L	0.35W
	width of solid, A	0.025W
	width non design domain, B	0.05W
	max. inlet velocity, $\max(v_{in})$	1.5/L
	outlet pressure, p_{out}	1
	density, ρ	1
	Reynolds number, Re	0.1, 10
optimization parameters (common)	KKT threshold, ϵ^{KKT}	10^{-3}
optimization parameters (XFEM approach)	optimizer step size, Δs	0.05
	constraint penalty, p_g	10
	relative smoothing radius, r^s	3.5
optimization parameters (porosity approach)	optimizer step size, Δs	0.05
	constraint penalty, p_g	10
	interpolation penalty, p_α	0.1

Table 3: Parameter settings for U-bend.

increases, the obtained material distributions become more erratic, c.p. Figs. 9e and 9f. While Fig. 9 shows that the porosity approach can reproduce results similar to the XFEM approach, c.p. Fig. 8, it also reveals that the Brinkman penalization is very sensitive to the material interpolation $\alpha(s)$. A Reynolds number dependent material interpolation $\alpha = \alpha(s, Re)$ as proposed by Borrvall and Petersson [1] as well as Khadra et al. [43] may improve the robustness of the porosity approach.

6.3 Nozzle with target total pressure ratio

The proposed XFEM approach does not rely on a material interpolation scheme and therefore does not require a tailored combination of objective and constraint to converge to a 0-1 material distribution. This feature is illustrated with the example depicted in Fig. 11a. Again, we are comparing the results of the XFEM and the porosity approach.

The goal of this optimization problem is to find a design that matches a specified total pressure ratio between inlet and outlet:

$$\begin{aligned} \min_{s_k} \quad & z = (p_{in}^{tot} - 4p_{out}^{tot})^2, \\ \text{s.t.} \quad & s_{min} \leq s_k \leq s_{max}, \end{aligned} \tag{28}$$

discretization:	**40×60**	**80×120**	**160×240**
error porosity approach $\left(\alpha_{\max} = 2.5 \cdot 10^4\right)$: e_r^p	63.83%	63.30%	63.02%
error porosity approach $\left(\alpha_{\max} = 2.5 \cdot 10^5\right)$: e_r^p	33.60%	31.24%	31.18%
error porosity approach $\left(\alpha_{\max} = 2.5 \cdot 10^6\right)$: e_r^p	2.08%	-19.08%	-18.53%
error XFEM approach: e_r^x	7.30%	-0.73%	0.35%

Table 4: Error comparison between porosity and XFEM approach for $Re = 0.1$.

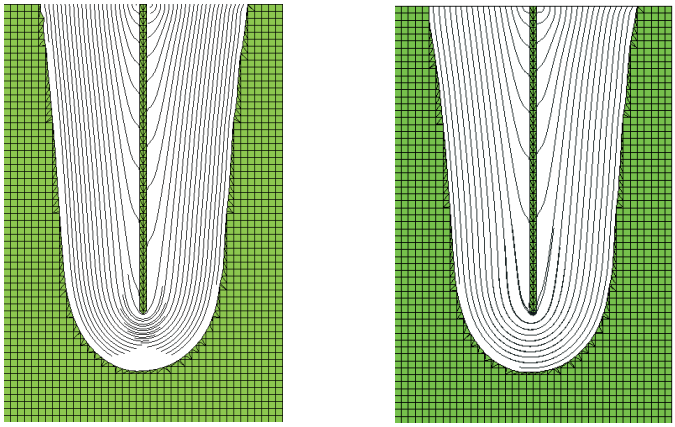

(a) $Re = 0.1$ (b) $Re = 10$

Figure 8: XFEM based optimized geometries for U-bend, with velocity streamlines.

i.e. we want to find a design for which the total pressure at the inlet is four times the total pressure at the outlet, subject to box constraints on the design variables.

The initial design for the XFEM case is shown in Fig. 11b, the porosity distribution is initialized as 100% fluid; both cases are discretized by 60×30 elements. The parameters defining this problem are listed in Tab. 5. The XFEM based optimization problem converges to the design depicted in Fig. 12a. The geometry has an objective of $z = 7.95 \times 10^{-4}$. Solving the optimization problem with the porosity approach leads to the porosity distribution in Fig. 12b which is of little value for identifying a reasonable geometry.

While the XFEM approach leads to an somewhat intuitive design that generates the desired pressure drop, we point out that the solution of the optimization problem (28) depends on the initial levelset field. For example, initializing the levelset fields with small circular solid areas at the bottom and top corner either at the inlet (case A) or the outlet (case B), as shown in Fig. 13a leads to the designs depicted in Fig. 13b. In case A the objective is $z = 1.48 \times 10^{-3}$ and in case B $z = 2.37 \times 10^{-3}$, thus both designs match the desired total pressure ratio well.

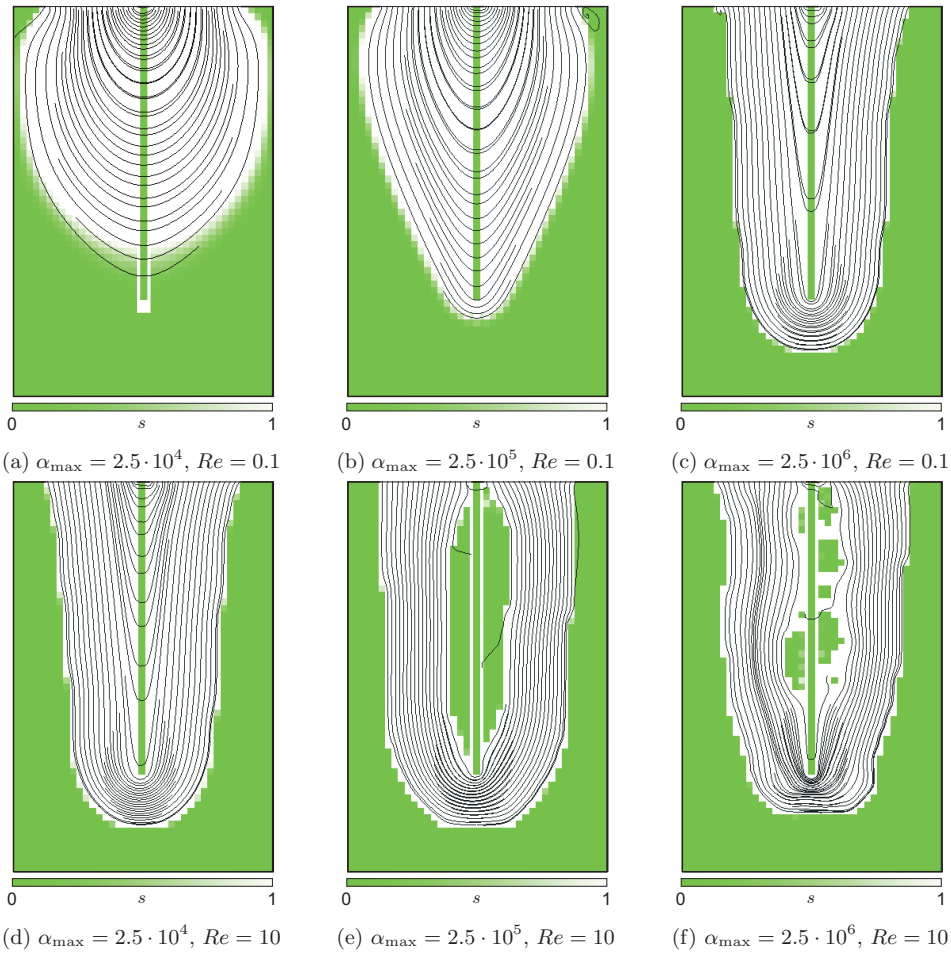

(a) $\alpha_{\max} = 2.5 \cdot 10^4$, $Re = 0.1$ (b) $\alpha_{\max} = 2.5 \cdot 10^5$, $Re = 0.1$ (c) $\alpha_{\max} = 2.5 \cdot 10^6$, $Re = 0.1$

(d) $\alpha_{\max} = 2.5 \cdot 10^4$, $Re = 10$ (e) $\alpha_{\max} = 2.5 \cdot 10^5$, $Re = 10$ (f) $\alpha_{\max} = 2.5 \cdot 10^6$, $Re = 10$

Figure 9: Porosity based optimized geometries for U-bend, with velocity streamlines.

7 Conclusion

This study has presented a topology optimization approach for flow problems combining a levelset description of the geometry and an XFEM formulation of the incompressible Navier-Stokes equations. As the proposed work does not rely on fictitious porous material, no material interpolation model has to be defined nor does it require particular objectives and constraints for driving the design to a 0-1 material distribution. Thus, the proposed topology optimization method provides great flexibility in solving optimization problems with a broad range of objectives and constraints. Further, the XFEM approach prevents spurious pressure diffusion through solid material as it occurs in the Brinkman formulation. Finally, it was shown for the Brinkman penalization that the accuracy of the flow field is very sensitive to material interpolation parameters, which may affect the optimization results.

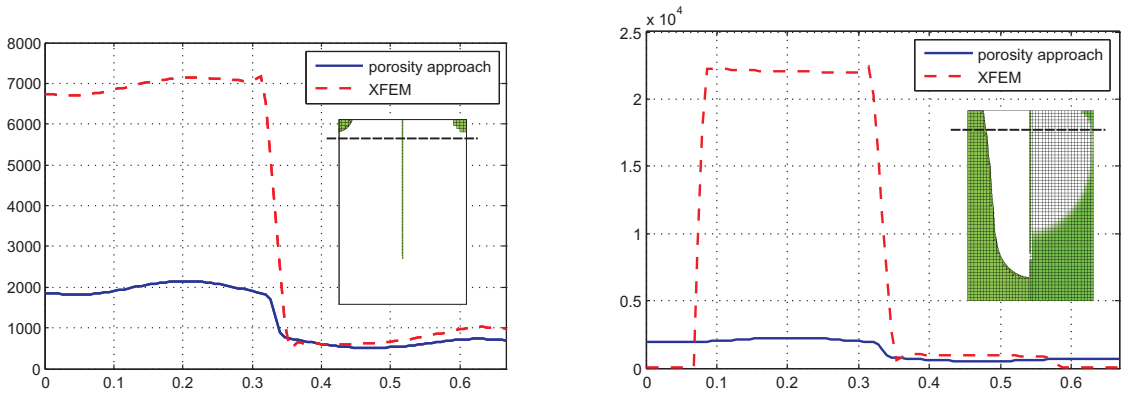

(a) Initial design (b) Optimized design

Figure 10: Pressure in x-direction at constant $y = 0.9H$ for $Re = 0.1$ and 41×61 discretization (for porosity approach: $\alpha_{\max} = 2.5 \cdot 10^4$).

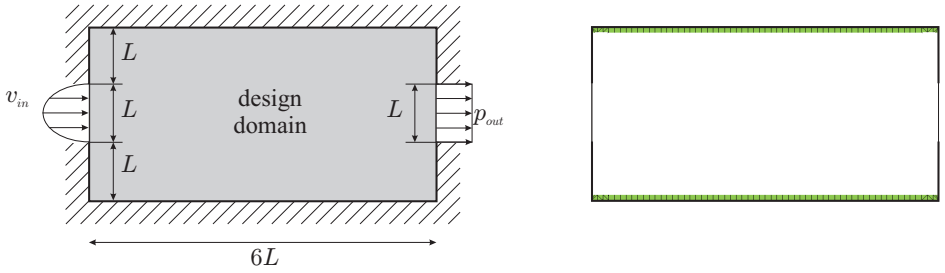

(a) Design domain (b) Initialization (for XFEM)

Figure 11: Nozzle example.

However, since the sensitivities only differ from zero within a band around the interface, it is only possible to systematically merge existing boundaries, but no new domains of solid can emerge. However, this limitation can be mitigated by seeding the initial design with a sufficient number of separated solid areas. Compared to the Brinkman penalization, the proposed approach is significantly more complex in regards of implementation, potentially preventing the use of commercial software tools.

Acknowledgments

The authors acknowledge the support of the National Science Foundation under grant DMI-0729529. The opinions and conclusions presented in this paper are those of the authors and do not necessarily reflect the views of the sponsoring organization.

Parameter type	**Parameter**	**Value**
nondim. flow parameters	reference length, L	1
	max. inlet velocity, $\max(v_{in})$	1.5
	outlet pressure, p_{out}	1
	density, ρ	1
	Reynolds number, Re	10
optimization parameters (common)	KKT threshold, ϵ^{KKT}	0.2
	design change threshold, ϵ^{d}	10^{-5}
optimization parameters (XFEM approach)	optimizer step size, Δs	0.02
	interpolation penalty, p_{α}	0.001
	constraint penalty, p_g	n/a
	relative smoothing radius, r^s	4.5
optimization parameters (porosity approach)	optimizer step size, Δs	10^{-4}
	constraint penalty, p_g	n/a
	interpolation penalty, p_{α}	0.1
	max. impermeability, $\alpha_{\max}$	$2.5 \cdot 10^4$

Table 5: Parameter settings for nozzle.

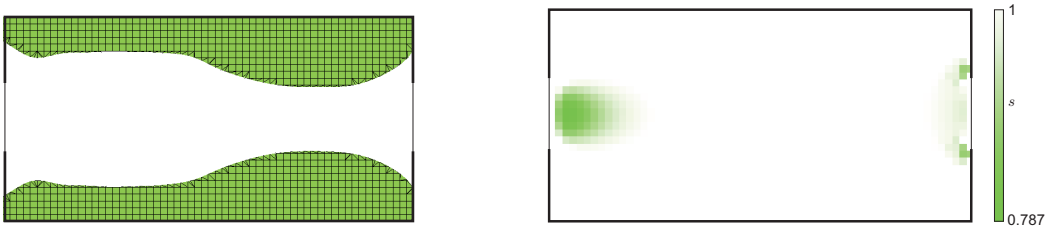

(a) XFEM (b) Porosity approach

Figure 12: Optimized nozzle geometries.

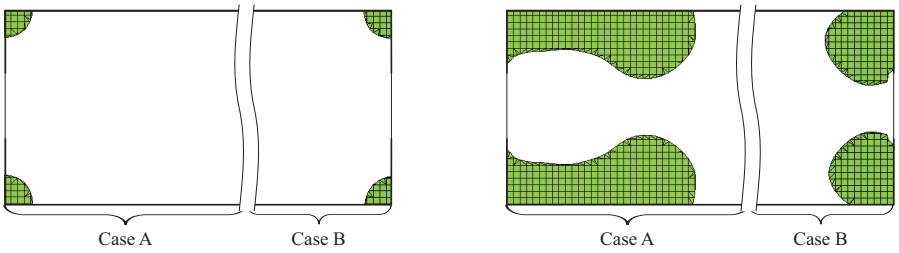

(a) Initial designs (b) Optimized geometries

Figure 13: Influence of initial design.

References

[1] T. Borrvall and J. Petersson. Topology optimization of fluids in Stokes flow. *International Journal for Numerical Methods in Fluids*, 41(1):77–107, 2003.

[2] L. H. Olesen, F. Okkels, and B. Bruus. A high-level programming-language implementation of topology optimization applied to steady-state Navier-Stokes flow. *International Journal for Numerical Methods in Engineering*, 65:975–1001, 2006.

[3] G. H. Yoon. Topology optimization for stationary fluid-structure interaction problems using a new monolithic formulation. In *8th World Congress on Structural and Multidisciplinary Optimization*, June 2009.

[4] S. Kreissl, G. Pingen, A. Evgrafov, and K. Maute. Topology optimization of flexible microfluidic devices. *Structural and Multidisciplinary Optimization*, 42:495–516, 2010.

[5] S. Kreissl, G. Pingen, and K. Maute. Topology optimization for unsteady flow. *International Journal for Numerical Methods in Engineering*, pages n/a–n/a, 2011.

[6] Y. Deng, Z. Liu, P. Zhang, Y. Liu, and Y. Wu. Topology optimization of unsteady incompressible Navier-Stokes flows. *Journal of Computational Physics*, In Press, Corrected Proof:–, 2011.

[7] M. P. Bendsøe and O. Sigmund. *Topology Optimization: Theory, Methods and Applications*. Springer, 2003.

[8] G. Allaire, F. Jouve, and A.-M. Toader. Structural optimization using sensitivity analysis and a level-set method. *Journal of Computational Physics*, 194(1):363 – 393, 2004.

[9] V. Challis and J. K. Guest. Level set topology optimization of fluids in Stokes flow. *International Journal for Numerical Methods in Engineering*, 79(10):1284–1308, 2009.

[10] G. Pingen, M. Waidmann, A. Evgrafov, and K. Maute. A parametric level-set approach for topology optimization of flow domains. *Structural and Multidisciplinary Optimization*, 41(1):117–131, 2009.

[11] S. Kreissl, G. Pingen, and K. Maute. An explicit level-set approach for generalized shape optimization of fluids with the lattice Boltzmann method. *International Journal for Numerical Methods in Fluids*, 2009. Available online: DOI 10.1002/fld.2193.

[12] M. Y. Wang and X. Wang. PDE-driven level sets, shape sensitivity and curvature flow for structural topology optimization. *Computer Modeling in Engineering & Sciences*, 6(4):373–395, October 2004.

[13] M. J. De Ruiter and F. van Keulen. Topology optimization using a topology description function. *Structural and Multidisciplinary Optimization*, 26(6):406–416, 2004.

[14] A. L. Cunha. *A Fully Eulerian Method for Shape Optimization with Application to Navier-Stokes Flows*. PhD thesis, Carnegie Mellon University, Pittsburgh, PA 15213, September 2004.

[15] B. Mohammadi and O. Pironneau. Theory and practice of optimal shape design. *European Journal of Computational Mechanics*, 17(1-2):13–30, 2008.

[16] G. Pingen, M. Waidmann, A. Evgrafov, and K. Maute. Application of a parametric level-set approach to topology optimization fluid with the Navier-Stokes and lattice Boltzmann equations. In *WCSMO07, May 21-25*, Seoul, Korea, 2007. ISSMO.

[17] X. Duan, Y. Ma, and R. Zhang. Optimal shape control of fluid flow using variational level set method. *Physics Letters A*, 372(9):1374—1379, 2008.

[18] X.B. Duan, Y.C. Ma, and R. Zhang. Shape-topology optimization of stokes flow via variational level set method. *Applied Mathematics and Computation*, 202(1):200 – 209, 2008.

[19] X.B. Duan, Y.C. Ma, and R. Zhang. Shape-topology optimization for Navier-Stokes problem using variational level set method. *Journal of Computational and Applied Mathematics*, 222(2):487 – 499, 2008.

[20] S. Zhou and Q. Li. A variational level set method for the topology optimization of steady-state Navier-Stokes flow. *Journal of Computational Physics*, 227(24):10178 – 10195, 2008.

[21] H. C. Brinkman. A calculation of the viscous force exerted by a flowing fluid on a dense swarm of particles. *Applied Scientific Research, Sect. A*, 1:27, 1947.

[22] P. Angot, C.-H. Bruneau, and P. Fabrie. A penalization method to take into account obstacles in viscous flows. *Numerische Mathematik*, 81:497–520, 1999.

[23] T. Belytschko and T. Black. Elastic crack growth in finite elements with minimal remeshing. *International Journal for Numerical Methods in Engineering*, 45, 1999.

[24] N. Moës, J. Dolbow, and T. Belytschko. A finite element method for crack growth without remeshing. *International Journal for Numerical Methods in Engineering*, 46, 1999.

[25] N. Sukumar, N. Moës, B. Moran, and T. Belytschko. Extended finite element method for three-dimensional crack modelling. *International Journal for Numerical Methods in Engineering*, 48(11):1549–1570, 2000.

[26] C. Daux, N. Moës, J. Dolbow, N. Sukumar, and T. Belytschko. Arbitrary branched and intersecting cracks with the extended finite element method. *International Journal for Numerical Methods in Engineering*, 48(12):1741–1760, 2000.

[27] L. van Miegroet and P. Duysinx. Stress concentration minimization of 2D filets using X-FEM and level set description. *Structural and Multidisciplinary Optimization*, 33(4-5):425–438, April 2007.

[28] P. Wei, M. Wang, and X. Xing. A study on X-FEM in continuum structural optimization using a level set model. *Computer-Aided Design*, 42(8):708 – 719, 2010. Application-driven Shape Development.

[29] S. Y. Wang and M. Y. Wang. A moving superimposed finite element method for structural topology optimization. *International Journal for Numerical Methods in Engineering*, 65(11):1892–1922, March 2006.

[30] J. Chessa and T. Belytschko. An extended finite element method for two-phase fluids. *Journal of Applied Mechanics*, 70(1):10–17, 2003.

[31] H. Sauerland and T.-P. Fries. The extended finite element method for two-phase and free-surface flows: A systematic study. *Journal of Computational Physics*, 230(9):3369 – 3390, 2011.

[32] A. Gerstenberger and W. A. Wall. Enhancement of fixed-grid methods towards complex fluidstructure interaction applications. *Int. J. Numer. Meth. Fluids*, 57(9):1227–1248, 2008.

[33] A. Gerstenberger and W. A. Wall. An embedded Dirichlet formulation for 3D continua. *Int. J. Numer. Meth. Engng.*, 82(5):537–563, 2010.

[34] T. E. Tezduyar, S. Mittal, S. E. Ray, and R. Shih. Incompressible flow computations with stabilized bilinear and linear equal-order-interpolation velocity-pressure elements. *Computer Methods in Applied Mechanics and Engineering*, 95:221–242, 1992.

[35] S. Osher and J. A. Sethian. Fronts propagating with curvature dependent speed: algorithms based on Hamilton-Jacobi formulations. *Journal of Computational Physics*, 79:12—49, 1988.

[36] O. Sigmund and J. Petersson. Numerical instabilities in topology optimization: A survey on procedures dealing with checkerboards, mesh-dependencies and local minima. *Structural and Multidisciplinary Optimization*, 16(1):168–75, August 1998.

[37] F. Daoud, M. Firl, and K.-U. Bletzinger. Filter techniques in shape optimization with CAD-free parametrization. In *6th World Congresses of Structural and Multidisciplinary Optimization*, Rio de Janeiro, Brazil, 2005.

[38] M. Burger, B. Hackl, and W. Ring. Incorporating topological derivatives into level set methods. *Journal of Computational Physics*, 194(1):344 – 362, 2004.

[39] M. J. De Ruiter. *Topology Optimization Using a Topology Description Function Approach*. PhD thesis, Technische Universiteit Delft, 2005.

[40] K. Svanberg. A globally convergent version of MMA without linesearch. In *Proceedings of the First World Congress of Structural and Multidisciplinary Optimization, 28 May - 2 June 1995*, pages 9–16, Goslar, Germany, 1995.

[41] H. W. Kuhn and A. W. Tucker. Nonlinear programming. In *Proceedings of the Second Berkeley Symposium on Mathematical Statistics and Probability, 1950*, pages 481–492, Berkeley and Los Angeles, 1951. University of California Press.

[42] G. Pingen, A. Evgrafov, and K. Maute. Topology optimization of flow domains using the lattice Boltzmann method. *Structural and Multidisciplinary Optimization*, 36(6):507–524, 2007.

[43] K. Khadra, P. Angot, S. Parneix, and J.P. Caltagirone. Fictitious domain approach for numerical modelling of Navier-Stokes equations. *International Journal For Numerical Methods In Fluids*, 34(8):651–684, DEC 30 2000.